SAPIENZA
UNIVERSITÀ DI ROMA

The gas and dust cycle in the first galaxies

Sapienza Università di Roma
PhD program in Physics (XXXVI cycle)

Claudia Di Cesare
ID number 1950556

Advisors
Prof. Raffaella Schneider
Dr. Luca Graziani
Dr. Michele Ginolfi

Coordinator
Prof. Federico Ricci Tersenghi
Academic Year 2023/2024

Thesis defended on 30 May 2024
in front of a Board of Examiners composed by:

Prof. Paola Leaci (chair)

Prof. Roberto Maiolino

Prof. Constança Providência

The gas and dust cycle in the first galaxies
Sapienza University of Rome

This thesis has been typeset by LaTeX and the Sapthesis class.

Author's email: claudia.dicesare@uniroma1.it

Alla mia famiglia, tutta

Contents

Introduction

The investigation of the evolution of high-redshift galaxies is a crucial field of research in modern astronomy. In fact, distant galaxies offer us a glimpse back into the cosmic history of our Universe, allowing us to study the early stages of structure formation and evolution. In this thesis, I explore the intricate landscape of high-redshift galaxy evolution, focusing on the physical properties of $z > 4$ galaxies and their interaction with the surrounding environment, with the aim of understanding the chemical maturity of such galaxies.

Our understanding of the primordial Universe has been revolutionized in the last decades thanks to technological advancements and the availability of advanced instrumentation such as HST, ALMA, and, more recently, JWST. In particular, the combination of multi-band observations from the above facilities has provided us with a more comprehensive picture of the evolution of high-redshift galaxies, not only allowing us to study in detail their physical integrated properties (e.g. stellar mass, dust mass, metallicity, etc.), but also their star formation and interaction with the surrounding environment. In fact, galaxies can be considered as complex ecosystems whose evolution is governed by the interplay of physical mechanisms involving both their Interstellar and Circumgalactic Media. Key processes such as the accretion of external cold gas, star formation, chemical enrichment, gas recycling in the ISM and the ejection of processed material through starburst/quasar-driven outflows constitute the building blocks of the so-called "baryon cycle" governing the evolution of galaxies. In addition, models and simulations are of paramount importance to lead our interpretation of the observations from telescopes. In fact, cosmological simulations play a pivotal role in helping us understand the aforementioned baryon cycle, its role in galaxy evolution, and the properties of our Universe at different epochs.

In this thesis, I employ both observations and simulations, highlighting their interplay in exploring and interpreting the primordial Universe. Generally, simulations have assisted us in predicting potential scenarios of galaxy evolution by reproducing the interplay among various feedback mechanisms and by interpreting observational data. Conversely, observations have been of vital importance for validating our models and providing evidence of the phenomena characterising the early Universe ($z \geq 4$).

The contents of the thesis are organized as follows.

In Chapter 1 I provide an overview of the cosmological context in which the work is situated, giving a basic description of the cosmic evolution of the large-scale structure and its assembly.

In Chapter 2 I give an introduction of the observational tools and techniques

adopted to identify high-z galaxies. Then, I discuss the two telescopes relevant to this thesis: ALMA (Section 2.2) and JWST (Section 2.3), specifically focusing on the main results obtained from the ALMA-ALPINE and ALMA-REBELS Large Programs as well as the early observations and questions about the high-z Universe posed by JWST.

In Chapter 3, I explore the numerical methods adopted in modern state-of-the-art simulations to model galaxy formation and evolution. Moreover, in Section 3.2 I introduce the cosmological simulation `dustyGadget` that has been adopted throughout this work, highlighting the simulation strategy and the novelty introduced by this simulation (i.e. the implementation of dust formation and evolution ensuring consistency with the metal content of galaxies).

The investigation of the build-up of galaxies stellar mass and the relations among the integrated physical properties of galaxies at $4 \leq z \leq 10$ is presented in Chapter 4. Specifically, I started studying the cosmic evolution of the star formation and cosmic stellar mass density. Then, I present numerous galaxy scaling relations that link the stellar mass of collapsed objects with various galaxy or dark matter halo properties. These include the main sequence of galaxy formation and the specific star formation rate evolution. Finally, I delve into the relation between stellar and dust mass which gives us hints about the chemical maturity of the interstellar medium of galaxies at $z > 4$. Through this chapter, I make use of `dustyGadget` predictions for high-z galaxies and I compare them with available observational data from both the ground-based telescope ALMA and the space telescope JWST.

More insights about the interaction between galaxies and their environment are given in Chapter 5, where I discuss the [CII] 158 µm line emission coming from the medium surrounding merging galaxies at $z \sim 4.5$. In this chapter, I first present the analysis conducted on observations of major merging systems from the ALMA-ALPINE survey giving insights into their properties and the relation between the [CII] 158 µm emission from their diffuse envelope and their integrated physical properties. Then, I adopt the cosmological simulation `dustyGadget` to search for the synthetic analogues of the observed objects to investigate the nature of such diffuse emission. This is possible due to the higher resolution we achieved in simulations compared to the ALMA-ALPINE observations.

Through this research work, I aim to contribute to the understanding of high-redshift galaxy evolution, providing new insights into the fundamental processes that have shaped the primordial Universe and influenced its evolution to the present day.

Frequently used acronyms

AGB(s): Asymptotic Giant Branch (stars)

AGN: Active Galactic Nuclei

ALMA: Atacama Large Millimeter/submillimeter Array

CMB: Cosmic Microrwave Background

CGM: Circumgalactic Medium

DM: Dark Matter

FIR: Far Infra-Red

FWHM: Full Width Half Maximum

HST: Hubble Space Telescope

IMF: Initial Mass Function

IGM: Intergalactic Medium

IR: Infra-Red

ISM: Interstellar Medium

MS: Main Sequence

NIR: Near-IR

SED: Spectral Energy Distribution

SFH: Star Formation History

SFR: Star Formation Rate

SFRD: Cosmic Star Formation Rate Density

SMD: Cosmic Stellar Mass Density

SMF: Stellar Mass Function

SN(e): Supernova(e)

sSFR: Specific Star Formation Rate

UV: Ultra-Violet

JWST: James Webb Space Telescope

Chapter 1

Cosmological context

Cosmology is the domain of physics that investigates the global characteristics of the Universe, defining the space-time structures on large scales where galaxy formation and evolution take place. Modern cosmology has its roots in (i) the cosmological principle, the hypothesis that the Universe is spatially homogeneous and isotropic, and (ii) Einstein's theory of General Relativity (GR), according to which the structure of space-time is determined by the mass distribution in the Universe. As we are going to see in the following, these two assumptions together lead to a cosmology that is completely defined by the curvature of the Universe, k, and the scale factor, $a(t)$, which describes how length scales of the Universe change with time. One of the most important observations in cosmology is that the Universe is expanding (see Section 1.2), i.e. the scale factor increases with time, implying that $a(t)$ must have been smaller in the past. Together with the observation that the Universe is filled with microwave photons, the so-called Cosmic Microwave Background, this time evolution of the scale factor determines the thermal history of the Universe. Being denser in the past, the Universe must have also been hotter compared to the present day. High density and high temperature lead to higher collisional probabilities among particles. The application of particle, nuclear and atomic physics to the thermal history of the Universe leads to predictions on the current matter content of the Universe, providing the basis for calculating relations between the components of the Universe. This chapter is only meant to be an introduction to the cosmological context in which galaxies evolve; the interested reader can find more details about modern cosmology in Kolb and Turner (1990); Peebles (1993); Peacock (1999); Coles and Lucchin (2002); Padmanabhan (2002); Mo et al. (2010).

1.1 The Cosmological Principle

The cosmological principle is at the basis of our understanding of the Universe and it affirms that, on sufficiently large scales (10^2 Mpc, Peebles 1993), the Universe is homogeneous and isotropic. Homogeneity means uniform conditions everywhere and at every given time, and isotropy means the same conditions in all directions

for any observers. The last one being also the strongest condition:

$$\text{isotropy for every observer} \Rightarrow \text{homogeneity}$$
$$\text{homogeneity} \not\Rightarrow \text{isotropy for every observer}$$

indeed, the Universe can be homogeneous but not isotropic (e.g. the expansion rate could vary according to the direction), but also isotropic and not homogeneous (e.g. we could be at the center of a spherically symmetric mass distribution). However, if it is isotropic for *every* observers, then it must also be homogeneous.

Because of the cosmological principle, a unique time coordinate throughout space can be established by distributing synchronised clocks all around the Universe, so that each clock would measure the same time t since the Big Bang i.e. clocks are moving along (comoving) with the expanding Universe (cosmic time). In this scenario, the space-time (4-dimensional) line element ds is described by the Friedmann-Lemaître-Robertson-Walker (FLRW) metric (Robertson, 1935):

$$ds^2 = c^2dt^2 - dl^2 \tag{1.1}$$

where c is the speed of light and dl is the line element. The space-time interval ds is real if two events are separated in time, zero if they are on the same light-path (null geodesic), and imaginary if they are separated in space.

The expansion of the Universe (see Section 1.2) can be parameterised by the dimensionless parameter $a(t)$, known as the *scale factor* which is defined as

$$a(t) = D(t)/D(t_0) \tag{1.2}$$

where $D(t)$ is the proper distance at some time t and $D(t_0)$ is the proper distance at some reference time t_0. This definition assures that $a(t_0) = 1$, and the present epoch is generally considered as the reference time, thus $a = 1$ today. Also, the scale factor is linked to the redshift (see Section 1.2 for the definition) by the relation $a(t) = 1/(1 + z(t))$.

Once we introduce $a(t)$, consider a spatially homogeneous and isotropic Universe and adopt spherical coordinates (r, θ, ϕ) Equation 1.1 becomes:

$$ds^2 = c^2dt^2 - a(t)\left[\frac{dr^2}{1 - k\,r^2} - r^2d\Omega^2\right] \tag{1.3}$$

where $d\Omega^2 = d\theta^2 + sin^2\theta d\phi^2$ and k is the space curvature. If $k > 0$, the Universe is positively curved and therefore is closed; if $k > 0$ it is negatively curved and then open; if $k = 0$ the Universe is flat. The $k = 0$ curvature of the Universe is the favoured one by recent observations (see for example Planck Collaboration et al. 2016).

Naturally, in an expanding Universe, we need to define different types of distance indicators. On one hand, two points whose distance changes in time only because of the expansion are said to be at a constant comoving distance. Thus comoving distance is defined as the distance measured in a coordinate system that follows the so-called Hubble flow. On the other hand, proper distance is measured with a coordinate system that does not take into account the expansion of the Universe, thus the distance between the two points will change according to the scale factor variation, i.e. proper distance is the distance between two regions of space at a constant cosmological time.

1.2 Hubble-Lemaître law and lookback time

Another ingredient of paramount importance in modern cosmology is the adherence of every cosmological model to cosmic expansion. In 1927-1929 based on galaxy samples for which radial velocities and distances were available, G. Lemaître and E. Hubble performed the first direct observations of the expansion of the Universe (see Hubble 1929), showing that local galaxies are receding from us. In particular, their radial velocity, v, is proportional, following a linear relation, to their distance from us, D: the farther away the galaxies, the higher the velocity at which they move away from us. Specifically, the Hubble-Lemaître [1] law is defined as:

$$v = H_0 D \tag{1.4}$$

where H_0 is the Hubble constant and it is usually expressed in km/sMpc^{-1}. Measuring the Hubble constant is one of the most important open problems in Cosmology and observations from early-time and late-time probes give statistically incompatible results, the so-called Hubble tension (see Di Valentino et al. 2021 for a recent review and, van Putten 2023; Lovell et al. 2023 for example, for observations with JWST). In this work, we use the reduced dimensionless Hubble constant defined as $h = H_0/(100\,\mathrm{km\,s^{-1}\,Mpc^{-1}})$ and assume $h = 0.6774$ following the results from the Planck mission (Planck Collaboration et al., 2016).

The Hubble-Lemaître law can be rewritten in terms of the scale factor, *a(t)*, by introducing one of the most important and used quantities in astrophysics: the redshift z, defined as:

$$z = \frac{\lambda_{obs} - \lambda_{em}}{\lambda_{em}} \tag{1.5}$$

where λ_{obs} and λ_{em} are respectively the observed and emitted wavelength. The shift between the observed and emitted wavelength can be caused by different factors, for example, the relative peculiar velocity of the source, the presence of a gravitational potential or by the expansion of the Universe which increases the radiation wavelength (hence decreases its energy). From special relativity, in the approximation of small v/c (see Hogg 1999) we have:

$$z = \sqrt{\frac{1 + v/c}{1 - v/c}} \approx \frac{v}{c} \tag{1.6}$$

which leads to:

$$z \simeq \frac{H_0 D}{v}. \tag{1.7}$$

Keeping in mind the relation between z and the scale factor, we can write:

$$\frac{a_{obs}}{a_{em}} = \frac{1}{a} = \frac{\lambda_{obs}}{\lambda_{em}} = 1 + z \tag{1.8}$$

with $a_{obs} \equiv a(t_{obs})$ and $a_{em} \equiv a(t_{em})$. This relation makes redshift, which is directly observable, a key quantity in cosmology. Indeed, the radiation coming from distant

[1] In 2018, the members of the International Astronomical Union (IAU) voted to rename the Hubble law as the Hubble-Lemaître law (https://www.iau.org/news/pressreleases/detail/iau1812/).

galaxies carries an imprint/information about the scale factor at the time of the signal emission. In an expanding Universe, $a(t_{obs}) > a(t_{em})$ thus, from Equation 1.8, $z > 0$ and the spectral features of galaxies are shifted redwards (redshift). On the other hand, in a contracting Universe, $a(t_{obs}) < a(t_{em})$, thus $z < 0$, and spectral features are shifted bluewards (blueshift). Distant galaxies in the Universe are all observed to have redshifted spectra, indicating that the Universe is expanding.

Because of the expansion of the Universe and of the finite value of the speed of light, the distance between two cosmological events is not a trivial concept. Indeed, being on Earth today ($z = 0$) an looking for objects which are far from us means that we are looking *back in time*. This introduces the concept of lookback time, which is a backward time in the history of the Universe, defined as as the difference between the age of the Universe today (~ 13.8 Gyr) and the age of the Universe at the time of signal emission (e.g. λ_{em}). Redshift and lookback time are two conceptually equivalent ideas to define the distance of a source, as both imply a measure of the separation between two events (emission of an electromagnetic wave) along the direction of photon propagation. The lookback time is linked to the redshift via the relation (Hogg, 1999):

$$t_L = \frac{1}{H_0} \int_0^z \frac{dz'}{(1+z')E(z')} \tag{1.9}$$

where $E(z)$ embeds the cosmology and it is defined as

$$E(z) = \sqrt{\Omega_{m,0}(1+z)^3 + \Omega_{k,0}(1+z)^2 + \Omega_{\Lambda,0}} \tag{1.10}$$

where the cosmological parameters $\Omega_{m,0}$, $\Omega_{k,0}$, $\Omega_{\Lambda,0}$, are derived from the Friedmann equations and introduced in Section 1.3.1 Here we assume $\Omega_{r,0} = 0$ (see Section 1.4). Using the definition of $E(z)$, from the Hubble-Lemaître law it follows that H_0 measured from an observed at redshift z is

$$H(z) = H_0 E(z). \tag{1.11}$$

Thus, the term $dz/E(z)$ in Equation 1.10 is proportional to the flight time of a photon traveling at c through the dz element of the Universe. Furthermore, through the function $E(z)$, the lookback time exhibits a strong dependence on the assumed cosmology (H_0, $\Omega_{m,0}$).

1.2.1 Distances in cosmology

In an expanding universe, the concept of distance is a very delicate topic as distances themselves don't have a universal definition. In this section, we are going to introduce different definitions of distance that are common in Astrophysics and that will be used in the present work.

Proper distance and comoving distance We already introduced the proper distance and its relation to the scale factor $a(t)$ in Section 1.1. The proper distance is the distance, as we intend it in everyday life, between two objects. However, in an expanding universe, the distance between two objects that are subject to the Hubble flow is not constant, as these objects are moving apart from each other.

The comoving distance, on the other hand, is the distance between two systems co-moving with the Hubble-flow.

The comoving distance is defined as a function of the scale factor or, equivalently, of the redshift:

$$D_c = \frac{c}{H_0} \int_0^z \frac{dz'}{E(z')} \ . \tag{1.12}$$

Defining D as the proper distance among the two sources, the relation between proper and comoving distance is

$$D_c = D(1+z) \tag{1.13}$$

so that today $D_c \equiv D$.

Transverse comoving distance As in astronomy we look at objects in the sky, it is useful to define the transverse comoving distance between objects, intended as the separation projected on the sky plane between two objects. This distance is defined for sources at the same redshift and separated in the sky by $\delta\theta$, so that:

$$D_c = D_M \delta\theta \tag{1.14}$$

with D_c the comoving distance. In a flat universe, with null curvature ($\Omega_k = 0$), $D_c \equiv D_M$.

Comoving volume After defining the comoving distance, it is possible to introduce the concept of comoving volume as the region of the Universe contained in a constant comoving space, meaning that it expands with the Hubble flow. This corresponds to the volume that contains a fixed total mass. Thus, if we use a comoving distance to define the side of the comoving volume, the average comoving density inside the volume remains constant (none of the galaxies/objects exits the unit volume while the Universe expands). Any variation in the density indicates a change in the population under study and cannot be attributed to the geometry of the Universe. The comoving volume at redshift dz can be expressed as:

$$dV_c = \frac{c}{H_0} \frac{D_M^2}{E(z)} d\omega dz \tag{1.15}$$

function of the solid angle $d\omega$, of the comoving distance D_c via D_M and cosmology via $E(z)$.

Angular distance Given the image of a source, the angular diameter distance, D_A, is defined as the ratio between the actual dimension of the object to the angular dimension under which it is projected in the sky, that is:

$$size = D_A \delta\theta \tag{1.16}$$

Using D_A, it is possible to convert the angular separation between two images detected by the telescope into the proper distance between the two sources. The relation between D_A and D_M and, as a consequence, D_c is:

$$D_A = \frac{D_M}{1+z} \tag{1.17}$$

which decreases above a certain redshift threshold established by the assumed cosmology. This means that D_A does not increase as $z \to \infty$, but rather shows a turnover beyond which it starts decreasing. This occurs because after a certain redshift threshold, the universe becomes smaller, looking back in time (high-z), means observing a younger universe of smaller dimensions.

Luminosity distance The luminosity distance is defined as a function of the flux from the source as

$$D_L = \sqrt{\frac{L}{4\pi F}} \tag{1.18}$$

with L being the bolometric (i.e. integrated over all frequencies) luminosity of the object. D_L is linked to the transverse comoving distance and to the angular diameter distance via

$$D_L = (1+z)D_M = (1+z)^2 D_A \, . \tag{1.19}$$

1.3 Friedmann equations

Our expanding Universe can be described using the FLRW metric together with Einstein equation of GR. In fact, in the standard model of cosmology the geometry of space-time is fully determined by the matter and energy content of the Universe through the Einstein field equation:

$$G_{\mu\nu} = \frac{8\pi \mathrm{G}}{c^4} T_{\mu\nu} \tag{1.20}$$

where G is the Newton gravitational constant, $G_{\mu\nu}$ is the Einstein tensor, and $T_{\mu\nu}$ is the so-called stress-energy tensor, which describes the influence of matter and energy on the dynamics of space-time. $G_{\mu\nu}$ is defined as:

$$G_{\mu\nu} = R_{\mu\nu} - \frac{1}{2} \mathrm{R} \, g_{\mu\nu} - \Lambda \, g_{\mu\nu} \tag{1.21}$$

where $R_{\mu\nu}$ is the Ricci tensor, that describes the local curvature of the space-time, R is the curvature scalar, $g_{\mu\nu}$ is the metric tensor[2] and Λ is the cosmological constant. The cosmological constant was initially introduced by Einstein to obtain a static solution (i.e. a solution describing a static Universe) to his equation. After Hubble and Lemaître discovery of an expanding Universe, Einstein discarded the constant Λ which has, nowadays, been reintroduced as representative of a uniform energy density (dark energy) that might explain the accelerated expansion of the Universe (Perlmutter et al., 1999). As already introduced, the stress-energy tensor $T_{\mu\nu}$ acts as the source term in Equation 1.20, dictating how energy and momentum contribute to the curvature of the space-time. If we consider an isotropic and homogeneous

[2] In GR the metric tensor is the mathematical object used to describe the space-time, which allows us to measure an infinitesimal interval ds between two events in space-time. Using the metric tensor, Equation 1.1 can be written as

$$ds^2 = g_{\mu\nu} \, dx^\mu \, dx^\nu \tag{1.22}$$

.

Universe, the mass and energy can be described as a perfect fluid. In this scenario, the energy-momentum tensor takes the form of:

$$T_{\mu\nu} = (\rho + P/c^2)\ u_\mu\ u_\nu - P\ g_{\mu\nu} \tag{1.23}$$

with $\rho\ c^2$ the energy density, P is the pressure, and $u^\mu = cdx^\mu/ds$ is the 4-velocity of the fluid. In a homogeneous and isotropic universe, the density and pressure depend only on the cosmic time, and the 4-velocity is $u^\mu = (c, 0, 0, 0)$ - no peculiar motion is allowed.

If we write the FLRW metric as $ds^2 = g_{\mu\nu}\ dx^\mu\ dx^\nu$ and keep in mind the FLRW metric in spherical coordinates (Equation 1.3), we obtain for the metric tensor:

$$g_{\mu\nu} = diag(1\ , -a(t)^2 \frac{1}{1 - k\ r^2}\ , -a(t)^2\ r^2\ , -a(t)^2\ r^2\ sin^2\theta) \tag{1.24}$$

which becomes $g_{\mu\nu} = diag(1, a^2, a^2, a^2)$ when we consider a flat Universe with a curvature $k = 1$ and Cartesian coordinates.

By using Equation 1.24 it is possible to compute the Ricci tensor and, as a consequence, to calculate the left-hand side of Equation 1.20. Then, by combining this result with the definition of $T_{\mu\nu}$, it is possible to derive a more explicit form of the components of the Einstein field tensor equation (Equation 1.20). The two non-null scalar equations are the so-called Friedmann equations. The first one describes the evolution of the homogeneous Universe, in the form of a differential equation for the scale factor:

$$\left(\frac{\dot{a(t)}}{a(t)}\right)^2 = \frac{8\ \pi\ \mathrm{G}}{3}\ \rho(t) - \frac{k\ c^2}{a(t)^2} + \frac{\Lambda\ c^2}{3} \tag{1.25}$$

and the second one is

$$\frac{\ddot{a(t)}}{a(t)} = -\frac{4\ \pi\ \mathrm{G}}{3}\left(\rho(t) + \frac{3\ P}{c^2}\right) + \frac{\Lambda\ c^2}{3}\ . \tag{1.26}$$

The continuity equation for a perfect fluid in an expanding Universe is given by the conservation of the energy-momentum tensor which leads to:

$$\frac{d\rho}{da} + 3\left(\frac{\rho + P/c^2}{a}\right) = 0\ . \tag{1.27}$$

Equation 1.27, together with the first Friedmann equation (Equation 1.25) and an equation of state (EoS) which provides pressure as a function of density (i.e. $P = P(\rho)$), defines a system of three equations with three variables ρ, P and a; which allows us to determine the time evolution of the scale factor and, therefore, to compute the expansion of the Universe along cosmic time.

We assume cosmological fluids to be described by a simple EoS of the form

$$P = w\rho c^2\ , \tag{1.28}$$

parametrised by w. Combining this EoS with the continuity equation we obtain

$$\rho \propto a^{-3(1+w)} \tag{1.29}$$

which gives the evolution of density as a function of the scale factor $a(t)$ under the assumption of a parameter w. In our Universe, the total amount of the mass-energy density $\rho \equiv \rho(t)$ is made of three constituents: matter, radiation, and dark energy. Thus, it can be expressed as:

$$\rho = \rho_m + \rho_r + \rho_\Lambda \tag{1.30}$$

with ρ_m is the non-relativistic matter energy density (baryonic and dark matter), ρ_r is the radiation energy density and ρ_Λ is dark energy which can be considered as a form of energy connected to the cosmological constant[3].

These three components have different dependencies on the scale factor, thus it is possible to identify three different epochs. In each epochs there is one component dominating over the others which makes up for most of the total amount of mass-energy density.

Radiation dominated era During this era, the dominant energy density source was radiation i.e. photons and relativistic particles. From statistical mechanics, the EoS for a generic relativistic component is $P = 1/3\ \rho c^2$, thus the continuity equation (Equation 1.27) becomes

$$\frac{d\rho}{\rho} = -4\frac{da}{a} \tag{1.31}$$

leading to a solution for $\rho_r \propto a^{-4}$. The physical interpretation of the dependence of ρ_r on $a(t)$ can be explained as (i) the factor a^{-3} is due to the geometrical dilution of the volume (number density of photons) and (ii) the additional factor a^{-1} is due to the elongation of particles wavelength, associated with their energy ($E = h\nu$). If we combine $\rho_r \propto a^{-4}$ with the first Friedmann equation (Equation 1.25) we derive the time dependence of $a(t)$ during the radiation era:

$$a(t) \propto t^{1/2} \tag{1.32}$$

this holds if we consider a flat Universe $k = 0$.

Matter dominated era During the matter-dominated era, the mass-energy density is dominated by baryonic and (cold) dark matter, whose velocities are much smaller than c. For this reason, we can neglect the net amount of pressure, $P \sim 0$. The continuity equation (Equation 1.27) becomes

$$\frac{d\rho}{\rho} = -3\frac{da}{a} \tag{1.33}$$

leading to $\rho_m \propto a^{-3}$. Again, substituting it into the first Friedmann equation we obtain:

$$a(t) \propto t^{2/3} \tag{1.34}$$

which is the time dependence of the scale factor during the matter-dominated era.

[3]The nature of the dark energy component is still debated, but it is thought to be responsible for the accelerated expansion of the Universe ($\ddot{a} > 0$), filling up the Universe with energy as it expands. The accelerated expansion of the Universe has been recently observed by measuring the luminosity distance of Type Ia SNe (SNeIa) at $z \sim 1$ (Riess et al., 1998; Garnavich et al., 1998; Perlmutter et al., 1999; Betoule et al., 2014), suggesting that we live in the Λ-dominated era.

Table 1.1. The equation of state parameter w, the dependence of the energy density on the scale factor, and the time evolution of $a(t)$ in each era.

radiation	$w = 1/3$	$\rho_r \propto a^{-4}$	$a(t) \propto t^{1/2}$
matter	$w = 0$	$\rho_m \propto a^{-4}$	$a(t) \propto t^{2/3}$
λ	$w = -1$	$\rho_\Lambda \propto const$	$a(t) \propto e^t$

Λ dominated era The cosmological constant Λ is, by definition, a time-independent constituent of the total energy density budget. Thus, it can be written as $\rho_\Lambda \sim constant$. Taking this assumption into account, the continuity equation (Equation 1.27) becomes

$$P = -\rho c^2 \tag{1.35}$$

yielding a time evolution for the scale factor during the Λ-dominated era of:

$$a(t) \propto e^t \ . \tag{1.36}$$

In Table 1.1 we summarise the EoS parameters w, the energy density dependence on the scale factor, and the time evolution of $a(t)$ in each era.

1.3.1 Evolving space-time in the standard cosmological model

So far, we introduced the Friedmann equations and defined the different eras of the Universe, obtaining the time evolution of the scale factor in each epoch. Now, we are going to introduce the Hubble parameter (as a function of $a(t)$), the critical density, and the density parameters to re-write the first Friedmann equation (Equation 1.25) and obtain the space-time evolution of the Universe.

We define the Hubble parameter as a function of the scale factor as

$$H \equiv \frac{\dot{a}}{a} \tag{1.37}$$

the critical density $\rho_{cr} = 3H^2/8\pi G$ and we introduce the density parameters, Ω_i, re-scaling each ρ_i for the critical density,

$$\Omega_m = \frac{\rho_m}{\rho_{cr}} \ ; \ \Omega_r = \frac{\rho_r}{\rho_{cr}} \ ; \ \Omega_\Lambda = \frac{\rho_\Lambda}{\rho_{cr}} \ . \tag{1.38}$$

By using the density parameters, the first Friedmann equation becomes :

$$\left(\frac{\dot{a}}{a}\right)^2 = H^2(\Omega_r + \Omega_m + \Omega_\Lambda) - \frac{kc^2}{a^2} = H^2\Omega_{tot} - \frac{kc^2}{a^2} \ . \tag{1.39}$$

If we rescale the quantities in Equation 1.39 to the Ω_i at the present time we obtain

$$H(t)^2 = H_0^2 \left(\frac{\Omega_{r,0}}{a^4} + \frac{\Omega_{m,0}}{a^3} + \Omega_{\Lambda,0} - \frac{\Omega_{tot} - 1}{a^2}\right) \tag{1.40}$$

which provides the dependence of the Hubble parameter, i.e. the expansion rate of the Universe, on the energy density parameters at the present time, which are

Table 1.2. Cosmological parameters by Planck Collaboration et al. (2016).

$\Omega_{m,0}$	$\Omega_{\Lambda,0}$	H_0
0.308 ± 0.012	0.629 ± 0.012	67.81 ± 0.92

measurable quantities. The sum of the density parameters give information about the curvature of the space-time:

$$\Omega_k = 0 \rightarrow \Omega_{\text{tot}} = 1 \rightarrow \text{flat geometry} \tag{1.41}$$

$$\Omega_k > 0 \rightarrow \Omega_{\text{tot}} < 1 \rightarrow \text{open geometry} \tag{1.42}$$

$$\Omega_k < 0 \rightarrow \Omega_{\text{tot}} > 1 \rightarrow \text{closed geometry} , \tag{1.43}$$

having defined $\Omega_{\text{tot}} = 1 - \Omega_{k,0} = \Omega_{\text{m},0} + \Omega_{\text{r},0} + \Omega_\Lambda$. Current observations and theoretical models tend to favor a flat geometry of the space-time $\Omega_k = 0$.

The Planck satellite, which is an ESA/NASA mission designed to map the anisotropies of the CMB at microwaves and IR frequencies, was launched into space in May 2009 and used to orbit in the second Lagrangian point of the Earth-Sun system[4]. It provided a detailed map of the CMB field over a large portion ($\sim 95\%$) of the sky, allowing for high-precision measurements of the cosmological parameters (Table 1.2, Planck Collaboration et al. 2016)[5]. Planck's results clearly show that dark energy currently dominates the Universe's dynamics, accounting for around 70%, while matter, primarily in the form of Cold Dark Matter (CDM), constitutes the majority of the remaining 30%. Given this prevailing influence of dark energy and CDM over other mass-energy components, the widely accepted cosmological model is commonly referred to as the ΛCDM model.

1.4 The evolution of the Universe

The homogeneity and isotropy of the expanding Universe allow us to examine its thermodynamic characteristics. If we consider a uniform, perfect gas confined within a (small) comoving volume $V \propto a(t)^3$ - expanding along with the Universe - because of the homogeneity and isotropy of the Universe, there should be no net heat flow ($dQ = 0$) across the boundaries of V. This allows us to treat that volume as an adiabatic system.

According to the first law of thermodynamics, we can link a variation of the internal energy of a system (U) to dQ, the heat transferred into the system, and dW, the work done on the system, via $dU = dQ + dW$. The second law of thermodynamics states that $dS = dQ/T$ with S being the entropy and T the temperature. In an adiabatic system of volume V we have

$$dU + PdV = 0 \qquad dS = 0 \tag{1.44}$$

with P the pressure. This indicates that the entropy per comoving volume is conserved, and the expansion of the Universe leads to a change in its internal energy,

[4] For more information visit https://www.esa.int/Science_Exploration/Space_Science/Planck

[5] In this thesis we are going to adopt the cosmological parameters by Planck Collaboration et al. (2016), however, more recent estimates can be found in Planck Collaboration et al. (2020b).

with a decrease or increase depending on whether $P > 0$ or $P < 0$, respectively. From the previous equation, we obtain $PV^{\gamma} = const$ that combined with the ideal gas law leads to

$$TV^{\gamma-1} = const \tag{1.45}$$

where T is the temperature in the volume V and γ is the adiabatic index (4/3 for relativistic particles and 5/3 for non-relativistic particles). As the volume expands under the effect of the evolving scale factor, we can write T as a function of a

$$T \propto \frac{1}{a} \tag{1.46}$$

for relativistic particles. Equation 1.46 tells us that: (i) the younger the Universe (i.e. the smaller the scale factor), the higher the temperature and (ii) during its expansion the Universe cools down. At its birth, when $a(0) = 0$, the Universe was infinitely hot and dense, this is the so-called Big Bang singularity, predicted by the ΛCDM model which occurred ~ 13.8 Gyr ago.

The initial moments following the birth of the Universe, often referred to as the Planck era, constitute the most enigmatic phase in its history. Currently, there is no available physical theory capable of describing the Universe before the Planck time, $t_P \sim 5 \times 10^{-44}$ s. During this time scale, quantum effects of gravity played a dominant role in physical interactions, thus a self-consistent theory of quantum gravity is needed for a comprehensive understanding of this period (see Rovelli 2004). The Planck era was then succeeded by the epoch of the Great Unification Theory (GUT; Witten 1981), where gravity finally separated from the unified force of the Standard Model[6].

Following the GUT epoch, at approximately 10^{-36} s from the Big Bang, the so-called inflation (Guth, 1981) commenced. During this epoch (presumed to have concluded around $t \sim 10^{-32}$ s), the Universe underwent a sudden and nearly instantaneous exponential expansion, increasing its linear dimensions by a factor of at least 10^{26}. Inflation provides an explanation for several critical issues in ΛCDM models, including the so-called cosmological paradoxes (e.g. Linde 1982), addressing perplexing aspects such as the remarkably high degrees of flatness, isotropy, and homogeneity observed in the Universe.

As introduced in Section 1.3 the three constituents of the mass-energy density (matter, radiation and dark energy) scale differently with $a(t)$, therefore they in turn dominate the Universe at different epochs (see Figure 1.1). From Equations 1.32,1.34 and 1.36 it is clear that at very early cosmological times ($a(t) \to 0$), the Universe was dominated by radiation. In this period, at about 3 minutes after the Big Bang, nucleosynthesis commenced, giving rise to the so-called primordial abundances of light elements (e.g. Boesgaard and Steigman 1985). Within less than 1 hour, the Universe cooled sufficiently to cease nucleosynthesis, consequently, only the fastest and simplest reactions took place (see Cyburt et al. 2016 for a comprehensive review), resulting in our Universe containing roughly 75% hydrogen (H), 24% helium (He) by mass (92% H and 8% He in number density), and trace amounts of other elements such as Lithium (Li) and deuterium (^{2}H).

[6]The Standard Model is the commonly accepted theory in particle physics that explains how the basic building block of matter (particles) interact. These interactions are of four types: the strong, weak, electromagnetic and gravitational interactions (see Patrignani et al. 2016 for a review).

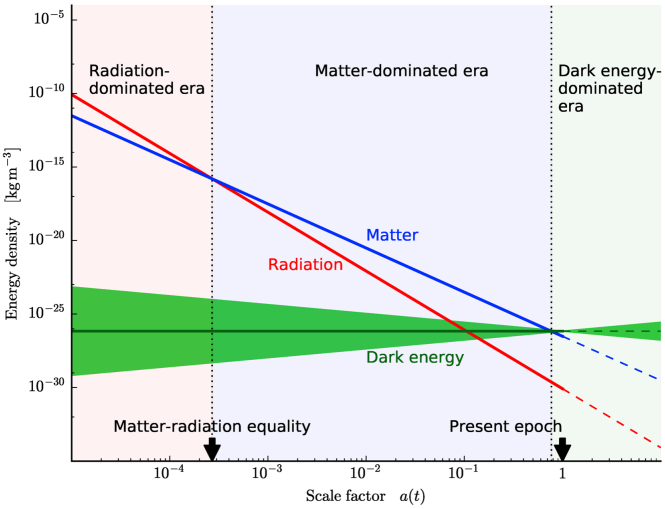

Figure 1.1. The density evolution of the main components of the Universe (i.e. radiation, matter and dark-energy) as a function of the scale factor $a(t)$. The Universe is radiation-dominated until t_{eq}, then it becomes matter-dominated, and, finally, dark energy became dominant at $z \sim 0.5$ until today. Taken from Debono and Smoot (2016).

The radiation dominated era lasted until $\frac{\Omega_{r,0}}{a^4} = \frac{\Omega_{m,0}}{a^3}$ (see Equation 1.40), thus until the so-called equivalence age $a(t_{eq}) = \frac{\Omega_{r,0}}{\Omega_{m,0}}$ with $t_{eq} \sim 50000$ years after the Big Bang, $z_{eq} \sim 3600$ (see Planck Collaboration et al. 2016, 2020b). During this new epoch (matter-dominated era) for several hundred thousand years, atoms were completely ionized because of the high temperature, matter and radiation coexisted in an opaque thermal bath dominated by photons-ions scattering. Only when the temperature decreased significantly did Thomson scattering become inefficient in balancing the electromagnetic attraction between protons and electrons, leading to hydrogen recombination at $z_{rec} \sim 1100 - 1300$ (Gott and Rees, 1975; Eisenstein et al., 2005). Once photons finally decoupled from matter, they started traversing the Universe without interacting with anything, constituting what we observe today as the CMB[7]. The CMB represents the last scattered radiation by ionized hydrogen, offering a primordial snapshot of the mass-energy distribution across the Universe (see Figure 1.2). The CMB spectrum, with an average present-day temperature of $T_{\rm CMB} \sim 2.725$ K, adheres to the expected thermal black-body spectrum across more than 5 orders of magnitude in intensity.

During the matter-dominated era, minor fluctuations in the gravitational potential, primarily governed by DM (refer to Section 1.5), began to grow, even though baryonic structures had not yet emerged. This stage is referred to as the Dark Ages, which ended when baryons collapsed to give rise to the first stars, galaxies, and quasars. Indeed, the emitted light from these structures started ionising the surrounding atoms, marking the start of the Epoch of Reionization (Barkana and Loeb, 2001).

[7]The existence of the CMB was postulated on theoretical grounds in the late 1940s by G. Gamow, R. Alpher, and R. Herman and then, accidentally discovered in 1964 by two Bell Laboratory radio astronomers Penzias and Wilson (1965) while they were trying to detect sources of radiation that may harm satellites - this discovery awarded them with the Nobel Prize in Physics in 1978.

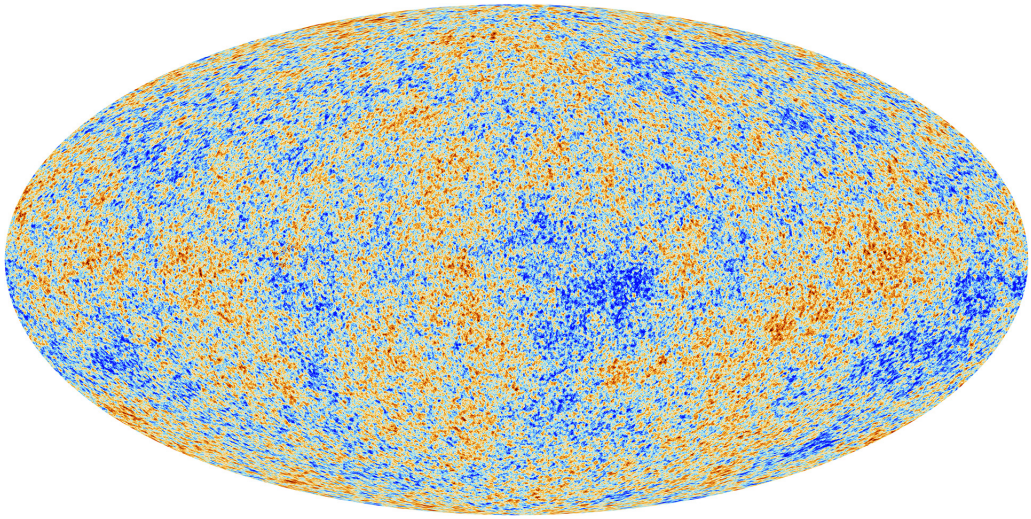

Figure 1.2. CMB seen by the Planck mission (see Planck Collaboration et al. 2020a for an overview). It shows the last scattered radiation by ionized hydrogen before recombination took place, giving us a picture of the primordial mass-energy distribution of the Universe at that time. Before Planck there were other space missions dedicated to the CMB: the first one specifically designed to study the CMB was the Cosmic Background Explorer (COBE), launched by NASA in 1989 (Bennett et al., 1993), NASA's second generation space mission, the Wilkinson Microwave Anisotropy Probe (WMAP) was launched in 2001 to study these very small fluctuations in much more detail (see for example Bennett et al. 2013) and, finally, ESA's Planck was launched in 2009 to study the CMB in even greater detail than ever before.

In the end, at $z \sim 0.5$, the energy dominated era begun (Frieman et al., 2008) initiating the accelerated expansion (Equation 1.36) of the Universe we measure today (e.g. Perlmutter et al. 1999).

1.5 Structure formation in a nutshell

As outlined in the previous sections, the ΛCDM model assumes the Universe to be homogeneous and isotropic. However, the current state of the Universe deviates significantly from the ideal FLRW metric, particularly on scales smaller than tens of Mpc: large-scale galaxy surveys have shown a complex structure of galaxies and matter organized in clusters, voids, and filaments (the cosmic web). Hence, the large-scale matter distribution breaks the assumption of isotropy and homogeneity: the widely accepted scenario is that these structures originated from small initial density perturbations, which seeds might derive from quantum fluctuations in the Planck era, and have expanded under the influence of gravity.

DM can be modeled as a pressure-less fluid, and for slight deviations from homogeneity, the growth of perturbations can be effectively described using the linear perturbation theory (see Section 1.5.1). This approach yields results in good agreement with observations of large-scale structures. However, on smaller scales, such as galactic scales, the assumption of minor deviations in local density from the background becomes inappropriate. In these cases, a complete Newtonian theory

of gravity - together with a set of fluid dynamics equations to depict the evolution of baryons - must be incorporated in what is known as the non-linear regime (see Section 1.5.2).

1.5.1 Linear growth

In this section, we describe the evolution of small-density perturbation employing a Newtonian approximation for gravity. Considering a fluid with a uniform distribution where small density fluctuations exist on every scale, and concentrating on a spherical overdensity, its dynamics is governed by the interplay between two processes: (i) gravitational instability (which makes the perturbation grow) and (ii) pressure or free streaming (which tends to downsize the perturbation). The evolution of density fluctuations in this framework is studied by the Jeans theory (Jeans, 1902). In this theory, the two regimes in which gravitation or pressure/ free streaming are dominant are separated by a characteristic length the so-called Jeans wavelength (λ_J).

Let's assume the Universe is a perfect fluid with density ρ, pressure P, velocity $\vec{v}$ and gravitational potential Φ. Its evolution is described by:

(i) the continuity equation (conservation of mass)

$$\frac{\partial \rho}{\partial t} = -\nabla \cdot (\rho \vec{v}) \; ; \tag{1.47}$$

(ii) the Euler equation (conservation of momentum):

$$\frac{\partial \vec{v}}{\partial t} + \vec{v} \cdot (\nabla \vec{v}) = -\frac{1}{\rho} \nabla P - \nabla \Phi \; ; \tag{1.48}$$

(iii) the Poisson equation (Newtonian gravity equation):

$$\nabla^2 \Phi = 4\pi G \rho \; . \tag{1.49}$$

Let's consider small perturbations around the mean value of density ($\rho = \rho_0 + \delta\rho$), pressure ($P = P_0 + \delta P$), velocity ($\vec{v} = \vec{v_0} + \delta\vec{v}$) and gravitational potential ($\Phi = \Phi_0 + \delta\Phi$). Then, let's substitute these quantities in the previous equations and define the dimensionless density contrast (also known as over-density) $\delta \equiv \delta\rho/\rho_0$. By ignoring terms higher than the first order, we obtain:

$$-\frac{d\delta}{dt} = \nabla \cdot (\delta \vec{v}) \; ; \tag{1.50}$$

$$\frac{\partial \delta\vec{v}}{\partial t} + (\delta\vec{v} \cdot \nabla)\vec{v_0} = -\frac{1}{\rho_0} \nabla \delta P - \nabla \delta\Phi \; ; \tag{1.51}$$

$$\nabla^2 \delta\Phi = 4\pi G \delta\rho \; . \tag{1.52}$$

We have three equations with four variables, thus we need to add a fourth equation to solve the system: the EoS. This equation typically is of the form $P = P(\rho, S)$ with S the entropy, assuming an adiabatic perturbation the EoS does not depend on entropy anymore, and we can relate pressure and density via $c_s^2 = \partial P/\partial\rho$ with c_s the speed of sound. Equations 1.50, 1.51 and 1.52 describe the evolution of small

perturbations in a static Universe. If we re-write these equations in the Fourier space, where each field f can be written as a combination of plane waves as

$$f(\vec{r},t) = \sum_k f_k e^{i(\vec{k}\cdot\vec{r}+\omega t)} \tag{1.53}$$

with f_k the amplitude, $\vec{k}$ the wave vector and ω the angular frequency, the system of linear differential equations becomes a system of algebraic equations. We can also define the dispersion relation of the system[8]:

$$\omega^2 = k^2 c_s^2 - 4\pi G\rho_0 \tag{1.54}$$

for $\lambda < \lambda_J$ the pressure term dominates and the solution for the density contrast is given by two acoustic waves propagating in opposite directions. For $\lambda > \lambda_J$ the gravitational instability dominates and we have a growing and decaying mode for the density contrast δ.

The Jeans theory can be easily extended to the case of an expanding Universe (Gamow and Teller, 1939; Lifshitz, 1946). In order to take into account cosmic expansion, a straightforward approach involves formulating the aforementioned equations in terms of the so-called comoving coordinates. The comoving position $\vec{r}$ is defined as a generalization of the Eulerian position $\vec{x}$, scaled by the cosmic scale factor $a(t)$:

$$\vec{x} = a(t)\vec{r}\,. \tag{1.55}$$

In this coordinate system, the perturbed position is written as $\delta\vec{x} = \vec{r}\delta a(t) + a(t)\delta\vec{r}$, while the velocity is made of two terms $\vec{v} = \partial\vec{x}/\partial t = \dot{a(t)}\vec{r} + a(t)d\vec{r}/dt$. The first term depends on the space-time expansion and the second term is the physical deviation from the expansion, defined as $\delta\vec{v} = a(t)\vec{u}$, where $\vec{u} = d\vec{r}/dt$ is the comoving peculiar velocity. The mathematical operator is also affected by the change of coordinates as $\nabla_{\vec{x}} = \partial/\partial\vec{x} = \partial/a\partial\vec{r} = \nabla_{\vec{r}}/a$.

Using the comoving coordinates, the equations describing the evolution of small perturbations in a homogeneous, expanding Universe become:

$$\frac{\partial}{\partial t}\delta\rho + \frac{\rho_0}{a}\nabla_{\vec{r}}\cdot\vec{v} + 3H\delta\rho = 0\,, \tag{1.56}$$

$$\frac{\partial}{\partial t}\vec{v} + H\vec{v} = -\frac{c_s^2}{a}\nabla_{\vec{r}}\delta - \frac{1}{a}\nabla_{\vec{r}}\Phi\,, \tag{1.57}$$

$$\frac{1}{a^2}\nabla^2_{\vec{r}}\Phi = 4\pi G\rho_0\delta\,. \tag{1.58}$$

To solve the above equations we can re-write them in Fourier space and look for solutions as a combination of plane waves. In general, we look for a solution f which can be written as $f(\vec{x},t) = f_k(t)e^{i\vec{k}\vec{x}}$ where $\vec{k}$ is the wave-number. This time we consider an amplitude f_k which is a function of time, thus it incorporates the term $e^{i\omega t}$ (see Equation 1.53). In Fourier space, the time and spatial derivatives become:

$$\frac{\partial f}{\partial t} = \dot{f_k}(t)e^{i\vec{k}\vec{x}}\,; \quad \nabla f = i\vec{k}f_k(t)e^{i\vec{k}\vec{x}}\,. \tag{1.59}$$

[8]We have employed the fact that $\delta P = c_s^2\delta\rho$, where $c_s^2 = \partial P/\partial\rho$ is the square of the speed of sound for a collisional fluid.

Hence, in the Fourier space, the continuity, Euler and Poisson equations are:

$$\dot{\delta_k} + \frac{i\vec{k}\vec{v}}{a} = 0 \tag{1.60}$$

$$\dot{\vec{v}_k} + \frac{\dot{a}}{a}\vec{v_k} = -\frac{i\vec{k}}{a}(c_s^2\delta_s + \Phi_k) \tag{1.61}$$

$$\Phi_k = -\frac{4\pi G\rho_0\delta_k a^2}{k^2} \, . \tag{1.62}$$

Rearranging these equations and their time derivative, we obtain

$$\ddot{\delta_k} + 2\left(\frac{\dot{a}}{a}\right)\dot{\delta_k} + \delta_k\left[\frac{kc_s^2}{a^2} - 4\pi G\rho_0\right] = 0 \tag{1.63}$$

which describes the evolution of density perturbations in an expanding Universe that is filled with a homogeneous density field ρ_0. The term $2\left(\frac{\dot{a}}{a}\right)\dot{\delta_k}$ is due to the expansion of the Universe. Indeed, if $a = const$ Equation 1.54 is recovered, while the terms $kc_s^2\delta_k$ and $-4\pi G\rho_0\delta_k$ are respectively the pressure/ free streaming and gravitational instability. Finally, as the mass-energy density has different time dependencies according to the epoch we are considering (see Section 1.3). Using Equation 1.63, we can calculate the evolution of mass-density fluctuations among any era as long as $\delta \ll 1$ is true.

It is important to highlight that, owing to the collisionless nature of DM particles, when assessing the evolution of DM, we must disregard the pressure term kc_s^2/a^2 in Equation 1.63. Consequently, the density perturbations of DM evolve according to the equation

$$\ddot{\delta_k} + 2\left(\frac{\dot{a}}{a}\right)\dot{\delta_k} - 4\pi G\rho_0\delta_k = 0 \, . \tag{1.64}$$

By solving Equation 1.63 and Equation 1.64 at various cosmic epochs, we can investigate the patterns and regimes governing the density contrast of baryons, dark matter, and radiation (δ_b, δ_{DM}, δ_r):

- for $t < t_{eq}$ the Universe is dominated by radiation, thus $\rho_0 = \rho_r$. On scales where the Jeans length scale is larger than the Hubble radius, $\lambda_J > d_H$, the density contrast grows as $\delta \propto a^2$. The Jeans-length scale is the minimum wavelength above which a perturbation can collapse under its own gravity and it is defined as $\lambda_J = c_s\sqrt{\pi/G\rho_0}$. While the Hubble radius is the distance of the observer at which the recession velocity of a galaxy would equal the speed of light; roughly speaking, it is the radius of the observable Universe and it is defined as $d_H = c/H$. On smaller scales, where $\lambda_J < d_H$, δ_r and δ_b oscillate as acoustic waves and do not amplify their size, while δ_{DM} grows very slowly ("stagnation" or "Meszáros effect", Meszaros 1974) and structure formation does not take place. Baryons are coupled to radiation by Thompson scattering as the Universe is still very hot and heavily ionised.

- for $t_{eq} < t < t_{rec}$ the Universe is dominated by matter and, in particular, dark matter, $\rho_0 \sim \rho_{DM}$. Baryons are still coupled with radiation. Thus, the general

trend is that δ_r and δ_b oscillate while DM particles, which do not interact with photons, collapse. The density perturbations can grow as $\delta_{DM} \propto a$ initiating the assembly of cosmic structures.

- for $t > t_{rec}$ the primary contribution to the mass-energy budget remains the one from dark matter (ρ_{DM}). However, this time, baryons are no longer coupled with radiation, thus they can freely track the growth of dark matter perturbations (catch-up). This catch-up phenomenon is of paramount importance, as without this phase of accelerated growth baryonic perturbations would not have enough time to grow from the highly homogeneous scenario observed at $z \sim 1100$ to the overdensities observed today in galaxies and clusters. In summary, δ_{DM} and δ_b are $\propto a$, while δ_r oscillates.

1.5.2 Non-linear growth

So far, we delved into the evolution of small perturbations in the linear regime, $\delta \ll 1$. However, the presence of current collapsed objects such as galaxies, which exhibit densities one or two orders of magnitudes higher than ρ_0, cannot be accounted for by a linear growth of perturbations. Indeed, once gravitational instability initiates the formation of structures, and the density contrast approaches $\delta \sim 1$, the linear theory loses its validity, and we enter the so-called non-linear regime. In this regime, the evolution of δ cannot be fully treated analytically. In a weakly non-linear regime, some conclusions can be drawn by using the so-called "Zel'dovich approximation" (Zel'dovich, 1970), but in a fully non-linear regime one either has to:

1. study the evolution of perturbations with ad hoc assumptions and in a very simplified scenario (e.g. spherical collapse)
2. rely on results of N-body simulations.

In the following, we introduce and briefly focus on the spherical collapse approach (first addressed by Gunn and Gott 1972), while N-body simulations will be discussed in detail in Chapter 3.

Spherical collapse model

The analytical solution to the formation of gravitationally bound structures is feasible only in the simplified, albeit illustrative, scenario of spherical collapse (Hernquist, 1990; Cole and Lacey, 1996; Pace et al., 2010). Consider a flat, matter-dominated, expanding Universe that contains a homogeneous, spherically symmetric region. The initial density contrast associated with the sphere is δ_{sph}. Assuming that the mass inside the sphere, M_{sph}, remains constant, the structure evolves under the influence of the Newtonian force:

$$\frac{d^2r}{dt^2} = -\frac{GM_{sph}}{r^2(t)} \tag{1.65}$$

where $r(t)$ is the time-evolving radius of every shell inside the sphere. By integrating the previous equation, we obtain:

$$\frac{1}{2}\left(\frac{dr}{dt}\right)^2 - \frac{GM_{sph}}{r} = E \tag{1.66}$$

where the integration constant E is the specific energy of a shell at radius r.

For $E = 0$, the solution of Equation 1.66 is

$$r(t) = \left(\frac{9GM}{2}\right)^{1/3} t^{2/3} \,. \tag{1.67}$$

During the matter-dominated epoch, $a(t) \propto t^{2/3}$ thus $r \propto a(t)$: the mass shell grows at the same rate as the Universe, $\delta_{sph} \propto \delta$, the sphere does not collapse.

For $E < 0$ we can write the solution in a parametric form as $r = A(1 - cos\theta)$ and $t = B(\theta - sin\theta)$ with $A = GM/2\,|E|$, $B = GM/(2\,|E|)^{3/2}$ and $\theta = [0, 2\pi]$. For $\theta = \pi$ we find the turn-around radius $r_{ta} = 2A$, which is defined as the radius at which expansion stops and the collapse phase begins. The interval between the start of the perturbation, t_{in}, and the point of collapse is defined as the turnaround time:

$$t_{ta} = \pi\sqrt{\frac{A}{GM_{sph}}} \sim 1.095\frac{t_{in}}{\delta_{sph}} \tag{1.68}$$

which shows that the higher the initial density contrast of the spherical region, the sooner the collapse begins.

After reaching the non-linear regime at a certain time, there are three characteristic timescales for structure formation in an expanding Universe:

1. the time of turn-around t_{ta}, when the maximum expansion is reached and the overdensity begins the collapse;
2. the time of collapse $t_{coll} = 2\ t_{ta}$ when an ideal perturbation would finally fall into a singularity;
3. the time of virialization $t_{vir} \sim 3\ t_{ta}$ when the perturbation reaches its actual minimum radius.

Dark matter Halos

As we already discussed, the above spherical collapse model is overly simplified and does not accurately represent the real Universe. In reality, density fluctuations are unlikely to be spherically symmetric or isolated. Also, after the collapse, there is typically a relaxation process known as virialization, where the collapsing material settles into an equilibrium configuration called halo. Once virialized, a halo of mass M_h can be characterized using the virial radius R_{vir}, the circular velocity v_h, and the virial temperature T_{vir} (for a more detailed derivation of these quantities, refer to Barkana and Loeb 2001):

$$R_{vir} = 0.784 \left(\frac{M_h}{10^8 h^{-1} M_\odot}\right)^{1/3} \left[\frac{\Omega_m \Delta_c}{18\pi^2 \Omega_m(z)}\right]^{-1/3} \left(\frac{1+z}{10}\right)^{-1} h^{-1}\ kpc \tag{1.69}$$

$$v_h = 23.4 \left(\frac{M_h}{10^8 h^{-1} M_\odot}\right)^{1/3} \left[\frac{\Omega_m \Delta_c}{18\pi^2 \Omega_m(z)}\right]^{1/6} \left(\frac{1+z}{10}\right)^{1/2} km/s \tag{1.70}$$

$$T_{vir} = 2 \times 10^4 \left(\frac{\mu}{0.6}\right) \left(\frac{M_h}{10^8 h^{-1} M_\odot}\right)^{2/3} \left[\frac{\Omega_m \Delta_c}{18\pi^2 \Omega_m(z)}\right]^{1/3} \left(\frac{1+z}{10}\right)^{-1} K \tag{1.71}$$

where μ is the mean molecular weight[9] and Δ_c is the final overdensity relative to the critical density at the redshift of collapse defined as

$$\Delta_c = 18\pi^2 + 82(\Omega_m(z) - 1) - 39(\Omega_m - 1)^2 \,. \tag{1.72}$$

Press and Schechter (1974) (PS) were the first to derive a prediction for the mass function of dark matter halos, based on the gravitational collapse of an initial Gaussian distribution of density fluctuations (for a comprehensive description of the full non-linear treatment, see Coles and Lucchin 2002). They derived the comoving number density of halos, dn, with mass between M and $M + dM$:

$$M\frac{dn}{dM} = \left(\frac{2}{\pi}\right)^{1/2} \frac{-d(ln\sigma)}{d(lnM)} \frac{\rho(0)}{lnM} \nu_c e^{-\nu_c^2/2} \tag{1.73}$$

with $\rho(0)$ the mean mass density today, σ the standard deviation of the density contrast smoothed through a specific window, and ν_c is the minimum number of standard deviations for a collapsed fluctuation. According to the PS theory, during very early times, the Universe is sparsely populated with gravitationally bound objects. Then, as time passes/redshift decreases, the number of dark matter halos increases, and the maximum halo mass grows through mergers of smaller halos. Conversely, the abundance of low-mass halos decreases with redshift, as a result of their mergers to build up larger halos. This constitutes the concept behind the hierarchical assembly of dark matter halos and galactic discs.

1.6 Brief overview of galaxy formation and evolution

The first ingredient to study galaxy formation and evolution requires the definition of a cosmological framework (ΛCDM model, Section 1.3) within which galaxies form and evolve; the second ingredient is to include the formation and evolution of DM halos which will host the first luminous objects and galaxies (Section 1.4), that we observe with our modern telescopes. In this section, we briefly introduce the assembly and evolution of galaxies (i.e. baryons) in our Universe.

The standard theoretical model of galaxy formation was outlined in the paper by White and Rees (1978) and predicts that baryons are accreted onto DM potential wells. In fact, while baryonic perturbations cannot grow until Recombination at $z \sim 1100$, DM perturbations are allowed to grow right after the equivalence time (t_{eq}) at $z \sim 3000$, therefore forming the potential wells in which baryonic matter falls after decoupling from radiation.

Throughout the accretion process, the infalling gas undergoes a thermal shock at R_{vir} (Equation 1.69) and is heated to the virial temperature T_{vir} (Equation 1.71) — the temperature characteristic of dark matter in the halo (see Binney 1977). The gaseous baryonic halo, nested within the dark matter halo, operates within a quasi-hydrostatic regime, counteracting gravitational collapse with pressure support. Over time, hot gas halos cool due to radiative processes, leading to a loss of pressure.

[9] In general, the value of μ depends on the ionization fraction and composition of the gas. Thus, for a primordial gas composition, it only depends on the ionization fraction of the gas resulting in: $\mu = 0.59$ for a fully ionized primordial gas and $\mu = 0.61$ for a gas with ionized hydrogen but only singly ionized helium.

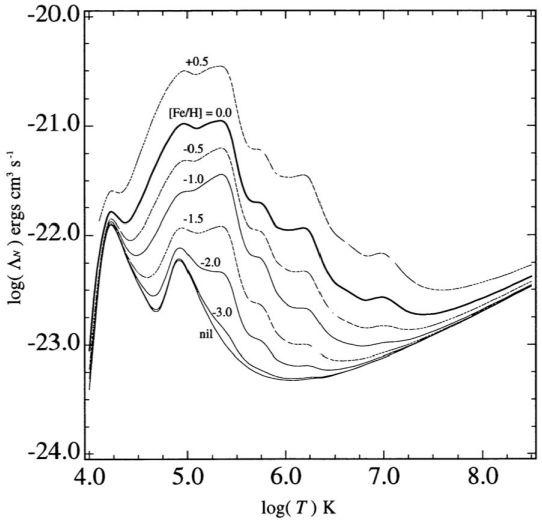

Figure 1.3. Cooling functions $\Lambda(T_{vir}, Z_{gas})$ for gas in collisional ionization equilibrium are shown as a function of temperature, for different metallicities. $\Lambda(T_{vir}, Z_{gas})$ increases with increasing metallicity, reducing the cooling time of metal-rich gaseous halos. The cooling function for the primordial composition of the gas (bottom line) is shown in Figure 1.4 as well. Adapted from Sutherland and Dopita (1993).

Consequently, the gas descends toward the center of gravitational potential wells, giving rise to the formation of disks[10]. The cooling efficiency of the gas depends on its temperature (T_{gas}, which determines its ionisation state) and its chemical composition. In particular, the main processes contributing to gas cooling are:

- line cooling, which is due to de-excitation emission of atoms recombining in an excited state from a collisionally ionised medium, or simply decaying radiatively to the ground state after a collisional excitation;
- roto-vibrational de-excitation emission of molecules, particularly H_2 molecules. This process is of paramount importance in a pristine medium to allow the formation of the first population of stars, at $T \lesssim 10^4$ K, so that the electronic levels of H are not efficiently excited/ionised by collisions, as it is the only available cooling channel;
- Bremsstrahlung or free-free emission, from the deceleration of electrons deflected in the field of atomic nuclei. Particularly efficient when the medium is almost entirely ionised;
- inverse Compton scattering, related to the Sunyaev Zel'dovich (SZ) effect in which CMB photons are scattered by hot electrons in the gas phase (e.g. in the intracluster medium). This process is only efficient at high redshifts ($z \geq 6$).

We can define the cooling timescale (t_{cool}) for the gas as:

$$t_{cool} = \frac{3}{2}\left(\frac{\rho_{gas}\ k\ T_{vir}}{\mu\ m_p}\right) \cdot \left[\rho_{gas}^2\ \Lambda(T_{vir}, Z_{gas})\right]^{-1} \tag{1.74}$$

with ρ_{gas} the density of the gas and $\Lambda(T_{vir}, Z_{gas})$ the cooling function, first introduced by Sutherland and Dopita (1993), which depends on the gas metallicity defined as $Z_{gas} = M_{Z,gas}/M_{gas}$ [11].

[10] A key requirement for galaxy formation is that gas cooling prevails overheating.
[11] With $M_{Z,gas}$ the total mass of metals in the gas phase.

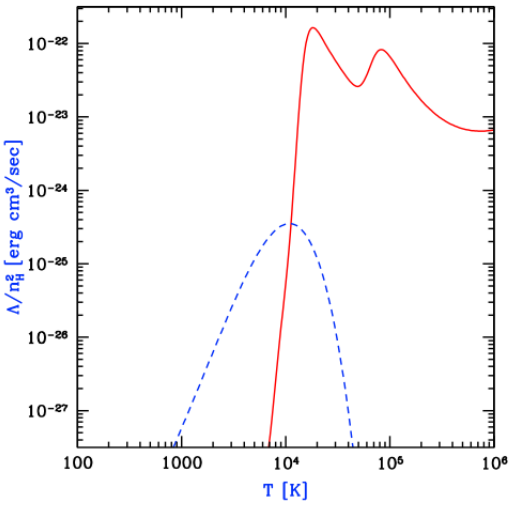

Figure 1.4. Cooling rates as a function of T for a primordial gas composed of H, He, and H_2. The assumed hydrogen number density is $n_H = 0.045 cm^{-3}$, however the quantity Λ/n_H^2 is roughly independent of density. The solid line is the cooling function for an atomic gas and the dashed line shows the additional contribution of molecular cooling assuming a molecular abundance equal to 0.1% of n_H. Taken from Barkana and Loeb (2001).

Figure 1.3 shows that the cooling function is strongly dependent on the metallicity of the gas: at high metallicity there are more channels available for line cooling, implying that metal-rich gas will cool more efficiently than metal-poor gas. Also, it can be seen that at any metallicity, the function drops at $T \leq 10^4$ K (see also Figure 1.4), as most of the electrons have recombined. Hence, collisional excitations/ionizations occur at much lower rates and, if molecules (e.g. H_2 and CO) are present in the gas, collisional excitations of their rotational and vibrational levels contribute to gas cooling. At $T \leq 10^6$ K, line cooling is dominant, as shown by the two peaks due to HI and HeII for a pristine gas, and the peak due to metals at $T \sim 10^5$ K for an enriched medium. Finally, at $T \geq 10^6$ K for a pristine medium and $T \geq 10^7$ K for an enriched one Bremsstrahlung dominates.

The importance of cooling can be understood by comparing t_{cool} with the free-fall timescale $\tau_{\rm ff} \sim 1/\sqrt{G\rho}$ which expresses the characteristic duration of gravitational collapse in the absence of pressure. In fact, if $t_{cool} > \tau_{\rm ff}$ the gas becomes pressure supported, the contraction slows down and proceeds quasi-statically forming a hot atmosphere within the DM halo and undergoing a gradual cooling process over an extended period (hot mode accretion) (Rees and Ostriker, 1977; White and Rees, 1978; Fall and Efstathiou, 1980). However, if $t_{cool} < \tau_{\rm ff}$ the gas can cool rapidly and collapse proceeds roughly in a free-fall time: cold gas from the IGM directly accrete onto the galaxy (cold mode accretion). This mode of gas accretion prevails in the case of less massive dark matter halos ($M_{DM} \leq 10^{12}$ $M_\odot$) and at high redshifts, progressing through cold, dense filaments (Birnboim and Dekel, 2003; Dekel and Birnboim, 2006; Ocvirk et al., 2008; Brooks et al., 2009; Kereš et al., 2009; Stewart et al., 2011). As the gas cools and condenses within DM halos, star formation has to occur in galaxies to produce the stellar light we observe. Gravitational instabilities within cold, dense gas clouds initiate the collapse of these clouds, eventually leading to the birth of stars (Schmidt, 1959; Kennicutt, 1998; McKee and Ostriker, 2007; Krumholz et al., 2012).

The cosmic epoch before the formation of the first collapsed objects (so-called first stars or Population III stars) is named Dark Ages because the Universe was completely dark, made only of neutral gas and luminous sources were completely

absent. Population III (PopIII) stars are thought to be formed about 100 million years after the Big Bang from the collapse of pristine gas (H, He, Li) within dark matter halos with masses around $\sim 10^6$ $M_\odot$ (see Klessen and Glover 2023 for a recent review). At these early epochs, the main gas coolants were roto-vibrational de-excitation emissions from primordial molecules. This collapse led to the formation of the first protostellar objects (i.e. PopIII) and subsequently of thermonuclear reactions in their cores. PopIII stars were very massive objects (stellar masses from ~ 10 $M_\odot$ up to > 100 $M_\odot$, see Bromm and Larson 2004; Klessen and Glover 2023), thus they ended their life very rapidly exploding as supernovae and clearing most of the gas from their DM halos[12]. Since these halos lost most of their gas because of the SN explosions, they are not able to host future episodes of star formation. Therefore, it is thought that the formation of the first galaxies (and Population II stars) occurred later, few hundred million years after the Big Bang, and in larger DM halos ($M_{DM} \sim 10^8$ $M_\odot$).

After this early phase, galaxy formation continued following a wide range of evolutionary scenarios depending on the local conditions, the properties of the gas and the interactions with other systems (e.g. merging) and with their surrounding environment. The evolution of galaxies is thought to be driven by the so-called baryon cycle, where galaxies accrete gas from the surrounding environment and then gradually convert this gas into stars. The cooling and condensation of H, and its conversion into H_2 to fuel star formation, are key processes driving galaxy evolution. Once the gas is accreted from outside the galaxy (inflows) and converted into stars, feedback mechanisms and gas ejections (outflows) come into play and pollute the environment (circumgalactic medium) around the galaxy with heavy elements that have been produced by stellar nucleosynthesis.

To fully understand galaxy formation and evolution a self-consistent treatment of the physical processes of baryonic matter (gas, stars, dust), their kinematics, their evolution within an expanding Universe and their gravitational interactions is required. The study of these processes requires both direct observations (done with cutting-edge space and ground-based telescopes, see Chapter 2) and theoretical models (e.g. hydrodynamical codes, see Chapter 3). The interplay between models and observations to study the evolution of galaxies and the relation with their surrounding medium have a crucial role in this thesis.

[12]So far PopIII stars have been studied using theoretical models and, only recently, thanks to the JWST there have been some tentative HeII line observations that can suggest the presence of these first stars (see for example Wang et al. 2022; Maiolino et al. 2023b; Vanzella et al. 2023).

Chapter 2

High-z galaxies: observations

In this Chapter we deal with the observations which are fundamental for the investigation of galaxy formation and evolution. In particular, we focus our attention on some state-of-the-art instruments and their results which are relevant for the aims of this thesis.

We are particularly interested in multi-wavelength observations, needed to obtain a complete view of galaxy properties and their evolution. Indeed, galaxies are multi-component systems that emit radiation in different regions of the electromagnetic spectrum through diverse processes. Ground-based telescopes, such as ALMA (see Section 2.2), can access millimeter and sub-millimeter wavelength windows[1] giving us information about the gaseous component and dust properties of early galaxies ($z \geq 4$). On the other hand, the information gained from ground-based telescopes has to be complemented with space telescopes (such as HST/ Spitzer and JWST, see Section 2.3) which are able to observe the UV, optical, and near-infrared thus the light mainly coming from the stellar component of galaxies at high-z.

2.1 Observational tools

Telescopes can be divided in two main categories: ground-based telescopes and space telescopes. The limits and strengths of one or the other category are due to our atmosphere and its emission and/or absorption. In fact, because of poor atmospheric transmission or strong atmospheric emission, observations in the X-ray ($\lambda \sim 0.1 - 10$ nm), UV ($\lambda \sim 120 - 300$ nm) and IR ($\lambda \sim 3 - 600$ μm) requires space telescopes. Optical ($\lambda \sim 300 - 800$ nm) and NIR ($\lambda \sim 0.8 - 2.5$ μm) observations can be performed from Earth, despite the presence of atmospheric OH line-emission, thermal emission (in K-band and mid-IR bands) and atmospheric absorption add some background to the NIR observations and turbulence in the atmosphere blurs images. In general, ideal locations for observations are high mountain peaks, above the atmospheric inversion layer (mountains in Chile), or in the vicinity of large oceans, because of their stabilising capability (e.g. Hawaii, USA and Canary Island,

[1] Here we only highlight the portion of the electromagnetic spectrum which is relevant for the investigation of the high-z Universe.

Spain). Millimeter and sub-mm ($\lambda \sim 0.5 - 3.5$ mm) observations[2] together with radio ($\lambda \sim 0.7 - 1000$ cm) observations can be performed using single dishes or interferometers.

To date, optical instruments are the most sensitive, being able to reach the lowest flux density noise levels, but interferometric (radio and sub-mm) observations can reach higher spatial resolutions. For the purpose of this thesis, we mainly deal with observations from the ground-based telescope ALMA (Section 2.2) and results from the space telescope JWST (Section 2.3).

2.1.1 Introduction to astronomical observations

Almost all the information we can obtain from galaxies is derived from the radiation (either in emission or absorption) we receive from them. The radiation emitted from a source is characterized by its SED, $f_\lambda \, d\lambda$, which is the total energy of emitted photons with wavelengths in the range λ to $\lambda + d\lambda$.

Photometry

Photometric observations are generally carried out at specific wavelengths, thus the observed flux from an object is related to its SED by

$$f_X = \int f_\lambda F_X(\lambda) R(\lambda) T(\lambda) d\lambda \tag{2.1}$$

with $F_X(\lambda)$ the transmission of the filter that defines the waveband (X), $T(\lambda)$ is the atmospheric transmission and $R(\lambda)$ incorporates both the telescope's transmission and the efficiency with which the instrument detects photons [3]. Note that, from Equation 2.1, the observed flux only depends on the spectral energy distribution and the chosen filter. In every photometric system, each filter is associated with a filter function which is characterised by an effective wavelength λ_{eff} and a bandwidth usually assumed as the FWHM, defined as $|\lambda_1 - \lambda_2|$ with $F_X(\lambda_1) = F_X(\lambda_2) =$ half of the peak value of $F_X(\lambda)$. Depending on the FWHM of the filters, we talk about "broad-band photometry" when the FWHM are all $\geq 10\%$ of the corresponding λ_{eff}, and this is particularly useful to characterise the overall shape of the SED. On the other hand, "narrow-band photometry" with much narrower filters is adopted to image objects in a specific emission line, or to study detailed properties of the SED. Medium and narrow-band filters deliver more detailed spectral information at the expense of costing more observing time to cover the full wavelength range.

Magnitudes

The flux of an astronomical object is usually referred to based on its apparent magnitude:

$$m_X = -2.5 \, log(f_X / f_{X,0}) \tag{2.2}$$

[2]These observations require low humidity levels, thus millimeter and sub-millimeter instruments are located on the driest places on Earth.

[3]In general f_X has to be corrected for atmospheric absorption and telescope efficiency. This is usually done by calibrating the data using standard objects with known f_λ.

with $f_{X,0}$ is a reference flux defined as the one in the X band of the bright star Vega. While for the 'AB-magnitudes' it is defined as:

$$f_{X,0} = 3.6308 \times 10^{-20} \text{ erg s}^{-1} \text{ cm}^{-2} \text{ Hz}^{-1}. \tag{2.3}$$

Similarly, the luminosity is often expressed in terms of absolute magnitude $M_X = -2.5 \log(L_X) + C_X$ with C_X the zero-point value.

Spectroscopy

Spectroscopic observations provide the source spectrum, i.e. its SED f_λ or f_ν defined so that $f_\lambda d\lambda = f_\nu d\nu$ is the flux received in the elemental wavelength range $d\lambda$ at λ and in the elemental frequency range $d\nu$ at ν.

Spectroscopic observations give us a lot of information about the galaxy we are observing that photometry cannot; spectroscopic techniques disperse the light over a range of spectral resolution elements, allowing for detailed measurements of specific features such as emission and/or absorption lines. Typical spectroscopic instruments can either observe a single target (through a slit) with high spectral resolution, or multiple targets at moderate spectral resolution. Another technique is adopted by integral field unit spectrographs (IFUs) where imaging is combined with spectroscopy and a spectrum is delivered for each pixel in the spatial coverage. This is particularly useful to study spatially resolved galaxies, but also to identify objects for which the line emission is offset from the continuum emission (hence possibly missed by slit spectroscopy) and objects which are very faint in the continuum, but with strong emission lines. The downsides are that the spatial coverage is smaller than that from imaging cameras, and the spectral resolution and wavelength coverage are limited compared to that attainable by slit spectroscopy.

By looking at a spectrum of an astronomical object, we not only have information about the continuum (thus the stellar contribution), but also on the emission and absorption features that are associated with the atoms and molecules present in the ISM and CGM of the galaxy. By analysing a spectrum and its characteristic emission/absorption features we can infer the physical properties of the galaxy, such as its metal content, dust mass budget, star formation activity etc. and its environment.

2.1.2 Selection techniques for distant galaxies

To understand galaxies in the distant Universe, one would need to construct a *complete* sample of galaxies, with minimal contamination, for example using spectroscopy. In fact, with a deep and wide spectroscopy surveys we can construct a galaxy sample with high-confidence redshifts, particularly when the continuum and/or emission lines are observed. This has been accomplished in the low-redshift Universe (e.g. Sloan Digital Sky Survey, Strauss et al. 2002), but because of the faintness of distant galaxies it has been more difficult to obtain wide-field, blind spectroscopic surveys for the $z \sim 6$ universe. JWST is opening a new window on the early universe as it makes it possible to perform these surveys to the high-z.

We can classify all the techniques needed to obtain samples of galaxies in the distant Universe, in three categories: identification of spectral breaks in the rest-

frame UV or optical continuum, emission line selection and infrared continuum selection.

Spectral break selection

The intrinsic spectra of star-forming galaxies exhibit two spectral breaks, (i) the Lyman break at 912 Å and (ii) the Balmer break at 4000 Å. The first one is due absorption of photons with $\lambda < 912$Å by neutral gas (HI) in the ISM of galaxies, while the second one is the result of absorption by the higher order Balmer series lines down to the Balmer limit (3646 Å). This break can become strong in galaxies dominated by older stellar populations, but it is typically much weaker than the Lyman break.

The neutral gas along the line-of-sight (either in the cosmic web or in the CGM of galaxies) absorbs the escaping ionising radiation (with rest-frame $\lambda < 912$ Å) enhancing the Lyman break. Additionally, the continuum of galaxy spectra between 912 and 1216 Å is attenuated by Lyα absorption lines (Lyman-α forest). This last effect depends on the redshift we are considering, as in high-z systems more opacity is encountered along the line-of-sight. In fact, by $z \geq 5$ the region of the spectrum between the Lyman continuum edge and the Lyα is essentially absorbed, such that no flux is received below 1216 Å, compared to 912 Å at lower redshifts.

While, the Lyman break is the primary spectral feature typically used in modern searches up to $z \sim 10$ galaxies (Bouwens et al., 2015), it is susceptible to contaminants such as extremely dust-obscured galaxies and brown dwarf stars in the Milky Way (Bowler et al., 2014). Moreover, another caveat is that the Lyman-break selection is biased against dust-obscured galaxies.

Emission line selection

Another method to select high-z galaxies is via strong emission lines. For example the Lyman-α ($\lambda_{rest} = 1216$ Å) can be recognised using narrow-band filters: a galaxy with a line at a specific wavelength covered with a narrow band filter will appear brighter than in a broadband filter covering the same wavelengths. The most common lines that are used to select galaxies are Lyα, $[OII]_{3727}$, $[OIII]_{5007}$ and Hα lines, but also the FIR [CII] line and other rest-frame UV lines. Emission lines selection is biased towards star-forming galaxies or galaxies with AGN activity, and it is not sensitive to passive galaxies. Similarly to Lyman-break selection, the rest-frame UV emission line samples may miss heavily obscured galaxies (Oteo et al., 2015).

Infrared selection

The previously discussed methods rely either on the detection of stellar continuum emission or of nebular gas emission. Another method to select galaxies is based on the FIR or sub-mm emission coming from the UV radiation that is re-processed by dust grains in the ISM (e.g. Hughes et al. 1998; Draine 2011). This method is less sensitive than optical surveys and source confusion, because of limited spatial resolution, is significant; sub-mm is particularly useful to characterise sources with a high dust mass content for which the Lyα is easily attenuated. The two strategies are therefore highly complementary.

2.2 ALMA telescope

ALMA is located in Chajnantor plateau (Chilean Andes), 5000 m high, and operated by the European Southern Observatory (ESO) together with the National Radio Astronomy Observatory (NRAO) and the National Astronomical Observatory of Japan (NAOJ). It is a state-of-the-art telescope, composed of 66 antennas which work together as a unified machine and that can be arranged in different configurations, where the maximum distance (baseline) between antennas can vary from 150 m to 16 km, going from a more compact to broader configuration. As the distance between the antennas increases, the resolution capacity of the interferometer increases, enabling it to capture more subtle details. The possibility of combining signals from antennas[4] separated by several kilometers of baseline is crucial to obtaining an extremely fine resolution and very detailed images.

ALMA operates in the wavelength range that goes from 0.32 to 3.6 mm, studying the building blocks of stars, planetary systems, galaxies and life itself, providing scientists with detailed images of stars and planets being born in gas clouds near our Solar System, and detecting distant galaxies forming at the edge of the observable Universe. It has recently opened a window to explore the cold neutral and molecular gas in early galaxies with unprecedented levels of detail (Capak et al., 2015; Le Fèvre et al., 2020; Bouwens et al., 2022b), topics that will be further addressed in this thesis. In the following sections, we are going to present two ALMA Large Programs which are relevant for our research and which help us investigate the early Universe and galaxies build up using large samples of $z > 4$ sources.

2.2.1 ALMA-ALPINE survey at $4 < z < 6$

The ALMA Large Program to INvestigate [CII] at Early times (ALPINE) features 118 normal star-forming galaxies (SFGs) observed in the [CII] 158 µm line and FIR continuum emission during the period of rapid mass assembly, right after the end of the HI reionization at redshifts of $4 < z < 6$. This redshift range is particularly interesting as it represents the transition phase between primordial galaxy formation (Epoch of Reionization, $z > 6$) and more mature galaxy evolution ($z \sim 2 - 3$), providing a crucial link between early galaxies and late galaxies (see Figure 2.1).

In this context, out of the sample of 118 galaxies, ALPINE detected 75 ($\sim 64\%$) in [CII] 158 µm with S/N > 3.5 and 23 ($\sim 20\%$) in dust continuum. A full description of line and continuum measurements can be found in Béthermin et al. (2020c). The complete ALPINE source list can be found in Table 1 of Le Fèvre et al. (2015), together with (RA,DEC) positions, spectroscopic redshift and [CII] S/N when detected above 3.5σ (95% purity, where purity $\equiv N_{real}/(N_{real} + N_{spurious})$, see Béthermin et al. 2020c).

The main science goals of the ALPINE survey can be summarised as follows:

- investigate the relation, if present, between [CII] 158 µm luminosity and star-formation in the early Universe. In fact, a correlation between [CII] 158 µm luminosity and total SFR is expected from studies at $z = 0 - 2$, and ALPINE has been conceived to study this relation at $z \sim 5$ using the largest sample of

[4] This can be done using a supercomputer called the Correlator.

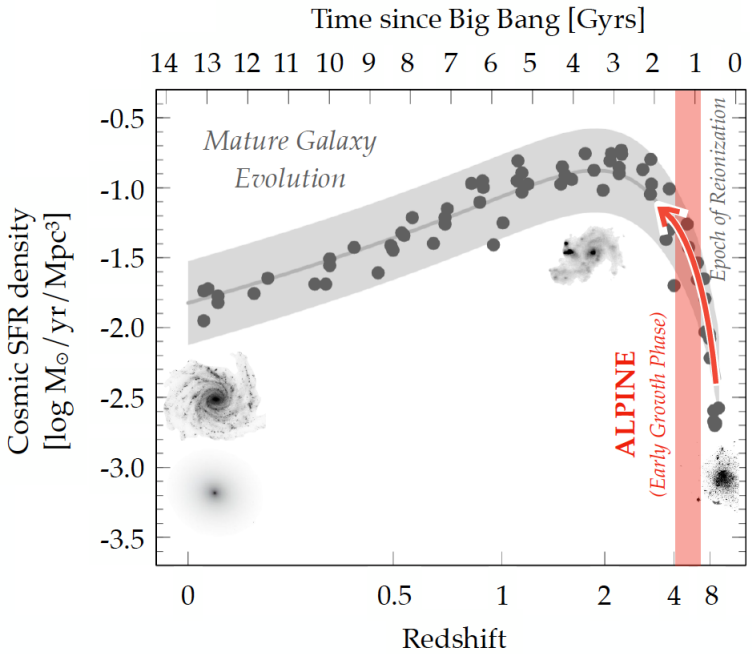

Figure 2.1. Cosmic SFR density as a function of cosmic time and redshift. It increases during primordial galaxy assembly and evolution, until it reaches a peak at $z \sim 2-3$. Then, it declines because of the emergence of quiescent galaxies during the mature galaxy evolution phase. ALPINE galaxies sit in the Early Growth Phase at $z \sim 4-6$ (red shaded area), which connects primordial and mature galaxy evolution. The data points are from Madau and Dickinson (2014a) and Bouwens et al. (2015), and the gray images show the change in galaxy structure across cosmic time. Taken from Faisst et al. (2022).

[CII] emitters to date and compare it to observations at lower redshifts as well as to theoretical models (e.g. Schaerer et al. 2020);

- use the dust continuum and [CII] emission to study the total SFR density at $z > 4$, including the contribution of dust-obscured star formation (e.g. Fudamoto et al. 2020; Gruppioni et al. 2020; Khusanova et al. 2021);
- investigate gas dynamics and merger statistics from [CII] kinematics and quantification of UV-faint companion galaxies (e.g. Le Fèvre et al. 2020; Jones et al. 2021; Romano et al. 2021);
- study the gas fraction and dust properties for $z > 4$ galaxies (e.g. Pozzi et al. 2021; Sommovigo et al. 2022a);
- characterise the ISM properties using L_{FIR}/L_{UV} and [CII]/FIR continuum diagnostics for a large sample of galaxies (e.g. Dessauges-Zavadsky et al. 2020);
- quantify outflows and feedback processes in $z > 4$ galaxies from [CII] line profiles, in particular from the width and broad component of the emission line (e.g. Ginolfi et al. 2020d).

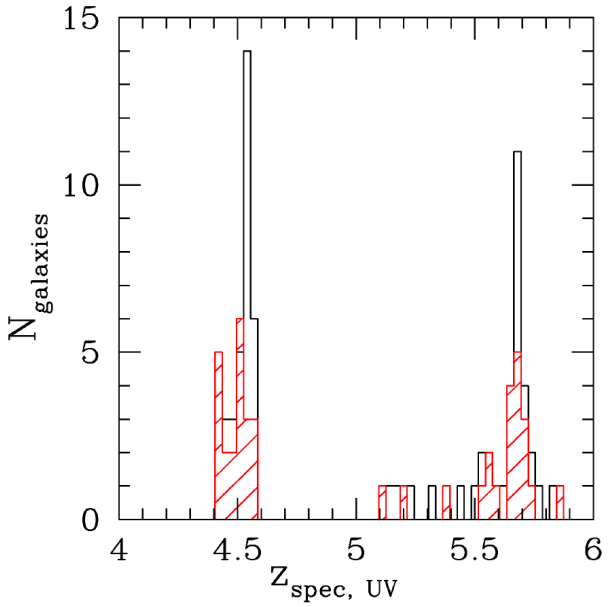

Figure 2.2. Redshift distribution of the ALPINE sample using spectroscopic redshifts from the UV-rest frame spectra (Le Fèvre et al., 2020; Hasinger et al., 2018). The red hatched part is for those sources with [CII] S/N $> 3.5\sigma$, while the empty histogram is for all the observed sources. Taken from Le Fèvre et al. (2020).

The ALPINE sample is drawn from large spectroscopic samples of normal SFGs in the Cosmic Evolution Survey (COSMOS, Scoville et al. 2007a,b) and Extended Chandra Deep Field South (E-CDFS, Giacconi et al. 2002; Giavalisco et al. 2004; Cardamone et al. 2010). Its selection is based on galaxies having a reliable spectroscopic redshift in $4.4 < z_{spec} < 5.9$ ($<z_{spec}> \sim 4.7$), excluding $4.65 < z < 5.05$ where the [CII] 158 µm line falls in a low transmission atmospheric window (see Figure 2.2). Accurate redshift determinations come from spectroscopic campaigns at the Very Large Telescope (VUDS, Le Fèvre et al. 2015; Tasca et al. 2017) and Keck (DEIMOS, Hasinger et al. 2018).

The campaign lasted for $\sim$ 70 hours, and the observations were carried out in Band 7 (275-373 GHz) during Cycles 5 and 6. Each target was observed for about 30 minutes and up to one hour of integration time, with the phase centers pointed at the UV rest-frame positions of the sources. The availability of spectroscopic redshifts allows to accurately set the main spectral window on the expected [CII] frequency.

Galaxies are UV-selected (Le Fèvre et al., 2015) with $L_{UV} > 0.6\ L^*$ to include most of the star formation traced by the UV and excluding type I AGN identified from broad spectral lines. The absolute UV luminosity cut ($M_{UV} < -20.2$) is equivalent to SFR $> 10\ M_\odot\ yr^{-1}$. Assuming the relation between the [CII] luminosity and the SFR proposed by De Looze et al. (2014a), the star formation rate limit is equivalent to a minimum [CII] 158 µm luminosity of $L_{[CII]} > 1.2 \times 10^8\ L_\odot$[5]. The cut in UV magnitude has been chosen in order to maximize the number of [CII] 158 µm line detections according to the $L_{[CII]}$ - M_{UV} relation found in Capak et al. (2015) based on 10 $z \sim 5.5$ galaxies with similar observations. Although naturally biased to the brightest galaxies, this diverse selection function makes ALPINE an exemplary panchromatic survey that enables the study of a representative high-z galaxy sample

[5]Some galaxies with SFR below $\sim$ 1 solar masses per year were included when made possible by the observational setup.

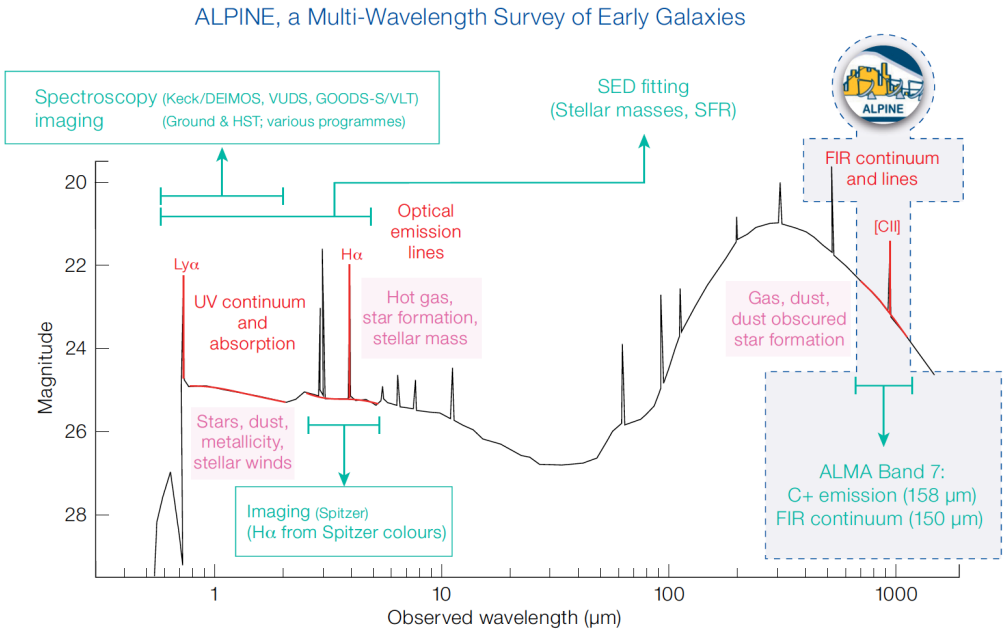

Figure 2.3. The diagram shows the multi-wavelength data products that are available for all the ALPINE galaxies. The spectrum sketch is based on a typical $z = 5$ galaxy. Adapted from Faisst et al. (2020) (see also Béthermin et al. 2020a).

at UV, optical, and FIR wavelengths.

To summarize, the ALPINE team combined ALMA observations in the far-infrared with ancillary imaging and spectroscopy products at the rest-frame UV and optical wavelengths. Figure 2.3 shows an example spectrum of a galaxy at $z = 5$ with an illustration of the various features probed by ALPINE and ancillary data.

The ALPINE sample is representative of the overall SFG population, meaning that most of its galaxies are positioned on or near the so-called main sequence in the SFR versus $M_\star$ plane observed at these redshifts. Figure 2.4 taken from Faisst et al. (2020), shows the ALPINE galaxies on the $z = 5$ main sequence. The galaxies are color-coded according to their [CII] emission measured by ALMA (in Jy km s^{-1}) [6]. In order to be consistent with other studies on the COSMOS field, the SED fitting code `LePhare` [7] (Arnouts et al., 1999; Ilbert et al., 2006) has been adopted to derive e.g. stellar masses, SFRs, absolute magnitudes, optical dust reddening and UV continuum slopes for the ALPINE galaxies. Stellar masses and SFRs are compared to all galaxies (with photometric redshifts) at $4 < z < 6$ in the COSMOS catalog (Laigle et al. 2016, blue points) as well as the main-sequence parameterization by Speagle et al. (2014) at $z = 5$. The comparison to the COSMOS parent sample

[6] This time the [CII] emission is measured combining the flux of the line (in Jy) together with the width of the line (in km/s) providing a measure of the total amount of energy emitted over a certain velocity range.

[7] `http://www.cfht.hawaii.edu/~arnouts/lephare.html`. Note that in Faisst et al. (2020), the authors compared the stellar mass, SFRs and absolute UV magnitudes derived using two SED-fitting codes. They concluded that most suitable code among the two was the `LePhare` one (see discussion in Section 4.1 of Faisst et al. 2020).

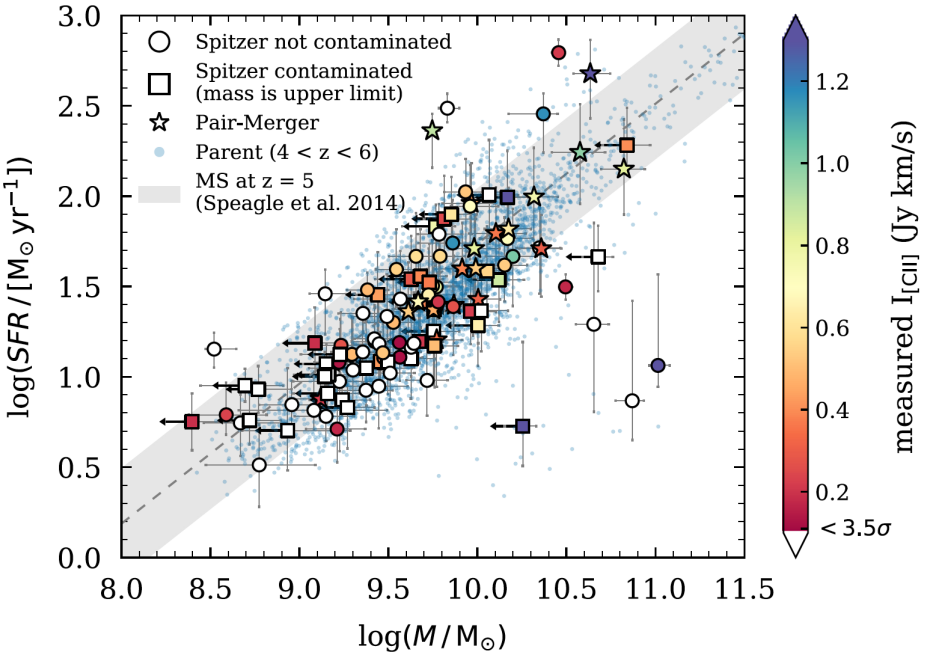

Figure 2.4. Relation between stellar mass and SFR (main-sequence) of ALPINE galaxies compared to all COSMOS galaxies at $4 < z < 6$ (blue points) and the main-sequence parameterization at $z = 5$ by Speagle et al. (2014) (gray band with ± 0.3 dex width). Galaxies with contaminated Spitzer photometry are marked with squares (their stellar mass is likely an upper limit) and mergers (classification by Le Fèvre et al. 2020) are shown as stars. The color denotes the [CII] flux in Jy km s^{-1} measured by ALPINE. Galaxies that are not detected at the 3.5 σ level are shown with white face color. Taken from Faisst et al. (2020).

indicates that the ALPINE one is a fair representation of the overall population of star-forming $z > 4$ galaxies. At higher stellar masses, it also includes galaxies that lie $2-3\,\sigma$ below the main-sequence. Note that two of these galaxies at $\mathrm{Log}(\mathrm{M}_\star/\mathrm{M}_\odot) \sim 10.3$ and 10.7 are upper limits[8] and the other two galaxies at $\mathrm{Log}(\mathrm{M}_\star/\mathrm{M}_\odot) \sim 10.6$ and 10.9 do not show [CII] emission, which is expected if they are systems of low SFR below the main-sequence. Moreover, there are galaxies with a SFR of less than ~ 10 M$_\odot$ yr^{-1}, below the threshold adopted in the initial selection. We emphasize that the initial selection was based on the observed absolute UV magnitude and not on any property derived from SED fitting (such as the SFR). This discrepancy is therefore expected within the uncertainty of measuring SFRs from SED fitting.

The ALPINE sample has been employed to study the dust mass content of main sequence galaxies at $z > 4$ with a statistically robust dataset for the first time. Before diving into the results obtained by the analysis of ALPINE sources, it is important to introduce how dust masses ($\mathrm{M}_{\mathrm{dust}}$) are estimated. In general,

[8]This is due to their contaminated Spitzer photometry. Indeed, ALPINE galaxies are also covered by four Spitzer channels from 3.6 μm to 8.0 μm from the SPLASH survey (Capak et al., 2013; Steinhardt et al., 2014; Laigle et al., 2016) and the large point spread function (PSF) sizes of Spitzer observations may lead to an overestimation of the flux, hence of the stellar masses. See Faisst et al. (2020) for more details on the photometry and SED fitting.

as dust absorbs the light in the optical/UV wavelengths and ri-emit (via thermal emission) in the IR/sub-mm part of the spectrum, in order to have a complete view of its role and abundance in the ISM of high-z galaxies we ideally need to cover both these wavelength ranges. When multi-wavelengths observations of dust continuum are available it is possible to fit a physical model to the dust emission in order to constrain dust grains properties (such as the dust mass and temperature, and IR luminosity). The modifies black body is adopted for the fitting procedure and it depends on three parameters: the dust temperature (T_{dust}), the dust mass (M_{dust}) and the dust emissivity (β). Moreover, the dust can be optically thick at short wavelengths ($\lambda \lesssim 100 - 200\ \mu m$; see for example Casey 2012) introducing the additional parameter $\lambda_{thick} = c/\nu_{thick}$ where the optical depth (τ_ν) equals unity. The optical depth is defined as the integral over the line of sight using $\tau_\nu = \int \kappa_\nu\ \rho_{dust}\ ds$ where κ_ν is the dust mass absorption coefficient [9] and ρ_{dust} is the dust mass density. The most general form for an optically *thick* modified black body can be written as:

$$S_{\nu_{obs}} = \left(\frac{1+z}{d_L^2}\right)\left(\frac{1-e^{-\tau_\nu}}{\tau_\nu}\right) M_{dust}\kappa_\nu B_\nu(T_{dust}) \tag{2.4}$$

with ν and ν_{obs} the frequencies in the source rest-frame and observed frame, d_L the luminosity distance at redshift z.

In Pozzi et al. (2021), the authors used the rest-frame FIR fluxes of the 23 continuum individually detected galaxies and stacks of continuum images to measure the dust content of the ALPINE galaxies concluding that they show dust masses and SFR values typically consistent with intermediate- and low-mass proto-spheroids which result in present-day bulges of spiral or elliptical galaxies. While, galaxy discs, such as that of the Milky Way, show at high-z SFR values smaller than 10 $M_\odot$/yr and dust masses much lower than the ones measured in ALPINE galaxies. Particularly relevant for this thesis is the analysis done by Pozzi et al. (2021) on the estimate of dust masses in ALPINE galaxies and its variation according to the assumed dust temperature. The authors derived the dust masses using a modified black body fit and under the optically *thin* approximation (Bianchi, 2013), thus $\tau_\nu \ll 1$ and $(1 - e^{-\tau_\nu})/\tau_\nu \sim 1$. In this approximation, Equation 2.4 can be written as:

$$M_{dust} = \frac{d_L^2 S_{\nu_{obs}}}{(1+z)\kappa_\nu B_\nu(T_{dust})} \tag{2.5}$$

with ν and ν_{obs} the rest-frame and observed frequencies, $B_\nu(T_{dust})$ is the Planck function, d_L the the luminosity distance, κ_ν the grain absorption cross section per unit mass and S_ν is the observed flux corresponding to a rest-frame frequency at which the dust can be considered optically thin. Figure 2.5 shows the dust mass of ALPINE galaxies as a function of redshift, in particular, the authors report the dust mass values for two different assumed dust temperatures: 25 K and 35 K. Pozzi et al. (2021) considered the fiducial temperature value to be T = 25 K, highlighting that T = 20 K would increase the dust masses by a factor of 20%, while T = 35 K would produce a decrease of the order of 60%. This temperature dependence of dust mass estimates is further investigated in Chapter 4 of this thesis, where we analyse the dust mass stellar mass relation at high-z.

[9] This coefficient is defined as $\kappa_\nu = \kappa_0(\nu/\nu_0)^\beta$ and it is normalized to ν_0.

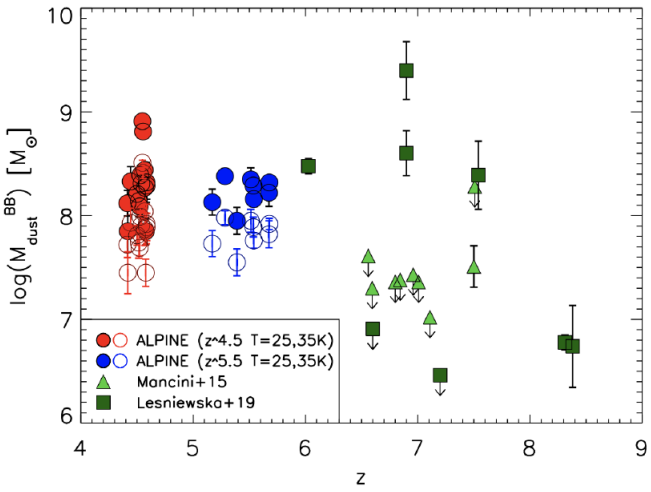

Figure 2.5. Dust masses of the ALPINE continuum selected galaxies as a function of redshift. Filled circles are the dust masses estimated assuming T = 25 K, while empty circles are those with T = 35 K. Blue and red colors show detections respectively in $4 < z < 5$ and $5 < z < 6$. Observations from Mancini et al. (2015) and Leśniewska and Michałowski (2019) are shown for comparison. Taken from Pozzi et al. (2021).

In addition, ALPINE also provides the first morpho-kinematic classification of galaxies, which allows us to study the build-up of structure in galaxies as well as the emergence of "disk galaxies" (i.e. smooth rotators). In fact, based on visual inspection (qualitative information) of the [CII] 3D (i.e. RA, DEC, velocity) data cubes, Le Fèvre et al. (2020) found a surprisingly wide range of galaxy types which define the morpho-kinematic classes of i) Rotator; ii) Interacting systems (mergers); iii) Extended Dispersion dominated; iv) Compact Dispersion dominated; v) too weak to be classified. This first qualitative classification leads to a galaxy sample which is composed of 40% of systems which are mergers, 20% extended and dispersion-dominated, 13% compact, and 11% rotating disks, with the remaining 16% too faint to be classified. Later on, Jones et al. (2021) expanded this initial classification characterizing in a quantitative way the ALPINE sample, applying to these data a tilted ring model fitting code ^{3D}Barolo (3D- Based Analysis of Rotating Objects from Line Observations, Di Teodoro and Fraternali 2015), a quantitative morphological classification (Lotz et al., 2004) and disk identification criteria (Wisnioski et al., 2015). From this analysis they robustly classified 14 out of 29 fitted sources[10] with the remaining sources showing a complex behaviour. This new quantitative analysis confirmed the morpho-kinematic diversity of the ALPINE galaxies found by Le Fèvre et al. (2020), but resulted in a somewhat different statistics with 43% of rotators, 36% of mergers and 21% of dispersion-dominated galaxies. Finally, Romano et al. (2021) performed an in-depth morpho-kinematic investigation of the ALPINE [CII]-detected galaxies based on the same classification criteria used in Le Fèvre et al. (2020) and on the results by Jones et al. (2021) to compute the contribution of mergers to galaxy assembly in the early Universe. They found a major merger

[10]Of the 75 [CII] detected, 29 have high enough significance and with sufficient spatial resolution to allow for tilted model fitting and the derivation of morpho-kinematic parameters.

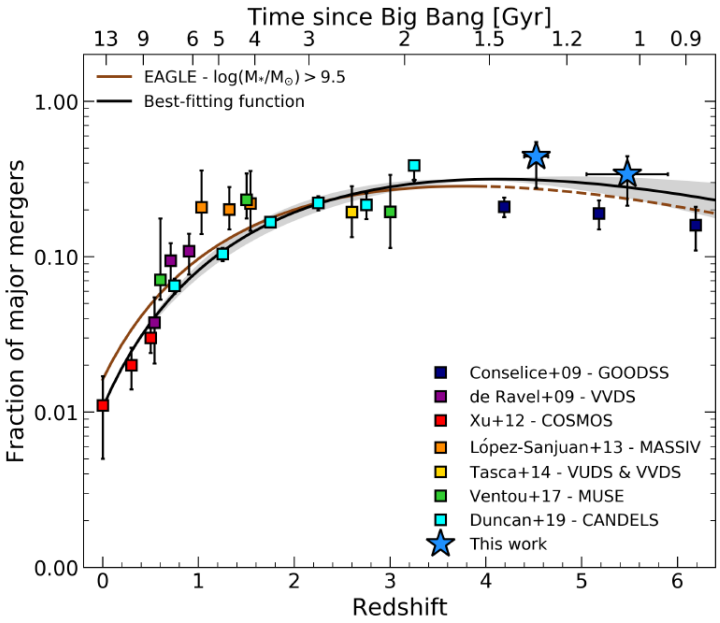

Figure 2.6. Cosmic evolution of the major merger fraction from the local to the early Universe. Colored squares are literature data (Conselice and Arnold, 2009; de Ravel et al., 2009; Xu et al., 2012; López-Sanjuan et al., 2013; Tasca et al., 2014; Ventou et al., 2017; Duncan et al., 2019), while blue stars are $f_{\rm MM}$ estimates from the ALPINE sample. The solid black line and the shaded region are the best-fit to data with a combined power-law and exponential function and the associated 1σ error, respectively. Finally, the solid brown line illustrates the parameterized redshift evolution (up to $z = 4$) of the major merger fraction from the Evolution and Assembly of Galaxies and their Environments (EAGLE, Schaye et al. 2015; Qu et al. 2017) simulation for galaxies with $\mathrm{Log}(\mathrm{M}_\star/\mathrm{M}_\odot) > 9.5$. The dashed line is an extension of that curve towards higher redshifts. Taken from Romano et al. (2021).

fraction ($f_{\rm MM}$) of 0.44 (0.34) at $z \sim 4.5\,(5.5)$. Moreover, by combining these results with merging rates at lower redshift, they computed the cosmic evolution of the merger fraction which is described by a rapid increase from the local Universe to higher redshifts, with a peak at $z \sim 3$ (see Figure 2.6). All these findings together indicate a striking diversity in the ALPINE sample, consequence of a wide range of physical processes at work during this epoch of galaxy assembly, first and foremost, galaxy mergers.

In Chapter 5 we discuss major merging systems in the ALPINE sample, with a particular focus on the connection between galaxies and their environment (CGM, IGM). Indeed, an extended dust continuum and [CII] 158 µm halo around high-z galaxies suggests chemical enrichment of the CGM. This [CII] envelope has been found in multiple $z > 4$ galaxies (Carniani et al., 2018b; Fujimoto et al., 2019) and the ALPINE sample allows, for the first time, a statistical study of these extended halos. In Fujimoto et al. (2020) the authors show that the extent of [CII] halos commonly exceeds the UV size of the galaxies by a factor 2-3 or more for galaxies with increasing stellar mass. Moreover, about 30% of isolated galaxies have [CII]

halos extending more than 10 kpc, at typical UV sizes of 1-2 kpc (Fujimoto et al., 2019). This trend of increasing [CII] to UV size ratio with increasing stellar mass and SFR can be explained by star-formation-driven outflows (e.g. Pizzati et al. 2020; Ginolfi et al. 2020d). In addition, galaxy interactions can contribute to the chemical enrichment of the CGM and IGM around galaxies (see Chapter 5; Jones et al. 2020; Ginolfi et al. 2020b).

2.2.2 ALMA-REBELS at z > 6.5

The Reionization Era Bright Emission Line Survey (REBELS) is an ALMA Cycle 7 Large Program (LP) which observes 40 of the brightest UV-selected and star-forming galaxies known in the $z > 6.5$ Universe. In particular, it targets [CII] 158 µm , [OIII] 88 µm (ISM cooling lines) and dust-continuum emission from these galaxies in order to characterise their ISM properties. The main science goals of REBELS can be summarised as follows:

- characterisation of the ISM properties using cooling lines such as [CII] 158 µm and [OIII] 88 µm emission and dust continuum (e.g. Inami et al. 2022; Aravena et al. 2023; Palla et al. 2023; Algera et al. 2024a);
- investigation of the galaxy stellar mass build-up and the properties of massive and dusty galaxies at $z > 6.5$ (e.g. Topping et al. 2022; Algera et al. 2023a; Sommovigo et al. 2022c; Bowler et al. 2024).

In constructing a sample of 40 UV-bright galaxies to follow up with the REBELS LP, the team made use of deep wide-area optical + NIR observations over the ~ 2 deg^2 COSMOS/UltraVISTA field (Scoville et al., 2007a; McCracken et al., 2012), the ~ 5 deg^2 UKIDSS/UDS + VIDEO/XMM-LSS fields (Lawrence et al., 2007), and a wide range of HST search fields, including CANDELS, CLASH, and the BoRG/HIPPIES pure parallel fields (see Bouwens et al. 2022b for a detailed description of the sample selection). Thus, these galaxies were drawn from a variety of well-studied extragalactic fields, spanning a total area of $\sim$ 7deg^2. Specifically, the selection according to which only UV-bright galaxies are considered originates from the fact that two pilot programs + other programs (Smit et al., 2018; Schouws et al., 2022a; Capak et al., 2015; Matthee et al., 2019) have demonstrated that a significant part of galaxies at $z \sim 5-7$ with especially large UV SFRs also emit brightly in the dust continuum and in various ISM cooling lines like [CII] 158 µm and [OIII] 88 µm .

Figure 2.7 shows the observed [CII] luminosity versus the observed SFR in the UV-rest frame (SFR_{UV}) for galaxies at $z \sim 4-7$. Blue circles are the results from the ALPINE survey (see Section 2.2.1 and references therein) and Capak et al. (2015) at $z = 4-6$ as well as REBELS pilot programs (Smit et al., 2018; Schouws et al., 2022a). Red circles are other $z > 6$ sources from Matthee et al. (2019) and black solid line shows the [CII] 158 µm - SFR relation at $z \sim 0$ (De Looze et al., 2014a). Particularly interesting is the increase in the [CII] luminosity as the SFR_{UV} increase from 5 to 30 $M_\odot$ yr^{-1}. REBELS sources are those in the shaded area with rest-UV SFRs larger than 11 $M_\odot$ yr^{-1} (vertical line), the horizontal dotted line shows the adopted 5σ sensitivity limit. In Bouwens et al. (2022b) the authors show

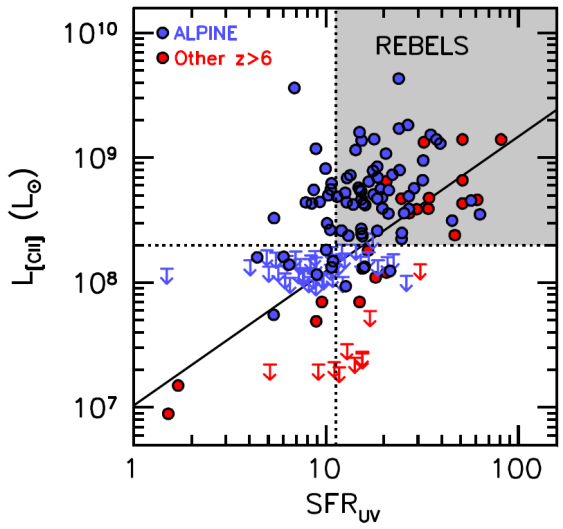

Figure 2.7. Observed luminosity of the [CII] 158 µm cooling line seen in galaxies at $z \sim 4-7$ versus the observed star formation rate of galaxies in the rest-UV. Shaded area highlight the part of the plane where REBELS galaxies are. Adapted from Bouwens et al. (2022b).

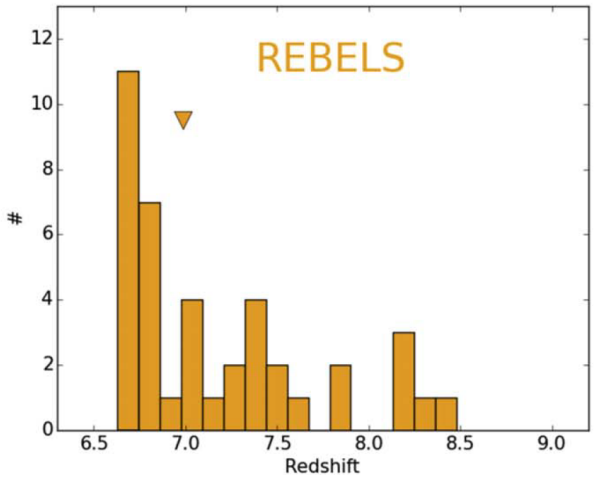

Figure 2.8. Redshift distribution of the REBELS targets. Adapted from Bouwens et al. (2022b).

that a significant fraction of galaxies with $SFR_{UV} > 10$ $M_\odot$ yr^{-1} and especially > 20 $M_\odot$ yr^{-1} have [CII] luminosity in excess of 2×10^8 $L_\odot$ (REBELS sensitivity limit); these high SFR sources at $z > 6.5$ are those the REBELS LP particularly targets in scanning for bright ISM-cooling lines.

All the observations were carried out in one of two compact ALMA configurations, resulting in a typical angular resolution of $1.2" - 1.6"$. The final REBELS targets set is presented in Table 1 of Bouwens et al. (2022b) together with their R.A. and DEC., UV luminosities and photometric redshifts. UV-continuum slopes β, stellar mass estimates, [O III] 4959,5007 μm + Hβ equivalent widths, and SFRs are presented in their Table 2 and here we report Figure 2.8 which shows the redshift distribution of the 40 REBELS galaxies.

Apart from exploring target selection criteria and redshift distribution for REBELS galaxies, it is interesting to investigate the redshift distribution of UV luminosities for targets in the REBELS program. Figure 2.9 shows that REBLES and ALPINE probe objects with consistent M_{UV}, $-23 < M_{UV} < -21.5$ and $-22.7 <$

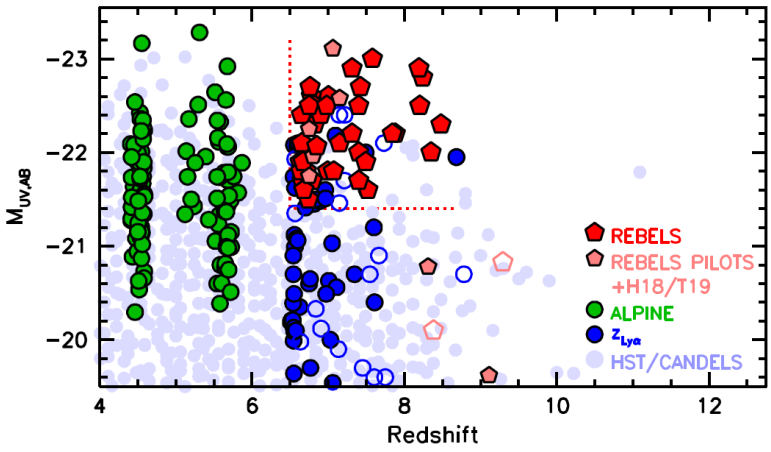

Figure 2.9. UV luminosity and photometric redshifts of REBELS galaxies (red pentagons), sources with spectroscopic redshifts from Lyα (dark blue circles), sources from pilots to REBELS (light red pentagons) all at $z > 6.5$. Galaxies from various HST legacy fields (Bouwens et al. 2021a; light blue circles), and sources with the ALPINE survey (green circles). Taken from Bouwens et al. (2022b).

$M_{UV} <$ - 20.2 respectively. In addition to this, they span a compatible range of stellar masses (from $\sim 10^{8.5}$ $M_\odot$ to $\sim 10^{11}$ $M_\odot$, see Figure 17 of Bouwens et al. 2022b) and target the same ISM cooling lines. Thus, these two surveys can be considered as complementary, allowing us to build a coherent view of galaxy evolution at early time. The evolution of galaxies and their properties at $4 \leq z \leq 10$ have been extensively studied in Di Cesare et al. (2023) (see also Chapter 4) by employing observations from ALPINE and REBELS programs and cosmological simulations, specifically the hydrodynamical code `dustyGadget` (Section 3.2).

Among the many results which have been obtained using REBELS galaxies, particularly interesting for this work are those concerning the ISM properties (e.g. dust content, chemical maturity), the mass build up of REBELS galaxies and the [CII] 158 µm halos around these systems.

As already mentioned, the REBELES LP targets UV-bright galaxies looking for [CII] 158 µm , [OIII] 88 µm and dust continuum (generally harder to detect compared to the lines) providing for the first time a statistical insights into the dust and ISM properties of $z \geq 6.5$ galaxies. In Section 2.2.1 we already introduced how to infer dust masses from observations (see Equation 2.4), however, before presenting the results obtained by the analysis of REBELS sources, it is fundamental to define the UV SFR (SFR_{UV}) and IR SFR (SFR_{IR}) as well. In general, the SFR_{UV} is computed as $SFR_{UV}/(M_\odot\ yr^{-1}) = 7.1 \times 10^{-29} \times (L_{UV}/(erg/s/Hz))$ and SFR_{IR} as $SFR_{IR}/(M_\odot\ yr^{-1}) = 1.2 \times 10^{-10} \times (L_{IR}/L_\odot)$. These values are obtained from Madau and Dickinson (2014a) assuming a constant star formation rate for 100 Myr and a fixed metallicity of Z = 0.002 [11].

Inami et al. (2022) report 18 dust continuum detections in the REBELS sample

[11] In general, precise conversion factors between SFR and IR (UV) luminosity depends on the assumed star formation history. However, the results we present in the following (e.g. Algera et al. 2023b) are, for simplicity, based on fixed value for the SFH (see also Topping et al. 2022; Whitler et al. 2023).

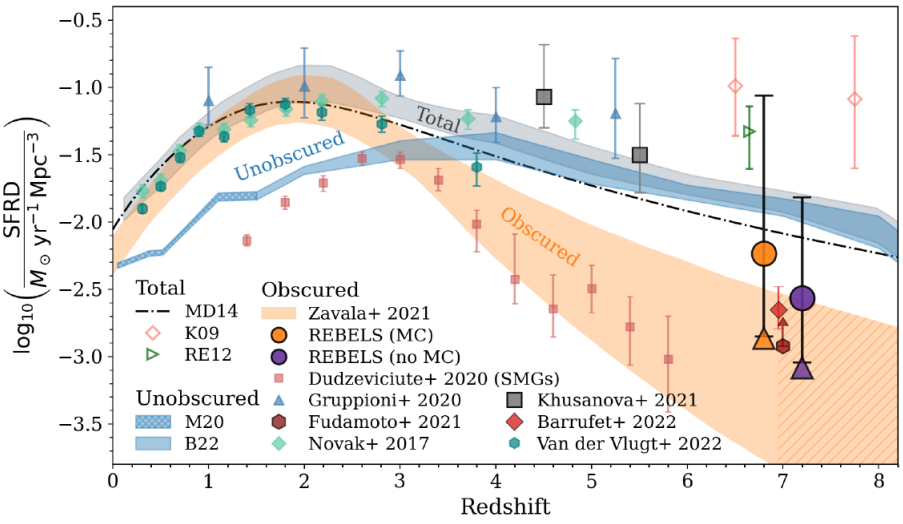

Figure 2.10. Constraints on the dust-obscured cosmic star formation density at $z \sim 7$ from the REBELS survey, using different approaches (purple and orange points, see Algera et al. 2023b for a detailed description) and the lower limits obtained considering only the REBELS galaxies with $8.8 \lesssim \mathrm{Log}(\mathrm{M}_\star/\mathrm{M}_\odot) \lesssim 10.8$ (purple and orange triangles). The authors compare their results with SFRD measurements and compilations from literature. At $z \lesssim 1.5$ they show the unobscured SFRD from Moutard et al. (2020) (M20) and at $z \gtrsim 2$ from Bouwens et al. (2022a) (B22) in blue. Overplotted in orange is the dust-obscured SFRD from Zavala et al. (2021) and in grey is the combined UV+IR SFRD. The REBELS measurements obtained in their work suggest significant dust-obscured star formation is already in place in the epoch of reionization. Taken from Algera et al. (2023b).

and its pilot programs increasing the number of dusty star-forming galaxies in the Epoch of Reionization by a factor of more than 3 and showing that dust is common even in the ISM of these high-redshift systems. Additionally, Algera et al. (2023b) use the dust continuum observations of a statistical sample of 45 galaxies from REBELS (36 sources Bouwens et al. 2021b) and its pilot surveys (9 sources, Smit et al. 2018; Schouws et al. 2022b,a) with the aim of understanding the dust-obscured star formation properties of galaxies in the EoR. The authors found that dust-obscured star formation contributes to $\sim 30\%$ of the total star-formation rate density, highlighting the importance of dust even within the first billion years of the Universe (Figure 2.10) - see also Fudamoto et al. (2021) where the authors found two heavily dust-obscured galaxies from the REBELS survey (REBELS-29-2 and REBELS-12-2) at $z \sim 7$ suggesting that these sources give a non-negligible contribution to the total cosmic SFR density at high-z. Algera et al. (2023b), by disentangling continuum detections and non-detections, estimated that the fraction of obscured star formation, defined as $f_{obs} = \mathrm{SFR_{IR}}/(\mathrm{SFR_{IR}} + \mathrm{SFR_{UV}})$, is ~ 0.70 and ~ 0.25, respectively. These results indicate a large variety in the dust properties of $z \sim 7$ galaxies, even across a sample uniformly selected based on rest-frame UV.

Finally, in Algera et al. (2024b) the authors studied in details three REBELS sources (REBELS-12, REBELS-25, REBELS-38) for which [CII] 158 µm , [OIII] 88 µm and dust continuum are available. Their analysis highlights that these three galaxies

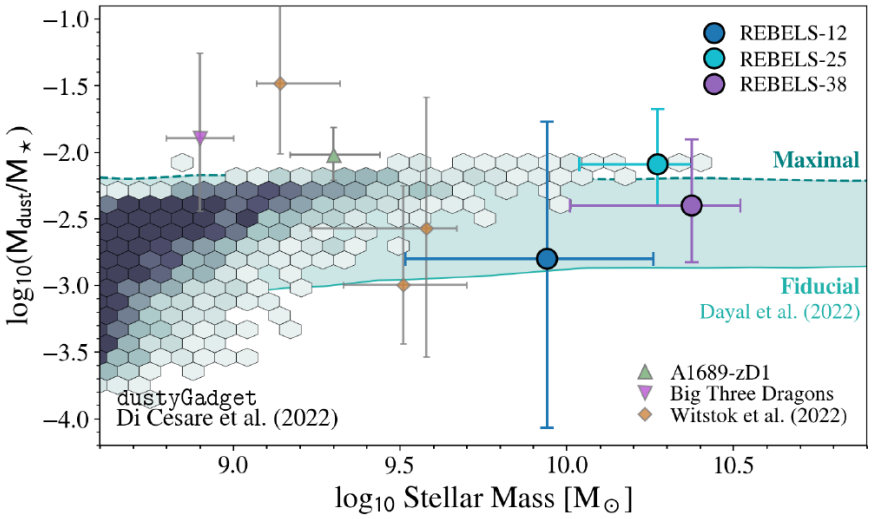

Figure 2.11. Dust-to-stellar mass ratios for three REBELS galaxies (REBELS-12, REBELS-25, REBELS-38) and their comparison with other observations and simulations of high-z galaxies. The authors show a compilation of $z \sim 7$ sources with robust temperature measurements (Witstok et al., 2022) and models from Dayal et al. (2022a) and Di Cesare et al. (2023). The dust masses inferred from REBELS massive galaxies at $z \sim 7$ can be reproduced by state-of-the-art models and simulations. Taken from Algera et al. (2024b).

are characterized by low dust temperatures ($T \sim 30 - 35$ K), high dust and stellar masses ($M_{dust} \sim 10^8 M_\odot$ and $M_\star \sim 10^{9.9-10.5} M_\odot$ respectively, see Figure 2.11) and low [OIII]/[CII] ratios (lower by 2-8× compared to the previously observed populations at $6 \leq z \leq 9$). All these results seem to point toward evolved star-forming galaxies at $z \sim 7$, with the low line ratios suggesting that these targets are forming stars in a less bursty way than expected, resulting into longer depletion timescales and a low heating efficiency per unit dust mass, thus in lower overall dust temperatures.

In Topping et al. (2022) the authors investigate the mass build-up in REBELS galaxies, in particular, the redshift evolution of the sSFR, (i.e. the SFR per unit stellar mass) at $z \sim 7 - 8$. For each source in the sample, they estimated the total SFR as the sum of both obscured (UV) and unobscured (FIR) components, and the stellar masses using SED fitting codes, assuming both a constant SFH with `BEAGLE` (Chevallard and Charlot 2016) and a non-parametric one with `Prospector` (Johnson et al. 2021) but identical initial assumptions[12]. As a result, they inferred a sSFR median value of ~ 18 Gyr^{-1} in the first case and of ~ 7 Gyr^{-1} in the second. Moreover, by complementing data from the Reionization era with literature data at lower redshifts they found that the sSFR computed under the assumption of a constant SFH increases with redshift as $(1+z)^{1.7}$, while, assuming non-parametric star formation histories at $z \sim 7$ it increases as $(1+z)^{1.6}$. In both cases, the power

[12]They found that the main difference in stellar mass estimates resides in the assumption of the SFH, which leads to over one order of magnitude difference, being more significant for the youngest galaxies with age ≤ 10 Myr which populate the lower mass end of the REBELS sample.

law increase in sSFR is only modestly shallower than the power law expected from evolving baryon accretion rates (see discussion Chapter 4).

Another relevant piece of information which comes from the study of REBELS sample, concerns [CII] 158 µm halos around high-z galaxies. Indeed, in Fudamoto et al. (2022) the authors performed a stacking analysis of the [CII] 158 µm emission lines and dust continua observed by ALMA for the REBELS LP finding that the average [CII] emission at $z \sim 7$ has an effective radius of $r_e \sim 2.2 \pm 0.2$ kpc. This radius is two times larger than the dust continuum and the rest-frame UV emission, in agreement with what has been found for $z \leq 6$ galaxies (for example ALPINE galaxies, see Section 2.2.1). Furthermore, the authors also compare their average [CII] size with $4 < z < 6$ galaxies observed by the ALPINE survey, finding that on average there is not an evident evolution in the size of the [CII] 158 µm emitting regions in star-forming galaxies in the redshift range $z = [4, 7]$. If confirmed with further (and deeper) observations, the constant [CII] size could be in contrast with UV size evolution (increasing going towards lower-z) found by Shibuya et al. (2015) (see also Fujimoto et al. 2020; Fudamoto et al. 2022). Also, it would suggest that [CII] emitting gas dominates high-z star-forming galaxies while star formation might occupy a progressively smaller fraction of size in galaxies going towards higher-z. [CII] halos have been already introduced in Section 2.2.1 when talking about ALPINE galaxies, and their nature in major merging systems will be explored in Chapter 5.

2.3 JWST contribution at z > 4

The launch of JWST prompts several questions e.g. What are the physical properties of high redshift galaxy population? What do we know about the impact of galaxies on the cosmic reionization process that transitioned the neutral IGM to an ionized state by $z \sim 6$? But also, how can JWST improve our knowledge of the Universe letting us ask *new* questions previously unanswerable? Moreover, it will - and already is - testing the understanding of the Universe we have built so far using other facilities, i.e. HST, Spitzer Space Telescope, ALMA, the Very Large Telescope (VLT) and the Keck Telescope to mention few of them, and simulations, i.e. Semi-analytical models, hydrodynamical simulations[13] and semi-numerical models.

JWST was launched on December 25$^{\text{th}}$, 2021. It is a 6.5 m diameter cold space telescope with cameras and spectrometers covering 0.6-27.9 μm wavelengths, orbiting in the second Lagrangian point (L2) of the Sun-Earth system and enabling observations of the early Universe. JWST is the result of the international partnership between NASA, ESA and the Canadian Space Agency (CSA).

2.3.1 JWST instruments

In the following, we briefly introduce the four science instruments on board of JWST: NIRCam, NIRSpec, NIRISS and MIRI[14] which make it possible to capture

[13] An extensively description of the hydrodynamical simulation adopted in this these is given in Chapter 3, while in Chapter 4 we compare JWST first results with available high-z simulations.

[14] More details on the instruments and their observational modes can be found in Gardner et al. 2023 and https://webbtelescope.org/news/webb-science-writers-guide/webbs-scientific-instruments

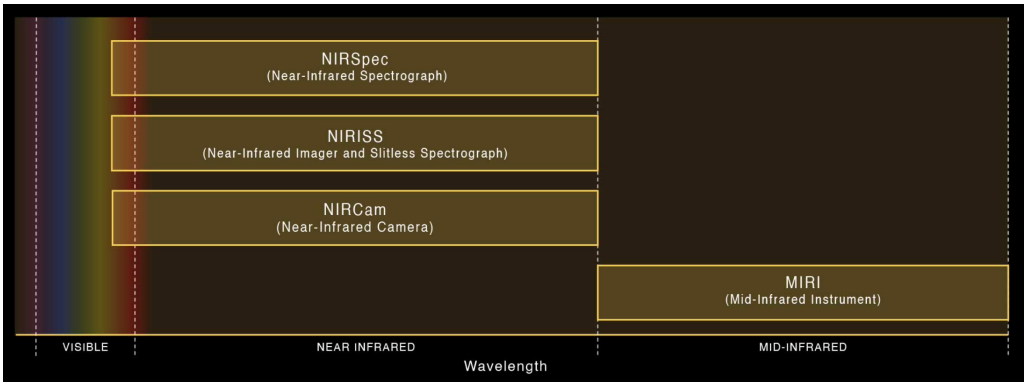

Figure 2.12. The JWST four science instruments and their sensitivity to a specific range of wavelengths. NIRCam, NIRSpec, and NIRISS all observe visible red to near-infrared light, while MIRI observes longer-wavelength mid-infrared light. Credits to STScI.

the light in the wavelength range from 0.6 to 27.9 μm (see Figure 2.12).

NIRCam

The Near Infrared Camera (NIRCam, Rieke et al. 2003; Horner and Rieke 2004; Rieke et al. 2023) provide imaging in broad-band, medium-band and narrow-band from 0.6 to 5.0 μm (red to NIR), and it has a wide-field slitless spectroscopy capability from 2.5 to 5.0 μm. NIRCam is designed with two identical modules (A and B) which observe parallel fields of view, with each module containing a dichroic at 2.4 μm to get simultaneous data in the filters longward and shortward of the dichroic. The total field of view (FoV) is 2.2×4.4 arcmin^2 and there are eight detectors in the short-wavelength channel and two in the long-wavelength channel.

NIRSpec

The Near Infrared Specrograph (NIRSpec, Jakobsen et al. 2022; Böker et al. 2023) offers spectroscopy across the wavelength range of 0.6 to 5.3 μm with varying resolutions of R $\sim$ 100, R $\sim$ 1000, and R $\sim$ 3000. This is achieved through the use of fixed slits, a microshutter assembly (MSA) (Ferruit et al., 2022), or an Integral Field Unit (IFU) (Böker et al., 2022). The pixels of the detector (made of mercury cadmium telluride) arrays, measuring 18 μm×18 μm, correspond to an average of 0.103" in the dispersion direction and 0.105" in the spatial direction. Dispersion is done using either a prism (R = 30–300) or gratings (R = 500–1343 or R = 1321–3690), which are combined with filters to control the bandwidth and length of the resulting spectra on the detectors. NIRSpec's FoV covers a total area of $\sim 3.3 \times 3.3$ arcmin^2.

NIRISS

The Near Infrared Imager and Slitless Specrograph (NIRISS, Doyon et al. 2012, 2023) offers three specialized scientific capabilities alongside redundant broad-band imaging, covering wavelengths from 0.7 to 5.0 μm. Packaged with the Fine Guidance

Sensor (FGS), NIRISS utilizes the signal to the fine-steering mirror and the attitude control system for target locking and precise guiding. With a FoV matching one of the two NIRCam channels at $2.2' \times 2.2'$.

MIRI

The Mid Infrared Instrument (MIRI, Wright et al. 2015, 2023) offers a comprehensive suite of capabilities, including broad-band imaging and Integral Field Unit (IFU) spectroscopy spanning the wavelength range of 4.9 to 27.9 μm (mid-IR). Additionally, it provides low-resolution slit spectroscopy from 5.0 to 12.0 μm, although sensitivity is constrained by the zodiacal light background, along with a coronagraphic function. It has two detectors (made of Arsenic-doped silicon) designated for medium-resolution spectroscopy, while the third serves imaging, low-resolution spectroscopy, and coronagraphy purposes. MIRI operates at an actively cooled temperature of 6.0 K, facilitated by a hybrid mechanical cooler. Its main FoV covers an area of 1.2×1.9 arcmin^2.

2.3.2 High-z Universe with JWST

On July 12$^{\text{th}}$, 2022 JWST has delivered the deepest and sharpest infrared image of the distant Universe to date, showing the galaxy cluster SMACS 0723 teeming with thousands of galaxies – including the smallest, faintest objects ever observed (Figure 2.13). The mass of this galaxy cluster acts as a gravitational lens, magnifying more distant galaxies, including some of them belonging to when the Universe was less than a billion years old ($z > 6$). This deep field, obtained by NIRCam, is a composite made from images at different wavelengths (totaling 12.5 hrs) achieving depths at infrared wavelengths beyond the HST's deepest fields and bringing distant galaxies into sharp focus – they have tiny, faint structures that have never been seen before, including star clusters and diffuse features. This field was also imaged by MIRI, which observes mid-infrared light, being able to highlight the presence of galaxies embedded in thick layers of dust (in red) or dust free (in blue), thus giving us information about the chemical maturity of the ISM of these early galaxies.

As a result of the giant leap in sensitivity, JWST has already started to revolutionize the field pushing our understanding of the Universe back beyond Epoch of Reionization to the eras when the very earliest galaxy forms and questioning the how galaxies form and evolve in the first billion years of cosmic evolution. With is unprecedented sensitivity, JWST is revolutionising the field.

JWST/NIRCam observations made it possible to detect galaxies at $z \gtrsim 10$ (Castellano et al., 2022; Labbe et al., 2022; Naidu et al., 2022a; Adams et al., 2022; Tacchella et al., 2022, 2023; Robertson et al., 2023) providing the first observational constraints on the UV luminosity function and and star formation history in the first 500 Myr of the Universe (Donnan et al., 2022; Harikane et al., 2022b) showing a lack of evolution in the number density of bright galaxies at $z \gtrsim 10$ galaxies. We have to bear in mind that some of these sources must be interpreted with caution as they can be mistaken with dusty, star-forming galaxies at $z \sim 5$ (Zavala et al., 2022; Naidu et al., 2022b; Arrabal Haro et al., 2023). However, JWST is showing that galaxies in the early Universe are characterized by diverse properties (Barrufet

Figure 2.13. JWST's first released image, the lensing cluster SMACS 0723, which was the deepest infrared image ever taken. Image credits: NASA, ESA, CSA, and STScI.

et al., 2022; Whitler et al., 2023), such as strong dust obscuration at $8 < z < 13$ (Rodighiero et al., 2023), massive quiescent objects at $3 < z < 5$ (Carnall et al., 2023) and low mass quenched galaxies out to $z \sim 7$ (Looser et al., 2023).

JWST/NIRSpec observations have spectroscopically confirmed several galaxies (see for example Nakajima et al. 2023 and references therein), including objects at $10 \leq z \leq 13.2$ (Bunker et al., 2023; Curtis-Lake et al., 2023; Robertson et al., 2023; Arrabal Haro et al., 2023). Many of these galaxies show strong nebular emission lines, suggesting extreme excitation conditions, with high ionization parameters and low-metallicities (Curti et al., 2023; Cameron et al., 2023c,b; Sanders et al., 2023, 2024).

Before JWST, the most remote galaxy observed with spectroscopic confirmation was GN-z11 detected using grism spectroscopy with HST and with emission lines from ground-based Keck observations (Oesch et al., 2016; Jiang et al., 2021). Nowadays, not only has GN-z11 been observed with JWST (both in imaging and spectroscopy, Tacchella et al. 2023; Bunker et al. 2023), but it has also been argued that, apart from being a possible host of PopIII stars (Maiolino et al., 2023b), this galaxy hosts a nuclear black hole with mass $M_{BH} \sim 2 \times 10^6 M_\odot$ accreting at super-Eddington rates (Maiolino et al., 2023a), that it has a dust poor nature (Fudamoto et al., 2023),

and that shows a nitrogen enhanced feature suggesting yields from runaway stellar collisions in a dense stellar cluster or a tidal disruption event as a promising solutions (Cameron et al., 2023a).

In the following, we highlight some of the main questions that have been posed by JWST which have started challenging the predictions from state-of-the-art models and simulations, and our understanding of the galaxy formation and evolution in the early Universe.

UV Luminosity Function

The bright end of the UV LF can be used to estimate the efficiency of star-formation and feedback mechanisms in the early Universe (Bowler et al., 2014; Tacchella et al., 2018; Bowler et al., 2020). It has been observed that the number density of fainter galaxies continue to decline with redshift, while the most UV luminous galaxies - that are also easier to follow-up with spectroscopic studies - seem to have formed rather early in the evolution of the Universe (see for example Stefanon et al. 2019; Bowler et al. 2020; Harikane et al. 2022b; Finkelstein et al. 2023). Figure 2.14 shows the UV LF at $z > 10$ from Naidu et al. 2022a where the authors analysed luminous galaxies from public JWST Early Release Science programs (CEERS and GLASS) and compared them with previous UV LF determination and extrapolations from lower redshifts. In particular, the authors show that the extrapolation of the Schechter function trends estimated at $z = 3 - 10$ results in a LF at $M_{UV} = -21$ that is a factor $> 10\times$ lower than their observed estimates. On the other hand, Naidu et al. (2022a) found a good agreement when extrapolating the trends in the double-power law LFs from Bowler et al. (2020) to $z \sim 11.5$. In addition to this, the comparison with models, `UniverseMachine` (Behroozi et al., 2019) and Delphi (Dayal et al., 2014, 2022a), shows that the model LFs evolve very rapidly at this early epochs such that the LF at $z \sim 12$ is $> 30\times$ below their estimate. *If* the candidates analysed in Naidu et al. (2022a) are *spectroscopically confirmed* as galaxies at $z = 10 - 12$ and together with GN-z11 (Oesch et al., 2016), this may start giving evidences that the star-formation efficiency in the early Universe is much higher than expected (Tacchella et al., 2013; Mason et al., 2015; Tacchella et al., 2018) resulting in the early appearance of UV-luminous galaxies with stellar masses as high as $\sim 10^9$ $M_\odot$ already a few hundred Myrs after the Big Bang. The existence of these massive galaxies at such early times raises interesting questions about how early such galaxies began forming, potentially earlier than current expectations. Diverse possible answers have been proposed by models suggesting that explanations for these very bright galaxies may reside in a disproof of the ΛCDM cosmological model (Boylan-Kolchin, 2023; Lovell et al., 2023; Gong et al., 2023; Haslbauer et al., 2022; Steinhardt et al., 2023; Menci et al., 2022; Desprez et al., 2023), in the need for a top-heavy IMF at high-z (see for example Riaz et al. 2022; Cameron et al. 2023b; Trinca et al. 2023; Zackrisson et al. 2023; Yung et al. 2024; Harikane et al. 2024; Ventura et al. 2024, but also Rasmussen Cueto et al. 2023 [15]), in dust clearing by radiation-driven outflows (see Ferrara et al. 2023; Ziparo et al. 2023; Fiore et al. 2023; Ferrara 2023) or, finally, in high star star formation efficiency in the high-z Universe,

[15] For a discussion on how top-heavier IMF alone is unlikely to explain the higher abundance of bright $z > 10$ sources.

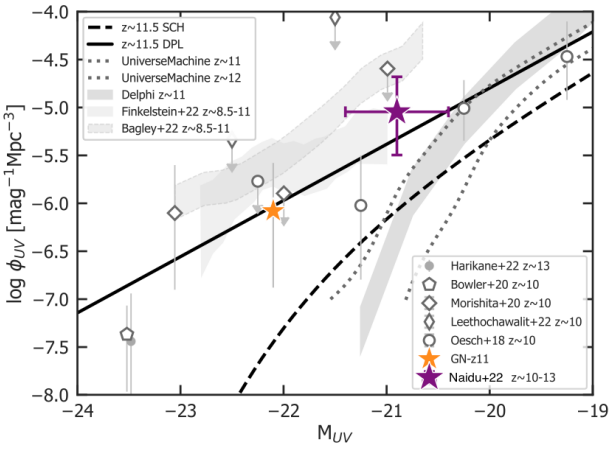

Figure 2.14. Constraints on the bright end of the UV LF at $z \sim 10 - 13$. Comparison between JWST data (stars), an extrapolation of Schechter function at $z = 11.5$ Bouwens et al. (2021a) (black dashed), a double-power law LFs from Bowler et al. (2020) (black solid line) and other LF estimates and upper limits at $z \sim 10$ (see legend for references). Adapted from Naidu et al. (2022a).

with implications on the UV LF (Dekel et al., 2023; Li et al., 2023b; Mason et al., 2023; Mirocha and Furlanetto, 2023; Muñoz et al., 2023; Pallottini and Ferrara, 2023; Shen et al., 2023; Sun et al., 2023; Kobayashi and Ferrara, 2024).

Faint AGN

In addition to the luminosity function at high-z, JWST also made it possible to observe faint AGN at $z \geq 5$ (Matthee et al., 2023; Kocevski et al., 2023; Kokorev et al., 2024; Pérez-González et al., 2024) that are key for understanding the formation of supermassive black holes and determine their role in cosmic reionization. Before the advent of JWST, samples of AGN at these redshifts were mainly restricted to relatively bright systems, with luminosities greater than or equal to $\gtrsim 5 \times L^{\star}$ ($M_{UV} \lesssim -22$), which allowed for ground-based rest-UV spectroscopy (see for example Kulkarni et al. 2019; Niida et al. 2020; Shin et al. 2022). Constraining the abundance and characteristics of these faint AGN, which is uncertain by more than two orders of magnitude (Parsa et al., 2018; Giallongo et al., 2019; Morishita et al., 2020; Shen et al., 2020; Finkelstein and Bagley, 2022), holds significant implications for various aspects of extragalactic astronomy as these sources could play a crucial role in the final stages of hydrogen reionization in the Universe (Madau and Haardt, 2015; Finkelstein et al., 2019), particularly if they exist in environments conducive to the escape of ionizing photons. Additionally, understanding the number density and properties of black holes with masses in the range of $M_{BH} \sim 10^{6-7}$ $M_{\odot}$ can provide insights into scenarios of black hole seeding and growth, shedding light on the presence of extreme supermassive black holes at $z \gtrsim 6$ (e.g. Volonteri 2010) that formed within a billion years of evolution of the Universe (Ricarte and Natarajan, 2018; Trinca et al., 2022; Li et al., 2023a; Schneider et al., 2023).

Cosmic Reionization

The cosmic reionization is the epoch in the evolution of the Universe when the hydrogen in the IGM transitioned from being nearly completely neutral to ionized. We know that this transition was driven by the Lyman continuum (LyC; $\lambda < 912$ Å) photons emitted by the first luminous sources in the Universe. However, the nature

of these sources remain elusive, in fact, star-forming galaxies can account for the photon budget to complete reionization only if a substantial fraction of the UV photons produced by their stellar populations escape from the ISM and CGM of the galaxies. Taking into account the density of star-forming galaxies in the EoR, it has been shown that on average a LyC escape fraction (f_{esc}) of 10% across all galaxies is needed (see for example Robertson et al. 2015; Finkelstein et al. 2019; Yung et al. 2020b,a) to reionize the Universe by $z = 6$, and match the Thomson optical depth of electron scattering in the CMB (Planck Collaboration et al., 2016). In this evolutionary scenario, the relative importance of massive and low-mass galaxies in driving reionization is still a matter of great debate as it is intrinsically related to its timeline and topology. If faint and low mass galaxies are considered to be the main drivers of such process, dominating over bright galaxies with higher f_{esc}, then we expect reionization to start earlier and perhaps proceed in a more homogeneous manner (Ferrara and Loeb, 2013; Finkelstein et al., 2019). Conversely, a delayed reionization is predicted if the contribution from faint galaxies ($M_{1500} \geq -18$) can be considered as subdominant compared to that of brighter systems (Robertson et al., 2015; Naidu et al., 2020). While both types of galaxies are likely to contribute to the ionizing budget, the balance and interplay between them remain uncertain. JWST enable observations of galaxies in the EoR, making the characterisation of this epoch and its drivers possible. So far, it seems to indicate that faint and low-mass galaxies potentially play a dominant role in the reionization process (see for example Saxena et al. 2023; Mascia et al. 2023b,a). However, to explore significantly large samples of such faint galaxies, it will be necessary to conduct ultra-deep observations in galaxy cluster fields, where gravitational lensing serves as an essential tool. This approach is exemplified by Atek et al. (2023), which extends observations to galaxies as faint as $M_{UV} = -15$.

2.4 Synergy among telescopes

In this Section, we briefly discuss the synergy among telescopes, focusing specifically on that between JWST and ALMA, which is of particular interest for the study conducted in this thesis

The cooperation of different telescopes, such as ALMA and HST, and - currently - ALMA and JWST, has always been of paramount importance to obtain a comprehensive understanding of galaxy evolution during cosmic history. Indeed, the complementarity of telescopes like HST/JWST and ALMA enables us to gather information not only on the stellar component of galaxies, but also on the gas and dust distribution in their ISM and CGM. In fact, the multi-wavelength view of JWST and ALMA allow us to better constrain the SED of high-z galaxies leading, for example, to a better understanding of the ISM properties and conditions in galaxies (see for example Valentino et al. 2024, A&A (in press), Fujimoto et al. 2022) helping us to better track the build-up of heavy elements in the distant Universe.

Moreover, ALMA has been also used to spectroscopically confirm the redshift of high-z galaxies via ISM coolants such as [OIII] 88 µm and [CII] 158 µm lines. One example is the object MACS0416-Y1 identified in the HST Frontier Fields (Zheng et al., 2012) which was spectroscopically confirmed at $z = 8.312$ with ALMA via

detections of [OIII] 88 µm , [CII] 158 µm lines and dust emission (Tamura et al., 2019; Bakx et al., 2020). More recently, Bakx et al. (2023) and Popping (2023) used ALMA observations to spectroscopically confirm the redshift of GHZ2/GLASS-z13 (identified in the GLASS-JWST Early Release Science Program, Treu et al. 2022) through the [OIII] 88 µm emission line finding no obvious line emission. In general, we must be very careful in interpreting line detections (or non-detections) with ALMA. In this regard, in Kaasinen et al. (2023) we analysed the galaxy HD1, which was proposed to be a $z \sim 13.27$ (Harikane et al., 2022a) based on its potential Lyman break and tentative [OIII] 88 µm detection with ALMA. In this paper, we made use of ALMA Band 4 observations[16] and re-analyse the existing ALMA Band 6 data to determine the proposed redshift. Our analysis suggested that we are more likely to be detecting noise features rather than both [OIII] 88 µm and [CII] 158 µm emissions from a source at $z \sim 13.27$. Although we had not found compelling evidence of a very high-z galaxy, we cannot completely dismiss this possibility. Non-detections may also occur for a $z \sim 13$ source with a low interstellar gas-phase metallicity or ionization parameter and/or high gas density. JWST/NIRSpec follow-up is needed to identify the precise nature and redshift of this object.

[16]This Band is where we expect the [CII] 158 µm emission be if HD1 is a $z \sim 13.27$ galaxy.

Chapter 3

High-z galaxies: simulations

In this Chapter we dive into the available numerical methods used in modern astronomy to model galaxy formation and evolution in a cosmological context. Over the past decades, advances in numerical methods and computing capabilities have allowed enormous progresses in our ability to simulate the formation and evolution of galaxies ab initio, and to make predictions for the expected observable properties of galaxies.

3.1 Cosmological simulations

3.1.1 N-body simulations

The DM large scale structure of our Universe is the back bone for any galaxy formation model, as DM forms the potential wells in which baryons fall and start collapsing to form, in the end, galaxies and stars (Section 1.6). In Section 1.5 we introduced the PS formalism that was initially adopted to make predictions on the halo mass function and DM halos merger trees (Lacey and Cole, 1993). However, as anticipated, in order to describe the non-linear regime of structure formation and to recover the complex structure of the Cosmic Web N-body simulations are needed. In general, the idea behind cosmological N-body simulations of the large scale structure is to simulate the gravitational evolution of the DM component in a representative portion of the Universe, by tracing single mass elements of the DM fluids (discretized into particles) with a given mass resolution. The force on each mass elements is computed by solving the classical N-body problem with N point masses m_i interacting via gravitational interaction in a comoving frame, and by adopting periodic boundary conditions for the volume. This gravitational potential can be computed using different techniques, for example, particle-based, mesh-based or hybrid methods that we introduce in the following. For a more detailed description of N-body simulations, we refer the interested reader to Gnedin et al. (2016).

Particle-based method

The most straightforward method is to compute the force acting on each particle i as a consequence of all the other particles j with a direct summation, by solving a system of N differential equations composed of the gravitational force, initial

positions and velocities (i.e. equations of motion for a system in a Newtonian approximation). This technique is very expensive as for each particle we have to calculate N-1 interactions for a total of N(N-1) computations to recover the force. Indeed, because of the long-range nature of the gravitational interaction, each particle interacts with every other particle in the volume. Therefore, the high accuracy of this method scales as $O(\mathrm{N}^2)$, rapidly becoming computationally unmanageable. A workaround in particle-based approaches is to use tree codes (Barnes and Hut, 1986), where the force from groups of particles distant from the i-th is approximated via their multipole moments. Specifically, the comoving volume is recursively split in many sub-boxes until each of them only contains one particle: the force acting on the i-th particle is exactly computed only for the nearest neighbours, while only the global effect for the farthest mass elements is considered. The number of operations required for this algorithm is of the order $O(\mathrm{N\,LogN})$, significantly less expensive than $O(\mathrm{N}^2)$, but the main drawback of this technique is the memory consumption as together with position and velocity of each particle it has to store an arbitrary number of multipoles for each group of particles.

Mesh-based method

In particle-mesh (PM) methods the potential is computed on a Cartesian grid composed of N_g points using a Fourier transform of the density field and the particles are moved according to potential gradients. Firstly, the mass density $\rho(\vec{x}, t)$ is calculated on the grid starting from the masses and positions of the particles[1], then, the solution of Poisson equation for the gravitational potential in Fourier space

$$\hat{\Phi}(\vec{k}, t) = -4\pi G a^2 \, \frac{\hat{\rho}(\vec{k}, t)}{k^2} \tag{3.1}$$

is computed. In this Equation, $\hat{\rho}$ and $\hat{\Phi}$ are the discrete Fourier transforms of the mass and density potential, respectively, and $\vec{k}$ is the wave vector. The gravity field is obtained by transforming the potential back to the spatial domain, the gravity is interpolated from the grid back to the particles with the same interpolation scheme used in the beginning (mass assignment). On the one hand the PM method requires $O(\mathrm{N}) + \mathrm{O}(\mathrm{N_g\,LogN_g})$ operations to evaluate the forces on all the particles, being faster than the tree algorithm. On the other hand, it approximates poorly the inverse law for pair separations smaller than the grid spacing, while in particle-based codes the forces can be accurately represented down to a chosen softening length.

Hybrid method

In the particle-particle-particle-mesh ($\mathrm{P^3M}$) method, which is a hybrid between the particle and mesh based ones, the forces are accurately computed with a direct sum or a tree code for pairs separated by less than two or three grids spacing (small-range forces), while long-range forces are computed using faster PM methods (see Bertschinger 1998 for a review on this technique).

[1] This first step is called mass assignment.

In general, the raw outputs from N-body simulations are given in term of positions and velocities of all the particles, thus, the identification of gravitationally bound systems, i.e. DM halos, is done in post-processing (or on-the-fly when needed) by halo finder algorithms. Either Friends-of-Friends (FoF) methods, where only the position of the particles is used to group those spatially closed, or 6D phase-space methods, which make also use of the particle velocity information, or spherical overdensity, which identify spherical regions with an average density corresponding to that of a virialised region, can be used. In the work by Knebe et al. (2011) the authors compared the performances of different halo finders for a set of mock halos; they found an overall agreement on the halo mass functions and on halo properties (for example mass and peak circular velocity), while for the identifications of substructures, collapsed at earlier epochs, a better performance by 6D phase-space methods is found.

Currently the largest N-body simulation of the Universe is the Millennium XXL (MXXL, Angulo et al. 2012) - extending and complementing the previous Millennium (Springel, 2005) and Millennium-II simulations (Boylan-Kolchin et al., 2009) - representative of a 3 h^{-1} cGpc volume by means of 6720^3 DM particles.

3.1.2 Hydrodynamical simulations

Baryonic physics

Modelling the DM component with N-body simulations is not enough if we want to simulate the behaviour of standard, i.e. baryonic, matter in our Universe. Hydrodynamical simulations are thus essential for this purpose. In hydrodynamical codes, the gas component is computed by solving the Navier-Stokes equations simultaneously to the gravitational component. Usually, for simplicity, the Euler equations for an ideal fluid are considered and the effects of discontinuities and shocks are simulated using an artificial viscosity term. There are two methods that have been developed for hydrodynamical simulations:

1. a Lagrangian method, which is a particle-based one;

2. an Eulerian method, which is a grid-based one.

The most popular method to study galaxy formation so far is the Lagrangian one (Lucy, 1977; Gingold and Monaghan, 1977), called Smoothed Particle Hydrodynamics (SPH), where the baryonic fluid is traced by particles (see for examples reviews by Monaghan 1992; Price 2005; Springel 2010; Price 2012). The information about the fluid is then recovered using a kernel-weighted sum over the particles close to j inside a given smoothing length h. For example, if we consider the field X_i we have:

$$X_i = \sum_j \frac{m_j X_j}{\rho_j} W(r_{ij}, h_i, h_j), \tag{3.2}$$

where W is the kernel or smoothing function, that takes into account the distance between particles in units of smoothing length.

Some examples of SPH methods applied to cosmological scales simulations are `Gadget` (Springel et al., 2001; Springel, 2005), `Gizmo` (Hopkins, 2015) and `Gasoline` (Wadsley et al., 2017), while on smaller scales there are `Phantom` (Price et al., 2018) and `Bonsai-SPH` (Bedorf and Portegies Zwart, 2020).

On the other hand, in Eulerian methods the fluid is discretised into grid cells, and the fluid equations are solved in the frame of the grid, rather than in the fluid frame as it is done in the Lagrangian approach. To deal with the wide dynamical range covered by cosmological simulations the Adaptive Mesh Refinement (AMR), in which high-density regions are sampled with increased resolution, has been implemented. This can be realised either by splitting cells down according to some local criteria (cell-based AMR, see for example `Ramses`, Teyssier 2002, 2010) or by superimposing a finer grid compared to the first one that does not have any correlation with it (patch-based AMR, see for example `Enzo`, Baldry et al. 2012). Apart from AMR codes, there are also the so-called Moving Mesh Refinement (MMR) codes, which adopt a deformable mesh that follows the fluid in a Lagrangian-like fashion. An example is `Arepo` (Springel, 2010) where a Voronoi tassellation is adopted.

The main advantage about the Lagrangian methods is that they have a high adaptivity and dynamic range for a given computational time (i.e. SPH codes can adjust their spatial resolution according to the clustering of matter). This makes them particularly suitable for cosmological simulations. Another advantage is that every particles movements is directly tracked (e.g. in galactic outflows, interactions among galaxies) by the code, allowing to follow the evolution of the galaxy components. On the other hand, Eulerian methods perform very well in the description of the small-scale behaviour of gaseous fluids and in modeling strong shocks and surface instabilities. This is a direct consequence of a more natural and coherent definition of volumes, defined by the size of each cell, in these methods. The gas density in a given cell is derived from the gas mass contained into a cell divided by its volume, while in SPH models the definition of volume relies on the assumptions made on smoothing length (i.e. range of action) of the kernel function. This inconsistency when considering different scales using a fixed kernel, has been addressed with two different approaches. The first one consists of considering adaptive softening lengths, depending on the relative positions of gas particles (an example is the code `Gasoline`), while the second one is to adopt an auxiliary mesh to recover the volume occupied by each SPH particle, the so-called Voronoi Particle Hydrodynamics (VPH, see for example `Gadget-3` Heß and Springel 2010 and `Gizmo` Hopkins 2015).

The definition of volumes and, as a consequence, of densities is important as they enter in the identification of star-forming regions. In fact, the prescriptions for star formation usually rely on density thresholds, meaning that an overestimation (underestimation) of the gas density can lead to an overproduction (underproduction) of stars. Apart from density, also a detailed implementation of the chemical, mechanical and radiative feedback plays a major role in star formation.

Radiative and chemical feedback and sub-grid physics

As hydrodynamical simulations model baryonic physics, they also have to deal with radiative transfer processes. Generally, radiative cooling and photo-ionization

heating are implemented in most hydro codes, while only some of them evolve the ionizing field together with baryons in a self consistent way (see for example Wise and Abel 2011). Another approach is to apply radiative transfer codes (such as `CRASH`, Maselli et al. 2003; Graziani et al. 2013) in the post-processing phase (see for example Graziani et al. 2018).

In addition to radiative processes, a model for the chemical enrichment of galaxies needs to be taken into account in hydrodynamical simulations. Indeed, chemical enrichment is not only important for cooling processes, thus for star formation activity, but also for the chemical evolution of galaxies themselves - the so-called galactic chemical evolution (GCE, see Gibson et al. 2003 and Prantzos 2008 for a review). Specifically, metal yields from Type II SNe (SNeII) are needed to track track Oxygen abundance, while Carbon and Iron are mainly produced by the delayed feedback from Type Ia SNe (SNeIa) and AGB stars. Usually, the Instantaneous Recycling Approximation (IRA)[2] is relaxed in codes that follow the chemodynamics of the gas, accounting for stellar lifetimes (see Padovani and Matteucci 1993). Hydrodynamical simulations, which have the advantage of accessing spatially resolved environments and their dynamics, have the obvious drawback of requiring a lot of computational resources and time as a consequence of the increased complexity of these environments. Moreover, processes happening on small scales, that cannot be directly followed in a cosmological context, require sub-grids prescriptions. This is the case for star formation and feedback processes which span a range of about 11 orders of magnitude in mass and 24 in density - individual galaxies can reach masses of $\sim 10^{11}$ $M_\odot$ with densities of $\sim 10^{-24}$ g cm^{-3} while the typical masses and densities of stars are of the order of ~ 1 $M_\odot$ and ~ 1 g cm^{-3} respectively.

In simulating galaxy evolution it is important to take into account feedback processes, fundamental for the star formation regulation and also the interaction between the galaxy and its environment. Feedback processes can be divided in two classes: (i) preventive feedback, which inhibits the star formation by stopping the gas from accreting into the ISM; (ii) ejective feedback, which removes the gas from the ISM after it has been accreted. This is needed to explain the stellar and baryonic fraction within galactic-sized halos ($\leq 20\%$, much lower than the universal value) and it has been ascribed to large-scale galactic outflows powered by massive stars, SNe and AGN.

In simulations, the first type of feedback is usually taken into account in the normalisation of the star formation recipes - the efficiency is nearly universal, as suggested by Krumholz et al. (2012) - while the second type, thus the modelling of galactic outflows, is far from being trivial. Different approaches have been suggested to model outflows (see for example Katz et al. 1996 or Navarro and White 1993). These models are usually implemented by mean of two free parameters: the mass loading factor $\eta = \dot{M}_{\rm wind}/{\rm SFR}$ (where $\dot{M}_{\rm wind}$ is the mass-loss rate that goes into the wind), and the wind velocity $v_{\rm wind}$. Detailed information on how the feedback physics has been implemented in the `Gadget` code is discussed in Springel and Hernquist (2003).

[2] In the IRA scenario stars release their metals right after being formed.

3.2 The dustyGadget simulation

In this Section we describe in more detail the hydrodynamical simulation `dustyGadget` (Graziani et al., 2020; Di Cesare et al., 2023; Venditti et al., 2023b,a) that has been employed throughout this work.

3.2.1 The code

To perform our simulations we adopt the hydrodynamical code `dustyGadget`, which is an extension of `Gadget-2/3` (Springel, 2005) and accounts for self-consistent dust production and evolution on top of the chemo-dynamical extensions of the original code (Tornatore et al., 2007b; Maio et al., 2010). An overview on the star formation receipt, metal enrichment schemes and the implementation of feedback processes adopted in `dustyGadget` can be found in Section 4.2 and Section 5.4.1. While, the dust model implemented in the simulation is detailed in the following.

Dust production by stars, AGB and SNe, is described using mass and metallicity dependant stellar yields, ensuring consistency with the gas phase metal enrichment. Specifically, yields for AGB stars are derived from Ferrarotti and Gail (2006) and Zhukovska et al. (2008), while yields from PISNe and SNeII are adopted from Schneider et al. (2004) and Bianchi and Schneider (2007) respectively. The effect of reverse shock, which leads to the fact that only a fraction among 2-20% of the dust is able to survive, is taken into account by considering an effective dust yield (see Schneider and Maiolino 2023 for a review). In Schneider and Maiolino (2023), the authors explore the relative importance of SNe and AGBs on dust masses assuming a Salpeter IMF in [0.1-100] $M_\odot$ and a single stellar population model. In Figure 3.1 different colors are different models of SN and AGB dust yields with the shaded regions representing the metallicity variation ($Z = [10^{-4}\text{-}1]\ Z_\odot$) [3], while the top and bottom panels show the results of SN dust production with and without reverse shock, respectively. As shows from Figure 3.1, in the first 3-5 Myr of evolution, before the explosion of the first SN progenitors, there is not any dust released in the ISM. Then, SNe dominate the dust production for the first 35-50 Myr, until the most massive AGBs start to contribute (dotted line at $t = 35$ Myr). On longer timescales the contribution of AGBs and SNe depends, for example, on dust destruction by the reverse shock, the adopted set of yields, and the initial metallicity of the stars.

In the current implementation we follow four classes of dust species: Carbon, Silicates, Aluminia and Iron; but it is also possible to implement alternative dust yields and to include different grain types. Once formed, dust is spread in the gas surrounding evolving stars together with metals[4]. After being produced, dust grains

[3] In general, the dust mass release from a star depends on the initial metallicity. However, the extent of this dependence varies among models, see for example Bianchi and Schneider (2007); Marassi et al. (2019) for SN dust yields and the ATON models (Ventura et al., 1998) for AGB dust yields.

[4] The wind prescription in `Gadget` follows that of Springel and Hernquist (2003) where a constant mass loading factor η is assumed. On top of that, by assuming that the wind carries a fixed fraction χ of the SN energy ϵ_{SN} and by equation the kinetic energy of the wind with the energy input by SNe, one can obtain the velocity of the wind $v_{\rm wind}$ when it leaves the disk. In `dustyGadget` galactic winds are modelled with a constant initial velocity of 500 km/s, comparable with outflows observed in ALMA-ALPINE galaxies (Ginolfi et al., 2020d).

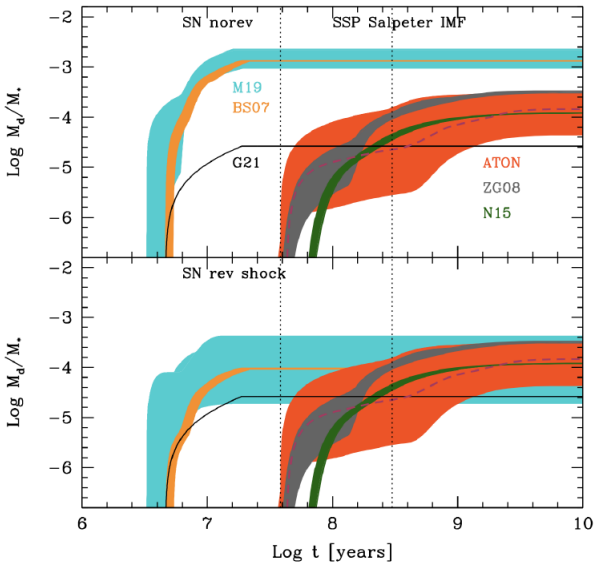

Figure 3.1. Relative importance of SNe and AGBs as stellar sources of dust. Different colors are different models for SN and AGB dust yields: SN dust yields from Bianchi and Schneider (2007) (BS07) are in orange, from Marassi et al. (2019) (M19) in cyan and from Galliano et al. (2021) (G21) in black. While, AGB dust yields from Zhukovska et al. (2008) (ZG08) are in gray, those from the COLIBRI (Marigo et al., 2013) and ATON (Ventura et al., 1998) models are respectively in green and red. The shaded regions take into account the variation of the initial stellar metallicity (Z = [10^{-4}-1] $Z_{\odot}$). Top and bottom panels compare the results of SN dust yields with and without reverse shock destruction. The vertical dotted lines mark the lifetimes of a 8 $M_{\odot}$ (35 Myr) and a 3 $M_{\odot}$ (300 Myr) star, which correspond to the maximum mass of AGBs and the transition mass from carbpn to silicate dust production. Taken from Schneider and Maiolino (2023).

are followed in their evolution through the hot and cold phases of the ISM, where they undergo a number of transformations regarding their chemical composition, charge and temperature and also they could be destroyed or grow by accretion of metals. At the moment, our simulation does not explicitly follow the evolution of the grain size distribution: it assumes that all the grains are spherical with a static average size of 0.1 μm. However, it considers physical processes which can directly alter the dust mass, in particular:

1. astration, i.e. the incorporation of matter into a stellar interior during star formation;
2. destruction by interstellar shocks from SNe;
3. grain sputtering, i.e. mass lost because of thermal collisions with He nuclei and protons in the hot phases of the ISM;
4. grain growth, i.e. the growth of dust grains in the cold ISM phase by means of metals sticking onto the grain surface[5].

[5]Note that while grain growth is not entirely justified from a physical viewpoint (e.g. Ceccarelli

The ISM dust is modelled by following the evolution of the dust mass in the cold ($M_{d,c}$) and hot ($M_{d,h}$) phases of the ISM for each star-forming particle using the equations:

$$\begin{cases} \dot{M}_{d,c} = \dot{M}_c^D - SFR(t) D_c + \frac{M_{d,c}(t)}{\tau_{gg}} \\ \dot{M}_{d,h} = -\dot{M}_c^D + \dot{Y}_d(t) - \frac{M_{d,h}(t)}{\tau_d} \end{cases} \tag{3.3}$$

where $D = M_d/M_{gas}$ is the dust to gas mass ratio, τ_d and τ_{gg} are respectively the dust destruction and accretion timescales, Y_d is the dust yield from stellar sources and $\dot{M}_c^D$ is the dust mass exchange between the hot and cold gas phases. The evolution of the total dust mass density for each SPH gas particle is then:

$$\dot{M}_d = -SFR(t) D_c + \frac{x_c M_d}{\tau_{gg}} - (1 - x_c) M_d \left(\frac{1}{\tau_d} + \frac{3}{\tau_{sp}} \right) + \dot{Y}_d(t) \tag{3.4}$$

with x_c the cold gas fraction and τ_{sp} the typical timescale of grain sputtering. This equation is a composition of the diverse processes that cause the SPH particle to lose - via astration, grain destruction and sputtering - or gain dust mass - through stellar evolution or grain growth - during a single time step dt.

Evolution of the dust density parameter

Figure 3.2 shows the cosmic dust density parameter Ω_d in the redshift range $4 \leq z \leq 10$. This parameter is defined as $\Omega_d(z) = \rho_d(z)/\rho_{cr,0}(z)$ with $\rho_d(z)$ the density of cosmic dust in the cosmological volume and $\rho_{cr,0}$ is the critical mass density of the Local Universe[6]. In the figure, blue lines shows the reference run which includes dust production and evolution (RefRun), while red lines are from a run where dust is produced only by stellar sources (ProdOnly). The increasing difference between these two lines for $z \lesssim 9$ can be ascribed to the role played by grain growth in the ISM of the most massive and metal enriched galaxies (Mancini et al., 2015), which leads to a Ω_d parameter at $z \sim 4$ which is almost one order higher in the RefRun than in the ProdOnly one. The `dustyGadget` prediction for this parameter at $z = 4$ is very close to that of Aoyama et al. (2018) (green) which use a similar `Gadget` based simulation, while it differs from the values computed by McKinnon et al. (2017) - mainly because of the τ_{gg} adopted. Also, the comparison between solid and dashed blue lines shows that the largest amount of dust mass can be attributed to the cold phase of the ISM (see also Aoyama et al. 2018). In Péroux and Howk (2020) the authors put observational constraints on the dust density parameter for $z \leq 5.5$ (see their Figure 12). In particular, they find that Ω_d increases by a factor of ~ 7 going from $z \sim 5$ to $z = 0$ and peaks at around $z \sim 1$. At $z = 4$ they estimate $\Omega_d \sim 5 \times 10^{-6}$ in agreement with the results shown by Graziani et al. (2020) (Figure 3.2).

The role of grain growth in the dust mass budget of massive galaxies has been also highlighted when investigating the dust mass-stellar mass relation and dust-to-stellar

et al. 2018), at the current stage is needed to match observations (see for example Section 4.3.8).

[6]The critical mass density at $z = 0$ was taken in accordance with the WMAP-7 cosmology ($\rho_{cr,0} \sim 2.775 \times 10^{11}\ h^2\ M_\odot\ cMpc^{-3}$, Komatsu et al. 2011) as these results from Graziani et al. (2020) are obtained using a different `dustyGadget` setup from the one adopted in this work.

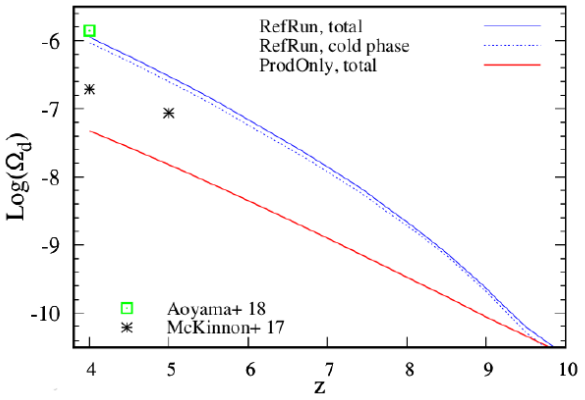

Figure 3.2. Logarithm of Ω_d as a function of redshift. The solid blue line shows the reference run including dust production and evolution (RefRun, total), the blue dashed line shows the value deriving from the cold dust phase environment in RefRun and the red solid line is computed from a run where dust is produced only by stellar sources (ProdOnly). Black asterisks are values extrapolated from McKinnon et al. (2017), while green squares refer to Aoyama et al. (2018). Taken from Graziani et al. 2020.

mass ratio (see Section 4.3.8). In fact, in Di Cesare et al. (2023) we found that according to our simulations - compared with the available observations at that time - dust enrichment at $z > 4$ is driven by stellar dust production (AGB and SNe) together with grain growth in the ISM of galaxies, with the latter mechanism providing a growing contribution at the high-mass end (see the interpretation of s-shape of the dust mass stellar mass relation shown in Figure 4.9).

3.2.2 Simulation strategy

The `dustyGadget` simulations adopted in the present work is made of eight cosmological volumes, each with a side length of 50 cMpc/h ($\sim$ 74 cMpc) and a mass resolution of 8.2×10^6 $M_\odot$ for baryonic particles and 5.2×10^7 $M_\odot$ for DM particles, with 2×672^3 being the total number of particles. The box size and mass resolution have been chosen in order to reach a good compromise between an adequate statistics and a good mass resolution, in a reasonable computational time. In fact, a good statistics is required to reproduce the cosmic star formation history, stellar mass density and stellar mass function (see Section 4.3.1) together with the main scaling relations such as the MS of galaxy formation (Section 4.3.4), halo mass-stellar mass and dust mass-stellar mass relations (Section 4.3.7 and Section 4.3.8 respectively). On the other hand, the ability to resolve star-forming environments and the inner CGM (i.e. immediately outside the ISM of galaxies) has been fundamental for the interpretation of observations (see Chapter 5).

The simulation of eight independent cosmic volumes is useful to exclude the dependence of our result on the cosmic variance (see Section 4.3.5), which is important especially at high redshifts ($z \geq 10$). Moreover, multiple independent volumes compared to a single, larger cube, help to further increase the statistics and explore a wider variety of star-forming environments. All the simulations are carried out from $z = 100$ down to $z = 4$ - where the first relaxed, disk structured Milky-Way galaxies start to set. Finally, to ensure consistency across simulations, all the volumes share common assumptions from the ΛCDM cosmology, with $\Omega_m = 0.3089$, $\Omega_{b,0} = 0.0486$, $\Omega_{\Lambda,0} = 0.6911$ and $h = 0.6774$, consistent with Planck 2015 (Planck Collaboration

et al., 2016).

3.2.3 Halo Finder

In `dustyGadget`, DM halos and their substructures are identified in post-processing by running the `Amiga` Halo Finder (AHF, Knollmann and Knebe 2009). Indeed, the simulation only follows the evolution of DM particles and gas particles, but it does not provide any information on the gravitational assembly properties. In AHF, a tree of nested grids is built by covering the whole simulation box with a regular grid that is progressively refined according to the density in each cell. Then, isolated regions in the finest level are marked as possible halos and the process continues inside-out, stepping in density contour levels from high density regions to the background density[7]. Note that, in general, there is not a one-to-one correspondence between galaxies and DM halos, as these are identified looking at the gravitational potential, essentially determined by the dominant DM component, while galaxies require a more in depth study of the gas and stellar components to be identified. In particular at high redshift, galaxies are often very complex systems with a central, irregular component surrounded by many smaller satellites.

[7]The classification of substructures is instead performed starting from the more coarse level going down to the finest.

Chapter 4

High-z scaling relations

This Chapter is based on

"The assembly of dusty galaxies at $z \geq 4$: the build-up of stellar mass and its scaling relations with hints from early JWST data"

Di Cesare C., Graziani L., Schneider R., Ginolfi M., Venditti A., Santini P., Hunt L. K. - March 2023, MNRAS, Volume 519, Issue 3, pp.4632-4650

and, in particular, Section 4.3.2 is adapted from

"A needle in a haystack? Catching Population III stars in the epoch of reionization: I. Population III star-forming environments"

Venditti A., Graziani L., Schneider R., Pentericci C., *Di Cesare C.*, Maio U., Omukai K. - July 2023, MNRAS, Volume 522, Issue 3, pp.3809-3830.

Apart from weekly discussions with Venditti A. on the topic, my main contribution to this publication resides in the comparison between simulations and observations, particularly for the SFRD and MS relations (Section 3.1 and Section 3.2), and in their interpretation.

The increasing number of distant galaxies observed with ALMA by the ALPINE and REBELS surveys and the early release observations of the JWST promise to revolutionize our understanding of cosmic star formation and the assembly of normal, dusty galaxies. Here we introduce a new suite of cosmological simulations performed with `dustyGadget` to interpret high-redshift data. We investigate the comoving star formation history, the stellar mass density and a number of galaxy scaling relations such as the galaxy main sequence, the stellar-to-halo mass and dust-to-stellar mass relations at $z > 4$. The predicted star formation rate and total stellar mass density rapidly increase in time with a remarkable agreement with available observations, including recent JWST ERO and DD-ERS data at $z \geq 8$. A well defined galaxy main sequence is found already at $z < 10$ following a non evolving power-law, which - if extrapolated at high-mass end - is in agreement with JWST, REBELS, and ALPINE data. This is consistent with a star formation efficiently sustained by gas

accretion and a specific star formation rate increasing with redshift, as established by recent observations. A population of low-mass galaxies ($8 < \mathrm{Log}(M_\star/M_\odot) < 9$) at $z \leq 6-7$ that exceeds some of the current estimates of the stellar mass function is also at the origin of the scatter in the stellar-to-halo mass relation. Future JWST observations will provide invaluable constraints on these low-mass galaxies, helping to shed light on their role in cosmic evolution.

4.1 Introduction

Since ALMA [1] started observing the Universe at the highest redshifts, our view of the first stages of cosmic star formation and galaxy assembly has significantly improved, and we discovered that within the first 1.5 billion years of galaxy evolution ($z > 4$) the process of cosmic star formation had a profound and immediate impact on the chemical evolution of young galaxies (Bromm and Yoshida, 2011).

Although deep observations of single, high-redshift dusty galaxies at the EoR significantly increased in the last decade (Cooray et al., 2014; Watson et al., 2015; Capak et al., 2015; Hashimoto et al., 2018; Laporte et al., 2017; Tamura et al., 2019; Bakx et al., 2020), as already mentioned, the advent of high-redshift surveys such as the ALMA-ALPINE [2] (see Section 2.2.1, Le Fèvre et al. 2020; Faisst et al. 2020; Béthermin et al. 2020c) and the ALMA-REBELS (see Section 2.2.2, Bouwens et al. 2021b) has opened up the possibility to build a coherent view of the early stages of galaxy evolution and to explore the early evolution of galaxy scaling relations, observationally well established at lower redshifts (see for example Zahid et al. 2013; Cresci et al. 2019; Ginolfi et al. 2020a; Hunt et al. 2020; Casasola et al. 2020; Kumari et al. 2021; Tortora et al. 2022; Hayden-Pawson et al. 2022). The combined dataset of the above surveys covers in fact two complementary redshift ranges: $4.4 \leq z \leq 5.9$ (ALPINE) and $6.5 \leq z \leq 9.4$ (REBELS), and already revealed the presence of chemically evolved, highly interacting galaxies in the early universe, with hints on an unexpected population of dusty, obscured star-forming objects (Fudamoto et al., 2021). Even more intriguing, a recent analysis of a limited sample of galaxies available at even higher redshifts ($z \geq 9$, Tacchella et al. 2022) provides indications of efficient metal production at the early stages of cosmic reionization.

The exciting, early release observations of the JWST have already provided evidence of a significant star formation activity at $z > 11$ (Adams et al., 2022; Atek et al., 2022; Castellano et al., 2022; Donnan et al., 2022; Harikane et al., 2022b; Naidu et al., 2022a; Yan et al., 2022; Zavala et al., 2022), with candidate galaxies showing a variety of physical properties (Leethochawalit et al., 2022; Santini et al., 2022). Another interesting candidate is found at $z \sim 14$ with $\mathrm{Log}(M_\star/M_\odot) \sim 8.5$ (Finkelstein et al., 2022), in addition to 7 massive objects with $\mathrm{Log}(M_\star/M_\odot) > 10$ at $7 < z < 11$, including two galaxies with a surprisingly high stellar mass of $\mathrm{Log}(M_\star/M_\odot) \sim 11$ at these early epochs (Labbe et al., 2022), then questioned by Steinhardt et al. (2022). Although preliminary and still not spectroscopically confirmed, these early results suggest an early onset of galaxy evolution, consistent with the picture outlined at longer wavelengths by the ALPINE and REBELS

[1] http://www.almaobservatory.org
[2] http://alpine.ipac.caltech.edu

surveys.

As mentioned in Section 2.2.1, the ALPINE collaboration provided the first comprehensive, statistically significant, multi-wavelength (from rest-frame UV to the far-infrared) sample of 118 spectroscopically selected main sequence galaxies evolving at the end of the Epoch of Reionization. The ALPINE sample targets the emission of single ionised carbon [CII] at 158μm, which traces both emission from star-forming regions and molecular hydrogen gas-clouds; the thermal continuum from dust emission is also available for a wide set of galaxies observed in the redshift range $4.4 < z < 5.9$. Using the ALPINE sample, both scaling relations and single objects properties have been deeply investigated: the star formation rate density (computed from the UV+IR emission), the main sequence and the specific star formation rate relations are discussed in Khusanova et al. (2021), while Pozzi et al. (2021) investigated the dust-to-stellar mass relation; the star formation rate density from the total IR luminosity function is finally estimated by Gruppioni et al. (2020). A careful analysis of the kinematic diversity and rotation of massive star-forming objects can be found in Jones et al. (2021); Ginolfi et al. (2020b) focused on the pollution of the circumgalactic medium of a merging system, while an interesting case of a triple merger at $z \sim 4.56$ is discussed in Jones et al. (2020). The aim here is just to mention few among the many works published by the ALPINE collaboration, and should not be considered as an exhaustive and complete list. Finally, ALPINE observations first revealed that a significant fraction of star formation in the post-reionization epoch is already hidden by dust clouds (Béthermin et al., 2020b).

The REBELS survey (Bouwens et al., 2021b) complements the ALPINE sample by dramatically increasing the number of spectroscopically confirmed galaxies and dust-continuum detections at $z > 6.5$. REBELS observations tripled the number of ISM cooling lines ([CII]158μm, [OIII]88μm, Schouws et al. 2022b) and dust continuum detections of galaxies found in the Epoch of Reionization (Inami et al., 2022), allowing us to explore the nature of dust-rich galaxies, to characterise their dust properties, and to study the dust buildup at these early cosmic epochs (e.g. Dayal et al. 2022b; Ferrara et al. 2022; Sommovigo et al. 2022b, Schneider et al., in prep., Graziani et al., in prep.). Detections of a strong Lyα line associated with the largest [CII] line widths present in some candidates at $z \sim 7$ is discussed in Endsley et al. 2022. Finally, for an extended discussion on the sSFR of all the galaxies in the sample, the interested reader is referred to Topping et al. (2022).

Interestingly, both surveys probe objects with clear detections of common lines and dust continua as well as consistent absolute UV magnitudes (from -21.3 to -23 in REBELS and -20.2 to -22.7 in ALPINE). Compatible ranges of stellar masses are also found, allowing us to trace galaxy properties across the redshift range $4 \leq z \leq 7$ and to extensively compare with galaxy formation models.

During the past few years, many studies which were based on data constrained models (Imara et al., 2018; Behroozi et al., 2019), classical semi-analytic methods (Popping et al., 2017; Somerville et al., 2018; Yates et al., 2021; Trinca et al., 2022), semi-numerical models running on halo merger histories extracted from N-body simulations (Mancini et al., 2015; Graziani et al., 2017a; Ginolfi et al., 2018a; Ucci et al., 2021; Wang et al., 2021), or hydrodynamical simulations (Sarmento et al., 2018; Pallottini et al., 2019, 2022a; Graziani et al., 2020; Kannan et al., 2022; Wilkins et al., 2022) investigated the high-redshift Universe. This has been done with the purpose

of either interpret datasets based on limited observational samples or to provide forecasts for JWST observations (Yung et al., 2019; Behroozi et al., 2020). The availability of coherent observational samples from surveys certainly offers remarkable advantages to cosmological models as they allow (i) to constrain the properties of a wide range of simulated galaxies discovered in models at progressively high-mass resolution; (ii) to assess the impact of feedback processes on galaxy evolution, (iii) to discover a possible redshift evolution in scaling relations well known at lower redshift. Although at low redshift ($z \leq 5$) the evolution of stellar mass functions is relatively consolidated (Baldry et al., 2012; Tomczak et al., 2016; Adams et al., 2021; Leslie et al., 2020), at higher redshifts disagreements emerge (Oesch et al., 2014; Bhatawdekar et al., 2019; Kikuchihara et al., 2020; Stefanon et al., 2021b; Harikane et al., 2022b). In addition, dust obscuration complicates the measurement of the SFR, leading to an uncertain picture of the cosmic SFRD above $z \geq 2$ (Casey et al., 2018; Gruppioni et al., 2020; Zavala et al., 2021; Barrufet et al., 2022). Such discrepancies suggest that at early times, the physical processes that regulate galaxy evolution are still not completely understood. Simulations and their comparison with observations provide an effective path forward, in order to better constrain galaxy properties and their evolution in the early Universe.

In this chapter we introduce a new suite of eight statistically independent hydrodynamical simulations evolving cosmic volumes of $50\mathrm{h}^{-1}$ cMpc / side length with a common chemical and mechanical feedback model; all runs are performed with the `dustyGadget` code (Graziani et al., 2020) improving the mass resolution and statistical significance of the original work. The new simulation suite provides then a large sample of dusty galaxies suitable to: (i) investigate fundamental galaxy scaling relations (e.g the galaxy main sequence, the stellar mass function, the specific star formation rate evolution, the dark matter halo mass-to-stellar mass etc...) at $z \geq 4$; (ii) have access to a rich set of dusty halo environments in which different galaxy populations assemble and evolve (Schneider et al., in prep; Graziani et al., in prep); (iii) explore the nature of the stellar populations and star-forming regions hosted by the brightest systems at $z > 6$ (Venditti et al., 2023b) - see also Section 5.4.1 for more information on the simulation.

In this work, we use the new `dustyGadget` simulation suite to investigate galaxy scaling relations at $z \geq 4$ as probed by current data at different wavelengths, including the early JWST observations. The redshift evolution of all the above objects and their placement on scaling relations allow to firmly connect the core data of the REBELS and ALPINE samples in a coherent evolutionary model and will serve to disentangle odd and more rare galaxy evolution histories (Di Cesare et al., in prep.).

The chapter is organized as follows: in Section 4.2 we introduce the `dustyGadget` model and the new simulation suite, while Section 4.3 discusses the results of our analysis. In Section 4.3.1 we discuss predictions of the cosmic star formation rate density and the stellar mass density, in Section 4.3.3 we explore the stellar mass functions. The canonical galaxy scaling relations are also investigated: the galaxy main sequence is discussed in Section 4.3.4 and 4.3.5, the specific star formation rate evolution in Section 4.3.6, the relation between dark matter halo mass and stellar mass in 4.3.7 and the $\mathrm{M_{dust}} - \mathrm{M_{\star}}$ relation in Section 4.3.8. Finally, Section 4.4 draws our conclusions.

4.2 Galaxy formation simulations

The hydrodynamical code `dustyGadget` (Graziani et al., 2020) has been already introduced in Section 5.4.1. In the following, we complement its description and focus on the features of the simulation that are relevant for the aims of this particular project. The hydrodynamical code `dustyGadget` extends the original implementation of `Gadget` (Springel, 2005) and its successive improvements (Tornatore et al., 2007b,a; Maio et al., 2009a) by implementing a model of dust production and evolution in the ISM of the simulated galaxies, consistent with the two-phase model of Springel and Hernquist (2003). The code also follows the spreading of grains and atomic metals through galactic winds at the scales of both CGM and IGM.

The chemical evolution model of `dustyGadget` for the gaseous components derives from the original implementation of Tornatore et al. (2007a): the model relaxes the *Instantaneous Recycling Approximation* (IRA) and follows the metal release from stars of different masses, metallicity and lifetimes. Different mass and metallicity-dependent yields are implemented for PopII/I stars: coming either from core-collapse SNe or SNIa. Stars with masses $\geq 40\,M_{\odot}$ are assumed to collapse into black holes and do not contribute to metal enrichment. PopIII stars with masses $140\,M_{\odot} \leq M_{\star} \leq 260\,M_{\odot}$ are expected to explode as PISNe, according to mass dependent yields from Heger and Woosley (2002). PopIII stars which masses lie outside the PISN mass range are assumed to collapse into black holes. The chemical network in `dustyGadget` also includes the evolution of both atomic and ionized hydrogen, helium, and deuterium by relying on the standard `Gadget` implementation of the cosmic UV background, first introduced in Haardt and Madau (1996a). The interested reader can find more details in Graziani et al. (2020) and references therein.

Cosmic dust is introduced in the previous chemical network consistently with the ISM cold and hot phases. As already mentioned, dust production by stars is implemented to ensure consistency with gas phase metal enrichment: mass and metallicity-dependent dust yields (Bianchi and Schneider, 2007; Marassi et al., 2019) are computed for different stellar populations (PopII, PopI and core-collapse SNe, PopIII and PISN) and eventually corrected for the effects of the reverse shock process occurring at unresolved scales (Bocchio et al., 2014, 2016a). Following Graziani et al. (2020), four grain species are modelled: Carbon (C), Silicates ($MgSiO_3, Mg_2SiO_4, SiO_2$), Aluminia ($Al_2O_3$) and Iron (Fe) dust. However, the chemical evolution model is flexible enough to include other grain types and to explore combinations of stellar yields and different assumptions on the shape of the stellar IMF. Once the grains produced by stars are released into the ISM, according to the properties of the environment in which they evolve, they experience different physical processes altering their mass, relative abundances, chemical properties, charge, and temperature. It is generally assumed that the dust-to-light interactions (e.g. photo-heating, grain charging) change the thermodynamic and electrical properties of the grains (see for example Glatzle et al. 2019a, 2022a) but have a negligible impact on the total dust mass unless the grain temperatures reach the sublimation threshold ($T_{d,s} \gtrsim 10^3$ K). Other physical processes (i.e. sputtering

and grain growth[3]) can alter, on the other hand, both the total dust mass and the grain size distribution (Draine, 2011; Aoyama et al., 2020). The last version of `dustyGadget` does not take into account the evolution of grain sizes, but it only considers physical processes which directly alter the dust mass e.g. grain growth, destruction by interstellar shocks, and grain sputtering in the hot ISM phase (see Graziani et al. 2020 for more technical details on their numerical implementation).

Finally, at the end of stellar evolution metals and dust are spread in the surroundings of star-forming regions. The dust distribution follows the atomic metal spreading without accounting for any momentum transfer through dust grains. At the same time, dusty particles associated with galactic winds evolve in their hot phase through sputtering. Therefore, the dust-to-metal ratio will be modulated depending on the environment, obtaining different values for the galactic ISM, CGM and IGM.

In Section 3.2.2 we introduced the suite of eight statistically independent cosmological simulations adopted in the present thesis. The eight cosmological simulations have an equal mass resolution of $3.53 \times 10^7 \mathrm{h}^{-1}\,\mathrm{M}_\odot$ for DM particles and of $5.56 \times 10^6 \mathrm{h}^{-1}\,\mathrm{M}_\odot$ for gas particles, setup with 2×672^3 total number of particles[4]. The cubic volume and SPH resolution are chosen to guarantee a good compromise between an adequate statistics in each run and an acceptable number of galaxies resolved with a total stellar mass $\mathrm{Log}(\mathrm{M}_\star/\mathrm{M}_\odot) \geq 8$ by $\mathrm{N}_\star > 54$ stellar particles of individual mass $1.3 \times 10^6 \mathrm{h}^{-1}\,\mathrm{M}_\odot$. In addition, all the above requirements ensure a reasonable computational time for eight runs performed in the redshift range $4 \leq z \leq 100$. A good statistics of galaxy candidates is required in fact to reproduce a reliable trend of cosmic star formation history and the main galaxy scaling relations, while the ability to resolve the most massive star-forming environments is fundamental to perform a first exploration of the internal properties of some of these candidates and their circumgalactic environments and compare with possible observational counterparts (see Section 5).

To ensure consistency across the simulations, all the volumes share common assumptions on star formation prescriptions, mechanical, chemical and radiative feedback processes as described in Graziani et al. (2020); in the following paragraph we briefly recap the main physical setup of the simulation. The simulations start at $z = 100$ assuming neutral pristine gas and evolve all particle components down to $z = 4$ with 40 outputs at intermediate redshifts. For a better comparison with previous work, and to assess the statistical convergence of the previously studied relations, we adopted a chemical network accounting for molecules and atomic metals (see Maio et al. 2010 for more details). Star formation occurs in the cold phase of gas particles once their density exceeds a value of $n_{\mathrm{th}} = 132\,\mathrm{h}^{-2}\mathrm{cm}^{-3}$ (physical)[5]. The IMF of the stellar populations, each represented by a single stellar particle, is assigned according to their metallicity $\mathrm{Z}_\star$, given a gas critical metallicity

[3]Note that a subtle interplay between grain charging and grain growth process could alter the efficiency of the latter, as discussed in Glatzle et al. (2022a).

[4]Note that both volume and the mass resolution of the present simulation is increased with respect to the one discussed in Graziani et al. (2020).

[5]This choice allows to capture all the relevant phases of cooling until the onset of runaway collapse, as discussed in Maio et al. (2009b).

$Z_{crit} = 10^{-4}\, Z_{\odot}$[6]. When $Z_{\star} < Z_{crit}$ we adopt a Salpeter IMF (Salpeter, 1955) in the mass range $[100 - 500]\, M_{\odot}$. Otherwise, the stars are assumed to form according to a Salpeter IMF in the mass range $[0.1 - 100]\, M_{\odot}$. Galactic winds are modelled with a constant velocity of 500 $km\, s^{-1}$, in line with outflows observed in ALPINE normal galaxies (Ginolfi et al., 2020d). Radiative feedback is implemented instead as in the original version of `Gadget`, i.e. by adopting a cosmic UV background (Haardt and Madau, 1996b). Apart from the aforementioned calibrations (i.e. galactic winds, radiative feedback), our model is not calibrated on any particular observational set or survey. We warn the reader that our simulations do not model the formation of AGN[7] and do not account for mechanical or radiative feedback of formed black holes.

Finally, a common post-processing setup is adopted as well, in order to identify DM halos and their substructures through the `AMIGA` halo finder (see Section 3.2.3 for more information about the halo finder).

4.3 Results

Here we discuss the results of our simulations. Section 4.3.1 investigates cosmic star formation and the galaxy stellar mass function is derived in Section 4.3.3. Then we introduce many galaxy scaling relations connecting the stellar mass of collapsed objects ($M_{\star}$) with other galaxy or DM halo properties, including the main sequence of galaxy formation in Section 4.3.4 and the specific star formation rate (sSFR-z) in Section 4.3.6. Finally, the relation connecting stellar and DM halo mass is discussed in Section 4.3.7, while the connection with the dust mass ($M_d - M_{\star}$) is investigated in Section 4.3.8.

4.3.1 Cosmic star formation history and cosmic stellar mass density

The history of cosmic star formation, i.e. the redshift evolution of the total CSFRD (Ψ) and/or the total SMD ($\rho_{\star}$) are discussed in this section, comparing the predictions of `dustyGadget` with available observations and recent theoretical models at $z \geq 4$. The relations investigated here account for quantities directly inferred from gas and stellar particles integrated into a comoving volume $V_C = (50 h^{-1})^3$ $cMpc^3$ without requiring any halo/galaxy definitions.

For each cube at a given redshift z, $\Psi(z)$ is computed as:

$$\Psi(z) = \frac{\sum_i SFR_i(z)}{V_C}, \tag{4.1}$$

where SFR_i is inferred from the i-th star-forming gas particle in the cube. While $\rho_{\star}(z)$ is defined as:

$$\rho_{\star}(z) = \frac{\sum_i M_{\star,i}(z)}{V_C}, \tag{4.2}$$

[6]Here, we assume $Z_{\odot} = 0.02$ (Grevesse and Anders, 1989).

[7]The AGN feedback is presumed to be responsible for the bending at the high mass end of the main sequence and, since we do not model the formation of AGN, we find a different shape for such relation if compared to models in which the AGN feedback is taken into account (see Appendix 4.6).

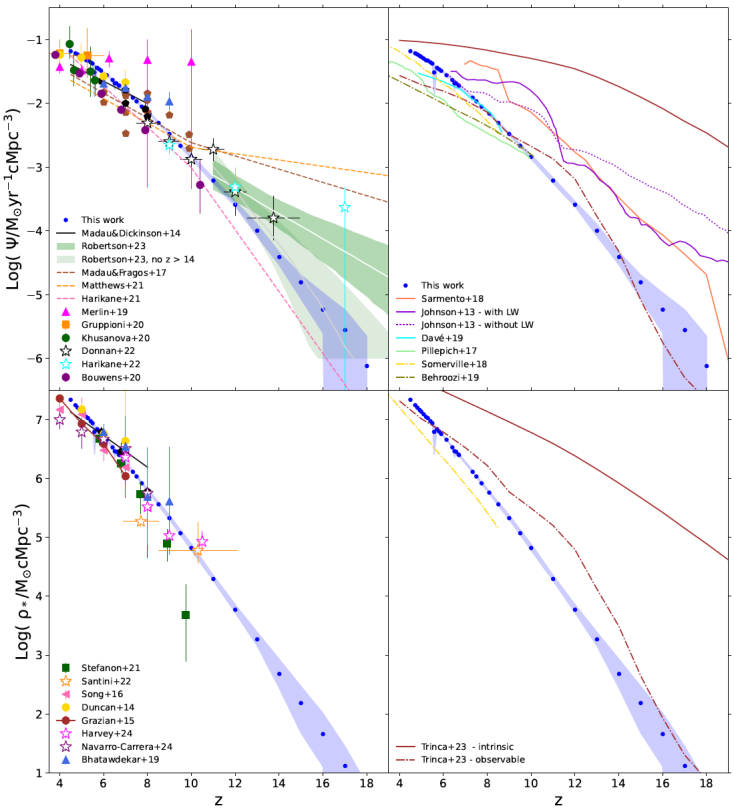

Figure 4.1. Cosmic SFRD Ψ (**top panels**) and SMD ρ_* (**bottom panels**) as a function of redshift z in the range $4 \leq z \leq 19$ and averaged through U6-U13. **Left panels:** mean value of Ψ and ρ_* (*blue dots*) and their spread between min/max found in the eight cubes (*blue shaded areas*). Observed points are taken from Madau and Dickinson (2014a) (*black pentagons*), Madau and Fragos (2017) (*sienna pentagons*), Bouwens et al. (2020) (*purple dots*), Gruppioni et al. (2020) (*orange squares*), Khusanova et al. (2021) (*green dots*), Merlin et al. (2019) (*magenta triangles*), Robertson et al. (2023) (*green shaded areas*), Stefanon et al. (2021b) (*green squares*), Duncan et al. (2014) (*yellow dots*), Bhatawdekar et al. (2019) (*sky-blue triangles*), Song et al. (2016) (*pink triangles*), Donnan et al. (2022) (*black stars*), Harikane et al. (2022b) (*cyan stars*), Santini et al. (2022) (*orange stars*), Navarro-Carrera et al. (2024) (*purple stars*) and Harvey et al. (2024) (*magenta stars*). The data constrained best-fit functions from Madau and Dickinson (2014a) are shown as *black solid lines*, while the fits from Madau and Fragos (2017), Matthews et al. (2021) and Harikane et al. (2021) are shown as *sienna/dark orange/pink dashed lines*; notice that from $z = 10$ these are extrapolations. **Right panels**: Comparison with the results from other models and simulations, when available: Sarmento et al. (2018) (numeric simulation, *coral solid line*), Johnson et al. (2013) (`FiBY` simulation, *violet lines* - the simulations with and without LW flux are shown respectively in *solid* and *dotted* line styles), Davé et al. (2019) (`SIMBA` simulation, *cyan solid line*), Pillepich et al. (2017) (`IllustrisTNG` simulation, *light green solid line*), Trinca et al. (2023) (`CAT` semianalytic model *brown lines* - intrinsic and observable models are respectively in *solid* and *dashed-dotted* line styles), Somerville et al. (2018), (semianalytic model, *golden dashed dotted line*), Behroozi et al. (2019) (`UNIVERSEMACHINE` semianalytic model, *olive dash dotted line*).

where $M_{\star,i}$ is the total mass of the i-th stellar particle in the cube. Both quantities are shown in Figure 4.1 in the redshift range $4 \leq z \leq 19$. Blue, filled dots indicate the mean values at any given redshift among the volumes (U6 - U13), while the shaded areas show the minimum-maximum spread found across the whole simulation sample. $\Psi(z)$ rapidly increases with decreasing z, from $\Psi \sim 10^{-6} - 10^{-7}$ $M_\odot$ yr^{-1} cMpc^{-3}, up to $\Psi \sim 10^{-2} - 10^{-1}$ $M_\odot$ yr^{-1} cMpc^{-3} by $z \sim 4$; this trend is mirrored by $\rho_\star(z)$ in all the volumes, as the stellar mass accumulates across cosmic time. In the same redshift range in fact, $\rho_\star(z)$ increases by more than 6 orders of magnitude, starting from $\rho_\star \sim 10$ $M_\odot$ cMpc^{-3}.

To better understand the scatter across the eight cubes, we investigate the values relative to each individual simulation finding a tight convergence starting at $z \sim 12$. Their spread becomes relevant instead at $z \gtrsim 12$, certainly because of the cosmic variance. At $z \gtrsim 12$, the number of star-forming systems is too scarce to collect detailed statistics from a single simulated volume, therefore their quantities hardly reflect the cosmological mean value. For this reason, having more than one cube is effective in increasing the global statistics at Cosmic Dawn. Despite the above improvement, star formation at these early times is not yet robustly structured and its evolution remains strongly dependent on both different initial conditions and assembly histories of each cube. In addition, our mass resolution does not allow us to resolve the first star-forming regions in minihalos, and the CSFRD and SMD are likely to be underestimated at the highest redshifts.

To verify the above predictions, in Figure 4.1 we compare them with the expectations of the data-constrained model of Madau and Dickinson (2014a) and Madau and Fragos (2017), and with other estimates of the SFRD based on IR (Khusanova et al., 2021; Gruppioni et al., 2020; Matthews et al., 2021; Merlin et al., 2019), rest frame UV (Donnan et al., 2022) and UV+dust corrected (Bhatawdekar et al., 2019; Bouwens et al., 2020; Duncan et al., 2014; Harikane et al., 2021; Harikane et al., 2022b) observations (top left panel). The JWST results are those from Donnan et al. (2022), Harikane et al. (2022b) and Robertson et al. (2023). The SMD is compared instead with Madau and Dickinson (2014a); Stefanon et al. (2021b); Song et al. (2016); Duncan et al. (2014); Grazian et al. (2015); Bhatawdekar et al. (2019) and the latest JWST estimates by Santini et al. (2022); Navarro-Carrera et al. (2024); Harvey et al. (2024) (bottom left panel). Our results for both SFRD and SMD relations are in overall agreement with Madau and Dickinson (2014a) at $z \lesssim 8$, even though our trends appear slightly steeper at decreasing redshifts, but still in excellent agreement with Duncan et al. (2014) and recent ALPINE estimates in Gruppioni et al. (2020) and Khusanova et al. (2021).

At higher redshifts ($z \geq 8$) the values predicted by `dustyGadget` are remarkably consistent with the recent results from JWST Early Release Observations (ERO), Early Release Science Program (ERS) and the JWST Advanced Deep Extragalactic Survey (JADES; Eisenstein et al. 2023) for the SFRD (Donnan et al., 2022; Harikane et al., 2022b; Robertson et al., 2023) and the estimates of the observed SMD (Santini et al., 2022; Navarro-Carrera et al., 2024; Harvey et al., 2024). This points to a higher rate of star formation at high-redshift than previously indicated by the ALMA Spectroscopic Survey Large Program (Bouwens et al., 2020), Harikane et al. (2021) (top left panel, in purple dots and pink dashed lines) and by Stefanon et al. (2021b) (bottom panel, green squares).

In the right panels of Figure 4.1, we compare our results with some predictions of other semi-analytic models and simulations i.e. Sarmento et al. (2018); Johnson et al. (2013); Davé et al. (2019); Pillepich et al. (2017); Somerville et al. (2018); Behroozi et al. (2019); Trinca et al. (2023). In particular, for the Cosmic Archaeology Tool (`CAT`, described in Trinca et al. 2022) we show the estimates for the intrinsic and observable SFRD and SMD: this last estimate has been obtained using a threshold at $M_{UV} < -17.5$. Unlike `CAT`, `dustyGadget` simulations are not able to resolve low-mass galaxies which have a non-negligible impact on the SFRD at high-z (see Venditti et al. 2023b for a discussion on the consequences it has on the PopIII star formation). In addition to this, it is important to keep in mind that `dustyGadget` and `CAT` adopt different feedback models and IMF which impact the evolution of the SFRD and SMD. To summarise, all the models presented in Figure 4.1 predict quite different trends, especially at high redshifts ($z > 8$), indicating that star formation at very early times is strongly dependent on the analysed cosmological volume and/or the adopted feedback model.

4.3.2 PopII and PopIII cosmic star formation history

Differently from Di Cesare et al. (2023), in Venditti et al. (2023b) we investigate the relative contributions of PopII (Ψ_{II}) and PopIII (Ψ_{III}) stars to the cosmic SFRD predicted using `dustyGadget` suite of simulations. Specifically, the SFR is derived by discretizing the time in temporal steps (Δt) smaller than those adopted from the hydrodynamical simulation. We start a $z \sim 20$ and compute $\Delta M_\star$ in each Δt by looking at the birth time of all the stellar particles. As an example, the SFRD of the i-th cube at time t is given by:

$$\Psi_i(t) = \frac{1}{V_c} \frac{\Delta M_\star(t, t - \Delta t)}{\Delta t}, \tag{4.3}$$

where $\Delta\ M_\star(t, t - \Delta t)$ i computed by summing over the masses of *all* the stellar particles with age between t and $t - \Delta t$ and V_c is the comoving volume ($V_c = 50^3$ $cMpc^3/h^3$). The redshift evolution of SFRD is investigated by adopting two values for the time interval: $\Delta t = 1$ Myr (i.e. smaller than the average time of PopIII stars $\tau \sim 3$ Myr) and $\Delta t = 10$ Myr. This is done considering that the star formation processes occurring on time steps smaller than the hydrodynamical simulation are stochastic, lower Δt result in more significant fluctuation of Ψ, and also choosing an appropriate time interval suitable to capture the formation of massive, short-lived PopIII stars.

In Figure 4.2 we show $\Psi = \Psi_{III} + \Psi_{II}$ with Ψ, Ψ_{III} and Ψ_{II} respectively in blue, green and red. The left hand panels shows the predicted Ψ fro `dustyGadget` adopting a $\Delta t = 10$ Myr and averaging across diverse universes (U6, U8, U10, U12, U13). Predictions are compared with observations from Bouwens et al. (2020), data constrained estimates (Madau and Dickinson, 2014b; Madau and Fragos, 2017) and ERS JWST data (Donnan et al., 2022; Harikane et al., 2022b; Bouwens et al., 2022b). While, on the right-hand side is the SFRD predicted in U12, which is the universe with the earliest onset of star formation, and assuming $\Delta t = 1$ Myr.

The right-hand panel of Figure 4.2 shows that in the redshift range $15 \leq z \leq 19$ the first episodes of star formation mix PopII and PopIII stars in U12, while for

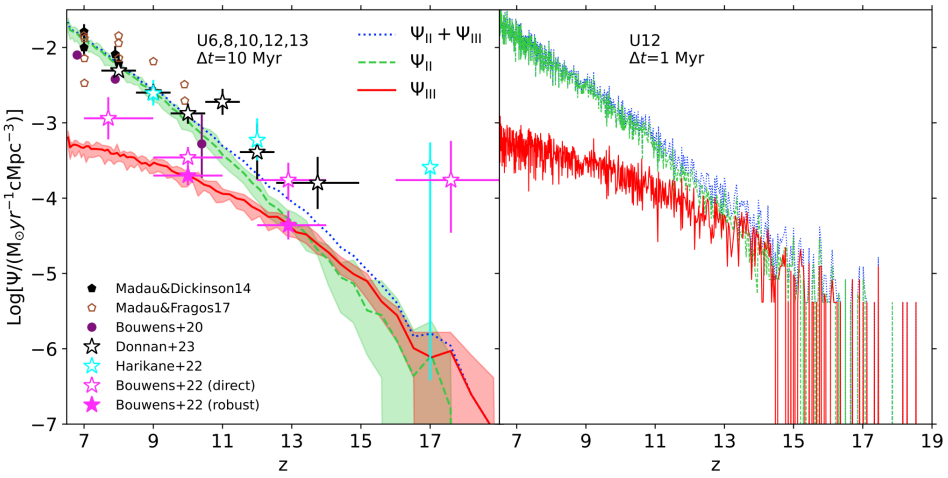

Figure 4.2. The SFRD for PopII ($\Psi_{\rm II}$), PopIII ($\Psi_{\rm III}$) and their sum as a function of redshift in the range $6.5 \leq z \leq 19$. **Left panel:** the SFRD is computed with a time step $\Delta t = 10$ Myr, averaged through the simulated cubes U6, U8, U10, U12, U13. In particular, red solid (green dashed) line are the mean value of Ψ for Pop III (Pop II) stars, while the red (green) shaded area is the spread between the minimum and maximum values across the cubes; the mean value of the total SFRD is shown by a blue dotted line. We also show observations from Madau and Dickinson (2014b) (black, filled pentagons), Madau and Fragos (2017) (sienna, empty pentagons), Bouwens et al. (2020) (purple, filled circles), Donnan et al. (2022) (black, empty stars), Harikane et al. (2022b) (cyan, empty stars) and Bouwens et al. (2021b) (hotpink, filled/empty stars). **Right panel:** evolution of Ψ in the simulated cube U12, computed with a time step $\Delta t = 1$ Myr, using the same color legend adopted in the left panel.

$z \leq 15$ there is an increase for both the populations. The ratio $\Psi_{\rm II}/\Psi_{\rm III}$ rapidly grows at $z \leq 13$, reaching $\Psi_{\rm II}/\Psi_{\rm III} \sim 30$ at $z = 6.5$. In this case, $\Psi_{\rm III}$ exhibits fluctuations - up to one order of magnitude - among consecutive time intervals. Then, towards the end of EoR, when PopIII star formation is disfavoured because of the increased metal pollution, the average $\Psi_{\rm III}$ flattens around $\Psi_{\rm III} \sim 10^{-3.2}$ $\rm M_\odot$ $\rm yr^{-1}$ $\rm cMpc^{-3}$, with oscillations of 10%. On the other hand, looking at the left panel ($\Delta t = 10$ Myr and averaging across simulations), the fluctuations of Ψ are suppressed in both populations and a global statistical trend emerges. It is evident that the first episodes of star formation occur, across universes, in the redshift range $16 \leq z \leq 19$ and are dominated by PopIII stars. At these redshifts PopIII star formation is confirmed to be highly stochastic in all the simulated volumes across cosmic time, because of the inhomogeneous nature of cosmic metal enrichment. The PopII contribution to the SFRD increased with time overcoming that of PopIII stars around $z \sim 13$, however, even if subdominant, the $\Psi_{\rm III}$ continues to persist with $\Psi_{\rm III} \leq 10^{-3}$ $\rm M_\odot$ $\rm yr^{-1}$ $\rm cMpc^{-3}$ in all cubes during the EoR. By $z = 6.5$ the evolution of $\Psi_{\rm III}$ has significantly flattened without showing a decline.

In conclusion, even if going towards lower redshifts PopIII star formation is suppressed by cosmic metal enrichment and, locally, by thermal feedback from supernova explosions, a late PopIII star formation is still occurring down to the end

of EoR ($z \sim 6-8$)[8]. Moreover, from this work emerges that even in some of the most massive galaxies, already hosting a persistent PopII star formation, PopIII stars can survive in isolated pristine clouds in the outskirts of the halo potentially allowing their direct detection. Indeed, in this case, their signal may be less contaminated by Pop IIs, although its detectability will strongly depend on the specific line-of-sight to the source, due to the complex morphology of the host galaxy and its highly inhomogeneous dust distribution (see Venditti et al. 2023b for details).

4.3.3 The stellar mass function

The growth of stellar mass ($M_\star$) during galaxy assembly is often investigated with the SMF (Φ) as it provides important hints on how the total stellar mass present in a cosmic volume (see the previous section) distributes across different luminous structures. Φ is usually defined as the number density of galaxies as a function of their $M_\star$, collected in a fixed redshift interval.

Here we investigate the evolution of $\Phi(z)$ in the redshift range $z = 10 - 4$ as predicted by `dustyGadget` runs computed as:

$$\Phi[\mathrm{dex}^{-1}\mathrm{Mpc}^{-3}] = \frac{d\mathrm{N_i}}{d\mathrm{LogM}_\star}\frac{1}{\mathrm{V_C}}, \tag{4.4}$$

where N_i is the number of galaxies in the i-th $\mathrm{Log}(M_\star/M_\odot)$ bin and $V_C = 50^3 h^{-3}$ cMpc^3 is the simulated comoving volume. In each simulated universe, galaxies are extracted from available catalogs at common, fixed redshifts and are selected in the mass interval $\mathrm{Log}(M_\star/M_\odot) \in [8-11]$[9], then binned within 0.2 dex. The resulting value in each bin is finally divided by the size of the bin and V_C.

From top left to bottom right, the panels of Figure 4.3 compare Φ in different redshift intervals[10] with available observations. The mean value of Φ in each mass bin is shown as magenta solid lines, the min-max spread found across the simulated sample as pink-shaded areas, while the Poissonian errors are shown as gray-shaded areas. Furthermore, we apply the proper conversion factors (Madau and Dickinson, 2014a) to stellar masses that were originally computed with an IMF different from the Salpeter (1955) one.

In recent years, predictions of the high-redshift SMF both from observed data samples and theoretical models have been published, complementing the estimates available in the Local Universe (see for example the GAMA survey, Baldry et al. 2012). Grazian et al. (2015) reconstructed the galaxy stellar mass function in the redshift range $3.5 \leq z \leq 7.5$ by collecting data from the CANDELS/UDS, GOODS-South, and HUDF fields also providing a careful analysis of the many sources of uncertainty when deriving Φ: stellar masses of observed galaxies, assumptions on the star formation histories and on the evolution of their metallicity. Random errors and discrepancies originating from the adopted statistical methods and their assumptions

[8] These redshifts are well within the reach of deep photometric and spectroscopic survey with JWST.

[9] The lower bound of the mass interval is set to properly resolve low-mass objects and the upper bound is linked to the size of the simulated volume.

[10] Each panel assumes the mid point of each specified interval as the reference redshift at which the analysis has been conducted.

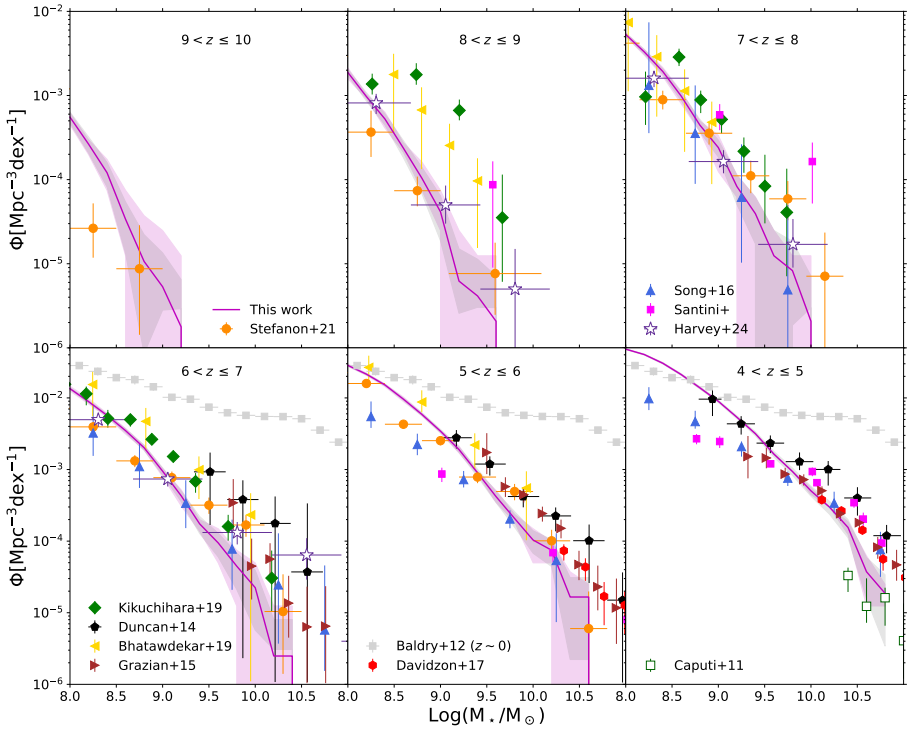

Figure 4.3. Mass Function obtained from our simulated galaxies in the range $z = 10 - 4$: *magenta solid lines* show mean values of our sample, *pink-shaded areas* the min-max spread of the simulations and *gray-shaded areas* the Poissonian error associated with our sample. The SMF from observed galaxies are also reported in each panel: Stefanon et al. (2021b); Song et al. (2016); Duncan et al. (2014); Bhatawdekar et al. (2019); Kikuchihara et al. (2020); Grazian et al. (2015); Davidzon et al. (2017); Caputi et al. (2011); Harvey et al. (2024) and Santini et al. (in prep) are respectively in *orange circles, blue triangles, black pentagons, yellow triangles, green diamonds, brown triangles, red hexagons, green empty squares, purple stars and magenta squares.* Finally, observational constraints at $z \sim 0$ (*gray squares*) from Baldry et al. (2012) are shown at $z < 6$ to guide the eye.

are also carefully discussed, such as the impact of nebular lines and the modelled continuum, the effects of cosmic variance and the possible contamination by AGN sources. The predicted SMF is represented in the figure panels as brown triangles and shows a good agreement with the simulated Φ at $\mathrm{Log}(\mathrm{M}_\star/\mathrm{M}_\odot) > 9.5$, while providing lower values for smaller objects observed at $4 < z \leq 5$ (see bottom right panel). Recently Santini et al. (in prep.) extended this analysis by combining all CANDELS fields and the parallel fields from the Hubble Frontier Fields program (Lotz et al., 2017), whose depth is crucial to probe the highest redshift galaxies. Details on the adopted technique can be found in Santini et al. (2021) and Santini et al. (2022, subm.). The results, shown in the figure as magenta squares, confirm the previous considerations for $\mathrm{Log}(\mathrm{M}_\star/\mathrm{M}_\odot) > 9.5$. To extend the comparison at

higher redshifts and provide a more precise indication on the scatter among different observations, we complement the above dataset with estimates from Duncan et al. (2014) (black pentagons[11]), Song et al. (2016) (sky blue triangles), Bhatawdekar et al. (2019) (yellow triangles), Kikuchihara et al. (2020) (green diamonds), Stefanon et al. (2021b) (orange dots) and recent JWST/NIRCam publicly available data (Harvey et al. 2024, purple stars). Finally, and as a reference, we show observational constraints obtained in the Local Universe (gray squares) by analysing the results of the Galaxy And Mass Assembly (GAMA) survey (Baldry et al., 2012).

As shown in Figure 4.3 an overall general agreement between the simulation and the observed samples can be found in the explored redshift range. At the highest redshifts, ($9 < z \leq 10$, top left panel) the simulation predicts a number density of faint objects that exceeds recent estimates provided by Stefanon et al. (2021b), but note that the statistical sample of simulated and observed systems with $\mathrm{Log}(\mathrm{M}_\star/\mathrm{M}_\odot) > 8$ in this redshift range is less significant than at lower redshift and more data is necessary to consolidate the trends. While at $8 < z \leq 9$ (top middle panel) `dustyGadget` seems to predict a lower number of objects compared with observations of Kikuchihara et al. (2020); Bhatawdekar et al. (2019) and Santini et al. (in prep.), it agrees with the estimates by Stefanon et al. (2021b) and Harvey et al. (2024). In the redshift range $4 < z \leq 7$ the low-mass end ($\mathrm{Log}(\mathrm{M}_\star/\mathrm{M}_\odot) < 9.5$) appears to be overestimated when compared with data in Song et al. (2016) and Santini et al. (in prep.), while the agreement improves when all the other observational estimates are accounted for. An opposite trend is found instead in the high-mass end ($\mathrm{Log}(\mathrm{M}_\star/\mathrm{M}_\odot) > 9.5$) where the number of objects predicted by our simulations is lower than estimates from observations. This can be due to the adopted volume in `dustyGadget` simulations which limits the number of high-mass ($\mathrm{Log}(\mathrm{M}_\star/\mathrm{M}_\odot) > 10.5$) galaxies. Finally, the interested reader is referred to Figure 4.11 in Appendix 4.5 for a comparison between our predictions and other available theoretical models.

Additional constraints from JWST observations on the population of luminous galaxies having $\mathrm{Log}(\mathrm{M}_\star/\mathrm{M}_\odot) < 9$ will be crucial for theoretical models in order to assess the properties of their metal/dust enriched ISM through emission lines, as well as their relevance to cosmic Reionization. `dustyGadget` simulations at present predict, in fact, that these systems contribute 80% of the total $\mathrm{M}_\star$ in a cosmic volume of $50\mathrm{h}^{-1}$ cMpc at $z \sim 7.5$, decreasing to 40% at $z \sim 4.5$. Assessing the statistical relevance of these galaxies with observations will be then crucial to characterise their properties and correctly model these environments in future simulations (Venditti et al., in prep.).

4.3.4 Main sequence of galaxy formation

The galaxy MS of star formation indicates that there is a strong correlation between the SFR and the stellar mass ($\mathrm{M}_\star$) of samples of galaxies observed at a given redshift. The MS encapsulates information on the mechanisms and the efficiency of gas conversion into stars at a fixed redshift; while robustly established at low

[11]These data are based on deep near-infrared observations that were available in the CANDELS GOODS South field.

redshift where large galaxy samples are available, several works suggest that it also holds up to the first couple of Gyr (Speagle et al., 2014).

In this section we investigate the redshift evolution of the MS, in the redshift range $4 < z \leq 10$, by comparing `dustyGadget` predictions with samples of isolated galaxies collected in Graziani et al. (2020) and Tacchella et al. (2022), the new datasets offered by the REBELS (Bouwens et al., 2022b; Topping et al., 2022) and ALPINE (Faisst et al., 2020; Khusanova et al., 2021) surveys, the analysis of HST Frontier Fields (Santini et al., 2017), the galaxies observed at $6 < z \leq 7$ by Witstok et al. (2022), and with the recent determinations based on JWST ERO and ERS (Barrufet et al., 2022; Curti et al., 2023; Leethochawalit et al., 2022; Rodighiero et al., 2023; Sun et al., 2022; Trussler et al., 2022). For comparison, we also show extrapolations of the MS based on low redshift observations (Speagle et al. 2014, dotted lines). Figure 4.4 shows galaxies found in U6 with $\mathrm{Log}(\mathrm{M}_\star/\mathrm{M}_\odot) > 8$ as grey dots, while their linear fits are indicated as magenta solid lines. Here and in the following figures, vertical gray dashed lines indicate the maximum stellar mass ($\mathrm{M}_{\star,\mathrm{max}}$) found in the simulation at each redshift, thus, the fit above $\mathrm{M}_{\star,\mathrm{max}}$ has to be interpreted as extrapolation based on $\mathrm{Log}(\mathrm{M}_\star/\mathrm{M}_\odot) < \mathrm{Log}(\mathrm{M}_{\star,\mathrm{max}}/\mathrm{M}_\odot)$. At $4 < z \leq 6$ the galaxy MS has been reliably measured over a large range of stellar masses by the analysis of HST Frontier Fields (Santini et al. 2017, black crosses) and by the ALPINE sample (Faisst et al. 2020, orange squares). Before JWST early results, the available constraints at $z > 6$ were limited at the high-mass end, for galaxies with $\mathrm{Log}(\mathrm{M}_\star/\mathrm{M}_\odot) > 9$. When needed, we multiply the stellar masses and star formation rates for the conversion factors by Madau and Dickinson (2014a) to convert them from others IMF to the Salpeter (1955) one. The first four panels show the results obtained by Tacchella et al. (2022) with a sample of 11 bright galaxy candidates[12] (green empty triangles), together with additional observations of single galaxies collected in Graziani et al. (2020) (red crosses) and the 5 bright Lyman-break galaxies at $z \sim 7$ by Witstok et al. (2022) (magenta diamonds). At $z > 6.5$ a very important improvement has been achieved by the REBELS collaboration (Bouwens et al., 2022b), which boosted by a factor of 3 the number of bright ISM-cooling lines discovered, significantly extending the number of available objects observed during the Epoch of Reionization (EoR). Here we show the results obtained by Topping et al. (2022) (blue pentagons), where $\mathrm{M}_\star$ are computed using a non-parametric SFH. Given the limited range in the stellar mass, Topping et al. (2022) fixed the slope of the main sequence to the values determined by Schreiber et al. (2015) at $z = 7$ and constrained the MS normalization for the REBELS sample, finding $\mathrm{Log}(\mathrm{SFR}/\mathrm{M}_\odot\mathrm{yr}^{-1}) = \mathrm{Log}(\mathrm{M}_\star/\mathrm{M}_\odot) - 8.12$ (see the dash-dotted line in the top-right panel of Figure 4.4).

A collection of data obtained by independent studies based on JWST ERO and ERS is also reported in Figure 4.4 (empty stars). Although the spectroscopic confirmation is available only for a small number of sources, this figure shows the enormous potential of JWST in constraining the slope of the galaxy MS at $z > 6$. The `dustyGadget` fit at $7 < z \leq 9$ appears very consistent with some JWST data at

[12]Note that among these galaxies, previously selected in the CANDELS fields by Finkelstein et al. (2021), only three are spectroscopically confirmed so far: EGS-6811, EGS-44164 and GOODSN-35589, respectively at z = 8.68, 8.66 and 10.96 (filled green triangles).

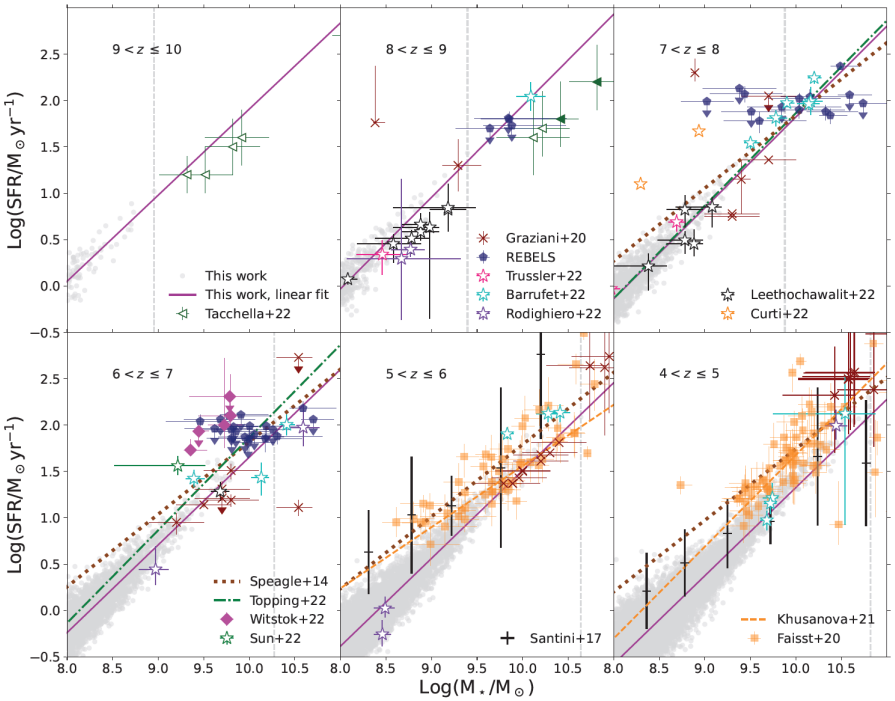

Figure 4.4. MS of star formation in the redshift range between 10 (*top left*) and 4 (*bottom right*): comparison between simulated galaxies with $\mathrm{Log}(\mathrm{M}_\star/\mathrm{M}_\odot) \geq 8$ from U6 (*gray points*), their linear fit in log-scale (*magenta solid line*), and observed galaxies found in the literature. *Green triangles* are the galaxies from the work by Tacchella et al. (2022) - filled triangles are for the sources that have been spectroscopically confirmed, while empty ones are for those which have not been confirmed yet (see the text for more details), *red crosses* are respectively single observations and upper limits collected in Table 2 of Graziani et al. (2020). *Blue pentagons* are the observations obtained by the REBELS survey described in Topping et al. (2022), empty stars with *cyan, purple, orange, black, green and pink borders* are the preliminary results from JWST respectively by Barrufet et al. (2022); Rodighiero et al. (2023); Curti et al. (2023); Leethochawalit et al. (2022); Sun et al. (2022); Trussler et al. (2022). *Magenta diamonds* are the recent observations by Witstok et al. (2022) and the *orange squares* show the ALPINE sample by Faisst et al. (2020) at $4.4 < z < 5.9$. Finally *black crosses* are the average values from the analysis of the HST Frontier Field by Santini et al. (2017).*Dotted brown lines* are the fitting functions by Speagle et al. (2014), *dash-dotted green lines* are from Schreiber et al. (2015) and the fitting functions of the ALPINE objects obtained by the Khusanova et al. (2021) are the *orange dashed lines*.

the low-mass end (Rodighiero et al., 2023; Trussler et al., 2022; Leethochawalit et al., 2022) and, when extrapolated at the high-mass end, with JWST data from Barrufet et al. (2022) and with the REBELS sample, favouring a steeper slope compared to Speagle et al. (2014); it is also in good agreement with the extrapolation of Schreiber et al. (2015) done by Topping et al. (2022) (see also Section 4.3.5 for the fitting functions based on `dustyGadget` predictions). While our simulation lacks a significant statistics at the extreme SFR and stellar mass end (see however Figure 4.5,

where we show the results for all our simulated cosmic volumes), we point out that some studies find a piecewise fit to the star-forming sequence at high-redshift (Lovell et al., 2021), to account for the bending seen in the sequence (Popesso et al., 2022; Sandles et al., 2022). A comparison with independent model results is illustrated in Figure 4.12 and a discussion of the evolution of the MS slope is presented in Section 4.3.5.

In the last two redshift panels, we show that our simulated sample is consistent with a number of ALPINE galaxies found in the post-EoR epoch ($6 < z < 4$), i.e. we find that 77% of the simulated candidates in the bottom mid panel and 73% in the bottom right panel are consistent with the ALPINE galaxies. In these redshift windows, a good agreement is also found with the trend suggested by the estimates of Santini et al. (2017), particularly at $4 < z \leq 5$, although the large standard deviations associated with the mid-points of mass bins do not allow to place stringent constraints. JWST early results allows us to constrain both the high-mass end (i.e. $\mathrm{Log}(\mathrm{M}_\star/\mathrm{M}_\odot) \geq 9.5$, see for example the data from Barrufet et al. 2022 and Rodighiero et al. 2023), as well as the low-mass end (Rodighiero et al., 2023) of the relation.

Finally, we compare the linear fit of our simulated universe (magenta solid line) with the fitting function of the MS by Speagle et al. (2014) (brown dotted line) and the fitting functions obtained from the ALPINE data by Khusanova et al. (2021) (dashed orange lines). In the redshift range $4 < z \leq 6$ our fit seems to predict a steeper MS compared to Speagle et al. (2014), while at $4 < z \leq 5$ a shallower slope is found compared to Khusanova et al. (2021)[13]. In the next section we provide a more in-depth analysis of our results.

4.3.5 Additional properties of the galaxy main sequence

In this section we discuss the impact of simulated cosmic variance and a possible redshift evolution of the slope of our fits. A comparison with the findings of other simulations adopting different simulated cosmic scales and numerical schemes is presented in Appendix 4.6.

Impact of simulated cosmic variance

To understand the impact of cosmic variance in our predictions, in Figure 4.5 we compare the linear fits of the predicted MS across the eight simulated volumes in the same redshift bins of Figure 4.4. We limit to the higher three redshift intervals, as at $z \sim 7$ all the predictions tightly converge. Due to fewer statistics, the largest deviation is found at the highest redshifts, with a deviation in the slope of $\Delta\mathrm{m} = 0.11$, while it reduces to $\Delta\mathrm{m} = 0.04$ in the lowest redshift bin. Within the above variations, our simulations confirm an even better agreement between the trends followed by simulated and observed galaxies. Note, for example, that in the redshift range $7 < z \leq 10$ a better consistency is found with the galaxies analyzed in Tacchella

[13]We remind the reader that the results are sensitive to the way the data is binned/aggregated in redshift. For example, in the work done by Faisst et al. (2020) the ALPINE collaboration finds that the entire galaxy sample $4 < z < 5.9$ (orange squares) is compatible with the relation found by Speagle et al. (2014) at $z = 5$ within a ± 0.3 dex width.

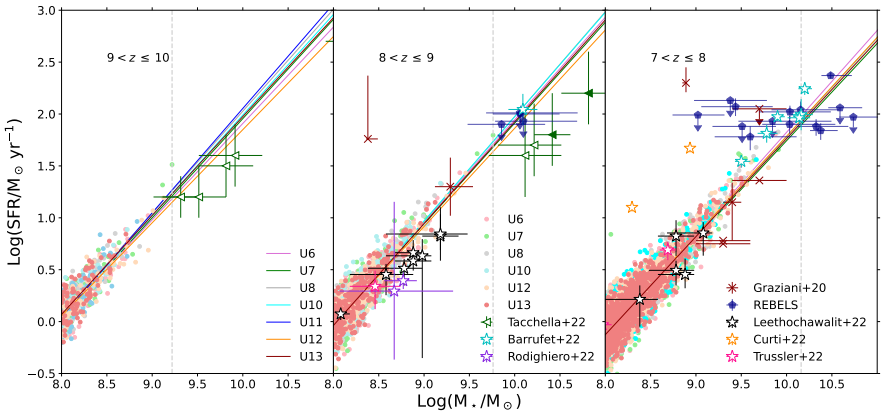

Figure 4.5. Here we explore the variance among our 8 independent simulations by comparing the linear fit of each universe from U6 to U13. The *solid lines* indicate the linear fit of each universe, each one with a different color, while the *points* are the simulated galaxies with $M_\star \geq 10^8 M_\odot$. For $z > 7$ different universes have different slopes, while at lower z the 8 simulations converge to a common trend.

et al. (2022); Graziani et al. (2020); Bouwens et al. (2022b); Leethochawalit et al. (2022); Curti et al. (2023); Trussler et al. (2022); Barrufet et al. (2022). As already mentioned, vertical gray dashed lines indicate $M_{\star,max}$ found in each simulation. Notice how, once we take into account all the available simulated cubes[14] , there is an increase in the statistics of the simulated objects resulting in higher upper limits for the stellar masses (i.e. vertical lines move towards higher mass values once compared to those in Figure 4.4).

Redshift evolution of the main sequence

There is a general consensus about the increasing normalization of the MS with redshift, which may be associated with a higher rate of gas accretion onto galaxies in the early Universe. However, a possible evolution in the slope of the MS is hard to constrain because of its dependence on the sample selection and the SFR tracer adopted (Speagle et al., 2014). At $z < 4$, observations seem to suggest that the MS is characterized by a constant slope that is close to unity when considering $M_\star < 10^{10.5} M_\odot$ (Whitaker et al., 2014; Tasca et al., 2015; Schreiber et al., 2015; Tomczak et al., 2016; Santini et al., 2017), suggesting a similarity in the gas accretion histories of galaxies. At higher redshifts Khusanova et al. (2021) investigated the MS using the ALPINE sample, finding no evidence for a change in the MS slope between $z \sim 4.5$ and $z \sim 5.5$. Very recently Popesso et al. (2022); Daddi et al. (2022) investigated the MS evolution in the redshift ranges $0 < z < 6$ and $0 < z < 4$ respectively. In both cases, they find that at the faint-end the MS has a linear slope that does not change with time, while at large stellar masses the MS bends, with a turn-over mass that is evolving with time. They interpret this result as an indication of a transition between a regime where star formation is efficiently

[14] In this work we usually consider U6 as our reference run (RefRun), unless otherwise specified.

sustained by gas accretion to a regime where star formation is suppressed by the interplay between the hot gas in massive halos and central black hole feedback (Popesso et al., 2022). However their turn-over mass is $\mathrm{Log}(\mathrm{M}_\star/\mathrm{M}_\odot) \sim 10.9$ at $z \sim 6$ and $\mathrm{Log}(\mathrm{M}_\star/\mathrm{M}_\odot) \sim 10.6$ at $z \sim 4$. As it can be seen from the two bottom right panels of Fig. 4.4, our simulation predicts zero or very few galaxies with masses above the turn-over mass and, as a consequence, our fit is sensitive to lower mass objects. Because of this, our simulation can only sample the regime of stellar masses where observations do not expect a significant evolution in the MS slope and galaxies are found to evolve with a constant SFR per unit stellar mass.

In order to study the main sequence slope at higher redshift ($z > 6$) and to have a significant number of simulated candidates, we restrict our analysis to the redshift range $6 < z \leq 9$ to explore if our simulations predict any evolution in the MS slope. Figure 4.6 shows the linear fit (green) we performed on our simulations when considering galaxies with $\mathrm{Log}(\mathrm{M}_\star/\mathrm{M}_\odot) \geq 8$ and the standard error associated with the value of the angular coefficient at each z (shaded region). In particular, solid lines correspond to the linear fit in the redshift range $8 < z \leq 9$, dashed lines to $7 < z \leq 8$ and dashed-dotted lines to $6 < z \leq 7$.

The best fits we obtained for each of the following redshift bins $6 < z \leq 7$, $7 < z \leq 8$, $8 < z \leq 9$ are respectively:

$$\mathrm{Log\,SFR} = (0.948 \pm 0.004)\mathrm{Log\,M}_\star - (7.83 \pm 0.03) \tag{4.5}$$

$$\mathrm{Log\,SFR} = (0.951 \pm 0.007)\mathrm{Log\,M}_\star - (7.73 \pm 0.06) \tag{4.6}$$

$$\mathrm{Log\,SFR} = (0.98 \pm 0.01)\mathrm{Log\,M}_\star - (7.8 \pm 0.1) \tag{4.7}$$

where $\mathrm{Log\,SFR} = \mathrm{Log}(\mathrm{SFR}/\mathrm{M}_\odot\mathrm{yr}^{-1})$ and $\mathrm{Log\,M}_\star = \mathrm{Log}(\mathrm{M}_\star/\mathrm{M}_\odot)$.

Both slope and normalization of the simulated MS appear to be constant, within the errors.

In Figure 4.6 we also compare our results with the best fit functions by Popesso et al. (2022) and Speagle et al. (2014) respectively in orange and blue. Both relations are calibrated on lower redshifts observations ($0 < z < 6$ and $0 < z < 4$) but they can be exploited to assess the MS evolution at higher z.

As expected, we are not able to reproduce the bending found by Popesso et al. (2022), whereas our predicted slope at $6 < z \leq 9$ is steeper than the extrapolation of Speagle et al. (2014) and favoured by JWST early results, as discussed above.

4.3.6 Redshift evolution of the specific star formation rate

The sSFR, i.e. the SFR per unit stellar mass, is often used as an additional diagnostic of how SFR and $\mathrm{M}_\star$ are related. Observational determinations of the sSFR at high-z have largely benefit from improved constraints on dust-obscured star formation coming from dust continuum detections with ALMA (Khusanova et al., 2021; Topping et al., 2022). This section investigates the redshift evolution of the median values of the sSFR in our simulations[15]. Figure 4.7, (adapted from Topping et al. 2022), shows `dustyGadget` predictions (magenta hexagons) and its comparison with theoretical models and observations. Theoretical models in which the growth of galaxies is mainly regulated by gas accretion through cold streams

[15]The sSFR is derived accounting for galaxies with masses in the range $\mathrm{Log}(\mathrm{M}_\star/\mathrm{M}_\odot) = [8 - 11]$.

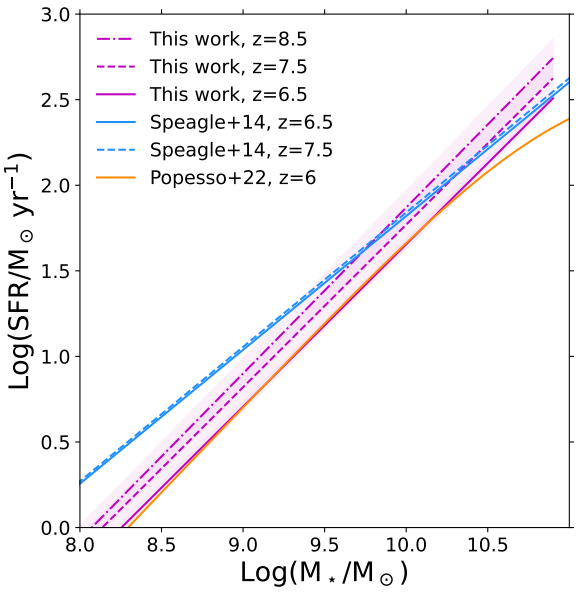

Figure 4.6. Linear fits of the data (*magenta*) from our simulations, considering galaxies with $\mathrm{Log}(M_\star/M_\odot) \geq 8$. Each fit has been performed in three different redshift bins $6 < z \leq 7$, $7 < z \leq 8$, $8 < z \leq 9$ considering all the available cubes at these redshifts, Together with the linear fit we also show here the standard error associated with the angular coefficient (*pink-shaded regions*). In *orange, green and light-blue* we report respectively the best fits obtained by Popesso et al. (2022) at $z = 6$, Schreiber et al. (2015) at $z = 7$ and Speagle et al. (2014) at $z = 6.5$ and $z = 7.5$.

(Dekel et al., 2009a; Davé et al., 2011; Sparre et al., 2015), predict a sSFR rapidly rising toward higher redshifts, with a dependence proportional to $(1+z)^{2.25}$ (gray dotted line). Deviations from this estimate could arise from a different behaviour of feedback processes in the high-z Universe. For example, a different efficiency in gas accretion could significantly alter the rate of star formation, and JWST data will certainly provide clues on how fast gas is converted into stars within the EoR.

At lower redshift, larger samples of galaxies with highly reliable spectroscopic redshift are available from: (i) the VIMOS Ultra-Deep Survey (VUDS) (yellow crosses, Tasca et al. 2015), (ii) the deep COSMOS-2015 and 3D-HST rest frame UV-IR photometric catalogs (turquoise points, Leja et al. 2019, 2021), clearly showing a redshift dependence of the sSFR.

The above evolution, on the other hand, is not confirmed by all data, especially at the highest redshifts. Observations from the first four HST Frontier Field clusters (orange triangles) collected with a fixed mass bin $9.5 \leq \mathrm{Log}(M_\star/M_\odot) \leq 10$ and an average value of $\mathrm{Log}(M_\star/M_\odot) \sim 9.7$ (Santini et al., 2017) confirm a mild evolution up to $z \sim 6$, while the ALPINE sub-sample analyzed by Khusanova et al. (2021) (green pentagons), with candidates in the mass bin $9.6 \leq \mathrm{Log}(M_\star/M_\odot) \leq 9.8$, shows little to no evolution at $4.5 \leq z \leq 5.5$. The REBELS collaboration (Topping et al. 2022) provided a power-law fitting of the REBELS galaxies and other available measurements adopting a fixed mass bin of $\mathrm{Log}(M_\star/M_\odot) = 9.6 - 9.8$ and a constant SFH, finding that the sSFR increases with redshift $\propto (1+z)^{1.7\pm0.3}$ over the redshift range $z \sim 1-7$. Using a non-parametric SFH for REBELS galaxies, which significantly affects the stellar mass derivation at the low-mass end, the evolution at a fixed stellar mass of $\mathrm{Log}(M_\star/M_\odot) = 9.7$ is only mildly affected[16], with sSFR

[16]The difference between stellar masses derived assuming a constant SFH or a non-parametric SFH is particularly significant for young and low-mass galaxies (i.e. Age < 10 Myr and $\mathrm{Log}(M_\star/M_\odot) < 9$

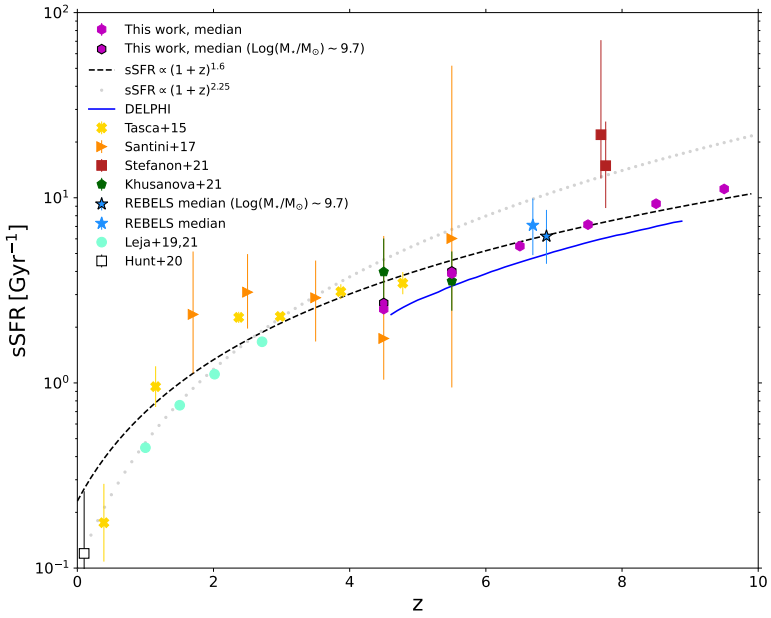

Figure 4.7. The redshift evolution of the sSFR, we show in *magenta* the results from our simulations in the redshift range $z = 4-10$ - the statistical errors for our data are smaller than the symbols - and in the mass range $8 < \mathrm{Log}(\mathrm{M}_\star/\mathrm{M}_\odot) < 11$. In *magenta with black borders* we show the sSFR in the mass range $9.6 < \mathrm{Log}(\mathrm{M}_\star/\mathrm{M}_\odot) < 9.8$, compatible with the median mass value of $\mathrm{Log}(\mathrm{M}_\star/\mathrm{M}_\odot) \sim 9.7$ present in observed samples. We compare our results with the models by Dekel et al. (2009b); Davé et al. (2011); Sparre et al. (2015) (*gray dotted line*), Topping et al. (2022) (*black dashed line*) and Dayal et al. (2022a) (*blue solid line*), and with the observations by the REBELS survey Topping et al. (2022) (*blue stars*), Tasca et al. (2015) (*yellow squares*), Santini et al. (2017) (*orange triangles*), Stefanon et al. (2021a) (*red squares*), Khusanova et al. (2021) (*green pentagons*), Leja et al. (2021) (*turquoise points*) and the *empty square with black border* is the estimate of the sSFR at z=0 by Hunt et al. (2020).

$\propto (1+z)^{1.6\pm0.3}$ in the same redshift range (black dashed line). Note, however, that - among the low-redshift observations - only the Leja et al. (2019, 2021) derivations are based on a non-parametric SFH, and this would favor a steeper evolution with redshift.

A non-parametric SFH increases the $\mathrm{M}_\star$, reducing the sSFRs to $\mathrm{sSFR} = 7.1^{+2.8}_{-2.2}\mathrm{Gyr}^{-1}$ when considering the entire REBELS sample, or to $\mathrm{sSFR} = 6.2^{+2.4}_{-1.8}\mathrm{Gyr}^{-1}$ when considering the mass range $9.6 < \mathrm{Log}(\mathrm{M}_\star/\mathrm{M}_\odot) < 9.8$, consistent with the ALPINE sample, at $z \sim 7$ (Topping et al., 2022). Finally, Stefanon et al. (2021a) (red squares) derived the sSFRs for a sample of Lyman-Break galaxies at $z \sim 8$ with M_{UV} similar to that of REBELS showing even higher sSFR at $z \sim 8$, compatible with the original trend (gray dotted line).

Recently, semi-analytic models provided theoretical estimates of the sSFR predicted by the REBELS collaboration (see Topping et al. 2022) as shown in Figure 4.7. The `DELPHI` model (Dayal et al., 2014, 2022a) for example, predicts a power-law

respectively). A detailed comparison of stellar masses derived by the two methods applied to the REBELS sample can be found in Topping et al. (2022).

evolution at $z \geq 4$ (solid blue line), consistent with REBELS power-law fitting up to a normalization factor. `dustyGadget` predictions are in agreement with the smooth evolution (black dashed) proposed by Topping et al. (2022). However, to guarantee consistency across observed and simulated data samples, a uniform stellar mass range is required. For the above reason we first computed the sSFR on the full galactic sample discussed in this chapter ($\mathrm{Log}(\mathrm{M}_\star/\mathrm{M}_\odot) \geq 8$) (magenta hexagons), and then we made the same estimates considering the mass range $9.6 < \mathrm{Log}(\mathrm{M}_\star/\mathrm{M}_\odot) < 9.8$, compatible with the median mass value of $\mathrm{Log}(\mathrm{M}_\star/\mathrm{M}_\odot) \sim 9.7$ present in observed samples. These results are shown in Figure 4.7 as magenta hexagons with black borders. More specifically, we find sSFR = 2.5 Gyr^{-1} at $z = 4.5$ and 3.9 Gyr^{-1} at $z = 5.5$, respectively, where a sufficiently large number of simulated galaxies is available. When restricting to the aforementioned stellar mass bin, our results increase by $\sim 3 - 8\%$ and we find sSFR = 2.7 Gyr^{-1} at $z = 4.5$ and 4.0 Gyr^{-1} at $z = 5.5$. Overall, our simulation suggests an increase of the sSFR with redshift in the range $4 < z < 10$, consistent with current observations and with theoretical expectations based on increased baryon accretion rates at high redshifts. As a comparison with the Local Universe, in Fig. 4.7 we also show the sSFR at $z = 0$ estimated by Hunt et al. (2020)[17]. Assuming the mid point of the observed mass range to be $\mathrm{Log}(\mathrm{M}_\star/\mathrm{M}_\odot) = 9.5$ and using Equation 1 of Hunt et al. (2020), we obtain a sSFR of 0.12 Gyr^{-1}.

4.3.7 Halo-Stellar mass relation

The relation between the dark matter mass of a halo ($\mathrm{M}_{\mathrm{halo}}$) and the stellar mass of its galaxies is often assumed by semi-analytic or data-constrained models which do not explicitly model baryonic processes with a hydrodynamical approach. Accordingly, to these theoretical schemes Rees and Ostriker (1977); White and Rees (1978); Fall and Efstathiou (1980), the assembly of the stellar mass is driven by the large-scale process of dark matter accretion either through mergers or smooth accretion from filaments, prompting the flow of cold gas into the central galaxy. As a result, the stellar-to-halo mass relation (SHMR) is a proxy of the star formation efficiency. The same scaling relation is often adopted by observers to provide lower limit constraints on DM overdensities associated with luminous objects. We multiply by a factor 1.7 (Madau and Dickinson, 2014a) the stellar masses to convert them from a Chabrier (2003a) to a Salpeter (1955) IMF.

Figure 4.8 shows results from our simulations (gray dots) and their median trends (magenta solid lines). Vertical and horizontal dashed lines show respectively the maximum halo mass ($\mathrm{M}_{\mathrm{halo,max}}$) and $\mathrm{M}_{\star,\mathrm{max}}$ found in the RefRun. We also report recent constraints on the SHMR from abundance matching techniques by Stefanon et al. (2021b) (orange circles) and Finkelstein et al. (2015) (red hexagons). Estimates by Harikane et al. (2016), which rely on the two-point correlation function of LBGs, are shown as light blue diamonds, while the recent estimates based on the COSMOS2020 catalog from Shuntov et al. (2022) are in orange dash-dotted lines. We also show the redshift dependent SHMR predicted by the data-constrained

[17] In estimating the sSFR we considered the mass range $8 < \mathrm{Log}(\mathrm{M}_\star/\mathrm{M}_\odot) < 11$ in order to be consistent with the one analysed in the present work. Notice that even at $z = 0$, where the data sample is larger, the sSFR changes by ~ 0.5 dex depending on the mass range considered.

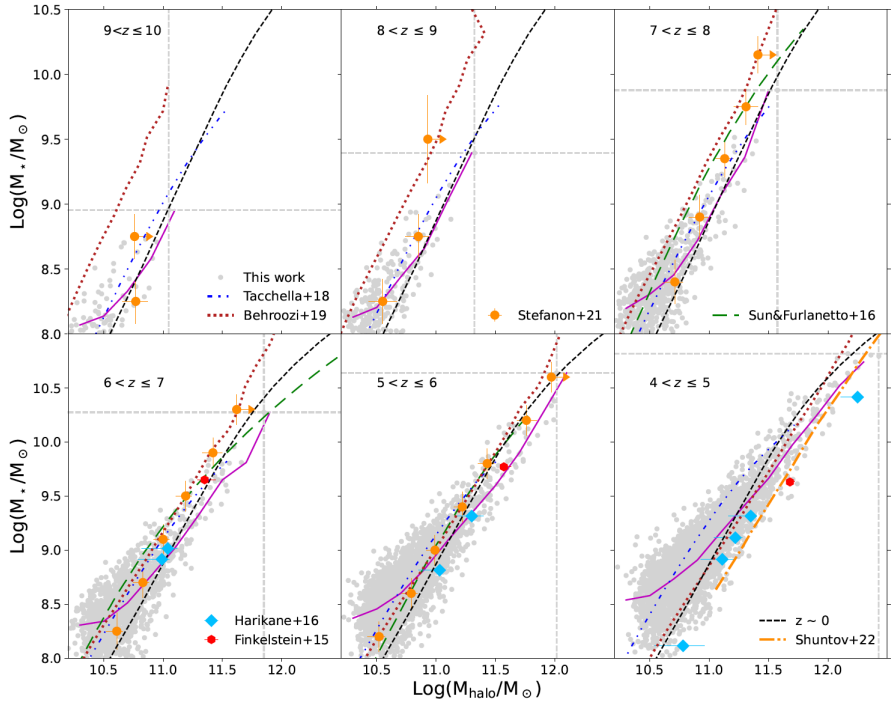

Figure 4.8. Redshift evolution of the stellar mass ($M_\star$) and halo mass (M_{halo}) relation. Here we compare our simulated galaxies (*gray points*) and their median trends (magenta solid lines) with the observations by Stefanon et al. (2021b) (*orange circles*), Harikane et al. (2016) (*light blue diamonds*), Finkelstein et al. (2015) (*red hexagons*), Shuntov et al. (2022) (*dash-dotted orange line*) and the predictions obtained by Behroozi et al. (2019); Tacchella et al. (2018); Sun and Furlanetto (2016) (respectively in *red dotted lines, dash double dotted blue lines and loosely dashed green lines*). The behaviour of the $M_{halo} - M_\star$ relation at $z \sim 0$ (Behroozi et al., 2019) (*dashed black lines*) has been shown to guide the eye.

model of Behroozi et al. (2019)[18] (red dotted lines and shaded areas) and additional theoretical models which either assume a constant SHMR above $z > 4$ (Tacchella et al., 2018), or introduce a redshift dependent conversion efficiency between the halo accretion rate and the star formation rate (Moster et al. 2018, dashed-dotted light blue lines, Sun and Furlanetto 2016, loosely dashed green lines). Finally, as a reference to predictions in the Local Universe, we also show the behaviour of the SHMR relation at $z \sim 0$ by Behroozi et al. (2019).

At all redshifts, our simulations indicate the expected monotonic increase of $M_\star$ with M_{halo}. The simulated systems show a significant scatter in the relation, particularly at the low-mass end, where we have larger statistics. At $5 < z \leq 6$, DM halos with mass $\mathrm{Log}(M_{halo}/M_\odot) = 10.5$ are predicted to host galaxies with stellar masses $8 \leq \mathrm{Log}(M_\star/M_\odot) < 9$, likely reflecting the ongoing process of galaxy assembly and the large variety of SFHs experienced by these systems. When compared to

[18]For this comparison, we considered the average halo masses as a function of observed stellar masses found in the database of Behroozi et al. (2019).

other models and observations, our median trends are generally consistent with previous results.

However, at $z \leq 6$ our simulated galaxies appear to grow in mass more efficiently, with a deviation in the median trend at $\mathrm{Log}(\mathrm{M_h}/\mathrm{M_\odot}) < 11$ that progressively increases with time. This is consistent with the estimated low-mass end of the SMF, which appears to predict a larger number density of systems compared to some observational determinations (see Section 4.3.3) and model predictions (see Appendix A) at $z \leq 6$, while being in agreement with other observational and theoretical studies. This may suggest that in low-mass galaxies feedback may be more effective than modeled by `dustyGadget` (see for example Graziani et al. 2015, 2017b), despite the encouraging agreement between our predicted galaxy MS and JWST early results in the mass range $10^8 - 10^{11}$ $\mathrm{M_\odot}$ at $z = 4 - 9$.

4.3.8 Dust-to-stellar mass scaling relation

This section updates our predictions on the relation between dust ($\mathrm{M_d}$) and stellar mass content in high-z galaxies. In Graziani et al. (2020) the same relation was shown for the first time as predicted by a lower mass resolution simulation performed on a $30\mathrm{h}^{-1}$ cMpc cosmological volume. The highest mass resolution of the new simulations allows to (i) better model processes occurring in the ISM of galaxies with $\mathrm{Log}(\mathrm{M_\star}/\mathrm{M_\odot}) \geq 9$, (ii) investigate in more detail systems in the intermediate mass range ($8 \leq \mathrm{Log}(\mathrm{M_\star}/\mathrm{M_\odot}) \leq 9$), and (iii) collect a larger number of assembly histories from the eight simulations, thanks to the increased statistics, particularly at the high-mass end. Here the simulations are also compared with the REBELS sample (dust mass estimates provided by Sommovigo et al. 2022c), with ALPINE galaxies (estimated in Pozzi et al. 2021 and Sommovigo et al. 2022a) and with a recent dataset provided in Witstok et al. (2022). Also in this case, we multiply by a conversion factor 1.7 the stellar masses to convert them from a Chabrier (2003a) to a Salpeter (1955) IMF.

Figure 4.9 shows the redshift evolution of the $\mathrm{M_d} - \mathrm{M_\star}$ relation for galaxies with $\mathrm{Log}(\mathrm{M_\star}/\mathrm{M_\odot}) \geq 8$ found in our RefRun (U6, gray points), while vertical dashed lines show the $\mathrm{M_{\star,max}}$ value at each redshift. We also show predictions from the empirical model by Imara et al. (2018) (green dotted lines), the semi-analytic model of Popping et al. (2017) (purple dash-dotted lines), and the median/maximal relation of Vijayan et al. (2019) (pink solid/dashed lines, respectively).

The new simulation confirms the s-shape trend found in Graziani et al. (2020) with increased statistics, extending it towards larger stellar masses. The $\mathrm{M_d} - \mathrm{M_\star}$ relation that we find confirms the good agreement with the predictions by Popping et al. (2017) in the redshift range $4 < z \leq 9$, and lies in between the median and the maximum relations of Vijayan et al. (2019). However, we systematically predict, both at $9 < z \leq 10$ and at $5 < z \leq 6$, less dust-enriched systems compared to Imara et al. (2018).

The observational dataset relies on single dusty galaxies (including the sample of ALESS galaxies) collected in Graziani et al. (2020) (red, Table 2 of their paper), on ALPINE continuum detection (orange, Pozzi et al. 2021) on the recent estimates of the dust mass budget in the ALPINE sample by Sommovigo et al. (2022a) (green) and on dust masses derived from dust continuum detection of REBELS galaxies

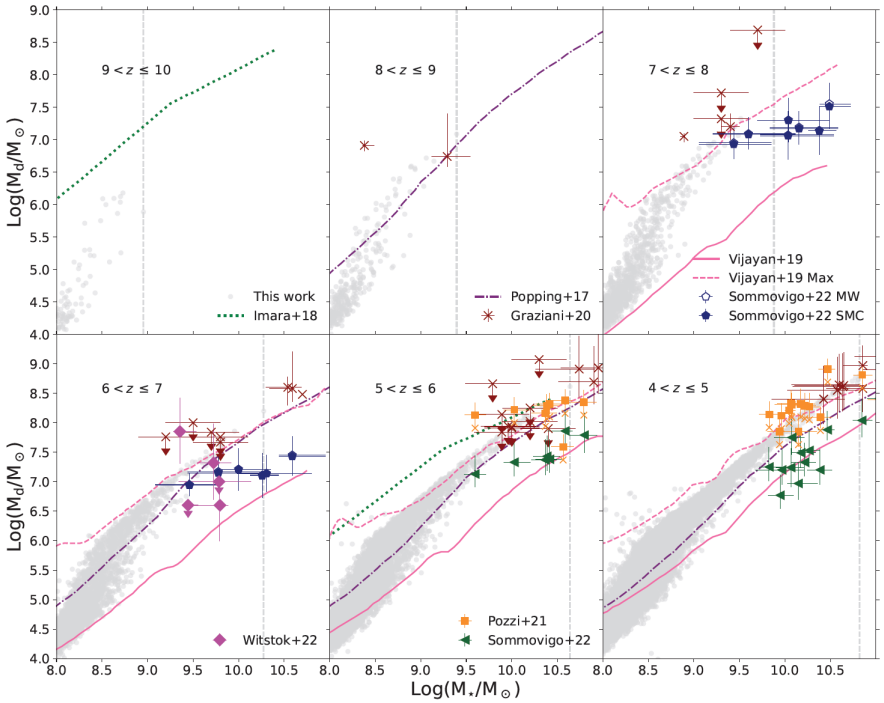

Figure 4.9. Dust mass (M_d) as a function of the stellar mass ($M_\star$) both in units of $M_\odot$ for simulated galaxies with $\mathrm{Log}(M_\star/M_\odot) > 8$ extracted from simulation U6 (gray points). The evolution is investigated in the redshift range $4 < z \leq 10$. *Red crosses* are observations from the compilation by Graziani et al. (2020) (see their Table 2), *blue pentagons* are from the REBELS survey Sommovigo et al. (2022c) and *magenta diamonds* are observations from Witstok et al. (2022). *Orange squares and crosses* are the dust masses obtained within the ALPINE survey by Pozzi et al. (2021) assuming respectively $T_d = 25$ K and 35 K, while *green triangles* are the recent estimates, for some of the ALPINE galaxies, by Sommovigo et al. (2022a) where $< T_d > = 48 \pm 8$ K. We also compare our results with other independent studies: *dash-dotted violet lines* are the averaged trends computed by Popping et al. (2017), *pink solid and dashed lines* are respectively the fiducial and maximum models of Vijayan et al. (2019), and *green dotted lines* show predictions by Imara et al. (2018).

(Inami et al., 2022) by Sommovigo et al. (2022c) (blue) assuming a Small Magellanic Cloud (SMC) dust model[19].

Dust mass estimates strongly depend on the assumed cold dust temperature: Pozzi et al. (2021) investigated this dependence for the ALPINE sample, finding that going from $T_d = 25$ K (fiducial value) to $T_d = 35$ K results in a decrease of the dust mass by 60% (these estimates are respectively shown as orange squares and crosses in Figure 4.9). Using the method described in Sommovigo et al. (2021), very recently Sommovigo et al. (2022a) derived new dust mass estimates of some of the

[19]Similarly to what we showed in the previous sections, the stellar masses considered here for REBELS galaxies are computed using a non-parametric SFH as in Topping et al. (2022).

ALPINE galaxies already analysed by Pozzi et al. (2021). The new analysis leads to warmer dust temperatures $< T_d > = 48 \pm 8$ K and, as a consequence, to M_d up to 7 times lower than those previously reported. The same analysis technique has been applied to a subsample of REBELS galaxies with [CII] and dust-continuum detections (Sommovigo et al., 2022c), finding a T_d that varies in the range between $39 - 58$ K, with an average dust temperature of $< T_d >= 47 \pm 6$ K. The red circles (ALESS galaxies from Table 2 of Graziani et al. 2020) are estimates with a T_d around 45 K, while the dust mass upper limits, since the dust temperature anti-correlates with the dust mass, are estimated using $T_d \sim 25$ K. As in Graziani et al. (2020), the gray points of simulated galaxies are in good agreement with estimates or compatible with upper limits of M_d obtained for singly detected objects. Despite the large uncertainties in the $M_\star$ of galaxies observed in the EoR, we are in agreement with REBELS galaxies with masses $\mathrm{Log}(M_\star/M_\odot) \lesssim 9.5$, while objects with $\mathrm{Log}(M_\star/M_\odot) > 9.5$ have estimated dust masses systematically lower than our predictions, indicating that either our high-mass objects are too dusty or that the dust temperature for some of these sources may have been over-estimated. Radiative transfer simulations performed with `SKIRT` (Baes and Camps 2015) on `dustyGadget` simulated galaxies, and a close comparison with photometric properties of the REBELS sample will help to shed some light on the above discrepancy (Schneider et al., in prep.). Interestingly enough, we find that at lower redshift the simulated sample is globally compatible with ALPINE/ALESS estimates found in Pozzi et al. (2021) and Graziani et al. (2020) for galaxies with $\mathrm{Log}(M_\star/M_\odot) > 9.5$, with only a few exceptions that lie above or below the trend followed by the simulated systems. Conversely, when compared to dust masses derived by Sommovigo et al. (2022a) for a subsample of ALPINE systems, our simulation predicts higher dust masses.

A further comparison with Witstok et al. (2022), provides us with five more observed galaxies in the redshift interval $6 < z \leq 7$. These galaxies have stellar masses in the range $\mathrm{Log}\ (M_\star/M_\odot) = 9.1 - 9.9$ and their FIR SED fits favour the following dust temperatures: $T_d = 59^{+41}_{-20}$ K for UVISTA-Z-001, $T_d = 47^{+40}_{-17}$ K for UVISTA-Z-019, and the extremely low value of $T_d = 29^{+9}_{-5}$ K for COS-3018555981. For the two additional sources, dust continuum was not confidently detected in any ALMA band, and they assumed a $T_d = 50$ K. The resulting dust masses are shown as magenta dots. With the exception of COS-3018555981 for which the low dust temperature favoured by the FIR fit suggests a very high dust mass, all the other sources appear to be consistent with the simulated galaxies, at least within the error bars. When interpreted at face value, the fact that COS-3018555981 is well above the simulated galaxies may imply a very efficient dust production mechanism in this system (Witstok et al., 2022), beyond what is predicted by `dustyGadget` for galaxies of comparable stellar mass and redshift when accounting for stellar dust production and ISM grain growth.

The dust-to-stellar mass ratio can give us some hints on how much dust per unit stellar mass survives the various destruction processes in galaxies. Also, it is a useful quantity to study the evolution of different types of galaxies (see for example Calura et al. 2017). Figure 4.10 shows the $M_d/M_\star$ ratio as a function of stellar mass for the simulated galaxies from 4 independent simulated volumes (U6, U7, U12 and U13) at $6 < z \leq 7$. The inferred ratios from observational data points of Witstok et al. (2022) presented in the bottom left panel of Figure 4.9 are

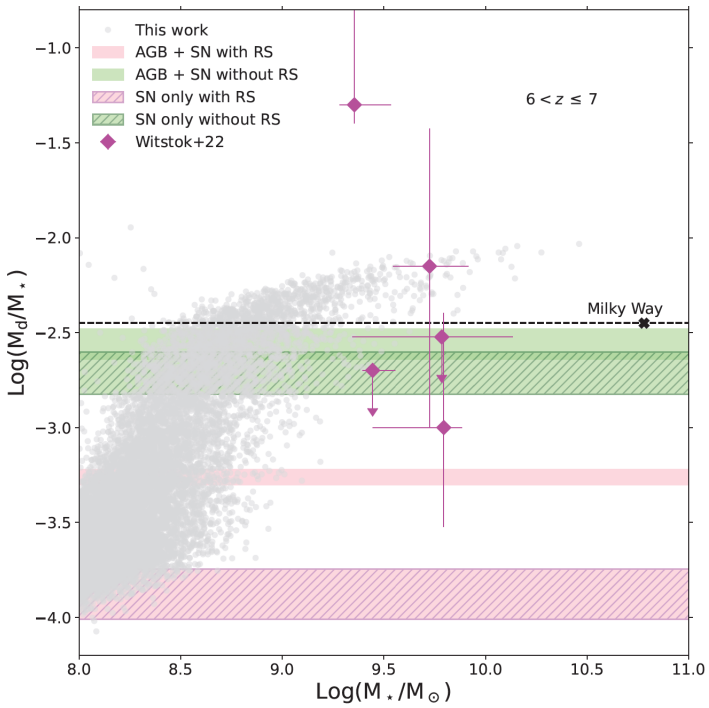

Figure 4.10. The dust-to-stellar mass ratio in the redshift range $6 < z \leq 7$ for the simulated galaxies (*gray dots*) in the RefRun (U6) and in simulations U7, U12 and U13. We also show the values reported by Witstok et al. (2022) as *magenta points*. The horizontal solid bands represent the value expected for a population age $t_\star = 650$ Myr (see the text on how this value has been computed), with upper and lower bounds corresponding to assuming $Z_\star = 1\,Z_\odot$ and $Z_\star = 0$. While the horizontal hatched bands represent the yields assuming a stellar population age of 15 (18.7) Myr, corresponding to the age of a minimum star that evolves as a core-collapse SN for a stellar metallicity of $Z_\star = 1\,Z_\odot$, upper bound ($Z_\star = 0$, lower bound). Here we assume the same dust yields adopted in the present `dustyGadget` simulations with (*pink*) and without (*green*) the SN reverse shock (RS) destruction. For comparison, we also report the dust-to-stellar mass ratio for the Milky Way (*dashed black line* and *black cross*).

shown again, together with the estimated Milky Way value (dashed black line and black filled point, Graziani et al. 2017a; Ginolfi et al. 2018a). We also show the yields expected for stellar sources assuming a maximum population age of 650 Myr (computed as the difference between the Hubble time at $z = 6.85$, the measured redshift of COS-3018555981, and the Hubble time at $z = 25$, assumed to be the onset redshift of star formation). Here we assume the same dust yields implemented in the current simulations (see Section 4.2) and a maximally efficient SN dust production, assuming no reverse shock (RS) destruction. For each of these two cases, represented respectively by pink and green horizontal shaded bands, the minimum (maximum) value corresponds to assuming a fixed stellar metallicity of $Z_\star = 0$ ($Z_\star = 1\,Z_\odot$). To appreciate the contribution of SNe to early dust production, we also show the same predictions but assuming a stellar population age of 15 (18.7) Myr, which corresponds to the age of the progenitor star with the minimum mass that evolves as a core-collapse SN ($12\,M_\odot$ in our chemical evolution model) for a stellar metallicity

of $Z_\star = 0$ ($Z_\star = 1\,Z_\odot$). These two additional cases are shown as horizontal hatched bands, with the same colour coding of the previous two cases. For the same set of yields (pink and green areas), the difference between the dust-to-stellar mass ratio for a $t_\star = 650$ Myr population and the latter cases is due to the contribution of the most massive AGB stars (with masses between $\sim 2 - 2.4\,M_\odot$ and $\sim 8\,M_\odot$).

The comparison between the dust yields and the simulated systems shows that the dust content of each galaxy is the result of a complex interplay between dust production/destruction mechanisms and that grain growth in the ISM contributes to the enrichment of high-mass galaxies (Valiante et al., 2014; Mancini et al., 2015; Graziani et al., 2020). While the other sources reported by Witstok et al. (2022) are consistent with this picture, COS-3018555981 stands out, requiring a substantially more efficient dust production mechanism, an upward revision of the estimated dust temperature, a higher dust emissivity, or a mix of the above.

4.4 Conclusions

The present work investigates the build-up of the stellar mass of galaxies at $z \geq 4$ and the scaling relations of their integrated physical properties. We selected observationally well-established correlations in the Local Universe, and thanks to a wealth of new data provided by recent high-redshift ALMA Large Programs, such as REBELS (Bouwens et al., 2022b) and ALPINE (Faisst et al., 2020), we were able to benchmark numerical predictions of the `dustyGadget` model (Graziani et al., 2020) with updated observations, including some of the early release observations of JWST.

With this aim in mind, we performed a new set of eight statistically independent cosmological simulations on a scale of $50h^{-1}$ cMpc in order to increase the statistical sample of predicted galaxies, to account for a larger scatter in their predicted properties and to have access to a wider sample of dusty environments produced by stellar feedback, dynamical encounters, and mergers as well as hydrodynamical effects. The resulting integrated dataset provides a statistically robust sample of dusty galaxies in the stellar mass range $8.0 \leq \mathrm{Log}(M_\star/M_\odot) < 11.0$ suitable to investigate the build-up of stellar mass and the redshift evolution of some galaxy scaling relations at $z \geq 4$. In particular, we find that:

- the total stellar build-up, both in terms of total star formation rate and total stellar mass density, rapidly increases from the onset of star formation occurring around $z \sim 20$, down to $z \sim 4$ with a remarkable agreement with available observations, including JWST ERO and ERS at $z \geq 8$;

- at $4 < z \leq 9$ the stellar mass function predicted by the simulation shows a broad agreement with observations and with independent theoretical predictions. At $z < 8$, `dustyGadget` predicts fewer massive objects compared to observed samples, due to the limited statistics of massive systems in the simulated volume at these redshifts.

- at $7 < z \leq 9$ we find that the simulated galaxy main sequence is in very good agreement with available data, including some of the first JWST ERO

and ERS which extends to lower stellar masses the observational constraints placed by REBELS on brighter and more massive systems. The fit to our simulated galaxies is consistent with a non-evolving linear slope. Our results are consistent with recent studies on the evolution of the galaxy main sequence at $z < 4 - 6$ (Popesso et al., 2022; Daddi et al., 2022), in that `dustyGadget` simulations sample the low-mass end of the MS, below the time-dependent turn-over mass that defines the transition between efficient and relatively inefficient star formation;

- a similarly good agreement is found when comparing the redshift evolution of the specific star formation rate predicted by the simulation with a recent analysis that includes REBELS sources out to $z \sim 7$;

- the relation between stellar and dark matter halo mass predicted by the simulations shows a large scatter, particularly at the low-mass end, likely reflecting the large variety of galaxy assembly histories. We find a broad agreement with some observational determinations (Finkelstein et al., 2015; Stefanon et al., 2021b), and with models that assume a redshift independent relation (Tacchella et al., 2018), indicating a constant star formation efficiency for a given halo mass across the redshift range we have investigated. However, at $z \leq 6$ the simulated galaxies appear to have stellar masses that grow more efficiently than predicted by abundance matching methods (Behroozi et al., 2019; Sun and Furlanetto, 2016), particularly at the low-mass end. This resonates with the large number density of galaxies at the faint end of the stellar mass function, at $\mathrm{Log}(\mathrm{M}_\star/\mathrm{M}_\odot) < 9$. Assessing the statistical relevance of these galaxies with JWST observations will be fundamental to characterise their properties and correctly model these environments in future simulations (Venditti et al., in prep.);

- dust and stellar mass are confirmed to be related with the s-shape relation found in Graziani et al. (2020) which changes its derivative for objects with stellar masses $\mathrm{Log}(\mathrm{M}_\star/\mathrm{M}_\odot) \geq 8.5$. According to our simulations, dust enrichment at $z > 4$ is driven by stellar dust production and ISM grain growth, with the latter mechanism providing a growing contribution at the high-mass end. Overall, we find a good agreement with dust mass determinations for ALPINE galaxies by Pozzi et al. (2021) at $4 \leq z \leq 6$ and with REBELS galaxies with stellar masses $\mathrm{Log}(\mathrm{M}_\star/\mathrm{M}_\odot) \leq 9.5$ at $6 < z \leq 8$ (Sommovigo et al., 2022c), while more massive REBELS galaxies appear to have dust masses systematically lower than our predictions, indicating that either our simulated high-mass galaxies are too dusty or that the dust temperature for some REBELS sources may have been over-estimated. Similar conclusions apply when the comparison is made with a subsample of ALPINE galaxies recently analysed by Sommovigo et al. (2022a). Interestingly, the recent detection of dust continuum from 3 galaxies at $6 < z \leq 7$ by Witstok et al. (2022) provides additional indications on their dust-to-stellar mass relation, with two galaxies being consistent with `dustyGadget` predictions and one galaxy showing a very large dust-to-stellar mass ratio, implying a very efficient dust production mechanism in this system, beyond what is predicted by `dustyGadget` for galaxies with comparable stellar

mass.

In summary, the stellar mass assembly and related scaling relations investigated in this manuscript indicate that on the cosmological scale `dustyGadget` prescriptions are in reasonable global agreement with current high-redshift data, including JWST ERO and ERS. The new set of simulations reveals, on the other hand, an interesting population of evolving galaxies with stellar masses in $8.0 \leq \mathrm{Log}(\mathrm{M}_\star/\mathrm{M}_\odot) \leq 9.0$. The number density of these galaxies exceeds some of the current observational estimates and model predictions for the stellar mass function at $z \leq 6$, and are at the origin of the large scatter found in the halo mass-stellar mass relation. This indicates that galaxies hosted in DM halos with similar mass may experience different SFHs and chemical enrichment timescales, as also reflected in the dust-to-stellar mass relation, where galaxies with $\mathrm{Log}(\mathrm{M}_\star/\mathrm{M}_\odot) \sim 8.5$ at $z \leq 6-7$ are characterized by a broad range of dust masses, with differences of up to 1.5 dex. We plan to explore some of these aspects in a forthcoming publication.

The impressive capabilities of the JWST already revealed by the early release observations will certainly shed some light on the relevance and physical properties of these low-mass objects, providing invaluable constraints to future theoretical models investigating the details of their ISM and their impact on cosmic reionization.

4.5 Appendix B: SMF comparison with other simulations

In this Section we compare `dustyGadget` results with independent model predictions[20]. The results are illustrated in Figure 4.11, where we have applied the proper conversion factors (Madau and Dickinson, 2014a) to stellar masses that were originally computed with an IMF different from the Salpeter (1955) one.

Semi-analytic forecasts from Yung et al. (2019)[21] are shown as purple dashed lines, while similar estimates based on the `GALFORM` code combined with a large DM simulation provided by Cowley et al. (2018) are shown as blue dash-dotted lines. Dotted red lines and loosely dashed green lines are respectively the predictions from the `UNIVERSEMACHINE`[22] (Behroozi et al., 2019) and from the `CAT` semi-analytic model by Trinca et al. (2022). Dashed olive lines are from the phenomenological model `JAGUAR` (Williams et al., 2018). This model is based on observed stellar mass and UV luminosity functions that have been measured in the redshift range $0 < z < 10$. The red dashed lines are from the N-body/hydrodynamical `Illustris-1` simulation by Genel et al. (2014), brown solid and dash-dotted light-blue lines are from cosmological zoom-in simulations, respectively from `FIRE-2` (version 2.0 of the `FIRE` project; Hopkins et al. 2018) by Ma et al. (2018) and `FLARES` (Lovell

[20] Some of the relevant data has been taken from the public repository at https://github.com/stephenmwilkins/flags_data

[21] https://www.simonsfoundation.org/semi-analytic-forecasts-for-jwst/

[22] The `UNIVERSEMACHINE` (https://www.peterbehroozi.com) applies simple empirical models of galaxy formation to dark matter halo merger trees. It keeps track of two stellar masses: the "true" $\mathrm{M}_\star$ given by the integral of past star formation minus stellar mass loss, and the "observed" $\mathrm{M}_\star$ which includes systematic offsets and scatter as a function of redshift. Here we consider the "observed" stellar mass.

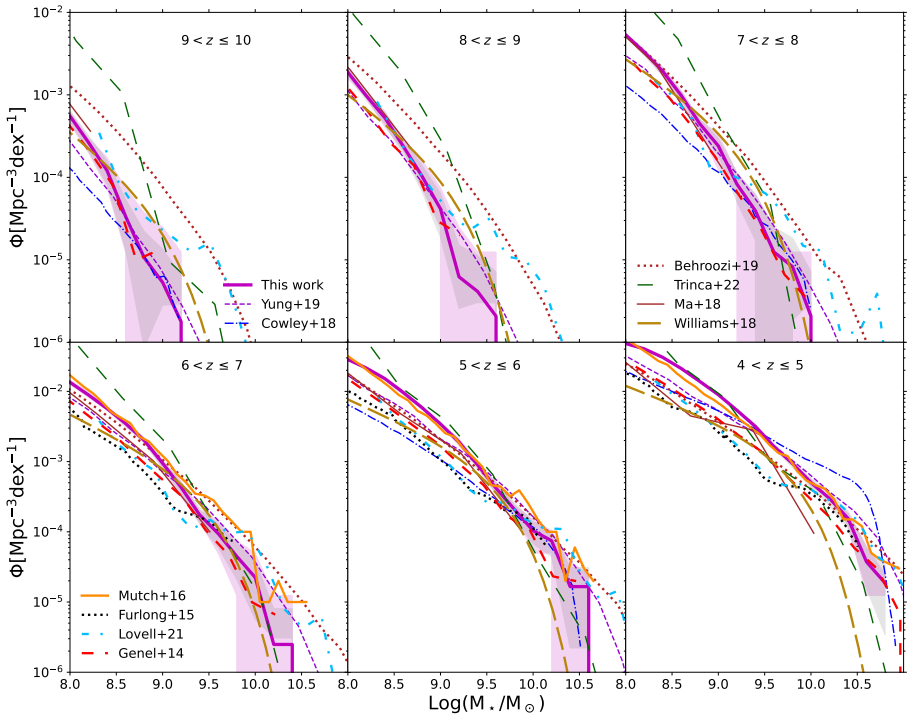

Figure 4.11. Mass Function obtained from our simulated galaxies in the range $z = 10 - 4$: *magenta solid lines* show mean values of our sample, *pink-shaded areas* the min-max spread of the simulations and *gray-shaded areas* the Poissonian error associated with our sample. The results of the semi-analytic model by Yung et al. (2019) are shown as *purple dashed lines* and those of the `CAT` (Trinca et al., 2022) semi-analytic model are in *green loosely dashed*, the results of the `UNIVERSEMACHINE` model by Behroozi et al. (2019) are in *dark-red dotted lines* and the predictions by Cowley et al. (2018) in *dash-dotted blue lines*. *Olive dashed lines* are the predictions from the `JAGUAR` model by Williams et al. (2018), *red dashed lines* are from the work by Genel et al. (2014) (`Illustris`) and the *dashed-dotted lightblue lines* are the predictions from the `FLARES` model (Lovell et al., 2021; Wilkins et al., 2022). Finally, *solid brown lines* are predictions from the `FIRE-2` simulation Ma et al. 2018, *black dotted lines* are from the `EAGLE` simulation by Furlong et al. (2015) and *orange solid lines* are from the `DRAGONS` simulation by Mutch et al. (2016).

et al., 2021; Wilkins et al., 2022). Predictions from the `EAGLE` hydrodynamical simulations (Furlong et al., 2015) are in black dotted lines, while those from the `DRAGONS` semi-analytic galaxy formation model (Mutch et al., 2016) are in orange solid lines.

The comparison among the SMFs predicted by different models shows a large scatter, which is mostly due to different star formation conditions/feedback implementations in each model. The scatter is particularly evident at high redshifts (top three panels) while it decreases at $z < 6 - 7$ (bottom three panels). At $7 < z \leq 10$

`dustyGadget` simulations are in better agreement with the predictions by Yung et al. (2019) and Genel et al. (2014), while they foresee a higher (lower) number of objects compared to Cowley et al. (2018) (`UNIVERSEMACHINE`, Behroozi et al. 2019, and `CAT`, Trinca et al. 2022). At $z \leq 7$, our predictions at the low-mass end are in excellent agreement with the results of Mutch et al. (2016), and converge to the number densities predicted by `CAT` at $z \leq 5$, but exceed the other model predictions. At all redshifts, the high-mass end ($\mathrm{Log}(\mathrm{M}_\star/\mathrm{M}_\odot) > 10$) of the relation shows a large scatter between the models, and our simulations can not constrain the SMF for $\mathrm{Log}(\mathrm{M}_\star/\mathrm{M}_\odot) > 10$, due to the limited number of galaxies predicted within the simulated volumes in this mass range.

Figure 4.3 shows that current observations start to constrain the SMF at $z < 7$, and future JWST data will provide invaluable indications on the physics of star formation and feedback to be implemented in galaxy evolution models.

4.6 Appendix B: MS comparison with other simulations

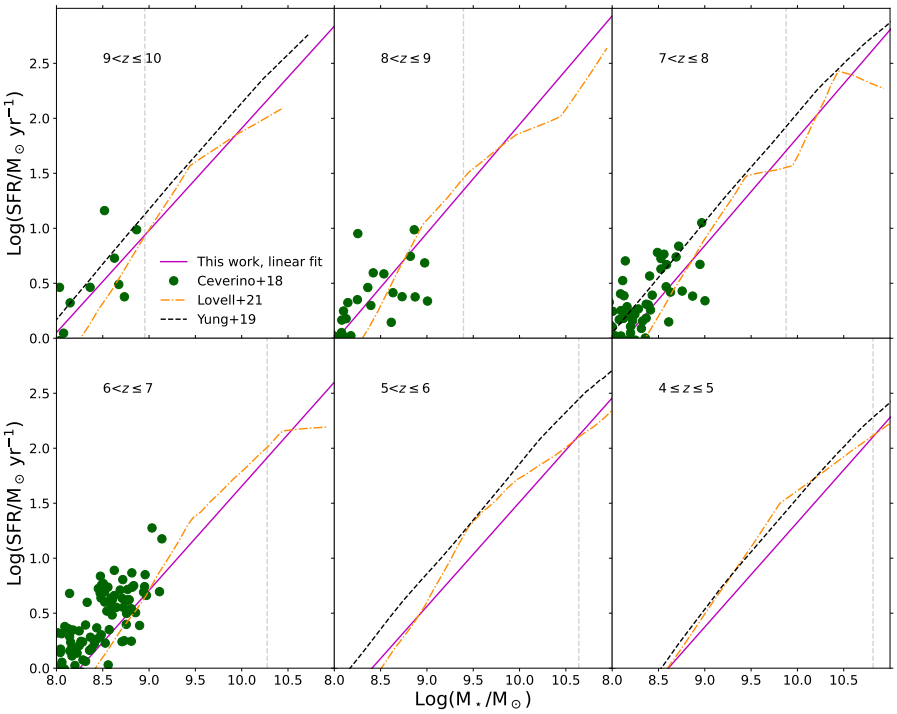

Figure 4.12. Comparison between the MS predictions from our work and other simulations. *Magenta lines* are our MS linear fit, *green dots* show galaxies from the `FirstLight` project (Ceverino et al., 2017, 2018), *dash-dotted orange lines* show the predictions from the `FLARES` simulation (Lovell et al., 2021) and *dashed black lines* are from the semi-analytic model of Yung et al. (2019).

To strengthen the reliability of our results, `dustyGadget` results are also compared with predictions from independent semi-analytical and numerical simulations. Wherever necessary, we use the conversion factors by Madau and Dickinson (2014a) to convert results based on different IMF assumptions to the Salpeter IMF (Salpeter, 1955) adopted in our simulations. In particular, we compared our predictions with the zoom-in simulations by the `FLARES` (Lovell et al., 2021) and `FirstLight` (Ceverino et al., 2017, 2018) projects. We also compare our results with the semi-analytic predictions by Yung et al. (2019), based on a slightly modified version of the Santa Cruz model to sample halos over a wide mass range. Yung et al. (2019) adopt a merger tree algorithm based on the Extended Press-Schechter formalism and, at each redshift, they set up a grid of root halos spanning a certain range in virial velocity and assign them their expected volume-averaged abundances. Finally, for each root halo in the grid, they generated one hundred Monte Carlo realizations of the merger histories. Comparing the predictions of different simulations is certainly not a straightforward task because of the different strategies each simulation adopts. Vertical dashed lines in Figure 4.12 show the $M_{\star,\max}$ found in our RefRun (U6), meaning that the fit above this mass has to be interpreted as an extrapolation. Despite their different physical assumptions and simulation techniques, a good agreement is found among model predictions at $\mathrm{Log}(M_\star/M_\odot) \leq \mathrm{Log}(M_{\star,\max}/M_\odot)$, as already discussed by Graziani et al. (2020). At larger masses, FLARES simulations find a piecewise fit to the star-forming sequence (Lovell et al., 2021), and Yung et al. (2019) find a change in slope at the high-mass end, to account for the bending seen in the sequence (Popesso et al., 2022; Sandles et al., 2022). Our simulations do not sample these high masses, and our extrapolated fit does not predict a change of slope (see also the discussion in Section 4.3.5).

Chapter 5

Carbon envelopes around merging galaxies at $z \sim 4.5$

This Chapter is based on

"Carbon envelopes around merging galaxies at $z \sim 4.5$"

Di Cesare C., Ginolfi M., Graziani L., Schneider R., Romano M., Popping G. - submitted to Astronomy&Astrophysics

Galaxies evolve through a dynamic exchange of material with their immediate surrounding environment, the so-called CGM. Understanding the physics of gas flows and the nature of the CGM is thus fundamental to studying galaxy evolution, especially at $4 \leq z \leq 6$ (i.e. at post-Reionization Epoch) when galaxies rapidly assembled their masses and reached their chemical maturity (see Péroux and Howk (2020) for a review on the baryon and metal cycles in galaxies). Galactic outflows are predicted to enrich the CGM with metals, although gas stripping in systems undergoing a major merger has also been suggested to play a role.

In this work, we explore the metal enrichment of the medium around merging galaxies at $z \sim 4.5$, observed by the ALMA-ALPINE survey. To do so, we study the nature of the [CII]158 μm emission in the CGM around these systems, using simulations to help disentangle the mechanisms contributing to the CGM metal pollution.

By adopting an updated classification of major merger systems in the ALPINE survey, we select and analyse merging galaxies whose components can be spatially and/or spectrally resolved in a robust way. In this way, we can distinguish between the [CII] emission coming from the single components of the system and that coming from the system as a whole. We also make use of the `dustyGadget` cosmological simulation to select synthetic analogues of observed galaxies and guide the interpretation of the observational results.

We find a large diffuse [CII] envelope ($\gtrsim$ 20 kpc) embedding all the merging systems, with around 50% of the total [CII] emission coming from the medium *between* the galaxies. Using predictions from `dustyGadget` we suggest that this

emission has a two-fold nature: it is due to both dynamical interactions between the galaxies which result in tidal stripped gas and the presence of star-forming satellites (currently unresolved by ALMA) that enrich the medium with heavy elements.

5.1 Introduction

The CGM is a buffer medium between interstellar and intergalactic media. It regulates gas flows, stellar feedback and, consequently, star formation activity and galaxy growth. Generally, one refers to the CGM as the gas outside the galaxy, but indicatively within one virial radius R_{vir} of its dark matter halo. However, it is important to keep in mind that some of the processes involving the CGM, for example, galactic outflows, can reach larger radii (Tumlinson et al., 2017; Faucher-Giguère and Oh, 2023). The CGM is a fundamental component in galaxy evolution, and studying it, both in emission and absorption provides hints on how galaxies assemble their masses through cosmic time. To understand the cycle of baryons between the ISM and the CGM we need observations of the stellar component and of the multiple gas phases both within and around galaxies. In this context, ALMA has recently opened a window to explore the cold neutral and molecular gas in early galaxies with unprecedented levels of detail (Capak et al., 2015; Le Fèvre et al., 2020; Bouwens et al., 2022b). On the other hand, we need simulations able to resolve the characteristic scales of CGM/ISM, which usually adopt zoom-in refinement schemes[1] (see Pallottini et al. 2017; Lupi and Bovino 2020; Lupi et al. 2020; Pallottini et al. 2022b), or cosmological boxes with a moderate ($\sim$ 100 pc) spatial resolution (see, for example, Katz et al. (2017) where the authors include on-the-fly radiative transfer and detailed non-equilibrium chemistry, to self-consistently modelling the ISM of high redshift galaxies). Finally, see Faucher-Giguère and Oh (2023) for a recent general review of the key physical processes that operate in the CGM from a theoretical point of view.

In the last decades, theories of galaxy evolution and cosmological numerical simulations have predicted that high-z galaxies assemble their masses via both cold gas accretion from the IGM (Dekel et al., 2009a; Topping et al., 2022) and major mergers i.e. dynamical interactions between galaxies of nearly equal stellar masses (Hopkins et al., 2010; Schaye et al., 2015; Duncan et al., 2019; Romano et al., 2021). In particular, dynamical interactions between galaxies can drive a significant amount of gas towards the center of the interacting system boosting the efficiency of star formation - up to a factor 2 for major mergers - and also trigger starburst and AGN activity (Oser et al. 2012; López-Sanjuan et al. 2012; Kaviraj et al. 2014; Behroozi et al. 2015; Reeves and Hudson 2023). Moreover, ongoing and post-mergers episodes can disturb and change the morphology of the galaxies involved, leading to tails of stripped material (i.e. tidal tails), irregular shapes, and disturbed velocity fields (Conselice et al., 2003, 2008; Casteels et al., 2014). Tidal tails are challenging to observe at high redshift because of the diffuse and faint nature of the stripped gas. However, thanks to ALMA we can study the efficiency of gas stripping and circumgalactic gas mixing in the early Universe, by mapping the morphology and

[1]Such as Adaptive Mesh Refinement Hummels et al. 2019; Peeples et al. 2019 and moving mesh codes van de Voort et al. 2019.

the kinematics of the CGM around merging galaxies using bright FIR lines such as the singly ionised carbon (hereafter [CII]) at 158 μm, which is generally the brightest FIR emission line for star-forming galaxies (Carilli and Walter, 2013).

[CII] 158 μm is an important tracer of the ISM in the local and high-z galaxies and, thanks to the low ionization potential (11.26 eV) of the neutral carbon, it is abundant in both the cold and warm ISM, as well as in the molecular one. Via its fine structure emission line at 158 μm ($^2P^0_{3/2} \rightarrow {}^2P^0_{1/2}$), it acts as a coolant in the cold ISM, then, it is considered as one of the main tracer of cold gas in galaxies, star-forming regions and molecular clouds. As a consequence, many studies focused on the investigation of the [CII] emission and, in particular, the [CII] - SFR relation in the local Universe and at high-redshift, using both observations (De Looze et al., 2014b; Herrera-Camus et al., 2015, 2018; Carniani et al., 2018a; Schaerer et al., 2020; Romano et al., 2022) and simulations (Katz et al., 2017; Popping et al., 2019; Ferrara et al., 2019; Lupi and Bovino, 2020; Vallini et al., 2020; Schimek et al., 2023).

Observations of [CII] in early main-sequence galaxies led to the discovery of extended [CII] *halos* (up to 10 kpc) around these systems. [CII] halos were first found by stacking the [CII] emission in 18 ALMA-detected star-forming galaxies at $5 < z < 7$ (Fujimoto et al., 2019) and in a large sample of normal star-forming galaxies at $4 < z < 6$ (Ginolfi et al., 2020b), and later confirmed, on an individual basis, by Fujimoto et al. (2020). Moreover, there is evidence of these extended halos up to $z \sim 7$, see for example Herrera-Camus et al. (2021); Fudamoto et al. (2022); Akins et al. (2022).

In this chapter, we present a study on the properties of [CII] emission around major merging systems at $z \sim 4.5$, with the aim of characterising the metal enrichment of their CGM and investigating how this depends on the dynamical interaction between the galaxies. Our target systems are drawn from the ALMA-ALPINE survey (see Section 2.2.1). The analysis of the [CII] emission has revealed a diverse distribution of morphological and kinematical properties in the ALPINE sample (Faisst et al., 2020; Jones et al., 2021), with the detection of signatures of metal-enriched gas outflows powered by star formation activity in the high-velocity tails of the stacked [CII] emission spectrum (Ginolfi et al., 2020d). Also, a detailed morpho-spectral decomposition analysis in one of the ALPINE systems undergoing major merging has revealed the presence of a widespread [CII] emission component, extending to scales of a few tens of kpc, which has been interpreted as a possible signature of processed ISM stripped by the strong gravitational interaction, suggesting that mergers could be an efficient mechanism of metal enrichment and gas mixing in the CGM around high-z galaxies (Ginolfi et al., 2020c; Jones et al., 2020).

Motivated by these findings, we apply a similar morpho-spectral decomposition analysis on additional systems classified as mergers in the ALPINE sample. To this aim, we make use of the merger classification of ALPINE galaxies carried out by Romano et al. (2021). The observational part of this work is complemented with predictions from cosmological simulations run with the hydrodynamical code `dustyGadget` (Graziani et al., 2020), which guide our interpretation of the results.

The chapter is organised as follows: in Section 5.2 we describe the selected observational sample and the analysis we carried out; Section 5.3 presents the [CII] diffuse emission that we find in the observed candidates, and its interpretation; in Section 5.4 we introduce the hydrodynamical code (`dustyGadget`), explain the

Table 5.1. Physical parameters of the major merging galaxies selected for this work. Together with the source ID and redshift estimates for both the components of the merger (z_1 and z_2), we also include the velocity offset (Δv) and projected distance (r_p) between the merger components and the [CII] flux ratio ($\mu_{[CII]}$) and K_s band flux ratio (μ_K) (Romano et al., 2021). The last two columns include the estimates for stellar masses and star formation rates for the entire merging system as estimated by Faisst et al. (2020) (see their paper for details on the photometry and SED fitting procedure), once we converted the IMF from Chabrier (2003b) to Salpeter (1955).

source ID	z_1	z_2	Δv [km/s]	r_p [kpc]	$\mu_{[CII]}$	μ_K	$\mathrm{Log}(M_\star/M_\odot)$	$\mathrm{Log}(SFR/M_\odot yr^{-1})$
DC_818760	4.5626	4.5609	92.3	9.9	1.3	2.6	$10.85^{+0.11}_{-0.10}$	$2.88^{+0.19}_{-0.25}$
DC_873321	5.1545	5.1544	4.5	6.5	1.2	3.1	$10.18^{+0.13}_{-0.16}$	$2.16^{+0.22}_{-0.17}$
vc_5100541407	4.5628	4.5628	1.9	13.8	1.6	1.4	$10.33^{+0.14}_{-0.15}$	$1.74^{+0.26}_{-0.23}$
vc_5100822662	4.5210	4.5205	22.3	10.9	1.6	1.7	$10.39^{+0.13}_{-0.14}$	$2.02^{+0.23}_{-0.24}$
vc_5101209780	4.5724	4.5684	217.3	10.8	4.1	2.5	$10.27^{+0.12}_{-0.12}$	$1.79^{+0.25}_{-0.21}$
vc_5180966608	4.5294	4.5293	8.9	7.2	3.0	3.7	$11.04^{+0.12}_{-0.13}$	$2.35^{+0.27}_{-0.25}$

adopted procedure to identify synthetic major mergers, their time evolution, and their gas distribution. Finally, we exploit the predictions from `dustyGadget` to interpret the observed [CII] diffuse emission, in Section 5.5. Our conclusions are drawn in Section 5.6.

Throughout this work, we assume a flat ΛCDM cosmology with cosmological parameters from Planck Collaboration et al. (2016) consistent with that assumed by `dustyGadget` simulation (see Section 5.4) and adopt a Salpeter (1955) IMF. All the stellar masses and star formation rates in this chapter have been converted to a Salpeter (1955) IMF following the conversion factors from Madau and Dickinson (2014b). At $z \sim 4.6$ - that is the mean redshift of our sample - 1 arcsecond corresponds to 6.69 proper kpc.

5.2 Observational sample and data processing

In this section we first briefly introduce the ALPINE survey and the properties of the target galaxy sample; and then discuss the classification done by Romano et al. (2021) on merging systems, and how we selected - among these - major mergers needed for the aim of this work. Finally, we describe the ALMA data reduction procedure and the analysis we performed on our sample of major merging galaxies.

5.2.1 Targets selection

ALPINE is an ALMA large program designed to detect the [CII] line at 158 μm rest-frame and the surrounding FIR continuum emission for a sample of 118 normal galaxies at $4.4 < z < 5.9$. ALPINE targets are selected from the Cosmic Evolution Survey (COSMOS; Scoville et al. 2007a,b) and Extended Chandra Deep Field South (E-CDFS; Giavalisco et al. 2004; Cardamone et al. 2010) fields. In the following, we use "vc" and "DC" to respectively refer to vuds_cosmos and DEIMOS_COSMOS sources. Since these fields have been targeted by several observational campaigns, a

wealth of ancillary multi-wavelength photometric data (from rest-frame UV to FIR) is available, which made it possible to recover physical properties such as stellar masses and SFRs through SED-fitting; these estimates have been performed adopting a Chabrier IMF (Chabrier 2003b, see Faisst et al. 2020 for a detailed description). With stellar masses in the range $9 \leq \mathrm{Log}(\mathrm{M}_\star/\mathrm{M}_\odot) \leq 11$ and star formation rates of $1 \leq \mathrm{Log}(\mathrm{SFR}/\mathrm{M}_\odot\mathrm{yr}^{-1}) \leq 3$, ALPINE galaxies lie on the so-called main sequence of star-forming galaxies (Rodighiero et al., 2011; Tasca et al., 2015), being thus representative of the underlying galaxy population at $z \sim 5$ (Speagle et al., 2014) - a detailed description of the survey and its main results can be found in Section 2.2.1.

To study the metal enrichment of the CGM around high-z merging galaxies we exploit the work of Romano et al. (2021), who combined the morpho-kinematic information provided by the [CII] emission with archival multi-wavelength photometry to identify merging systems in the ALPINE sample, and the fraction of major mergers within this subset (see also Le Fèvre et al. 2020; Jones et al. 2021). According to their classification criteria, Romano et al. (2021) found that the ALPINE sample is composed of 31% of mergers (23 out of 75 [2]), leading to a major merger fraction of MM ~ 0.44 (0.34) at $z \sim 4.5$ (5.5). This result is in good agreement with morphological studies by Conselice and Arnold (2009) at the same redshift and, when combined with other works down to the Local Universe, suggests a rapid increase in the cosmic merger fraction from $z = 0$ to $z \sim 2$, a peak at $z \sim 2 - 3$ and a possible slow decline for $z \geq 3$.

For the aim of this study, starting from the classification by Romano et al. (2021), we selected major merging systems that are spatially and/or spectrally separated in a robust way. In particular, we looked for merging systems with:

1. a velocity separation $\Delta v \leq 500\,\mathrm{km/s}$, so that the two systems can be considered as gravitationally bound (see Patton et al. 2000; Lin et al. 2008; Ventou et al. 2017);

2. a projected distance $r_\mathrm{p} > 4\,\mathrm{kpc}$, where $r_\mathrm{p} = \theta \times d_\mathrm{A}(z_m)$, θ is the angular separation in arcsec in the sky between the two galaxies, and $d_\mathrm{A}(z_m)$ is the angular diameter distance (in $\mathrm{kpc\,arcsec}^{-1}$) calculated at the mean redshift z_m of the two sources (see Romano et al. 2021 for more details). With this condition, the projected distance between the merging systems is larger than the typical [CII] size of individual galaxies, which on average is estimated to be ~ 2.1 kpc for ALPINE galaxies at these redshifts (Fujimoto et al., 2020; Romano et al., 2021). Indeed, closer components could just be clumps of star formation within the same galaxy, affecting the morphology and kinematics of [CII] emission;

3. a relative stellar mass ratio of $1 < \mu_\mathrm{K} < 4$. Here μ_K is defined as the ratio between the UltraVista $\mathrm{K_s}$-band fluxes of the merging components[3], which is

[2] Among the 118 main sequence galaxies of the ALPINE sample, 75 are detected in [CII] at S/N > 3.5 (Béthermin et al., 2020c)

[3] In general, μ can be defined as :

$$\mu = X_1^i / X_2^i \tag{5.1}$$

where X_1^i and X_2^i are the physical properties (X^i = stellar mass; [CII] fluxes; $\mathrm{K_s}$-band fluxes) of the primary and secondary galaxy, with $X_1^i > X_2^i$.

used as a proxy for the mass ratio of galaxies (hereafter, $\mu_K \equiv \mu_\star$) since the K_s-band flux is a good tracer of the stellar mass of galaxies up to z $\sim$ 4 (Laigle et al., 2016).

We shall note that the K_s-band ratio is available for 9 out of 23 merging systems; for the other 14 systems, only the [CII] flux ratio, $\mu_{[CII]}$, is available, from which Romano et al. (2021) cannot draw conclusions about the nature of the merger (see their Section 4 for more details). By taking this into account and applying the previously mentioned criteria to the merging systems with K_s-band ratio estimates, for which the nature of the merger is known, we end up with a sample of six targets.

Table 5.1 lists the 6 observational targets selected for our study, and summarizes their merging properties (Δv, r_p, $\mu_{[CII]}$, K_s; Romano et al. 2021) and their stellar masses and SFRs as estimated by Faisst et al. (2020).

5.2.2 Observational analysis

In this section, we describe processing and analysis performed on the major merging systems whose properties have been reported in Table 5.1.

Firstly, we reduce the ALMA data for these targets using the Common Astronomy Software Applications (CASA; McMullin et al. 2007) pipeline. Each data cube is continuum-subtracted using the CASA task `uvcontsub` over the line-free visibilities in all spectral windows to obtain line-only cubes. The [CII] datacubes are generated from the continuum-subtracted visibilities using the task `tclean` until we reach a S/N $<$ 2 for the residuals. We choose a natural weighting of the visibilities to maximize the sensitivity, a common pixel size of 0.15", and a common spectral bin of 25 km s^{-1} (beam size of $\sim$ 1").

Secondly, we visually inspect ALMA datacubes, looking for [CII] emissions coming from the components of each merging system. Every time we find such an emission, we adopt a 1" aperture centered on the emitting galaxy to extract a preliminary [CII] spectrum, which is then fitted using a single 1D Gaussian model.

Finally, we consider the 2σ confidence interval of the Gaussian fit to get the min-max frequency range that we collapse to generate the moment-0 (i.e. velocity integrated) maps of each merging component (dubbed as #A, #B, etc) using the CASA `immoments` task. The moment-0 map of the entire system is then obtained by collapsing the absolute minimum and maximum of the previously obtained frequency (i.e. $min[\min^{A}_{freq}, \min^{B}_{freq}]$ and $max[\max^{A}_{freq}, \max^{B}_{freq}]$).

Figure 5.1 shows the total velocity-integrated [CII] maps for our sample; white contours indicate the 2σ [4] region and black crosses are the centers of each emitting component (see procedure described in the following), and all the S/N are consistent with those of the ALPINE survey (Béthermin et al., 2020c). Having the moment-0 maps we then fit a single 2D Gaussian model to each merging component, masking it, and retrieving morphological information such as the coordinates of the [CII] emission peak, the FWHM of the major and minor axis of the Gaussian and its position angle (PA). For one system, DC_873321, we had to perform a two 2D Gaussian components fit, because of the little spatial separation and similar [CII] luminosity ($\mu_{[CII]} \sim 1$; see Table 5.1) of the merging galaxies, which prevent us from fitting single

[4] computed as the standard deviation in the total moment-0 map once we mask the source.

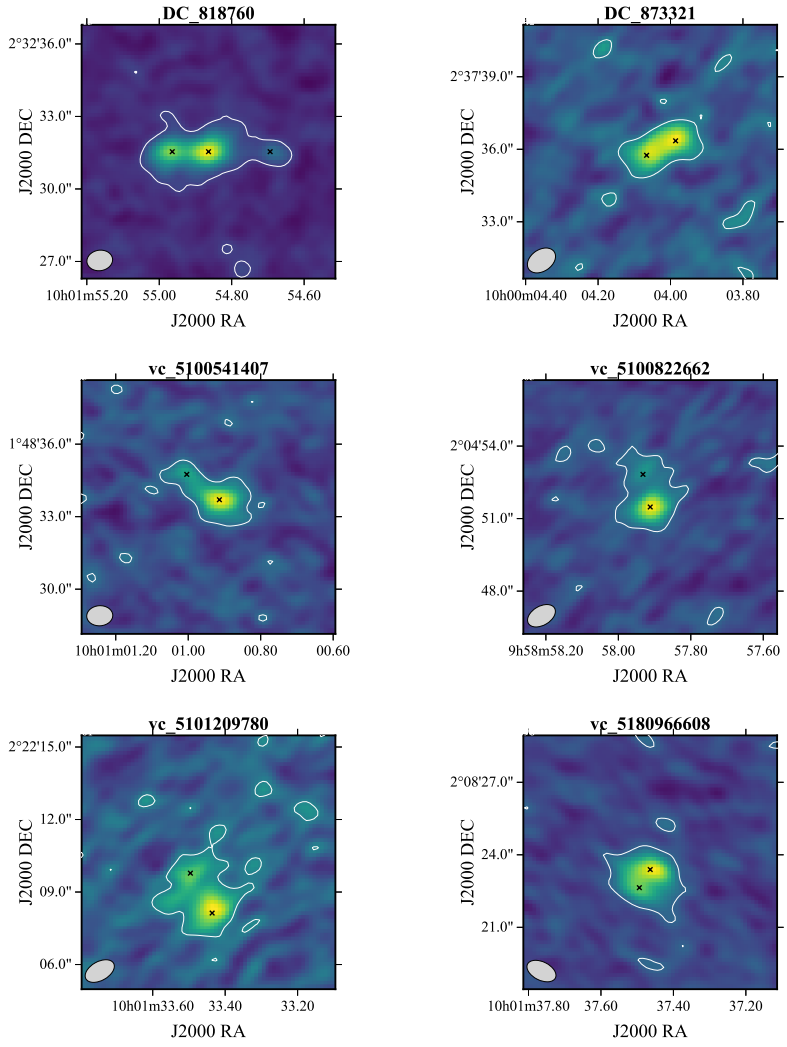

Figure 5.1. Total velocity integrated [CII] map of the six selected systems. On top of each panel is the ID of the source. White contours indicate the positive significant level at 2σ of [CII] emission. Black crosses mark the center of each galaxy (see the text for more information). The ALMA beam size is given in the bottom-left corners.

2D Gaussian models. Once we estimate the coordinates of the [CII] emission peaks of each source, we use it to center different size apertures. In particular, we employ a 1" aperture, a 2x2 pixel square aperture (hereafter "*peak*"), and $\mathrm{FWHM_x} \times \mathrm{FWHM_y}$ aperture (hereafter "*optimal*") - with x and y being respectively the major and minor axis of the 2D Gaussian model. From these apertures, we extracted the [CII]

emission fluxes in mJy km s^{-1}. In doing this analysis we assume that all the [CII] emission coming from these apertures is associated with the merging galaxies, while that coming from the 2σ contour is the total emission (galaxies + diffuse [CII] halo).

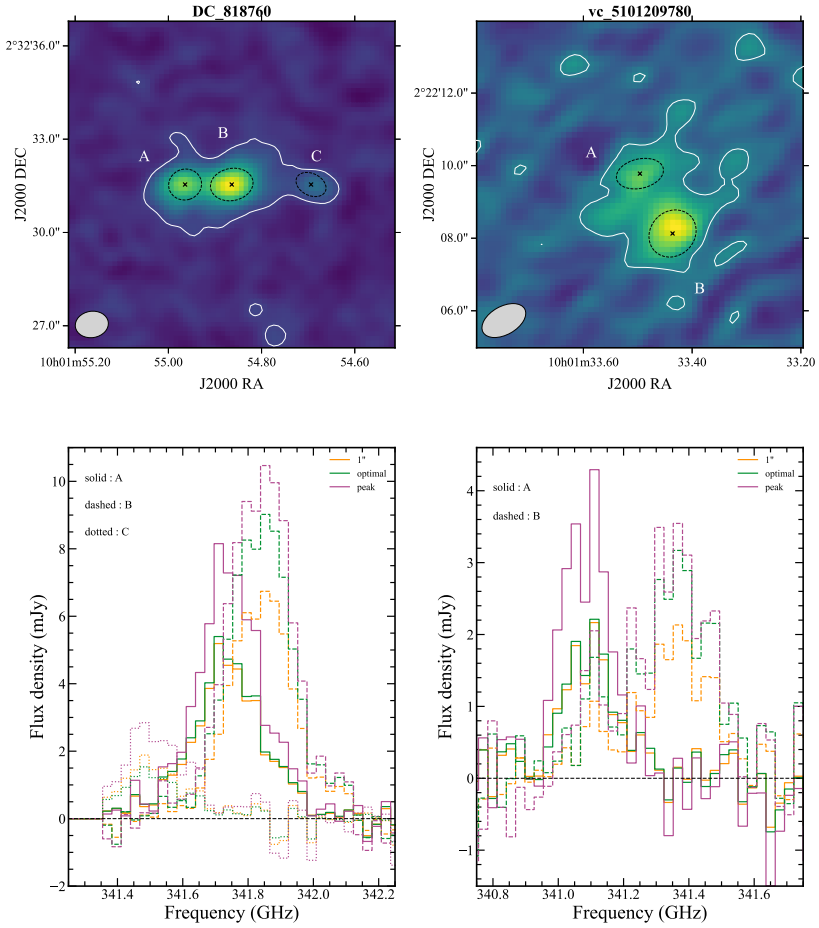

Figure 5.2. *Upper panel:* Same as Figure 5.1, but for two specific systems: (a) DC_818760 (left) and (b) vc_5101209780 (right). The white contour indicates the positive significant level at 2σ of [CII] flux, where $\sigma_{[CII]} = 84$ mJy km/s in (a) and $\sigma_{[CII]} = 95$ mJy km/s in (b). The dashed black ellipses indicate the $FWHM_x \times FWHM_y$ regions obtained by 2D Gaussian models and correspond to the apertures used to extract the optimal [CII] spectra of (a) and (b); finally, the black crosses mark the center of each ellipse (i.e. the center of each galaxy). The ALMA beam size is given in the bottom-left corners. *Lower panel:* [CII] spectra for each component of the merging system (different line styles) extracted using 1" (orange), optimal (FWHM, green), and peak apertures (pink).

Figure 5.2 shows, in the upper panels, the total velocity-integrated [CII] maps for two systems highlighting the optimal apertures for each merging component (dashed black lines), the center of each galaxy (black crosses) and the 2σ regions (white contours) and, in the lower panels, the [CII] flux density. In particular, different line styles correspond to each merging component, while different colors (orange, green, and pink) to line spectra extracted considering 1", *optimal* and *peak* apertures

respectively. Looking at the spectra we note that the brightest emission is the one coming from the *peak* aperture (pink) i.e. the center of each galaxy, while 1" and *optimal* apertures in some cases have comparable emissions (see for example component #A of both DC_818760 and vc_5101209780).

The merging system DC_818760 is the only triple merger in our sample. The bottom left panel of Figure 5.2 shows that the emission coming from component #C is $\sim$ 4 and 5 times dimmer than the one coming from components #A and #B respectively. The major merger is indeed happening between galaxies #A and #B, which are closely associated both spatially and in velocity, while #C is identified as an upcoming minor merger (see Jones et al. 2020 for a detailed discussion about this system).

Finally, Figure 5.3 shows the [CII] emission arising from the total system (black) together with the sum of the emissions arising from each component of the merging system when we adopt an *optimal* aperture (green). The difference between these two emissions (green hatched area) can be interpreted as due to the diffuse [CII] envelope around the galaxies. Already in Ginolfi et al. (2020c) the authors analysed in detail the merging system vc_5101209780, finding that about 50% of the total [CII] emission arises from a gaseous envelope distributed between the individual components of the system.

From the analysis of the observational sample used in this work we not only confirm the conclusion by Ginolfi et al. (2020c), but also extend this result to a larger sample of 5 additional ALPINE major merging systems, finding that an important fraction of the total [CII] emission arises from the diffuse gas *between* the galaxies, as qualitatively shown in Figure 5.3.

Notice that DC_873321 is the system with the least [CII] emission associated with the diffuse component, according to Figure 5.3 (top right panel), and it is also the only system where we had to perform a two components 2D Gaussian fit instead of two *single* component 2D Gaussian models (see previous discussion). Because of the difficulty in separating the emission from the galaxies and that of the surrounding medium, it is likely that part of the [CII] emission from the diffuse halo is instead wrongly associated with the individual components of the system. Also, note that systems in which is more difficult to separate the components may be in a more advanced phase of the merger (i.e. a closer interaction).

5.3 [CII] emission from the CGM

In this section, we investigate the amount of [CII] emission arising from the diffuse halo in a more quantitative way, in order to identify possible trends between the diffuse emission and the physical properties of the merging galaxies, such as their [CII] luminosity ($L_{[CII]}$), stellar mass ($M_\star$) and SFR. We also explore possible trends between the fraction of [CII] emission associated with the diffuse component, or inner CGM of the galaxies, and the relative properties of the merging systems, such as the projected distance between the centers of merger components (r_p), mass ratio ($\mu_\star$), and [CII] luminosity ratio ($\mu_{[CII]}$). Indeed, these trends can give us hints about the nature of the diffuse [CII] halo we observe, helping us to understand if this originates from metal-enriched gas outflows, from tidally stripped material during

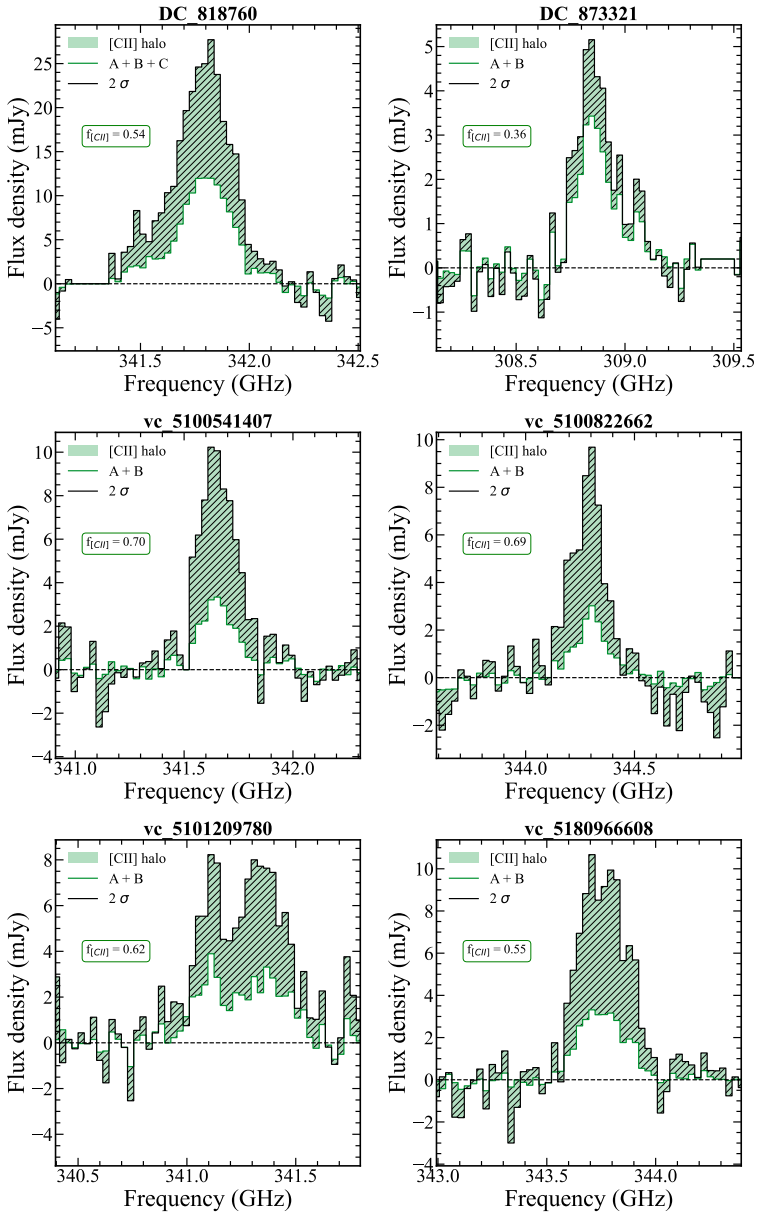

Figure 5.3. The [CII] flux density in mJy as a function of frequency (GHz) for the galaxies in our sample. Black lines are the total [CII] emission arising from the full system (galaxy + diffuse [CII] halo) and green solid lines are the sum of the emissions coming from each component of the merging system when we consider the optimal aperture, $\mathrm{FWHM_x} \times \mathrm{FWHM_y}$. Green hatched areas show the emission coming from the diffuse [CII] halo and the [CII] fraction is in green boxes (see Section 5.3 for the definition of this quantity and discussion).

the gravitational interaction between the merging galaxies, and/or it pertains to small satellites lying around the merging galaxies (see discussion in Ginolfi et al. 2020c).

In order to estimate the *total* [CII] fluxes in Jy km/s we extract the spectrum from the 2σ region and fit it using a single Gaussian model. We then convert the measured fluxes in [CII] luminosity following the relation (Solomon et al., 1992; Carilli and Walter, 2013):

$$\mathrm{L_{[CII]}} = 1.04 \times 10^{-3}\ \mathrm{F_{[CII]}}\ D_L^2(z)\ \nu_{obs}(z) \tag{5.2}$$

where $\mathrm{L_{[CII]}}$ is in $\mathrm{L_\odot}$, $D_L(z)$ is the luminosity distance (in Mpc) at the redshift of the merging system and $\nu_{obs}(z)$ is the observed frequency of the [CII] line (in GHz). We dub the total luminosity of the merging system $\mathrm{L^{2\sigma}_{[CII]}}$, and we estimate the error associated with this luminosity as $\sqrt{\mathrm{N}} \times$ rms of the moment-0 map, where N is the number of ALMA beams enclosed in that region. To quantify the emission associated with the individual merging galaxies, we extract the spectra of each component using three different apertures centered on each galaxy (see Section 5.2.2 for a description of the adopted method). For a fixed aperture, we sum together the spectrum of each component and integrate it into the 2σ confidence interval found before. Using Equation 5.2, we obtain the luminosity coming from the galaxies for each of the three apertures, $\mathrm{L^i_{[CII]}}$, where i = 1", *optimal*, *peak*; the error associated with the luminosity coming from these apertures is the rms of the moment-0 map, since the apertures are comparable to the ALMA beam.

Having estimated the total [CII] luminosity of the merging system and the luminosity coming from the galaxies, we compute the [CII] emission coming from the diffuse halo as:

$$\mathrm{L^{diffuse,i}} \equiv \mathrm{L^{2\sigma}} - \mathrm{L^i} \tag{5.3}$$

where we have dropped the subscript [CII]. We also define the fraction of [CII] emission coming from the inner CGM of the merging system (hereafter, $\mathrm{f_{[CII]}}$) as:

$$\mathrm{f^i_{[CII]}} \equiv \frac{\mathrm{L^{diffuse,i}}}{\mathrm{L^{2\sigma}}}. \tag{5.4}$$

Figure 5.4 shows the relation between $\mathrm{L^{diffuse}}$ and some integrated properties of the system, such as the total [CII] luminosity, star formation rate, and stellar mass of the entire merging system listed in Table 5.1 (see Faisst et al. 2020 for the discussion on photometry and SED fitting procedure). For each of these relations, we compute the Spearman coefficient, ρ, to see how reliable the suggested trend is: if $\rho \sim 1$ a strong correlation between the quantities is present, while for $\rho \sim -1$ there is a strong anti-correlation. Finally, although we report the results obtained for each of the three apertures, we mainly draw our conclusions by looking at the trends suggested when the emission from the galaxies is computed in the *optimal* case, which provides the cleanest separation between the galaxy and the diffuse components.

The figure shows that there is a strong positive correlation ($\rho = 1$) between the [CII] luminosity of the diffuse halo and the total [CII] luminosity of the system, suggesting that the diffuse component is an important component of the total luminosity of the merging systems. We shall note that this conclusion depends on the chosen aperture used to estimate the luminosity of the galaxy, and the above interpretation applies when the optimal aperture is adopted. Indeed, for the peak aperture, one would infer that the diffuse component provides 100% of the

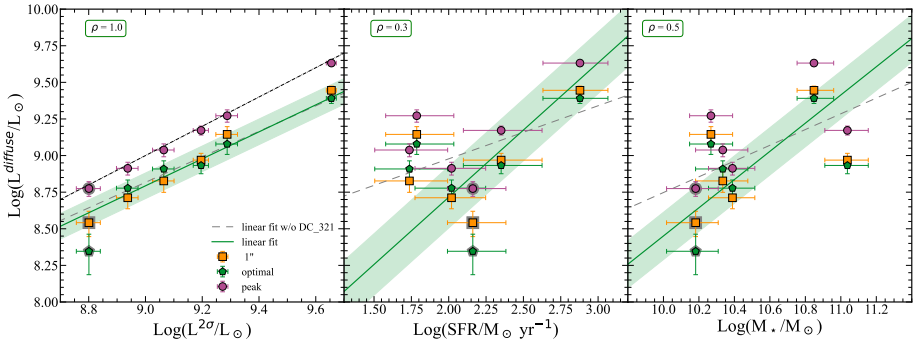

Figure 5.4. Trends between the [CII] luminosity coming from the diffuse halo around merging systems, $L^{\rm diffuse}$, and their integrated physical properties. Different colors refer to different apertures adopted to extract the emission from the merging galaxies, L^{i}, with $i = 1$" (orange), *optimal* (FWHM, green), and *peak* (pink). In each panel, the green solid line and shaded areas are respectively the linear fit and the associated error when adopting the optimal aperture, and we also report the Spearman coefficient (ρ) of the analysed relation. *Left:* $L^{\rm diffuse}$ is shown as a function of the total luminosity coming from the 2σ region, $L^{2\sigma}$. The black dot-dashed line is the 1:1 relation. *Middle and Right:* $L^{\rm diffuse}$ as a function of the total SFR and total stellar mass of the merging systems (see Table 5.1). Highlighted in gray is DC_873321, see the main text for the discussion on this candidate, and the gray dashed line is the linear fit without taking into account DC_873321.

total luminosity of the system, see the pink data points in the left panel and their proximity to the gray diagonal lines which shows the 1:1 relation. This result is a direct consequence of the definition of the *peak* case.

We also find a tentative ($\rho = 0.3$) relation between the diffuse [CII] luminosity and the SFR of the system, and a stronger positive correlation ($\rho = 0.5$) between $\rm L^{diffuse}$ and the stellar mass of the system (see the middle and right panels of Figure 5.4). These results provide some tentative indications of the origin of the metal-enriched gas powering the diffuse [CII] luminosity. In fact, stronger gas outflows are expected in more star-forming systems (Ginolfi et al., 2020c), while more massive galaxies trace the possible presence of small unresolved satellite galaxies and/or a stronger dynamical interaction between the merging components and are associated with more SF galaxies resulting in a greater outflows activity. The tentative trends found so far suggest that the inner CGM is polluted with heavy elements by means of outflows, dynamical interactions, and small star-forming satellites. In particular, we can assume that stripping mechanisms have a dominant role in this scenario as we observe a more extended [CII] halo in interacting systems compared to non-interacting galaxies with similar SFRs - thus with comparable outflows activity. This conclusion is also supported by the relation between $\rm f_{[CII]}$ and $\mu_{\star}$ (see Figure 5.5 and its discussion) which suggests that systems with the strongest gravitational interaction, i.e. $\mu_{\star}$ closer to unity, have a higher fraction of [CII] emission coming from the diffuse halo.

In Figure 5.5 we further explore the dependence of the fraction of [CII] emission coming from the inner CGM of the merging systems, $\rm f_{[CII]}$, and the properties of

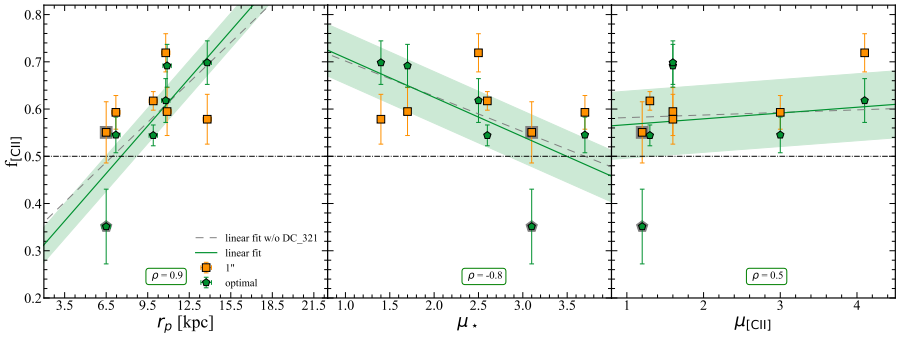

Figure 5.5. Trends between the fraction of [CII] emission coming from the inner CGM ($f_{[CII]}$, see Equation 5.4) and the properties of the merging systems, such as the projected distance (r_p) between the galaxies (*Left*), the stellar mass ratio ($\mu_\star$, *Middle*), and the [CII] emission ratio ($\mu_{[CII]}$, *Right*). We show the results obtained when adopting different apertures (1" in orange, and optimal in green) needed to define the [CII] emission associated with each component of the merger. In each panel, the green solid line and shaded areas are respectively the linear fit and the associated error when adopting the optimal aperture, and we specify the Spearman coefficient (ρ) of the corresponding relation. The horizontal dot-dashed black line indicates the 0.5 value, the system DC_873321 is highlighted in gray (see text for discussion on it) and the gray dashed line is the linear fit without DC_873321.

the merging pairs, such as the projected distance (r_p) between the galaxies, the stellar mass ratio, and the [CII] emission ratio. In each panel, the green solid line and shaded areas are respectively the linear fit and the associated error when adopting the optimal aperture, and we specify the Spearman coefficient (ρ) of the corresponding relation. In Figure 5.5 we do not include the peak aperture as we obtain $f_{[CII]} \sim 0.95$ in all the systems given that, in this case (i.e. unresolved merging galaxies), most of the [CII] emission is associated with the inner CGM.

From this figure, we note that the fraction of [CII] emission coming from the inner CGM of the merging system is in the range $f_{[CII]} \simeq 0.3 - 0.7$ for the systems we have analysed, the black horizontal line corresponds to $f_{[CII]} = 0.5$. On average, we find that $\simeq 55$ % of the [CII] emission of the merging systems comes from the inner CGM, confirming what was previously found by Ginolfi et al. (2020c) for the system vc_5101209780 alone, and quantifying the emission we found looking at the spectra in Figure 5.3 (green hatched area). The left panel of Figure 5.5 indicates that there is a strong positive correlation ($\rho = 0.9$) between $f_{[CII]}$ and r_p, meaning that merging systems with larger projected separations appear to have a larger $f_{[CII]}$ compared to systems with smaller r_p, where a clean separation between the emission coming from the diffuse component and that coming from the galaxies is more challenging. However, it could also be that galaxies that are interacting for a longer period of time result in a more carbon-rich envelope (see Appendix 5.8). Note that to investigate this possibility we need to have information on the time evolution of the system, which is beyond the scope of the present work.

We also find an anti-correlation ($\rho = -0.8$) between the fraction of [CII] emission coming from the inner CGM and the mass ratio of the galaxies: the larger $\mu_\star$ the

smaller $f_{[CII]}$. This may suggest that the dynamical interaction between mergers where galaxies have similar masses ($\mu_\star \sim 1$) results in stronger tidal stripping and, as a consequence, in a more polluted CGM. Finally, we analyzed the relation between $f_{[CII]}$ and $\mu_{[CII]}$ (right panel), finding a mild correlation, $\rho = 0.5$, which suggests that the fraction of [CII] emission from the diffuse halo does not depend on the ratio between the $L_{[CII]}$ associated with the galaxies.

We shall note that the system that appears to be an outlier and is highlighted in gray in Figure 5.4 and Figure 5.5, is DC_873321. This system is the only one for which we had to perform a two 2D Gaussian components fit instead of two *single* 2D Gaussian models (see Section 5.2.2), because of the difficulty in separating the emission from the galaxies and that of the diffuse halo; hence, it might be that part of the [CII] emission from the diffuse halo is wrongly associated with the galaxies, and this could partially explain the fact that DC_873321 does not follow the trends that we infer for the rest of the sample. To investigate if this different procedure changes our results, we perform the same analysis as before excluding DC_873321. We find that in this case the mean [CII] fraction goes up to ~ 60 %, suggesting a larger [CII] emission from the diffuse medium between galaxies. Also, in Figure 5.4 and Figure 5.5 we show in gray dashed lines linear fits once we exclude DC_873321 from the analysis. Looking at these figures we notice that we recover very similar trends in all the panels, with the exception of the relation with SFR and $M_\star$, where we find a shallower trend. In addition, Spearman coefficients in this case suggest a stronger correlation between $L^{diffuse}$ and SFR ($\rho = 0.5$), while milder correlations - $\rho \sim 0.15$ - for both $L^{diffuse}$ - $M_\star$ and $f_{[CII]}$ - $\mu_{[CII]}$. We can conclude that even taking into account the different procedures we apply in the analysis of one observed system, the interpretation and conclusions drawn so far still stand.

To summarize, our observational analysis shows that a consistent part ($\gtrsim 55\%$) of the [CII] emission of major merging galaxies identified in the ALPINE survey originates from a diffuse gas envelope around the merging galaxies or inner CGM. Also, we find tentative trends between the emission arising from the diffuse halo and the physical properties of the merging systems, which provide some indication of the possible mechanisms that are responsible for the presence of a diffuse metal-enriched cold gas component surrounding these galaxies, such as small satellite companions, gravitational interaction resulting in tidal stripping and outflows activity.

In the next section, we compare the above findings and observational sample with synthetic merging systems at similar redshift selected from a cosmological hydrodynamical simulation, to gain a more in-depth understanding of the physical processes shaping the origin and metal enrichment of their CGM.

5.4 Comparison with simulations

5.4.1 `dustyGadget`

In this section, we provide a synthetic summary of the key features of the cosmological hydrodynamical code `dustyGadget`, and we refer the interested reader to Graziani et al. (2020) and Chapter 3 for a detailed description of the code, as well as Chapter 4, Di Cesare et al. (2023); Venditti et al. (2023a,b) for its latest results.

`dustyGadget` is an extension of the particle-based SPH code `Gadget-2/3` (Springel,

2005; Springel et al., 2021) which provides a self-consistent implementation of dust production and evolution, on top of the improvements to the chemical evolution module by Tornatore et al. (2007b,a), and to molecular chemistry and cooling by Maio et al. (2009a). In particular, the gas chemical evolution scheme is inherited from Tornatore et al. (2007b): it follows the metal release from stars of different masses, metallicity, and lifetimes. Yields depending on mass and metallicity are implemented for both PopII and PopI stars and stars with masses $\geq 40\,\mathrm{M}_\odot$ are assumed to collapse into black holes and do not contribute to metal enrichment. PopIII stars with masses inside the range $140\,\mathrm{M}_\odot \leq \mathrm{M}_\star \leq 260\,\mathrm{M}_\odot$ are expected to explode as PISN, while those with masses outside the PISN range are assumed to collapse into black holes. We warn the reader that the formation of AGN is not modeled in our simulations, thus we do not account for mechanical or radiative feedback from accreting nuclear black holes. Following Maio et al. (2009a), the chemical network in `dustyGadget` also includes the evolution of both H and H^+, He, D, and primordial molecules by relying on the standard `Gadget` implementation of the cosmic UV background as a photo-heating mechanism, first introduced by Haardt and Madau (1996a). The IMF of the stellar populations, each represented by stellar particles, is assigned according to their metallicity $\mathrm{Z}_\star$, given a gas critical metallicity $\mathrm{Z}_{\rm crit} = 10^{-4}\,\mathrm{Z}_\odot$, where $\mathrm{Z}_\odot = 0.02$ (Grevesse and Anders, 1989). When $\mathrm{Z}_\star < \mathrm{Z}_{\rm crit}$ we adopt a Salpeter IMF (Salpeter, 1955) in the mass range $[100-500]\,\mathrm{M}_\odot$; otherwise, the stars are assumed to form according to a Salpeter IMF in the mass range $[0.1-100]\,\mathrm{M}_\odot$.

The production of dust grains by stars in SN explosion and AGB stellar winds is described by means of a set of mass- and metallicity-dependent yields (Bianchi and Schneider, 2007; Marassi et al., 2014, 2015; Bocchio et al., 2016b; Ginolfi et al., 2018b; Graziani et al., 2020; Pizzati et al., 2020; Romano et al., 2023), which closely follow the chemical network adopted for metal yields Tornatore et al. (2007b). Once the grains produced by stars are released in the ISM, they can undergo diverse physical processes that can alter their mass, relative abundances, chemical properties, charge, and temperature. Generally, it is assumed that the dust-to-light interactions (e.g. photo-heating, grain charging) change the thermodynamic and electrical properties of the grains (see for example Glatzle et al. 2019b, 2022b), but these processes have a negligible impact on the total dust mass unless the grain temperatures reach the sublimation threshold ($\mathrm{T}_{\rm d,s} \gtrsim 10^3$ K). Other physical processes (i.e. sputtering and grain growth) can alter the total dust mass and the grain size distribution (Draine, 2011; Aoyama et al., 2020). The spreading of dust grains and atomic metals in the ISM, CGM, and IGM is done through galactic winds, which are modeled with an initial velocity of 500 km/s, following typical outflow velocities observed in main sequence galaxies at $z \gtrsim 4$ (Gallerani et al., 2018; Sugahara et al., 2019; Ginolfi et al., 2020d). Finally, the identification of DM halos and their substructures is performed in post-processing with the AMIGA halo finder (see Section 3.2.3).

In this work we make use of *one* of the eight statistically independent cosmological simulations (U6-U13) which have been analysed in Di Cesare et al. (2023), where we have investigated the redshift evolution of the SFR, stellar mass density, stellar mass function, and galaxy scaling relations, at $z \geq 4$, comparing our results with observational data.

The physical setup of the runs and simulated cosmic volumes are the same as in

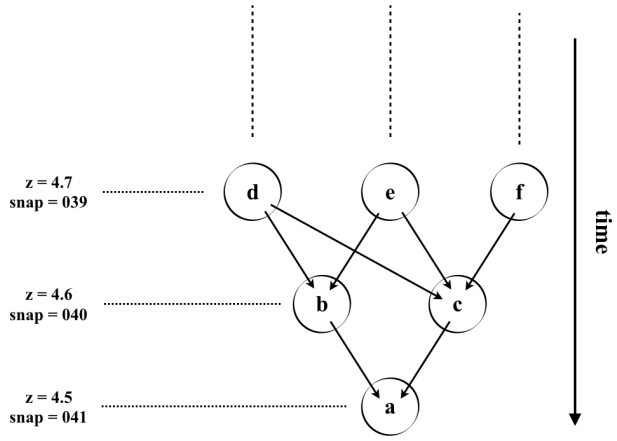

Figure 5.6. Illustration of an example of merger tree reconstruction. Starting from galaxy "a" at z = 4.5 (snap = 041), its progenitors at the previous snapshot are "b" and "c". Merger trees have been reconstructed for each of all simulated galaxies at $z = 4.5$ with masses $M_\star \geq 10^{10} M_\odot$, up to $z = 5.1$ (snap = 035). This allows us to reconstruct the mass assembly history of the simulated galaxies, identifying those systems that undergo major mergers, defined as galaxy interactions where the relative stellar mass ratio of the merging pair is $1 < \mu_\star < 4$ (see text).

Di Cesare et al. (2023); in particular, we consider a cubic volume with $50\mathrm{h}^{-1}$ cMpc (~ 74 cMpc) side length, with 2×672^3 particles, corresponding to a mass resolution of $5.2 \times 10^7\,\mathrm{M}_\odot$ for DM particles, and of $8.2 \times 10^6\,\mathrm{M}_\odot$ for gas particles. Using the current version of `dustyGadget` we can resolve down to the scale of a giant molecular cloud (a few tens up to hundreds pc), but for the purpose of this work, we are only interested in scales of the order of tens kpc.

In the following, whenever we refer to units we mean *physical* one, unless otherwise stated.

5.4.2 Identifying galaxy mergers

In Di Cesare et al. (2023) we already compared the integrated properties (SFR, $\mathrm{M}_\star$, $\mathrm{M}_{\mathrm{dust}}$) of our synthetic galaxies with those observed in the ALPINE survey, finding a remarkable agreement between the two (see for example their Figure 3 and Figure 8).

In this work, we start from the galaxy catalogues generated by the simulation and select synthetic merging galaxies whose physical, integrated properties resemble the observed ones, as described in Section 5.2.1. We analyse the simulation snapshots (hereafter referred as snap) from snap = 041 ($z = 4.495$) to snap = 035 ($z = 5.098$), which encompass the redshift range of the observed systems ($z = 4.5 - 5.1$, see Table 5.1), and a physical time interval of $\Delta \mathrm{t_H} = (1.338 - 1.145)$ Gyr = 193 Myr, for our assumed cosmology. Hence, we end up having six galaxy catalogues, with $\Delta z = 0.1$, containing simulated systems with masses in the range $\mathrm{M}_\star \sim 10^8 - 10^{11}\,\mathrm{M}_\odot$ (~ 14000 objects at snap = 041, and ~ 9400 at snap = 035). Among these, we consider only galaxies with stellar mass $\mathrm{M}_\star \geq 10^{10}\,\mathrm{M}_\odot$, to match the properties of the observed systems (see Table 5.1), ending up with ~ 40 galaxies at snap = 041 and ~ 15 galaxies at snap = 035. Within these smaller samples of objects, which match the observed systems in terms of redshift and stellar mass, we must identify possible galaxy mergers. Mergers are identified considering galaxies at $z \simeq 4.5$ and

Table 5.2. Properties of the 8 simulated systems classified as major mergers. For each redshift, z, we show the system ID, the distance obtained averaging over distances between merging galaxies on the x,y,z projections, r_m [kpc], the carbon mass ratio, μ_C, the relative mass ratio of the merging pair, $\mu_\star$, the total stellar mass, $M_\star$ [$M_\odot$] and SFR [$M_\odot$ yr^{-1}]. In the last two rows, we report integrated properties for non-interacting systems which we use together with merging systems, see discussion in Section 5.5.

system ID	z	r_m [kpc]	μ_C	$\mu_\star$	Log($M_\star/M_\odot$)	Log(SFR/$M_\odot$yr^{-1})
merging galaxies						
H2	4.495	11.3	2.0	4.1	10.44	1.84
H4	4.495	16.3	2.3	1.5	10.55	1.96
H5	4.495	6.3	1.3	1.9	10.49	1.83
H6	4.495	5.3	1.3	1.9	10.43	1.81
H10	4.495	10.3	3.2	1.3	10.51	1.90
H25	4.495	40.3	2.8	2.3	10.30	1.70
H28	4.495	32.3	3.6	4.1	10.27	1.74
H0	4.988	13.3	4.6	1.5	10.58	2.17
single galaxies						
H7	4.495	-	-	-	10.43	1.84
H29	4.495	-	-	-	10.58	1.85

reconstructing their merger trees (i.e. their past assembly histories in gas, dark matter, and stellar particles) up to $z \simeq 5.1$. Figure 5.6 shows a schematic view of a merger tree reconstruction: we start at $z = 4.495$ (snap = 041) with a galaxy dubbed "a", and go backward in time up to $z = 5.1$ (snap = 035); at each intermediate redshift step, we identify the ancestors of "a" (i.e. halos "b" and "c" contributing particles to "a" at $z = 4.6$). Once we have reconstructed the merger tree of each galaxy, we can then follow its evolution forward in time and characterise the origin of its mass assembly, whether this is the result of a major merger, smooth accretion, or minor mergers.

In particular, we follow the same criterion adopted for the observed systems, and we assume that two ancestors undergo a major merger when their relative stellar mass ratio (defined as the ratio between the most massive and the least massive) is $1 < \mu_\star < 4$.

After applying this condition and checking that we are not double counting merging episodes[5], we end up with 8 unique candidates (7 at $z \simeq 4.5$ and one at $z \simeq 5.0$), which undergo major mergers during their history. In Table 5.2, we provide a summary of their physical properties, where each row corresponds to one of these synthetic major mergers. In particular, we report their IDs, redshift, the mean projected (r_m)[6] distance in kpc, the relative carbon mass ratio of the merging pair (μ_C), the relative stellar mass ratio of the merging pair, $\mu_\star$, the total stellar mass ($M_\star$) in $M_\odot$ and the SFR in $M_\odot$ yr^{-1}.

[5]Notice that double counting can happen if we count as different mergers those happening during the evolution of the same galaxy among the same ancestors across different redshift steps of its merger tree.

[6]This distance has been calculated averaging over the projected distances between the merging galaxies on the x,y,z planes.

Compared to the observed sample (see Table 5.1), the simulated systems appear to span a similar range of properties and can be considered as good synthetic analogues of the systems that we have analysed in Section 5.2. This sample of synthetic galaxies can help us interpret the observed trends that we presented in Section 5.3. As an illustrative example, in the next section, we discuss the time evolution of the simulated system H4 at $z = 4.495$, which provides the best synthetic analogue of vc_5100822662.

5.4.3 Time evolution of a representative merger

The simulated system H4 at $z = 4.495$ and the observed system vc_5100822662 (hereafter, vc_662) at $z = 4.5210$ have stellar mass and SFR which are consistent within the errors: $\mathrm{Log}(\mathrm{M}_\star/\mathrm{M}_\odot) = 10.6$ (H4) and $\mathrm{Log}(\mathrm{M}_\star/\mathrm{M}_\odot) = 10.4^{+0.1}_{-0.1}$ (vc_662); $\mathrm{Log}(\mathrm{SFR}/\mathrm{M}_\odot\ \mathrm{yr}^{-1}) = 2.0$ and $\mathrm{Log}(\mathrm{SFR}/\mathrm{M}_\odot\ \mathrm{yr}^{-1}) = 2.0^{+0.2}_{-0.2}$, respectively. Moreover, H4 and vc_662 have similar stellar mass ratios μ_{H4}=1.5 and $\mu_{\mathrm{vc\_662}}$=1.7, and projected distance of 16 kpc and 11 kpc respectively. It is important to keep in mind that from the simulation, we not only have information on projected distances but also on the physical (3D) distance between the merging galaxies, which we compute to be $r = 21$ kpc for this synthetic system.

Figure 5.7 shows the merger tree reconstruction for H4 (see Table 5.2 for its integrated physical properties) from $z = 4.5$ to $z = 5.1$, together with maps (80 × 80) kpc and (60 × 60) kpc showing respectively the (x,y) projection of the dark matter particles and stellar particles. These maps are centered respectively in the center of mass of the dark matter halo and of the baryonic component. Here we dubbed the merging galaxies H4 and H98 at $z = 4.5$ as "a" and "b", respectively, so that it is easier to follow their past history along the merger tree reconstruction. In the illustration provided, we connect with solid black lines each component of the merging pair to its main galaxy progenitor at the preceding redshift[7]: as an example, the galaxy dubbed as "a" at $z = 4.6$ (H3) is considered as the main progenitor of galaxy "a" at $z = 4.5$ (H4). At each redshift, we also indicate the stellar mass ratio ($\mu_\star$) of the galaxies undergoing the major merger. For the sake of clarity, the projections of the dark matter and baryonic components in the middle and right panels of Figure 5.7 are shown only at four redshifts, and particles belonging to each merging component are color-coded to match those in the corresponding merger tree. In the following section, we discuss how the spatial distribution of the gaseous component is generated.

Looking at the dark matter and baryonic matter visualisations in the middle and right panels of Figure 5.7, it is interesting to notice how dark matter halos merge and coalesce in a shorter time compared to galaxies themselves (i.e. to the baryonic components). Indeed, by $z = 4.5$, the dark matter halos of the two systems can be considered as a single virialised object, while the baryonic components are still largely spatially segregated, and undergoing the merger. Moreover, notice that as soon as the gravitational interaction between galaxies becomes stronger (i.e. they move closer), galaxies appear to be more clumpy and rich in satellites, and undergo disruption events which lead to filamentary structures by $z = 4.5$. In addition to

[7]Main progenitor is the galaxy which contributes the most, in terms of stellar mass, to the descendant at the subsequent redshift.

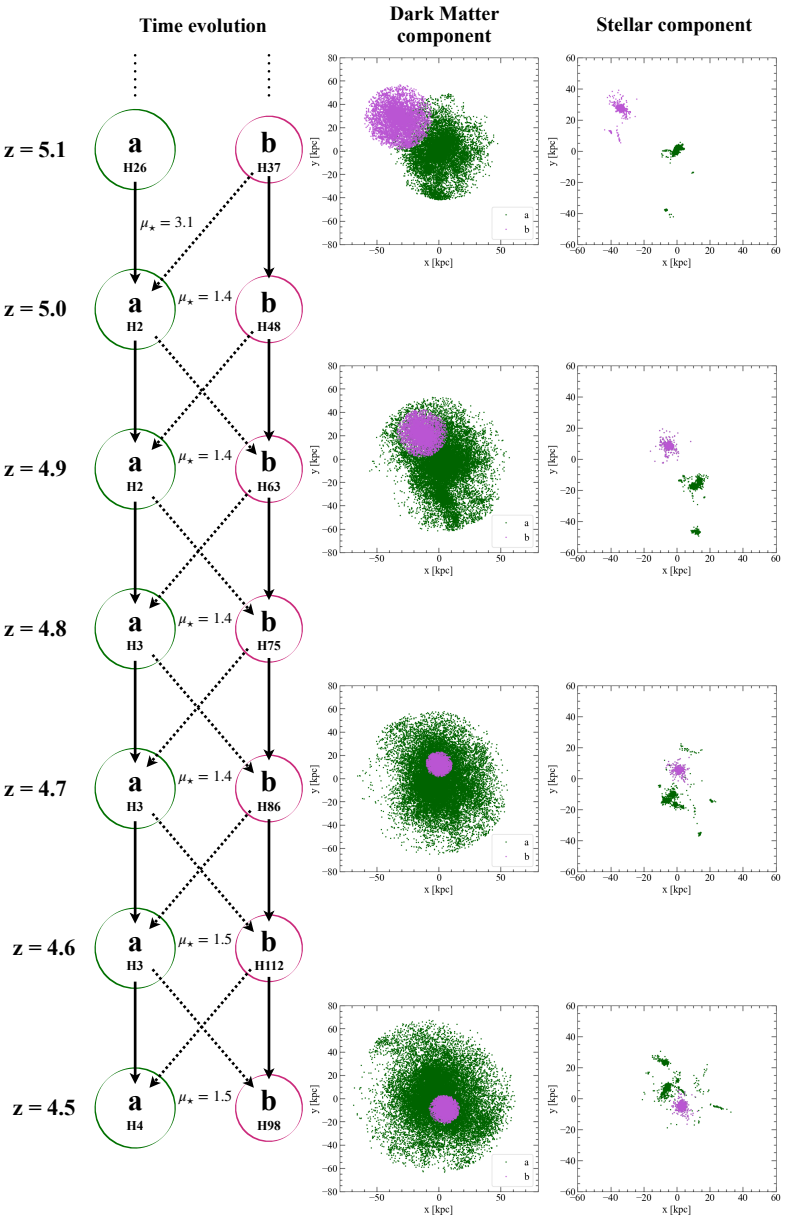

Figure 5.7. *Left:* History of two merging galaxies, H4 and H98 (dubbed as "a" and "b"), reconstructed along their past merger tree, starting from $z = 4.5$ up to $z = 5.1$. At each redshift, we show both the main progenitor (black solid line) and secondary progenitor (black dashed lines), we also report the stellar mass ratio $\mu_\star$ of the primary (green) and secondary (magenta) merging galaxies. In the *Middle and Right* panels we show the projection on the (x,y) plane of the merging galaxies as seen in dark matter and baryonic matter components, respectively. For the sake of clarity, we only show the maps at four redshift steps ($z = 5.1$, 4.9, 4.7, and 4.5, from top to bottom) and galaxies are color-coded as in the merger tree.

this, we also have to consider that the merger between the dark matter halos of the galaxies may lead to the formation of overdense regions which result in dense clouds where star formation can be triggered.

All this qualitative information coming from the simulation provides us with fundamental indications on the evolution of merging pairs, inaccessible using only observations, and helps us interpret the results from the observational part of this work. In fact, simulated galaxies have higher spatial resolution compared to ALPINE observations, and we are able to resolve small satellite galaxies and filamentary structures. This allows us to infer the origin of the enriched diffuse gas surrounding the galaxies, which powers the observed [CII] emission coming from the inner CGM of merging galaxies: whether this is due to unresolved satellites galaxies, filamentary structures, outflows or maybe a combination of the three. In the following, we will explore these options in a more quantitative way.

5.4.4 Dependence of galaxy properties and their CGM on the mass ratio of merging pairs

In this section, we focus on two synthetic candidates (H2 and H10) at $z = 4.5$ which have been selected as their merging pairs are characterised respectively by the highest ($\mu_\star = 4.1$) and lowest ($\mu_\star = 1.3$) stellar mass ratios in our sample. Our aim is to investigate whether systems with extreme $\mu_\star$ may be characterised by different morphological properties of the stellar and gas components, on scales comparable to the diffuse [CII] emission component quantified in Section 5.3.

Figure 5.8 shows the stellar particle distributions (first row) and carbon surface density maps (Σ_C, second and third rows) for H2 and H10 projected on the plane perpendicular to the line-of-sight along the x-axis. Specifically, in orange/violet tones is the carbon in regions with gas temperature $T < 5 \times 10^4$ K, used as a proxy for $L_{[CII]}$ - see following discussion.

In general, to characterise the gas and metals spatial distributions we project gas and metals particles onto Cartesian grids with 256 or 512 cells/side and each particle contribution is weighted with the SPH kernel adopted in `dustyGadget`. These maps are centered either in the halo mass center (H2, H4, H5, H6, H10, H0) or in the center of mass of the merging system (H25, H28), depending on how diverse these two values are, while the side of the Cartesian grid is chosen to capture the whole merging system. Specifically, we chose a box side of 60 kpc (256 cells/side) for all the synthetic candidates but for H25 and H28 for which we adopted a side length of 100 kpc (512 cells/side). Both grids have a spatial resolution (pixel dimension) of $\sim$0.2 kpc, thus a factor of $\sim$ 20-30 more resolved than the ALMA-ALPINE beam.

As for the panels showing stellar particles (scatter plots), color-coded in red are the ages of such particles, while, we highlight in dark blue stellar populations with ages $\leq$ 10 Myr and in light blue those with ages $\leq$ 100 Myr. This is done in order to characterise younger populations and star-forming regions (blue) in contrast to more mature stellar populations in red. Observations interpreted with photo-ionization models suggest that the bulk of [CII] emission is coming from neutral atomic gas clouds in photo-dissociation regions (PDRs) surrounding young stars (Hollenbach and Tielens, 1999), thus we expect that a consistent part of the carbon mass predicted by `dustyGadget` simulations will be associated with young

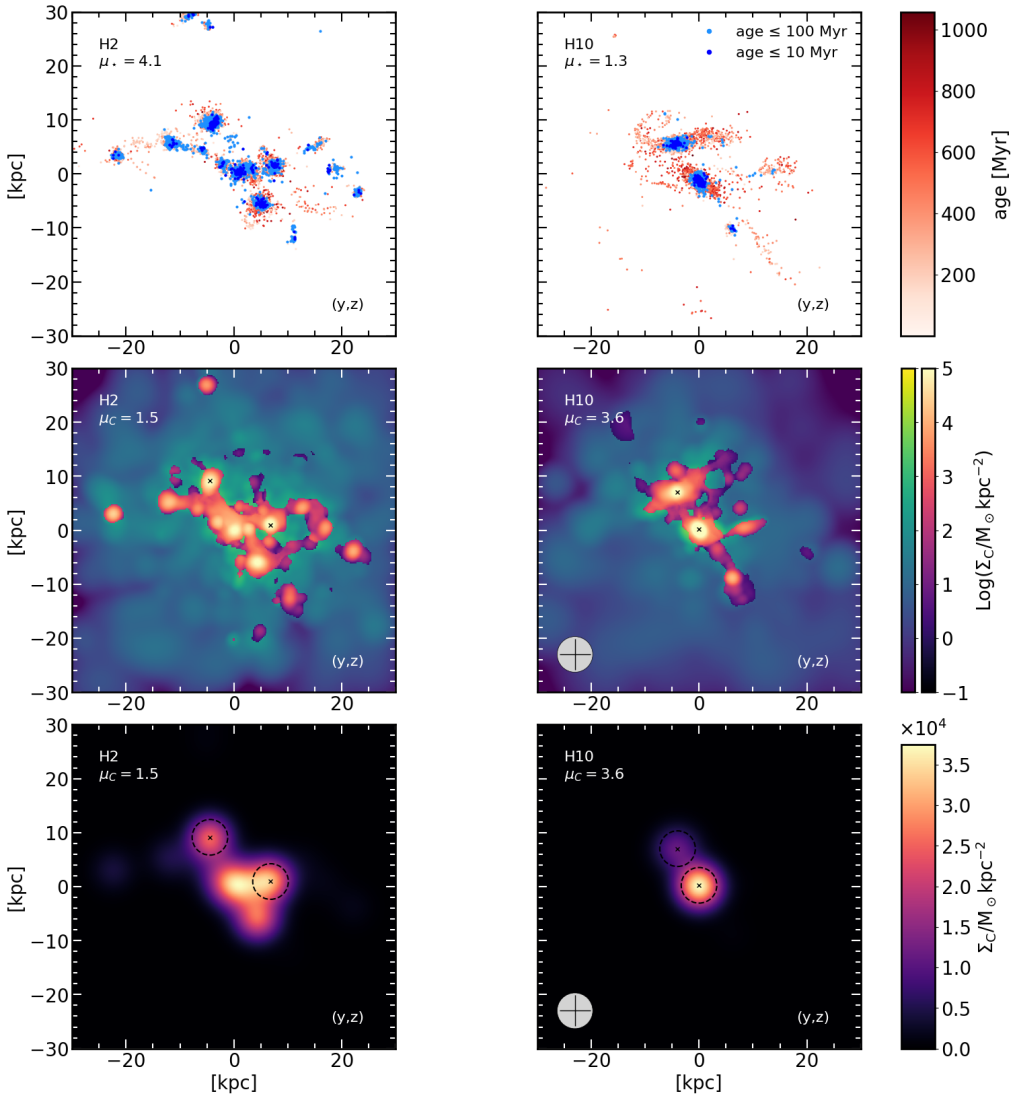

Figure 5.8. Properties of two examples of synthetic merging systems with high ($\mu_\star = 4.1$, H2, left panels) and low ($\mu_\star = 1.3$, H10, right panels) stellar mass ratios at $z = 4.5$. *First row:* maps of the stellar surface density projected along a line-of-sight parallel to the x-axis. Stellar particles are color-coded according to their age, with age ≤ 10 Myr in dark blue, age ≤ 100 Myr in light blue, and 100 Myr $<$ age ≤ 1 Gyr in red colour scale. *Second row:* same as before but for the carbon surface density distribution of H10 ($\mu_C = 3.6$) and H2 ($\mu_C = 1.5$), respectively. The green color map shows the *total* carbon surface density distribution and overplotted on that, in orange tones, is the carbon distribution in the *cold gas phase* (i.e. with T$< 5 \times 10^4$ K). *Third row:* carbon in the cold gas phase surface density distribution once we convolve the original simulated map with the ALMA PSF. Black ellipses indicate the optimal apertures used to extract the carbon content associated with each merging galaxy. In the bottom left corner is a beam of ~ 1" as a reference.

stellar populations (ages $\leq$ 10 Myr) - see discussion in Section 5.5.

In the second row of Figure 5.8, we color in blue/green tones the *total* carbon surface density, while in orange/violet the carbon surface density found in regions with gas temperature T $< 5 \times 10^4$ K [8]. This cut has been done as the [CII] emission is expected to be associated with cold-warm gas phases, and at higher temperatures we expect the C atoms to be in higher ionization states.

The third row of Figure 5.8 shows the surface density distribution of the carbon associated with gas at a temperature below the adopted cut (hereafter "cold" gas phase) once it is convolved with the ALMA PSF (i.e. we applied a Gaussian smoothing with FWHM = 1"). This step is needed since we want to compare the results from simulations with those from observations (see Section 5.4.5). The black crosses mark the center of the two interacting galaxies and the gray circle in the bottom left corner shows a reference beam of $\sim$ 1".

The comparison between the two systems presented in Figure 5.8 shows that the two merging pairs appear to be in very different environments, with the H2 system being characterised by a dominant component and several smaller satellites ($\mu_\star \sim 4$), and the H10 system being characterised by an almost equal mass merging pair ($\mu_\star \sim 1$). This translates into different stellar and metal-enriched gas spatial distributions in the two cases.

Also, it is interesting to notice how diverse the scenarios appear when comparing carbon maps with and without the convolution with ALMA PSF, with the latter lacking the detailed spatial distribution inferred from the simulation.

5.4.5 Statistical properties

Here we analyse in a more quantitative way the relations between the carbon mass - in the cold phase - present in the diffuse halo around merging galaxies and the integrated properties of such systems, to identify possible trends. The aim is to derive scaling relations that can be compared to the observational ones (see Figure 5.4 and Figure 5.5) using the carbon in the cold gas phase as a proxy for [CII] luminosity. In fact, once similar relations are recovered, predictions from `dustyGadget` can help us interpret the observations.

From now on, whenever we talk about the carbon mass we refer to the M_C in the cold phase, T $< 5 \times 10^4$ K, orange/violet tones in Figure 5.8. As previously stated, this cut in temperature is necessary in order to highlight the regions from which we expect [CII] emission to be more likely. Briefly, we generate the gas and carbon 3D distributions, apply the cut in temperature to these cubes, and then project this result on planes perpendicular to the lines of sight parallel to the z, y, and x-axis. We repeat this procedure to all our selected synthetic galaxies (see Table 5.2) and, once we have an image for each candidate and its three plane projections, we convolve the image with the ALMA PSF and fit a 2D Gaussian model to it, retrieving morphological information such as the coordinate of the main M_C clumps that are associated with the major merging galaxies. Then, we use the mean value of all the *optimal* apertures adopted for the observational part as the standard aperture

[8] This temperature is the hydrodynamical one, thus it does not take into account cooling effects which may arise once we apply radiative transfer codes.

to be used in simulations (black dashed circles in Figure 5.8, last row) and associate all the carbon inside the aperture as belonging to the galaxy.

Knowing the coordinates of the center and the dimensions of all the apertures, for each 2D projection (lines of sight, $i = z, y, x$), we can distinguish between the carbon mass associated with the galaxies - sum of the carbon mass inside the apertures - and the total one - sum over the entire plane projection. At this point, we can define the M_C associated with the diffuse halo as :

$$M^{\mathrm{diffuse,i}} \equiv M^{\mathrm{total}} - M^{\mathrm{i}} \tag{5.5}$$

where we dropped the subscript C. The fraction of M_C in the envelope around merging systems (hereafter, f_C) is :

$$f_C^{\mathrm{i}} \equiv \frac{M^{\mathrm{diffuse,i}}}{M^{\mathrm{total}}}. \tag{5.6}$$

Figure 5.9 shows the relation between M^{diffuse} and some integrated properties of the systems, such as the total carbon mass, SFR, and stellar mass. For each relation, we calculate the Spearman coefficient (ρ) to understand how reliable the suggested trend is. Moreover, different colors correspond to projected quantities along lines of sight parallel to the z (blue), y (pink), and x (red) axis, and projections associated with the same system are connected by gray vertical lines quantifying the variation of M^{diffuse}.

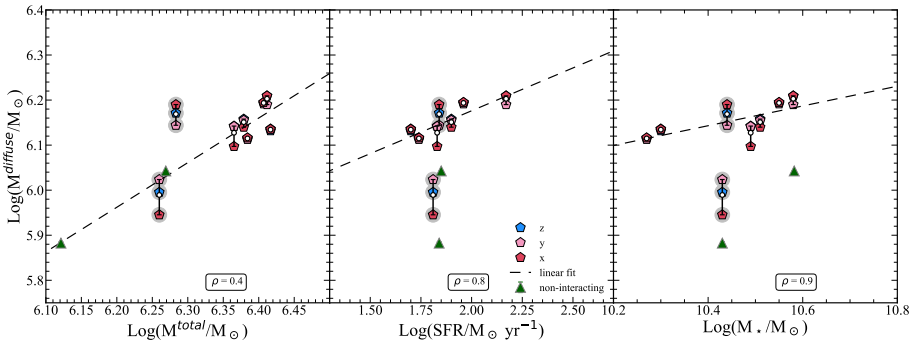

Figure 5.9. Trends between the carbon mass in the cold gas phase ($T < 5 \times 10^4$K) coming from the diffuse halo around merging systems, M^{diffuse}, and their integrated physical properties. Different colors refer to projected quantities along different lines of sight parallel to the z (blue), y (pink), and x (red) axis. In each panel, white dots are M^{avg} (i.e. the average among the three projections), the black dashed line is the linear fit once we consider M^{avg}, and ρ is the Spearman coefficient corresponding to the analysed relation. *Left:* M^{diffuse} is shown as a function of the total carbon mass in the cold gas phase (M^{total}). *Middle and Right panels:* M^{diffuse} as a function of the total SFR and total $M_\star$ of the merging systems. Highlighted in gray are H2 and H6, which have peculiar structures, and for this reason, they have not been included in the fit. Green triangles are single non-interacting galaxies, see the end of this section for discussion.

The black dashed line is the result of the linear fit once we consider the carbon mass value in the diffuse halo averaged on the three projections (hereafter, M^{avg}

shown using a gray cross in the figures) and the corresponding x-axis quantity. Finally, highlighted in gray are H2 which has a peculiar morphological structure rich in clumps and satellites, and H6 whose galaxies are closely interacting (see Appendix 5.7). For these reasons, they are considered as not belonging to the fiducial simulated sample and have not been included in the fit.

The figure shows positive $\rho = 0.4$ and strong positive $\rho = 0.8, 0.9$ correlations respectively in the first, second, and third panels, adding some information to the analysis done with observations. In fact, as discussed in Section 5.3 and shown in Figure 5.4, from observations we were only able to find a tentative trend between diffuse [CII] emission and star formation rate/stellar mass of merging systems. The results obtained for the simulated galaxies suggest that their inner CGM is characterised by a significant carbon mass, which appears to be well correlated with the SFR and stellar mass of the systems, indicating the important role that current and past star formation activity has in enriching the CGM with outflows from the merging pairs and smaller satellite systems.

In Figure 5.10 we explore the dependence between the fraction of carbon mass in the diffuse halo (f_C) and the mean[9] projected distance between the galaxies (r_m), the stellar mass ratio ($\mu_\star$) and the carbon mass ratio (μ_C). In the middle and right panels, different colors correspond to different projections, with those associated with the same system connected by gray vertical lines. In each panel we specify the Spearman coefficient of the corresponding relation and the black dashed line is the linear fit once we consider the fraction of carbon in the diffuse envelope averaged on the three projections (f^{avg}) and the corresponding x-axis quantity. f^{avg} is shown with a violet square/star in the left panel and with white dots in the middle and right panels. The synthetic galaxy H2 has not been included in these plots being considered an outlier with $f_C \sim 0.8$, then out of scale; H6, instead, has been highlighted in gray and not considered in the fits and computation of the Spearman coefficients.

On average, we find that, when considering the entire simulated sample, $\sim 59\%$ of carbon mass resides in the envelope around merging systems, while if we exclude H2 as being an outlier, particularly rich in carbon, it becomes $\sim 57\%$. In both cases, we find an agreement between the prediction from `dustyGadget` and the observations, thus between the carbon mass in the diffuse halo and the [CII] luminosity. In the left panel of Figure 5.10 we show f^{avg} as a function of the mean projected distance (violet square) and physical distance (violet stars) between merging galaxies, with the physical distance being larger than the projected one in all the systems. The Spearman coefficient for the f^{avg} - r_m relation is $\rho = -0.5$ suggesting a correlation with negative trend between these two quantities. This result seems to disagree with what has been found in observations, but we have to keep in mind that in simulations we are considering systems with mean distances r_m up to ~ 50 kpc, while in the ALPINE sample, the projected distance goes up to ~ 16 kpc. This is further discussed in Appendix 5.8.

The middle panel suggests an anti-correlation between the fraction of carbon mass in the diffuse halo and the stellar mass ratio of the merging galaxies, indicating that systems with $\mu_\star$ closer to unity have stronger interactions which result in more

[9]We perform the average between the distance found on the three projected maps.

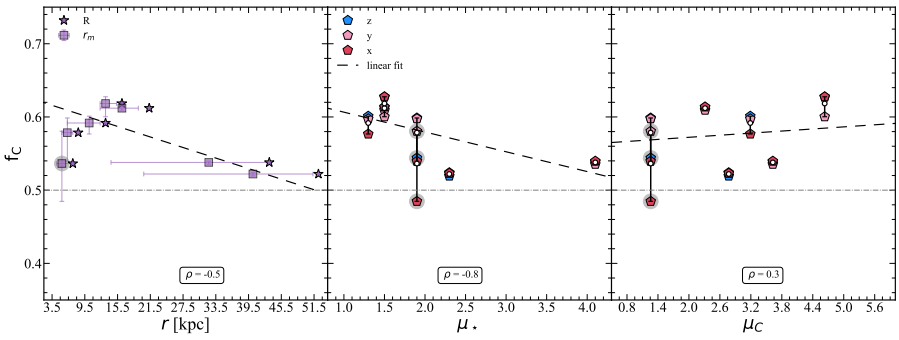

Figure 5.10. Trends between the fraction of carbon mass in the cold gas phase ($T < 5{\times}10^4$K) in the diffuse halo (f_C) and the distance (r) between the galaxies (*Left*), the stellar mass ratio ($\mu_\star$, *Middle*), and the carbon mass ratio (μ_C, *Right*). In particular, in the *Left* panel we show f^{avg} (i.e. the average among the three projections) as a function of both the distance averaged on the three projections (r_m, violet squares) and the physical distance between the galaxies (R, violet stars). In the *Middle and Right* panels different colors refer to f_C estimated by projecting the carbon surface density along lines-of-sight parallel to the z (blue), y (pink), and x (red) axis. In each panel, white dots are f^{avg}, the black line is the linear fit considering f^{avg} versus r_m, $\mu_\star$, μ_C respectively. We also specify the Spearman coefficient (ρ) of each relation. H2 is not included in these plots as this system is characterised by an out-of-scale value of $f_C = 0.8$ and H6 is highlighted in gray. The horizontal gray dot-dashed line shows the value of $f_C = 0.5$.

metal-enriched inner CGM. This may be a clue that dynamical interaction at high-z can be an efficient mechanism for extracting material out of galaxies and mixing it in the CGM. Finally, the right panel shows f_C as a function of μ_C, suggesting that there is not a correlation between the amount of M_C found in the diffuse halo and the ratio between carbon masses of each merging component (μ_C).

5.5 Discussion

In this section, we interpret the observations using our simulated galaxies and discuss the results. In the first place, it is important to keep in mind that the comparison between observations and simulations is not straightforward, as in simulations we are looking at the carbon mass in the cold phase which is more likely to emit in [CII], but not the actual [CII] luminosity. In fact, to recover luminosity information from simulations we would need to couple our result with radiative transfer codes, such as `SKIRT` (for dust continuum, Baes and Camps 2015) and `Cloudy` (for line transfer, Ferland et al. 2017). We are planning to implement these features for follow-up work. That said, preliminarily, we assume that the carbon mass in the cold gas phase ($T < 5 \times 10^4$ K) can be considered as a good proxy for [CII] luminosity, to guide the interpretation of the observational results illustrated in Section 5.3.

[CII] emission halos have been observed and studied at first in non-interacting galaxies (e.g. Fujimoto et al. 2019; Ginolfi et al. 2020b; Fujimoto et al. 2020; Herrera-Camus et al. 2021), where halos extending up to $\sim$ 10-15 kpc outside the galaxies

have been reported. A possible explanation for this finding has been provided by Pizzati et al. (2020, 2023), who adopt a semi-analytical model to interpret the presence of [CII] halos in high-z galaxies concluding that they can be produced by ongoing (or past) starburst-driven outflows which transport carbon and other heavy elements in the CGM. Later on Ginolfi et al. (2020c) found an even more extended (> 20 kpc) halo in one interacting galaxy from the ALPINE sample, arguing that most of the detected circumgalactic emission is a consequence of the effect of gas stripping induced by strong gravitational interaction.

In this work by analysing major merging systems in the ALMA-ALPINE survey, we confirm the presence of extended [CII] envelopes around interacting galaxies, finding that around 55 % of the total [CII] emission comes from the medium between the interacting galaxies. All the analysed systems have an extended halo (mean value of ~ 27 kpc), suggesting that the gravitational interaction between galaxies which results in tidal tails is responsible for an extended carbon-enriched envelope. This scenario has been investigated using the hydrodynamical simulation `dustyGadget` and comparing merging and not merging systems (see discussion in the following). Specifically, the anti-correlation between f_C and $\mu_\star$ indicate that systems that interact more strongly result in a more enriched halo (i.e. higher f_C) - supporting the conclusion from Ginolfi et al. (2020c). Also, starburst-driven outflows which spread metals outside the galaxies are still at work, in interacting systems. In fact, as shown in the middle panel of Figure 5.9, there is a correlation between the carbon in the diffuse medium and the SFR of galaxies which can be associated with outflows. To quantify the importance of that mechanism compared to the others we need to look at galactic winds of interacting galaxies, which is something outside the aims of this work.

Predictions from `dustyGadget` helped us corroborate and interpret the observational results. In addition, we can also use them to disentangle the different mechanisms that contribute to metal enrichment of the inner CGM of interacting galaxies. To do so, we consider SFRs, $M_\star$, and $\mu_\star$ as proxies for outflows, SF clumps, and tidal interactions, respectively, and study their contribution to the carbon-enriched envelope.

As already mentioned, H6 is considered as a peculiar merging system being in an advanced phase of interaction (very close merging components), and H2 is considered an outlier in the synthetic sample, because of its high f_C which can be due to its peculiar morphology rich in satellites/star-forming clumps. To further investigate this hypothesis, we study the relation among f_C and the fraction of young, age $\leq$ 10 Myr, stellar populations ($f_\star$) that reside in the inner CGM of the systems. This quantity is defined as :

$$f_\star^i \equiv \frac{N_\star^{total} - N_\star^i}{N_\star^{total}}. \tag{5.7}$$

with $N_\star^{total}$ being the total number of young stellar populations and $N_\star^i$ the sum of stellar particles associated with merging galaxies for each projection ($i = z, y, x$).

In Figure 5.11 we show mean values for $f_\star$ and f_C for interacting, in orange, and non-interacting, in green, systems (see discussion in the following); error bars on both axes give us an idea of the variations of $f_\star$ and f_C among different projections. This figure shows a linear relation and positive trend between the fraction of carbon

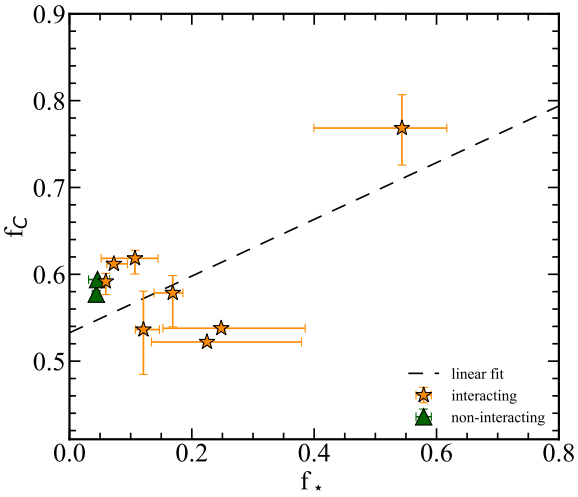

Figure 5.11. Relation between the fraction of carbon mass (f_C) and the fraction of young - age $\leq$ 10 Myr - stellar populations ($f_\star$) present in the diffuse halo of interacting (orange stars) and non-interacting (green triangles) systems. We show the mean value of f_C and $f_\star$ of all the simulated galaxies, together with the error bars representative of the variations in different projections and the linear fit.

and that of young stellar populations in the diffuse halo, suggesting that clumps of star-forming regions, which are unresolved by ALMA, can play a role in enriching the gas envelope with carbon. Also, as shown in Figure 5.7, the merger between dark matter halos happens on smaller timescales compared to those needed for the merger in the baryonic component and may lead to the formation of overdense regions at the periphery of merging systems triggering star formation and enriching their surrounding medium with carbon and other heavy elements.

In addition to the previous analysis, by comparing results from major merging systems (dubbed as "interacting") with those from systems which are not in major mergers (dubbed as "non-interacting/single"[10]) we can estimate the importance of gravitational interactions, which result in tidal stripping, for the enrichment of the inner CGM. The purpose of this test is to get information from simulations (non-interacting synthetic systems) to better interpret observational results. To do so, we select two non-interacting galaxies with stellar masses and SFRs similar to the interacting synthetic candidates - see Table 5.2. These two galaxies are also representative of other synthetic single galaxies at the same redshift that we find in our simulation.

In the single-galaxy case, we recover an extended carbon-rich halo going up to $\sim$ 10 kpc, in agreement with what has been previously estimated by Fujimoto et al. (2019, 2020); Ginolfi et al. (2020b); Herrera-Camus et al. (2021). This is shown in Figure 5.12, and confirms that the diffuse halo in non-interacting galaxies is less extended than the one estimated for interacting systems ($>$ 20 kpc).

In Figure 5.9 we compare $M^{diffuse}$ in interacting (coloured pentagons) and non-interacting (green triangles) galaxies. In general, we notice that single galaxies have lower $M^{diffuse}$ values than interacting systems, and also that they result in similar diffuse carbon masses no matter the adopted line-of-sight, indicating a more compact and regular morphology i.e. not disturbed by dynamical interactions. The first panel

[10]For simplicity we dubbed systems which are not undergoing major merger as "non-interacting/single", but it is important to keep in mind that these systems are interacting with their surrounding environments and other satellite galaxies, i.e. they are not isolated.

of Figure 5.9 suggests that both interacting and non-interacting systems follow a similar trend when comparing $M^{diffuse}$ and the total carbon mass. On the one hand, the relation between the diffuse carbon mass and the SFR (second panel) shows that for non-interacting systems, the ongoing SFR is not a good proxy for the amount of carbon mass in the inner CGM. We also note that H6, which is an interacting system in an advanced phase of the merger, places itself close to non-interacting systems on the $M^{diffuse}$-SFR relation. On the other hand, looking at the third panel which shows $M^{diffuse}$ as a function of $M_\star$, we see that interacting systems have $\sim 1.4\times$ more carbon mass in the diffuse halo than single galaxies. This result suggests that stripping mechanisms seem to be responsible for bringing metals into the CGM. This conclusion is further corroborated by the fact that the fraction of SF clumps and carbon mass present in the diffuse halo of non-interacting galaxies is comparable to that of interacting galaxies, as shown in Figure 5.11.

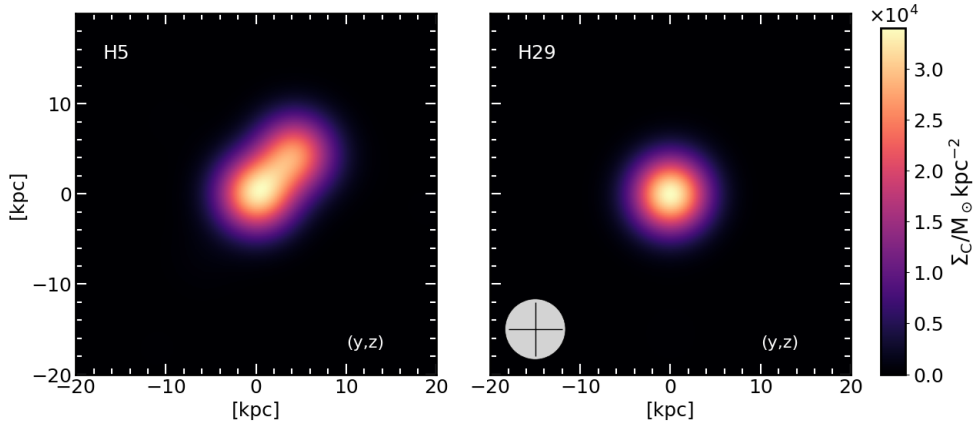

Figure 5.12. As an example we show the surface density distribution of carbon in the cold gas phase once we convolve the original simulated map with the ALMA PSF, for interacting (left) and non-interacting (right) systems. The line-of-sight is chosen parallel to the x-axis, in the bottom left corner is a beam of ~ 1" as a reference.

In summary, stripping mechanisms in interacting systems are responsible not only for bringing carbon into larger scales but also for enhancing [CII] emission possibly via shocks (see also Ginolfi et al. 2020c). Indeed, observations show that interacting galaxies have $\sim 10\times$ higher [CII] luminosity from the diffuse halo compared to single objects (Fujimoto et al., 2019; Ginolfi et al., 2020c; Fujimoto et al., 2020), while this difference is only a factor 1.4 when considering $M^{diffuse}$, as shown in Figure 5.9.

The interacting systems that we have analysed could be considered as high-z analogues of circumgalactic stripped carbon and shock-induced [CII] emission in local studies (Appleton et al., 2013; Velusamy and Langer, 2014). These are qualitative conclusions, based on a comparison between the properties of the inner CGM found around single and major merging galaxies in our simulation, and need to be reinforced by performing a more quantitative analysis of the specific effects of all feedback processes at play, both mechanical and radiative, which is beyond the scope of the present work.

5.6 Summary and conclusions

In this chapter, we analyse a sample of merging galaxies observed by the ALMA-ALPINE survey at redshift $4.5 < z < 5.1$, to investigate the [CII] emission coming from the gas *between* the galaxies. We complement the observational analysis with cosmological simulations, specifically the hydrodynamical code `dustyGadget`, looking for synthetic merging systems that helped us interpret the nature of such emission. Our main results can be summarized as follows:

1. We analyse major merging systems in the ALPINE survey and confirm the presence of an extended (> 20 kpc) [CII] halo in interacting galaxies. This extended halo is larger than the one observed in isolated galaxies as a consequence of the dynamic interaction between galaxies.

2. We find that more than 50% of the total [CII] emission associated with these systems comes from the medium surrounding the merging system, thus between the galaxies. This result confirms what has been previously found by Ginolfi et al. (2020c) for one merging system in ALPINE.

3. We establish the presence of correlations, either strong or tentative, between the amount (fraction) of [CII] emission from the diffuse halo and integrated (relative) properties of galaxies.

4. We find that an extended carbon-rich halo is present in interacting systems selected from the `dustyGadget` simulation as well. In particular, extended halos of around 10 kpc and larger than 20 kpc have been found in non-interacting and interacting systems respectively. Also, we find strong correlations between diffuse carbon in the cold gas phase - used as a proxy for [CII] emission - and the physical properties of galaxies, in particular, with their total carbon mass, SFR, and stellar mass, suggesting that different mechanisms reside behind [CII] emission.

5. Using `dustyGadget` we investigate the nature of the metal-enriched envelope, which, apart from outflow mechanisms, can be attributed to dynamical interaction between merging galaxies, that extract carbon-rich gas out of galaxies, and the presence of star-forming satellites, that enrich the inner CGM with newborn stellar populations. We argue that most of the [CII] emission observed in the ALPINE systems originates from gas stripping mechanisms in turbulent collisional environments (see discussion in Section 5.5), in analogy with broad [CII] emission observations of tidal tails of shock-excited carbon in local groups (Appleton et al., 2013).

Altogether our findings suggest that dynamical interactions and star-forming clumps at high-z can be an efficient mechanism for extracting gas out of galaxies and enriching the CGM with chemically evolved material. Deeper and higher resolution ALMA data and highly resolved simulations are necessary to study more in details the key role of mergers in the baryon cycle of distant galaxies.

5.7 Appendix A: The merging system H6

The synthetic merging system H6 has been considered as a peculiar system and excluded from the statistical analysis previously performed, as the two interacting galaxies are very close to each other (mean distance value: $r_m = 5.3$ kpc, see Table 5.2) resulting in a smaller fraction of carbon associated to the diffuse envelope. Indeed, it is difficult to distinguish the two merging galaxies, as shown by the x-projection in the smoothed case (see the bottom right panel in Figure 5.13). For this reason, we do not consider it as belonging to the "fiducial sample" of galaxies. In

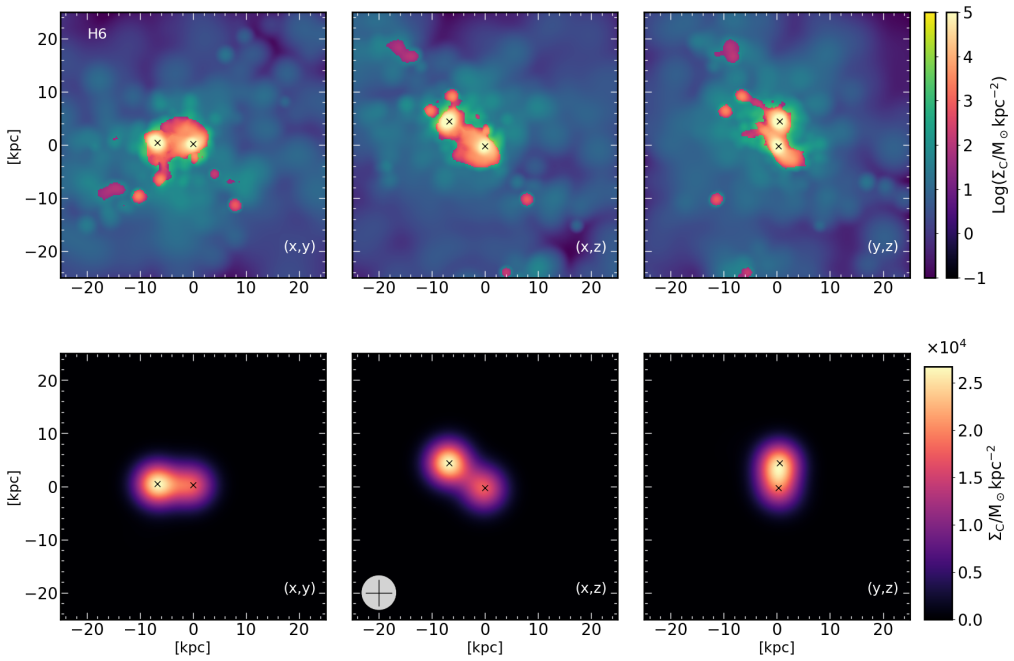

Figure 5.13. The carbon surface density distribution in the synthetic merging system H6, each column is a projection. *Top row:* The green color map shows the *total* surface density distribution of carbon and overplotted in orange tones is the carbon distribution in the cold gas phase ($T < 5 \times 10^4$ K). *Bottom row:* Surface density distribution of carbon once we convolve the original map with the ALMA-ALPINE PSF. Black crosses indicate each merging galaxy and in the bottom left corner is a beam of ~ 1" as a reference. The x-projection in the bottom-right panel shows that it is difficult to discriminate between the two interacting galaxies.

this system the interaction between galaxies is in such an advanced phase that the carbon mass belonging/associated to the galaxies and that of the diffuse envelope are mixed together, leading to a tricky analysis and interpretation. Moreover, the system appears differently depending on the chosen projection, resulting in large error bars (see Figures 5.9 and 5.10). This peculiar system, which can be considered as the synthetic counterpart of DC_873321 (see Section 5.3) needs to be treated and interpreted with care.

5.8 Appendix B: Carbon fraction versus average distance between galaxies

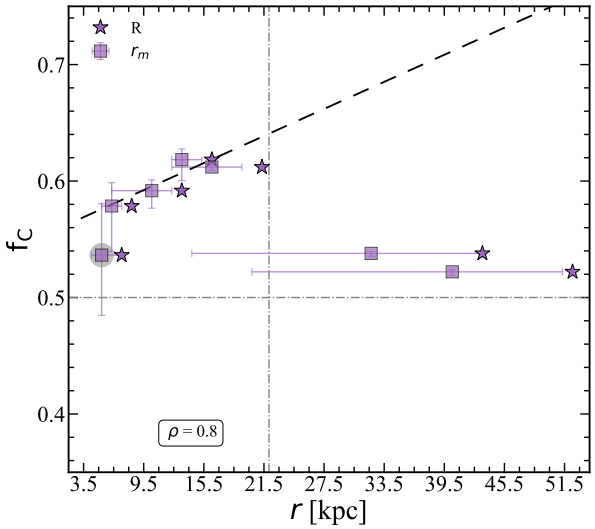

Figure 5.14. Fraction of carbon mass in the cold gas phase as a function of the mean distance (r_m, violet square) and physical distance (R, violet stars) between the galaxies. The horizontal and vertical gray dot-dashed lines show the $f_C = 0.5$ value and $r = 21.5$ kpc, the maximum value for the x-axis in Figure 5.5, respectively.

In the left panel of Figure 5.10 we show the correlation between the fraction of carbon in the cold gas phase that resides in the diffuse envelope and the mean distance between the merging galaxies. The relation between these two quantities leads to a correlation with $\rho = -0.5$ and a negative trend which seems in disagreement with what has been found from the observational sample ($\rho = 0.9$). However, by further analysing this trend we see that the positive or negative correlation depends on the considered r range. Indeed, as shown in Figure 5.14, if we consider only r_m up to ~ 16 kpc (maximum value for the projected distance in the ALPINE sample) we recover the positive trend ($\rho = 0.8$) found in observations. In conclusion, this result highlights that the distance between the galaxies, thus the amount of time galaxies have been interacting for, plays a fundamental role in the pollution of their inner CGM, suggesting that systems in their early phase of interaction (at larger distances) have a less carbon-rich envelopes.

Conclusions and Future Perspectives

The work presented in this thesis is based on the synergy between simulations and observations to study the evolution of galaxies and their interaction with the surrounding environment at $z > 4$. In particular, we adopted the state-of-the-art cosmological simulation `dustyGadget`, and complemented its results and predictions with observational data from ALMA and JWST. Through this synergistic approach, we have demonstrated how simulations provide invaluable insights into the underlying physical processes governing the evolution of cosmic structures, while observations serve as crucial benchmarks for validating these models and providing empirical evidence of phenomena occurring in the distant Universe.

By using the hydrodynamical code `dustyGadget`, we provided predictions about the formation and evolution of galaxies, dark matter halos, and large-scale structures in the early Universe. These simulations have allowed us to explore a wide range of physical scenarios and investigate the interplay between different physical processes, providing a deeper understanding of the complex mechanisms driving galaxy formation and evolution. On the other hand, observations, both from ground-based (ALMA) and space-based telescopes (JWST), have played a pivotal role in constraining theoretical models and providing observational constraints on the properties of galaxies and their surrounding environment.

Chapter 1 gives a general introduction on the cosmological framework where this thesis places itself, and focuses on the large-scale structure formation in our Universe as well as on the standard theoretical model of galaxy formation. After this broad introduction, we delve into a detailed description of observations and simulations relevant to this work (Chapters 2 and 3), and then, we present the specific questions that have been tackled in this manuscript (Chapters 4 and 5).

The content of this thesis can be described as follows.

In Chapter 2 we introduce the observational tools and results we used during this thesis. In particular, we highlighted the results from two ALMA Large Programs, namely ALPINE Faisst et al. (2020) and REBELS (Bouwens et al., 2021b), which are relevant to this work, giving an overview of the state-of-the-art observations in the mm and sub-mm wavelengths and discussing the insights these observations offer into the gaseous component and dust content of high-redshift galaxies. Additionally, we briefly introduce the instruments on board of the space telescope JWST and the queries that this revolutionary instrument has begun to address and pose from its initial observations. In the end, we stressed the importance of cooperation

among telescopes in conducting multi-wavelength observations to tackle fundamental questions about the formation and evolution of high redshift galaxies.

In Chapter 3 we describe the cosmological simulation `dustyGadget` (Graziani et al., 2020) whose predictions about the evolution of the scaling relations of high-z galaxies and Population III stars have been extensively explored in Di Cesare et al. (2023) and Venditti et al. (2023b), respectively. The `dustyGadget` suite of simulations have both the volume and resolution are chosen to guarantee a good compromise between an adequate statistics in each run and an acceptable number of galaxies resolved with a total stellar mass $\mathrm{Log}(\mathrm{M}_\star/\mathrm{M}_\odot) \geq 8$, allowing us not only to conduct statistical studies, but also to analyse the environment around single objects. Moreover, all the above requirements ensure a reasonable computational time for eight runs performed in the redshift range $4 \leq z \leq 100$. One of the strengths of our simulations is that it extends the original implementation of `Gadget` (Springel, 2005) by implementing a model of dust production and evolution in both the cold and hot phases of the ISM of simulated galaxies. The code also follows the spreading of grains and atomic metals through galactic winds at the scale of both the CGM and IGM, allowing to trace the metal pollution of the environments in which galaxies reside at diverse cosmic epochs. Thus, it give us an idea of the chemical maturity and the ongoing processes in high-z galaxies.

Chapter 4 is based on "The assembly of dusty galaxies at $z \geq 4$: the build-up of stellar mass and its scaling relations with hints from early JWST data", Di Cesare et al. (2023) where we studied the stellar mass build-up of galaxies at $z \geq 4$ and investigated the scaling relations of their integrated physical properties. Making use of well-established correlations observed in the Local Universe and the data provided by REBELS and ALPINE, we have benchmarked numerical predictions of the `dustyGadget` model. From this work we argue that the total stellar build-up, in terms of both total star formation rate and total stellar mass density, exhibits a rapid increase from the onset of star formation at approximately $z \sim 20$, to $z \sim 4$ in agreement with available observations, including JWST ERO and ERS beyond $z \geq 8$. In the redshift range $7 < z \leq 9$, our simulated galaxy MS closely mirrors available data, extending observational constraints from REBELS to fainter, lower stellar masses with some of the first JWST results. Our findings also agree with studies on the evolution of the galaxy main sequence at $z < 4 - 6$ (Popesso et al., 2022; Daddi et al., 2022), indicating that our simulations capture the low-mass end of the main sequence below the time-dependent turn-over mass that defines the transition between efficient and relatively inefficient star formation. Moreover, we show that dust enrichment at $z > 4$ is driven by stellar dust production and ISM grain growth, with the latter mechanism increasingly contributing at the high-mass end. Overall, our findings align well with dust mass determinations for ALPINE galaxies by Pozzi et al. (2021) at $4 \leq z \leq 6$ and REBELS galaxies with stellar masses $\mathrm{Log}(\mathrm{M}_\star/\mathrm{M}_\odot) \leq 9.5$ at $6 < z \leq 8$ (Sommovigo et al., 2022c). Notably, the detection of dust continuum from three galaxies at $6 < z \leq 7$ by Witstok et al. (2022) provides additional insights into their dust-to-stellar mass relation, with two galaxies aligning with `dustyGadget` predictions and one exhibiting a high dust-to-stellar mass ratio, indicative of an exceptionally efficient dust production mechanism beyond our model's predictions for galaxies of comparable stellar mass.

In summary, on a cosmological scale, `dustyGadget` prescriptions offer reasonable

agreement with current high-redshift data, including JWST early results.

Chapter 5 is based on "Carbon envelopes around merging galaxies at $z \sim 4.5$", Di Cesare at al., subm. where we analyze a selection of merging galaxies observed by the ALMA-ALPINE survey within the redshift range $4.5 < z < 5.1$ with the aim of investigating the [CII] 158 µm emission originating from the gas located between these interacting galaxies. To complement our observational analysis, we employ the hydrodynamical code `dustyGadget`, and identify synthetic merging systems that aid in interpreting the nature of this emission. From our study not only we confirm the presence of an extended [CII] 158 µm halo (> 20 kpc) surrounding interacting galaxies, larger than those observed in isolated galaxies, indicating the influence of dynamic interactions between galaxies. But also, that more than 50% of the total [CII] emission associated with these systems originates from the medium between the merging galaxies, confirming previous findings from Ginolfi et al. (2020c) for an individual merging system in ALPINE. Moreover, by studying synthetic candidates from the `dustyGadget` simulation we reveal strong correlations between diffuse carbon in the cold gas phase ($T \lesssim 10^4$ K, used as a proxy for [CII] emission) and various physical properties of galaxies, suggesting diverse mechanisms behind [CII] emission. Supported by the simulations we have been able to investigate the nature of the metal-enriched envelope, attributing it to dynamical interactions between merging galaxies and star-forming satellites, which extract carbon-rich gas from galaxies and enrich the inner CGM with newborn stellar populations. We suggest that much of the observed [CII] emission in ALPINE systems arises from gas stripping mechanisms in turbulent collisional environments, akin to observations of shock-excited carbon in local groups (Appleton et al., 2013).

Overall, our findings indicate that dynamical interactions and star-forming clumps at high redshifts can efficiently extract gas from galaxies and enrich the CGM with chemically evolved material. However, deeper and higher resolution ALMA data, coupled with highly resolved simulations, are required to further investigate the pivotal role of mergers in the baryon cycle of distant galaxies.

As pointed out in Chapter 4, `dustyGadget` simulations uncovered an intriguing population of evolving galaxies with stellar masses in the range $8.0 \leq \mathrm{Log}(M_\star/M_\odot) \leq 9.0$. The number density of these galaxies lies above some current observational estimates and model predictions for the stellar mass function at $z \leq 6$, contributing to the substantial scatter observed in the halo mass-stellar mass relation. This suggests that galaxies hosted within DM halos of comparable mass may experience varied star formation histories and chemical enrichment timescales, as reflected in the dust-to-stellar mass relation, where galaxies with $\mathrm{Log}(M_\star/M_\odot) \sim 8.5$ at $z \leq 6-7$ exhibit a wide range of dust masses, differing by up to 1.5 dex. This population of low-mass galaxies and the scatter in the dust-to-stellar mass relation represent a natural and intriguing subject for future studies. Apart from that, a complementary study on the mass-metallicity relation and the fundamental plane relation at $z > 4$, using both simulations and observations, is needed to give a complete view of the chemical evolution of high-z galaxies in our Universe.

On the other hand, future prospects and implementations of the study described in Chapter 5 lie in developing a model capable of predicting emission lines (i.e.

using the photoionizing code `Cloudy`), thus enabling direct comparisons between simulations and observations and providing a more detailed interpretation of the latter. Furthermore, given the ability of simulations to track the temporal evolution of interacting systems, it becomes intriguing for future research to investigate the time evolution of the physical properties of merging galaxies. In fact, this provides a more comprehensive understanding of the consequences mergers have on the surrounding galactic environment, thus shedding light on the evolution of high-z galaxies.

Overall, the combination of simulations and observations has been instrumental in advancing our knowledge of the Universe at $z > 4$. Moving forward, it is crucial to continue this interdisciplinary approach, leveraging the strengths of both simulations and observations to address outstanding questions in astronomy and unravel the mysteries of the early Universe.

List of Publications

- **Di Cesare C.**, Graziani L., Schneider R., Ginolfi M., Venditti A., Santini P., Hunt L. K. -"The assembly of dusty galaxies at $z \geq 4$: the build-up of stellar mass and its scaling relations with hints from early JWST data" - March 2023, MNRAS, Volume 519, Issue 3, pp.4632-4650

- Venditti A., Graziani L., Schneider R., Pentericci C., **Di Cesare C.**, Maio U., Omukai K. -"A needle in a haystack? Catching Population III stars in the epoch of reionization: I. Population III star-forming environments" - July 2023, MNRAS, Volume 522, Issue 3, pp.3809-3830

- Kaasinen M., van Marrewijk J., Popping G., Ginolfi M., Di Mascolo L., Mroczkowski T., Concas A., **Di Cesare, C.**, Killi M., Langan, I. - "To see or not to see a $z \sim 13$ galaxy, that is the question. Targeting the [CII] 158 μm emission line of HD1 with ALMA" - March 2023, A&A, Volume 671, id.A29, 13 pp.

- Valentino F., Fujimoto S., C. Giménez-Arteaga C., Brammer G., Kohno K., Sun F., Kokorev V., Bauer F. E., **Di Cesare C.**, Espada D., Lee M., Dessauges-Zavadsky M., Ao Y., Koekemoer A. M., Ouchi M., Wu J. F., Egami E., Jolly J.-B., Lagos C. del P., Magdis G. E., Schaerer D., Shimasaku K., Umehata H., Wang W.-H. - "The cold interstellar medium of a normal sub-L* galaxy at the end of Reionization" - May 2024, A&A, Volume 685, id.A138, 16 pp.

- **Di Cesare C.**, Ginolfi M., Graziani L., Schneider R., Romano M., Popping G. - "Carbon envelopes around merging galaxies at $z \sim 4.5$" - submitted to A&A

Useful Numbers

Constants	
Gravitational constant	$G = 6.674 \times 10^{-8}$ cm^3 g^{-1} s^{-2}
Planck constant	$h_P = 6.626 \times 10^{-27}$ cm^2 g s^{-1}
Speed of light	$c = 2.998 \times 10^{10}$ cm/s
Boltzmann constant	$k_B = 1.381 \times 10^{16}$ erg/K
Proton mass	$m_p = 1.673 \times 10^{-24}$ g
Neutron mass	$m_n = 1.675 \times 10^{-24}$ g
Electron mass	$m_e = 9.109 \times 10^{-28}$ g
Thomson cross-section	$\sigma_T = 6.652 \times 10^{-25}$ cm^2
Stefan-Boltzmann constant	$\sigma_{SB} = 5.67 \times 10^{-5}$ erg cm^{-2} K^{-4} s^{-1}

Units	
Solar mass	$1M_\odot = 1.99 \times 10^{33}$ g
Solar luminosity (bolometric)	$1L_\odot = 3.827 \times 10^{33}$ erg/s
Astronomical Unit	$1AU = 1.496 \times 10^{13}$ cm
Parsec	$1pc = 3.086 \times 10^{18}$ cm
Electron volt	$1eV = 1.602 \times 10^{-12}$ erg
Angstrom	$1Å = 1 \times 10^{-8}$ cm

Cosmological Parameters	
Hubble constant	$H_0 = 100h$ km/s Mpc^{-1}
Present Hubble time	$H_0^{-1} = 9.78h^{-1}$ Gyr
Present Hubble radius	$cH_0^{-1} = 2997.9h^{-1}$ Mpc

Bibliography

N. J. Adams, R. A. A. Bowler, M. J. Jarvis, B. Häußler, and C. D. P. Lagos. Evolution of the galaxy stellar mass function: evidence for an increasing M* from z = 2 to the present day. MNRAS, volume 506(4):4933–4951, 2021. doi:10.1093/mnras/stab1956.

N. J. Adams, C. J. Conselice, L. Ferreira, D. Austin, J. A. A. Trussler, I. Juodžbalis, S. M. Wilkins, J. Caruana, P. Dayal, A. Verma, and A. P. Vijayan. Discovery and properties of ultra-high redshift galaxies (9 < z < 12) in the JWST ERO SMACS 0723 Field. MNRAS, 2022. doi:10.1093/mnras/stac3347.

H. B. Akins, S. Fujimoto, K. Finlator, D. Watson, K. K. Knudsen, J. Richard, T. J. L. C. Bakx, T. Hashimoto, A. K. Inoue, H. Matsuo, M. J. Michałowski, and Y. Tamura. ALMA Reveals Extended Cool Gas and Hot Ionized Outflows in a Typical Star-forming Galaxy at Z = 7.13. ApJ, volume 934(1):64, 2022. doi:10.3847/1538-4357/ac795b.

H. S. B. Algera, H. Inami, P. A. Oesch, L. Sommovigo, R. J. Bouwens, M. W. Topping, S. Schouws, M. Stefanon, D. P. Stark, M. Aravena, L. Barrufet, E. da Cunha, P. Dayal, R. Endsley, A. Ferrara, et al. The ALMA REBELS survey: the dust-obscured cosmic star formation rate density at redshift 7. MNRAS, volume 518(4):6142–6157, 2023a. doi:10.1093/mnras/stac3195.

H. S. B. Algera, H. Inami, P. A. Oesch, L. Sommovigo, R. J. Bouwens, M. W. Topping, S. Schouws, M. Stefanon, D. P. Stark, M. Aravena, L. Barrufet, E. da Cunha, P. Dayal, R. Endsley, A. Ferrara, et al. The ALMA REBELS survey: the dust-obscured cosmic star formation rate density at redshift 7. MNRAS, volume 518(4):6142–6157, 2023b. doi:10.1093/mnras/stac3195.

H. S. B. Algera, H. Inami, L. Sommovigo, Y. Fudamoto, R. Schneider, L. Graziani, P. Dayal, R. Bouwens, M. Aravena, E. da Cunha, A. Ferrara, A. P. S. Hygate, I. van Leeuwen, I. De Looze, M. Palla, et al. Cold dust and low [O III]/[C II] ratios: an evolved star-forming population at redshift 7. MNRAS, volume 527(3):6867–6887, 2024a. doi:10.1093/mnras/stad3111.

H. S. B. Algera, H. Inami, L. Sommovigo, Y. Fudamoto, R. Schneider, L. Graziani, P. Dayal, R. Bouwens, M. Aravena, E. da Cunha, A. Ferrara, A. P. S. Hygate, I. van Leeuwen, I. De Looze, M. Palla, et al. Cold dust and low [O III]/[C II] ratios: an evolved star-forming population at redshift 7. MNRAS, volume 527(3):6867–6887, 2024b. doi:10.1093/mnras/stad3111.

R. E. Angulo, V. Springel, S. D. M. White, A. Jenkins, C. M. Baugh, and C. S. Frenk. Scaling relations for galaxy clusters in the Millennium-XXL simulation. MNRAS, volume 426(3):2046–2062, 2012. doi:10.1111/j.1365-2966.2012.21830.x.

S. Aoyama, H. Hirashita, and K. Nagamine. Galaxy simulation with the evolution of grain size distribution. MNRAS, volume 491(3):3844–3859, 2020. doi:10.1093/mnras/stz3253.

S. Aoyama, K.-C. Hou, H. Hirashita, K. Nagamine, and I. Shimizu. Cosmological simulation with dust formation and destruction. MNRAS, volume 478:4905–4921, 2018. doi:10.1093/mnras/sty1431.

P. N. Appleton, P. Guillard, F. Boulanger, M. E. Cluver, P. Ogle, E. Falgarone, G. Pineau des Forêts, E. O'Sullivan, P. A. Duc, S. Gallagher, Y. Gao, T. Jarrett, I. Konstantopoulos, U. Lisenfeld, S. Lord, et al. Shock-enhanced C^+ Emission and the Detection of H_2O from the Stephan's Quintet Group-wide Shock Using Herschel. ApJ, volume 777(1):66, 2013. doi:10.1088/0004-637X/777/1/66.

M. Aravena, K. E. Heintz, M. Dessauges-Zavadsky, P. A. Oesch, H. S. B. Algera, R. J. Bouwens, E. Da Cunha, P. Dayal, I. De Looze, A. Ferrara, Y. Fudamoto, V. Gonzalez, L. Graziani, H. Inami, A. Pallottini, et al. The ALMA Reionization Era Bright Emission Line Survey (REBELS): The molecular gas content of galaxies at z$\sim$7. arXiv e-prints, arXiv:2309.15948, 2023. doi:10.48550/arXiv.2309.15948.

S. Arnouts, S. Cristiani, L. Moscardini, S. Matarrese, F. Lucchin, A. Fontana, and E. Giallongo. Measuring and modelling the redshift evolution of clustering: the Hubble Deep Field North. MNRAS, volume 310(2):540–556, 1999. doi:10.1046/j.1365-8711.1999.02978.x.

P. Arrabal Haro, M. Dickinson, S. L. Finkelstein, J. S. Kartaltepe, C. T. Donnan, D. Burgarella, A. C. Carnall, F. Cullen, J. S. Dunlop, V. Fernández, S. Fujimoto, I. Jung, M. Krips, R. L. Larson, C. Papovich, et al. Confirmation and refutation of very luminous galaxies in the early Universe. Nature, volume 622(7984):707–711, 2023. doi:10.1038/s41586-023-06521-7.

H. Atek, I. Labbé, L. J. Furtak, I. Chemerynska, S. Fujimoto, D. J. Setton, T. B. Miller, P. Oesch, R. Bezanson, S. H. Price, P. Dayal, A. Zitrin, V. Kokorev, J. R. Weaver, G. Brammer, et al. First spectroscopic observations of the galaxies that reionized the Universe. arXiv e-prints, arXiv:2308.08540, 2023. doi:10.48550/arXiv.2308.08540.

H. Atek, M. Shuntov, L. J. Furtak, J. Richard, J.-P. Kneib, G. Mahler, A. Zitrin, H. J. McCracken, S. Charlot, J. Chevallard, and I. Chemerynska. Revealing galaxy candidates out to z 16 with JWST observations of the lensing cluster SMACS0723. MNRAS, 2022. doi:10.1093/mnras/stac3144.

M. Baes and P. Camps. SKIRT: The design of a suite of input models for Monte Carlo radiative transfer simulations. Astronomy and Computing, volume 12:33–44, 2015. doi:10.1016/j.ascom.2015.05.006.

T. J. L. C. Bakx, Y. Tamura, T. Hashimoto, A. K. Inoue, M. M. Lee, K. Mawatari, K. Ota, H. Umehata, E. Zackrisson, B. Hatsukade, K. Kohno, Y. Matsuda, H. Matsuo, T. Okamoto, T. Shibuya, et al. ALMA uncovers the [CII] emission and warm dust continuum in a z = 8.31 Lyman break galaxy. arXiv e-prints, arXiv:2001.02812, 2020. https://ui.adsabs.harvard.edu/abs/2020arXiv200102812B.

T. J. L. C. Bakx, J. A. Zavala, I. Mitsuhashi, T. Treu, A. Fontana, K.-i. Tadaki, C. M. Casey, M. Castellano, K. Glazebrook, M. Hagimoto, R. Ikeda, T. Jones, N. Leethochawalit, C. Mason, T. Morishita, et al. Deep ALMA redshift search of a z $\sim$ 12 GLASS-JWST galaxy candidate. MNRAS, volume 519(4):5076–5085, 2023. doi:10.1093/mnras/stac3723.

I. K. Baldry, S. P. Driver, J. Loveday, E. N. Taylor, L. S. Kelvin, J. Liske, P. Norberg, A. S. G. Robotham, S. Brough, A. M. Hopkins, S. P. Bamford, J. A. Peacock, J. Bland-Hawthorn, C. J. Conselice, S. M. Croom, et al. Galaxy And Mass Assembly (GAMA): the galaxy stellar mass function at z $<$ 0.06. MNRAS, volume 421(1):621–634, 2012. doi:10.1111/j.1365-2966.2012.20340.x.

R. Barkana and A. Loeb. In the beginning: the first sources of light and the reionization of the universe. Phys. Rep., volume 349(2):125–238, 2001. doi:10.1016/S0370-1573(01)00019-9.

J. Barnes and P. Hut. A hierarchical O(N log N) force-calculation algorithm. Nature, volume 324(6096):446–449, 1986. doi:10.1038/324446a0.

L. Barrufet, P. A. Oesch, A. Weibel, G. Brammer, R. Bezanson, R. Bouwens, Y. Fudamoto, V. Gonzalez, G. Illingworth, K. E. Heintz, B. Holden, I. Labbe, D. Magee, R. P. Naidu, E. Nelson, et al. Unveiling the Nature of Infrared Bright, Optically Dark Galaxies with Early JWST Data. arXiv e-prints, arXiv:2207.14733, 2022. https://ui.adsabs.harvard.edu/abs/2022arXiv220714733B.

J. Bedorf and S. Portegies Zwart. Bonsai-SPH: A GPU accelerated astrophysical Smoothed Particle Hydrodynamics code. SciPost Astronomy, volume 1(1):001, 2020. doi:10.21468/SciPostAstro.1.1.001.

P. Behroozi, C. Conroy, R. H. Wechsler, A. Hearin, C. C. Williams, B. P. Moster, L. Y. A. Yung, R. S. Somerville, S. Gottlöber, G. Yepes, and R. Endsley. The Universe at z $>$ 10: predictions for JWST from the UNIVERSEMACHINE DR1. MNRAS, volume 499(4):5702–5718, 2020. doi:10.1093/mnras/staa3164.

P. Behroozi, R. H. Wechsler, A. P. Hearin, and C. Conroy. UniverseMachine: the correlation between galaxy growth and dark matter halo assembly from z = 0-10. Monthly Notices of the Royal Astronomical Society, volume 488(3):3143–3194, 2019. http://dx.doi.org/10.1093/mnras/stz1182.

P. S. Behroozi, G. Zhu, H. C. Ferguson, A. P. Hearin, J. Lotz, J. Silk, S. Kassin, Y. Lu, D. Croton, R. S. Somerville, and D. F. Watson. Using galaxy pairs to probe star formation during major halo mergers. MNRAS, volume 450(2):1546–1564, 2015. doi:10.1093/mnras/stv728.

C. L. Bennett, N. W. Boggess, E. S. Cheng, M. G. Hauser, T. Kelsall, J. C. Mather, J. Moseley, S. H., T. L. Murdock, R. A. Shafer, R. F. Silverberg, G. F. Smooth, R. Weiss, and E. L. Wright. Scientific results from COBE. Advances in Space Research, volume 13(12):409–423, 1993. doi:10.1016/0273-1177(93)90150-A.

C. L. Bennett, D. Larson, J. L. Weiland, N. Jarosik, G. Hinshaw, N. Odegard, K. M. Smith, R. S. Hill, B. Gold, M. Halpern, E. Komatsu, M. R. Nolta, L. Page, D. N. Spergel, E. Wollack, et al. Nine-year Wilkinson Microwave Anisotropy Probe (WMAP) Observations: Final Maps and Results. ApJS, volume 208(2):20, 2013. doi:10.1088/0067-0049/208/2/20.

E. Bertschinger. Simulations of Structure Formation in the Universe. ARA&A, volume 36:599–654, 1998. doi:10.1146/annurev.astro.36.1.599.

M. Béthermin, M. Dessauges-Zavadsky, A. L. Faisst, M. Ginolfi, C. Gruppioni, G. C. Jones, Y. Khusanova, B. Lemaux, P. L. Capak, P. Cassata, O. Le Fèvre, D. Schaerer, J. D. Silverman, L. Yan, and Alpine Collaboration. The ALPINE-ALMA [CII] Survey: Exploring the Dark Side of Normal Galaxies at the End of Reionisation. The Messenger, volume 180:31–36, 2020a. doi:10.18727/0722-6691/5198.

M. Béthermin, M. Dessauges-Zavadsky, A. L. Faisst, M. Ginolfi, C. Gruppioni, G. C. Jones, Y. Khusanova, B. Lemaux, P. L. Capak, P. Cassata, O. Le Fèvre, D. Schaerer, J. D. Silverman, L. Yan, and Alpine Collaboration. The ALPINE-ALMA [CII] Survey: Exploring the Dark Side of Normal Galaxies at the End of Reionisation. The Messenger, volume 180:31–36, 2020b. doi:10.18727/0722-6691/5198.

M. Béthermin, Y. Fudamoto, M. Ginolfi, F. Loiacono, Y. Khusanova, P. L. Capak, P. Cassata, A. Faisst, O. Le Fèvre, D. Schaerer, J. D. Silverman, L. Yan, R. Amorin, S. Bardelli, M. Boquien, et al. The ALPINE-ALMA [CII] survey: Data processing, catalogs, and statistical source properties. A&A, volume 643:A2, 2020c. doi:10.1051/0004-6361/202037649.

M. Betoule, R. Kessler, J. Guy, J. Mosher, D. Hardin, R. Biswas, P. Astier, P. El-Hage, M. Konig, S. Kuhlmann, J. Marriner, R. Pain, N. Regnault, C. Balland, B. A. Bassett, et al. Improved cosmological constraints from a joint analysis of the SDSS-II and SNLS supernova samples. A&A, volume 568:A22, 2014. doi:10.1051/0004-6361/201423413.

R. Bhatawdekar, C. J. Conselice, B. Margalef-Bentabol, and K. Duncan. Evolution of the galaxy stellar mass functions and UV luminosity functions at z = 6-9 in the Hubble Frontier Fields. MNRAS, volume 486(3):3805–3830, 2019. doi:10.1093/mnras/stz866.

S. Bianchi. Vindicating single-T modified blackbody fits to Herschel SEDs. A&A, volume 552:A89, 2013. doi:10.1051/0004-6361/201220866.

S. Bianchi and R. Schneider. Dust formation and survival in supernova ejecta. MNRAS, volume 378(3):973–982, 2007. doi:10.1111/j.1365-2966.2007.11829.x.

J. Binney. The physics of dissipational galaxy formation. ApJ, volume 215:483–491, 1977. doi:10.1086/155378.

Y. Birnboim and A. Dekel. Virial shocks in galactic haloes? MNRAS, volume 345(1):349–364, 2003. doi:10.1046/j.1365-8711.2003.06955.x.

M. Bocchio, A. P. Jones, and J. D. Slavin. A re-evaluation of dust processing in supernova shock waves. A&A, volume 570:A32, 2014. doi:10.1051/0004-6361/201424368.

M. Bocchio, S. Marassi, R. Schneider, S. Bianchi, M. Limongi, and A. Chieffi. Dust grains from the heart of supernovae. A&A, volume 587:A157, 2016a. doi:10.1051/0004-6361/201527432.

M. Bocchio, S. Marassi, R. Schneider, S. Bianchi, M. Limongi, and A. Chieffi. Dust grains from the heart of supernovae. A&A, volume 587:A157, 2016b. doi:10.1051/0004-6361/201527432.

A. M. Boesgaard and G. Steigman. Big Bang nucleosynthesis: theories and observations. ARA&A, volume 23:319–378, 1985. doi:10.1146/annurev.aa.23.090185.001535.

T. Böker, S. Arribas, N. Lützgendorf, C. Alves de Oliveira, T. L. Beck, S. Birkmann, A. J. Bunker, S. Charlot, G. de Marchi, P. Ferruit, G. Giardino, P. Jakobsen, N. Kumari, M. López-Caniego, R. Maiolino, et al. The Near-Infrared Spectrograph (NIRSpec) on the James Webb Space Telescope. III. Integral-field spectroscopy. A&A, volume 661:A82, 2022. doi:10.1051/0004-6361/202142589.

T. Böker, T. L. Beck, S. M. Birkmann, G. Giardino, C. Keyes, N. Kumari, J. Muzerolle, T. Rawle, P. Zeidler, Y. Abul-Huda, C. Alves de Oliveira, S. Arribas, K. Bechtold, R. Bhatawdekar, N. Bonaventura, et al. In-orbit Performance of the Near-infrared Spectrograph NIRSpec on the James Webb Space Telescope. PASP, volume 135(1045):038001, 2023. doi:10.1088/1538-3873/acb846.

R. Bouwens, J. González-López, M. Aravena, R. Decarli, M. Novak, M. Stefanon, F. Walter, L. Boogaard, C. Carilli, U. Dudzevičiūtė, I. Smail, E. Daddi, E. da Cunha, R. Ivison, T. Nanayakkara, et al. The ALMA Spectroscopic Survey Large Program: the Infrared Excess of z = 1.5–10 UV-selected galaxies and the implied high-redshift Star Formation History. The Astrophysical Journal, volume 902(2):112, 2020. https://ui.adsabs.harvard.edu/abs/2020ApJ...902..112B/abstract.

R. J. Bouwens, G. Illingworth, R. S. Ellis, P. Oesch, and M. Stefanon. z 2-9 Galaxies Magnified by the Hubble Frontier Field Clusters. II. Luminosity Functions and Constraints on a Faint-end Turnover. ApJ, volume 940(1):55, 2022a. doi:10.3847/1538-4357/ac86d1.

R. J. Bouwens, G. D. Illingworth, P. A. Oesch, M. Trenti, I. Labbé, L. Bradley, M. Carollo, P. G. van Dokkum, V. Gonzalez, B. Holwerda, M. Franx, L. Spitler, R. Smit, and D. Magee. UV Luminosity Functions at Redshifts z ∼ 4 to z

$\sim$ 10: 10,000 Galaxies from HST Legacy Fields. ApJ, volume 803:34, 2015. doi:10.1088/0004-637X/803/1/34.

R. J. Bouwens, P. A. Oesch, M. Stefanon, G. Illingworth, I. Labbé, N. Reddy, H. Atek, M. Montes, R. Naidu, T. Nanayakkara, E. Nelson, and S. Wilkins. New Determinations of the UV Luminosity Functions from z 9 to 2 Show a Remarkable Consistency with Halo Growth and a Constant Star Formation Efficiency. AJ, volume 162(2):47, 2021a. doi:10.3847/1538-3881/abf83e.

R. J. Bouwens, R. Smit, S. Schouws, M. Stefanon, R. Bowler, R. Endsley, V. Gonzalez, H. Inami, D. Stark, P. Oesch, J. Hodge, M. Aravena, E. da Cunha, P. Dayal, I. de Looze, et al. Reionization Era Bright Emission Line Survey: Selection and Characterization of Luminous Interstellar Medium Reservoirs in the z>6.5 Universe. arXiv e-prints, arXiv:2106.13719, 2021b. https://ui.adsabs.harvard.edu/abs/2021arXiv210613719B.

R. J. Bouwens, R. Smit, S. Schouws, M. Stefanon, R. Bowler, R. Endsley, V. Gonzalez, H. Inami, D. Stark, P. Oesch, J. Hodge, M. Aravena, E. da Cunha, P. Dayal, I. d. Looze, et al. Reionization Era Bright Emission Line Survey: Selection and Characterization of Luminous Interstellar Medium Reservoirs in the z $>$ 6.5 Universe. ApJ, volume 931(2):160, 2022b. doi:10.3847/1538-4357/ac5a4a.

R. A. A. Bowler, J. S. Dunlop, R. J. McLure, A. B. Rogers, H. J. McCracken, B. Milvang-Jensen, H. Furusawa, J. P. U. Fynbo, Y. Taniguchi, J. Afonso, M. N. Bremer, and O. Le Fèvre. The bright end of the galaxy luminosity function at z $\sim$ 7: before the onset of mass quenching? MNRAS, volume 440(3):2810–2842, 2014. doi:10.1093/mnras/stu449.

R. A. A. Bowler, H. Inami, L. Sommovigo, R. Smit, H. S. B. Algera, M. Aravena, L. Barrufet, R. Bouwens, E. da Cunha, F. Cullen, P. Dayal, I. De Looze, J. S. Dunlop, Y. Fudamoto, V. Mauerhofer, et al. The ALMA REBELS survey: obscured star formation in massive Lyman-break galaxies at z= 4-8 revealed by the IRX-β and $M_\star$ relations. MNRAS, volume 527(3):5808–5828, 2024. doi:10.1093/mnras/stad3578.

R. A. A. Bowler, M. J. Jarvis, J. S. Dunlop, R. J. McLure, D. J. McLeod, N. J. Adams, B. Milvang-Jensen, and H. J. McCracken. A lack of evolution in the very bright end of the galaxy luminosity function from z $\sim$ 8 to 10. MNRAS, volume 493(2):2059–2084, 2020. doi:10.1093/mnras/staa313.

M. Boylan-Kolchin. Stress testing ΛCDM with high-redshift galaxy candidates. Nature Astronomy, volume 7:731–735, 2023. doi:10.1038/s41550-023-01937-7.

M. Boylan-Kolchin, V. Springel, S. D. M. White, A. Jenkins, and G. Lemson. Resolving cosmic structure formation with the Millennium-II Simulation. MNRAS, volume 398(3):1150–1164, 2009. doi:10.1111/j.1365-2966.2009.15191.x.

V. Bromm and R. B. Larson. The First Stars. ARA&A, volume 42(1):79–118, 2004. doi:10.1146/annurev.astro.42.053102.134034.

V. Bromm and N. Yoshida. The First Galaxies. ARA&A, volume 49(1):373–407, 2011. doi:10.1146/annurev-astro-081710-102608.

A. M. Brooks, F. Governato, T. Quinn, C. B. Brook, and J. Wadsley. The Role of Cold Flows in the Assembly of Galaxy Disks. ApJ, volume 694(1):396–410, 2009. doi:10.1088/0004-637X/694/1/396.

A. J. Bunker, A. Saxena, A. J. Cameron, C. J. Willott, E. Curtis-Lake, P. Jakobsen, S. Carniani, R. Smit, R. Maiolino, J. Witstok, M. Curti, F. D'Eugenio, G. C. Jones, P. Ferruit, S. Arribas, et al. JADES NIRSpec Spectroscopy of GN-z11: Lyman-α emission and possible enhanced nitrogen abundance in a z = 10.60 luminous galaxy. A&A, volume 677:A88, 2023. doi:10.1051/0004-6361/202346159.

F. Calura, F. Pozzi, G. Cresci, P. Santini, C. Gruppioni, L. Pozzetti, R. Gilli, F. Matteucci, and R. Maiolino. The dust-to-stellar mass ratio as a valuable tool to probe the evolution of local and distant star-forming galaxies. MNRAS, volume 465(1):54–67, 2017. doi:10.1093/mnras/stw2749.

A. J. Cameron, H. Katz, M. P. Rey, and A. Saxena. Nitrogen enhancements 440 Myr after the big bang: supersolar N/O, a tidal disruption event, or a dense stellar cluster in GN-z11? MNRAS, volume 523(3):3516–3525, 2023a. doi:10.1093/mnras/stad1579.

A. J. Cameron, H. Katz, C. Witten, A. Saxena, N. Laporte, and A. J. Bunker. Nebular dominated galaxies in the early Universe with top-heavy stellar initial mass functions. arXiv e-prints, arXiv:2311.02051, 2023b. doi:10.48550/arXiv.2311.02051.

A. J. Cameron, A. Saxena, A. J. Bunker, F. D'Eugenio, S. Carniani, R. Maiolino, E. Curtis-Lake, P. Ferruit, P. Jakobsen, S. Arribas, N. Bonaventura, S. Charlot, J. Chevallard, M. Curti, T. J. Looser, et al. JADES: Probing interstellar medium conditions at z $\sim$ 5.5-9.5 with ultra-deep JWST/NIRSpec spectroscopy. A&A, volume 677:A115, 2023c. doi:10.1051/0004-6361/202346107.

P. Capak, H. Aussel, K. Bundy, M. Bethermin, M. Carollo, R. Ram-Chary, F. Civano, J. Coupon, C. Diener, J. Donley, J. Dunlop, M. Elvis, A. Faisst, S. Foucaud, J. Green, et al. SPLASH: Spitzer Large Area Survey with Hyper-Suprime-Cam. Spitzer Proposal ID #10042, 2013. https://ui.adsabs.harvard.edu/abs/2013sptz.prop10042C.

P. L. Capak, C. Carilli, G. Jones, C. M. Casey, D. Riechers, K. Sheth, C. M. Carollo, O. Ilbert, A. Karim, O. Lefevre, S. Lilly, N. Scoville, V. Smolcic, and L. Yan. Galaxies at redshifts 5 to 6 with systematically low dust content and high [C II] emission. Nature, volume 522:455–458, 2015. doi:10.1038/nature14500.

K. I. Caputi, M. Cirasuolo, J. S. Dunlop, R. J. McLure, D. Farrah, and O. Almaini. The stellar mass function of the most-massive galaxies at 3 $\leq$z $<$ 5 in the UKIDSS Ultra Deep Survey. MNRAS, volume 413(1):162–176, 2011. doi:10.1111/j.1365-2966.2010.18118.x.

C. N. Cardamone, P. G. van Dokkum, C. M. Urry, Y. Taniguchi, E. Gawiser, G. Brammer, E. Taylor, M. Damen, E. Treister, B. E. Cobb, N. Bond, K. Schawinski, P. Lira, T. Murayama, T. Saito, et al. The Multiwavelength Survey by

Yale-Chile (MUSYC): Deep Medium-band Optical Imaging and High-quality 32-band Photometric Redshifts in the ECDF-S. ApJS, volume 189(2):270–285, 2010. doi:10.1088/0067-0049/189/2/270.

C. L. Carilli and F. Walter. Cool Gas in High-Redshift Galaxies. ARA&A, volume 51(1):105–161, 2013. doi:10.1146/annurev-astro-082812-140953.

A. C. Carnall, D. J. McLeod, R. J. McLure, J. S. Dunlop, R. Begley, F. Cullen, C. T. Donnan, M. L. Hamadouche, S. M. Jewell, E. W. Jones, C. L. Pollock, and V. Wild. A surprising abundance of massive quiescent galaxies at $3 < z < 5$ in the first data from JWST CEERS. MNRAS, volume 520(3):3974–3985, 2023. doi:10.1093/mnras/stad369.

S. Carniani, R. Maiolino, R. Amorin, L. Pentericci, A. Pallottini, A. Ferrara, C. J. Willott, R. Smit, J. Matthee, D. Sobral, P. Santini, M. Castellano, S. De Barros, A. Fontana, A. Grazian, et al. Kiloparsec-scale gaseous clumps and star formation at z = 5-7. MNRAS, volume 478(1):1170–1184, 2018a. doi:10.1093/mnras/sty1088.

S. Carniani, R. Maiolino, R. Smit, and R. Amorín. ALMA Detection of Extended [C II] Emission in Himiko at z = 6.6. ApJ, volume 854(1):L7, 2018b. doi:10.3847/2041-8213/aaab45.

V. Casasola, S. Bianchi, P. De Vis, L. Magrini, E. Corbelli, C. J. R. Clark, J. Fritz, A. Nersesian, S. Viaene, M. Baes, L. P. Cassarà, J. Davies, I. De Looze, W. Dobbels, M. Galametz, et al. The ISM scaling relations in DustPedia late-type galaxies: A benchmark study for the Local Universe. A&A, volume 633:A100, 2020. doi:10.1051/0004-6361/201936665.

C. M. Casey. Far-infrared spectral energy distribution fitting for galaxies near and far. MNRAS, volume 425(4):3094–3103, 2012. doi:10.1111/j.1365-2966.2012.21455.x.

C. M. Casey, J. Hodge, J. A. Zavala, J. Spilker, E. da Cunha, J. Staguhn, S. L. Finkelstein, and P. Drew. An Analysis of ALMA Deep Fields and the Perceived Dearth of High-z Galaxies. ApJ, volume 862(1):78, 2018. doi:10.3847/1538-4357/aacd11.

K. R. V. Casteels, C. J. Conselice, S. P. Bamford, E. Salvador-Solé, P. R. Norberg, N. K. Agius, I. Baldry, S. Brough, M. J. I. Brown, M. J. Drinkwater, S. P. Driver, A. W. Graham, J. Bland-Hawthorn, A. M. Hopkins, L. S. Kelvin, et al. Galaxy And Mass Assembly (GAMA): refining the local galaxy merger rate using morphological information. MNRAS, volume 445(2):1157–1169, 2014. doi:10.1093/mnras/stu1799.

M. Castellano, A. Fontana, T. Treu, P. Santini, E. Merlin, N. Leethochawalit, M. Trenti, E. Vanzella, U. Mestric, A. Bonchi, D. Belfiori, M. Nonino, D. Paris, G. Polenta, G. Roberts-Borsani, et al. Early Results from GLASS-JWST. III. Galaxy Candidates at z 9-15. ApJ, volume 938(2):L15, 2022. doi:10.3847/2041-8213/ac94d0.

C. Ceccarelli, S. Viti, N. Balucani, and V. Taquet. The evolution of grain mantles and silicate dust growth at high redshift. MNRAS, volume 476(1):1371–1383, 2018. doi:10.1093/mnras/sty313.

D. Ceverino, S. C. O. Glover, and R. S. Klessen. Introducing the FirstLight project: UV luminosity function and scaling relations of primeval galaxies. MNRAS, volume 470(3):2791–2798, 2017. doi:10.1093/mnras/stx1386.

D. Ceverino, R. S. Klessen, and S. C. O. Glover. FirstLight - II. Star formation rates of primeval galaxies from z=5-15. MNRAS, volume 480(4):4842–4850, 2018. doi:10.1093/mnras/sty2124.

G. Chabrier. Galactic Stellar and Substellar Initial Mass Function. PASP, volume 115(809):763–795, 2003a. doi:10.1086/376392.

G. Chabrier. Galactic Stellar and Substellar Initial Mass Function. PASP, volume 115(809):763–795, 2003b. doi:10.1086/376392.

J. Chevallard and S. Charlot. Modelling and interpreting spectral energy distributions of galaxies with BEAGLE. MNRAS, volume 462(2):1415–1443, 2016. doi:10.1093/mnras/stw1756.

S. Cole and C. Lacey. The structure of dark matter haloes in hierarchical clustering models. MNRAS, volume 281:716, 1996. doi:10.1093/mnras/281.2.716.

P. Coles and F. Lucchin. Cosmology: The Origin and Evolution of Cosmic Structure, Second Edition. 2002. https://ui.adsabs.harvard.edu/abs/2002coec.book.....C.

C. J. Conselice and J. Arnold. The structures of distant galaxies - II. Diverse galaxy structures and local environments at z = 4-6 implications for early galaxy assembly. MNRAS, volume 397(1):208–231, 2009. doi:10.1111/j.1365-2966.2009.14959.x.

C. J. Conselice, M. A. Bershady, M. Dickinson, and C. Papovich. A Direct Measurement of Major Galaxy Mergers at z<∼3. AJ, volume 126(3):1183–1207, 2003. doi:10.1086/377318.

C. J. Conselice, S. Rajgor, and R. Myers. The structures of distant galaxies - I. Galaxy structures and the merger rate to z ∼3 in the Hubble Ultra-Deep Field. MNRAS, volume 386(2):909–927, 2008. doi:10.1111/j.1365-2966.2008.13069.x.

A. Cooray, J. Calanog, J. L. Wardlow, J. Bock, C. Bridge, D. Burgarella, R. S. Bussmann, C. M. Casey, D. Clements, A. Conley, D. Farrah, H. Fu, R. Gavazzi, R. J. Ivison, N. La Porte, et al. HerMES: The Rest-frame UV Emission and a Lensing Model for the z = 6.34 Luminous Dusty Starburst Galaxy HFLS3. ApJ, volume 790(1):40, 2014. doi:10.1088/0004-637X/790/1/40.

W. I. Cowley, C. M. Baugh, S. Cole, C. S. Frenk, and C. G. Lacey. Predictions for deep galaxy surveys with JWST from ΛCDM. MNRAS, volume 474(2):2352–2372, 2018. doi:10.1093/mnras/stx2897.

G. Cresci, F. Mannucci, and M. Curti. Fundamental metallicity relation in CALIFA, SDSS-IV MaNGA, and high-z galaxies. A&A, volume 627:A42, 2019. doi:10.1051/0004-6361/201834637.

M. Curti, F. D'Eugenio, S. Carniani, R. Maiolino, L. Sandles, J. Witstok, W. M. Baker, J. S. Bennett, J. M. Piotrowska, S. Tacchella, S. Charlot, K. Nakajima, G. Maheson, F. Mannucci, A. Amiri, et al. The chemical enrichment in the early Universe as probed by JWST via direct metallicity measurements at z 8. MNRAS, volume 518(1):425–438, 2023. doi:10.1093/mnras/stac2737.

E. Curtis-Lake, S. Carniani, A. Cameron, S. Charlot, P. Jakobsen, R. Maiolino, A. Bunker, J. Witstok, R. Smit, J. Chevallard, C. Willott, P. Ferruit, S. Arribas, N. Bonaventura, M. Curti, et al. Spectroscopic confirmation of four metal-poor galaxies at z = 10.3-13.2. Nature Astronomy, volume 7:622–632, 2023. doi:10.1038/s41550-023-01918-w.

R. H. Cyburt, B. D. Fields, K. A. Olive, and T.-H. Yeh. Big bang nucleosynthesis: Present status. Reviews of Modern Physics, volume 88(1):015004, 2016. doi:10.1103/RevModPhys.88.015004.

E. Daddi, I. Delvecchio, P. Dimauro, B. Magnelli, C. Gomez-Guijarro, R. Coogan, D. Elbaz, B. S. Kalita, A. Le Bail, R. M. Rich, and Q. Tan. The bending of the star-forming main sequence traces the cold- to hot-accretion transition mass over $0 < z < 4$. A&A, volume 661:L7, 2022. doi:10.1051/0004-6361/202243574.

R. Davé, B. D. Oppenheimer, and K. Finlator. Galaxy evolution in cosmological simulations with outflows - I. Stellar masses and star formation rates. MNRAS, volume 415(1):11–31, 2011. doi:10.1111/j.1365-2966.2011.18680.x.

I. Davidzon, O. Ilbert, C. Laigle, J. Coupon, H. J. McCracken, I. Delvecchio, D. Masters, P. Capak, B. C. Hsieh, O. Le Fèvre, L. Tresse, M. Bethermin, Y. Y. Chang, A. L. Faisst, E. Le Floc'h, et al. The COSMOS2015 galaxy stellar mass function . Thirteen billion years of stellar mass assembly in ten snapshots. A&A, volume 605:A70, 2017. doi:10.1051/0004-6361/201730419.

R. Davé, D. Anglés-Alcázar, D. Narayanan, Q. Li, M. H. Rafieferantsoa, and S. Appleby. SIMBA: cosmological simulations with black hole growth and feedback. Monthly Notices of the Royal Astronomical Society, volume 486(2):2827–2849, 2019. http://dx.doi.org/10.1093/mnras/stz937.

P. Dayal, A. Ferrara, J. S. Dunlop, and F. Pacucci. Essential physics of early galaxy formation. MNRAS, volume 445(3):2545–2557, 2014. doi:10.1093/mnras/stu1848.

P. Dayal, A. Ferrara, L. Sommovigo, R. Bouwens, P. A. Oesch, R. Smit, V. Gonzalez, S. Schouws, M. Stefanon, C. Kobayashi, J. Bremer, H. S. B. Algera, M. Aravena, R. A. A. Bowler, E. da Cunha, et al. The ALMA REBELS survey: the dust content of z 7 lyman break galaxies. MNRAS, 2022a. doi:10.1093/mnras/stac537.

P. Dayal, A. Ferrara, L. Sommovigo, R. Bouwens, P. A. Oesch, R. Smit, V. Gonzalez, S. Schouws, M. Stefanon, C. Kobayashi, J. Bremer, H. S. B. Algera, M. Aravena,

R. A. A. Bowler, E. da Cunha, et al. The ALMA REBELS survey: the dust content of z 7 Lyman break galaxies. MNRAS, volume 512(1):989–1002, 2022b. doi:10.1093/mnras/stac537.

I. De Looze, D. Cormier, V. Lebouteiller, S. Madden, M. Baes, G. J. Bendo, M. Boquien, A. Boselli, D. L. Clements, L. Cortese, A. Cooray, M. Galametz, F. Galliano, J. Graciá-Carpio, K. Isaak, et al. The applicability of far-infrared fine-structure lines as star formation rate tracers over wide ranges of metallicities and galaxy types. A&A, volume 568:A62, 2014a. doi:10.1051/0004-6361/201322489.

I. De Looze, D. Cormier, V. Lebouteiller, S. Madden, M. Baes, G. J. Bendo, M. Boquien, A. Boselli, D. L. Clements, L. Cortese, A. Cooray, M. Galametz, F. Galliano, J. Graciá-Carpio, K. Isaak, et al. The applicability of far-infrared fine-structure lines as star formation rate tracers over wide ranges of metallicities and galaxy types. A&A, volume 568:A62, 2014b. doi:10.1051/0004-6361/201322489.

L. de Ravel, O. Le Fèvre, L. Tresse, D. Bottini, B. Garilli, V. Le Brun, D. Maccagni, R. Scaramella, M. Scodeggio, G. Vettolani, A. Zanichelli, C. Adami, S. Arnouts, S. Bardelli, M. Bolzonella, et al. The VIMOS VLT Deep Survey. Evolution of the major merger rate since z $\sim$1 from spectroscopically confirmed galaxy pairs. A&A, volume 498(2):379–397, 2009. doi:10.1051/0004-6361/200810569.

I. Debono and G. F. Smoot. General Relativity and Cosmology: Unsolved Questions and Future Directions. Universe, volume 2(4):23, 2016. doi:10.3390/universe2040023.

A. Dekel and Y. Birnboim. Galaxy bimodality due to cold flows and shock heating. MNRAS, volume 368(1):2–20, 2006. doi:10.1111/j.1365-2966.2006.10145.x.

A. Dekel, Y. Birnboim, G. Engel, J. Freundlich, T. Goerdt, M. Mumcuoglu, E. Neistein, C. Pichon, R. Teyssier, and E. Zinger. Cold streams in early massive hot haloes as the main mode of galaxy formation. Nature, volume 457(7228):451–454, 2009a. doi:10.1038/nature07648.

A. Dekel, R. Sari, and D. Ceverino. Formation of Massive Galaxies at High Redshift: Cold Streams, Clumpy Disks, and Compact Spheroids. ApJ, volume 703(1):785–801, 2009b. doi:10.1088/0004-637X/703/1/785.

A. Dekel, K. C. Sarkar, Y. Birnboim, N. Mandelker, and Z. Li. Efficient formation of massive galaxies at cosmic dawn by feedback-free starbursts. MNRAS, volume 523(3):3201–3218, 2023. doi:10.1093/mnras/stad1557.

G. Desprez, N. S. Martis, Y. Asada, M. Sawicki, C. J. Willott, A. Muzzin, R. G. Abraham, M. Bradač, G. Brammer, V. Estrada-Carpenter, K. G. Iyer, J. Matharu, L. Mowla, G. Noirot, G. T. E. Sarrouh, et al. ΛCDM not dead yet: massive high-z Balmer break galaxies are less common than previously reported. arXiv e-prints, arXiv:2310.03063, 2023. doi:10.48550/arXiv.2310.03063.

M. Dessauges-Zavadsky, M. Ginolfi, F. Pozzi, M. Béthermin, O. Le Fèvre, S. Fujimoto, J. D. Silverman, G. C. Jones, L. Vallini, D. Schaerer, A. L. Faisst, Y. Khusanova,

Y. Fudamoto, P. Cassata, F. Loiacono, et al. The ALPINE-ALMA [C II] survey. Molecular gas budget in the early Universe as traced by [C II]. A&A, volume 643:A5, 2020. doi:10.1051/0004-6361/202038231.

C. Di Cesare, L. Graziani, R. Schneider, M. Ginolfi, A. Venditti, P. Santini, and L. K. Hunt. The assembly of dusty galaxies at z $\geq$ 4: the build-up of stellar mass and its scaling relations with hints from early JWST data. MNRAS, volume 519(3):4632–4650, 2023. doi:10.1093/mnras/stac3702.

E. M. Di Teodoro and F. Fraternali. ^{3D} BAROLO: a new 3D algorithm to derive rotation curves of galaxies. MNRAS, volume 451(3):3021–3033, 2015. doi:10.1093/mnras/stv1213.

E. Di Valentino, L. A. Anchordoqui, Ö. Akarsu, Y. Ali-Haimoud, L. Amendola, N. Arendse, M. Asgari, M. Ballardini, S. Basilakos, E. Battistelli, M. Benetti, S. Birrer, F. R. Bouchet, M. Bruni, E. Calabrese, et al. Cosmology Intertwined II: The hubble constant tension. Astroparticle Physics, volume 131:102605, 2021. doi:10.1016/j.astropartphys.2021.102605.

C. T. Donnan, D. J. McLeod, J. S. Dunlop, R. J. McLure, A. C. Carnall, R. Begley, F. Cullen, M. L. Hamadouche, R. A. A. Bowler, D. Magee, H. J. McCracken, B. Milvang-Jensen, A. Moneti, and T. Targett. The evolution of the galaxy UV luminosity function at redshifts z $\approx$ 8 - 15 from deep JWST and ground-based near-infrared imaging. MNRAS, 2022. doi:10.1093/mnras/stac3472.

R. Doyon, J. B. Hutchings, M. Beaulieu, L. Albert, D. Lafrenière, C. Willott, D. Touahri, N. Rowlands, M. Maszkiewicz, A. W. Fullerton, K. Volk, A. R. Martel, P. Chayer, A. Sivaramakrishnan, R. Abraham, et al. The JWST Fine Guidance Sensor (FGS) and Near-Infrared Imager and Slitless Spectrograph (NIRISS). In M. C. Clampin, G. G. Fazio, H. A. MacEwen, and J. Oschmann, Jacobus M., editors, Space Telescopes and Instrumentation 2012: Optical, Infrared, and Millimeter Wave, volume 8442 of Society of Photo-Optical Instrumentation Engineers (SPIE) Conference Series, page 84422R. 2012. doi:10.1117/12.926578.

R. Doyon, C. J. Willott, J. B. Hutchings, A. Sivaramakrishnan, L. Albert, D. Lafrenière, N. Rowlands, M. Begoña Vila, A. R. Martel, S. LaMassa, D. Aldridge, É. Artigau, P. Cameron, P. Chayer, N. J. Cook, et al. The Near Infrared Imager and Slitless Spectrograph for the James Webb Space Telescope. I. Instrument Overview and In-flight Performance. PASP, volume 135(1051):098001, 2023. doi:10.1088/1538-3873/acd41b.

B. T. Draine. Physics of the Interstellar and Intergalactic Medium. Princeton University Press, 2011. http://adsabs.harvard.edu/abs/2011piim.book.....D.

K. Duncan, C. J. Conselice, A. Mortlock, W. G. Hartley, Y. Guo, H. C. Ferguson, R. Davé, Y. Lu, J. Ownsworth, M. L. N. Ashby, A. Dekel, M. Dickinson, S. Faber, M. Giavalisco, N. Grogin, et al. The mass evolution of the first galaxies: stellar mass functions and star formation rates at 4 < z < 7 in the CANDELS GOODS-South field. MNRAS, volume 444(3):2960–2984, 2014. doi:10.1093/mnras/stu1622.

K. Duncan, C. J. Conselice, C. Mundy, E. Bell, J. Donley, A. Galametz, Y. Guo, N. A. Grogin, N. Hathi, J. Kartaltepe, D. Kocevski, A. M. Koekemoer, P. G. Pérez-González, K. B. Mantha, G. F. Snyder, et al. Observational Constraints on the Merger History of Galaxies since z ≈ 6: Probabilistic Galaxy Pair Counts in the CANDELS Fields. ApJ, volume 876(2):110, 2019. doi:10.3847/1538-4357/ab148a.

D. J. Eisenstein, C. Willott, S. Alberts, S. Arribas, N. Bonaventura, A. J. Bunker, A. J. Cameron, S. Carniani, S. Charlot, E. Curtis-Lake, F. D'Eugenio, R. Endsley, P. Ferruit, G. Giardino, K. Hainline, et al. Overview of the JWST Advanced Deep Extragalactic Survey (JADES). arXiv e-prints, arXiv:2306.02465, 2023. doi:10.48550/arXiv.2306.02465.

D. J. Eisenstein, I. Zehavi, D. W. Hogg, R. Scoccimarro, M. R. Blanton, R. C. Nichol, R. Scranton, H.-J. Seo, M. Tegmark, Z. Zheng, S. F. Anderson, J. Annis, N. Bahcall, J. Brinkmann, S. Burles, et al. Detection of the Baryon Acoustic Peak in the Large-Scale Correlation Function of SDSS Luminous Red Galaxies. ApJ, volume 633(2):560–574, 2005. doi:10.1086/466512.

R. Endsley, D. P. Stark, R. J. Bouwens, S. Schouws, R. Smit, M. Stefanon, H. Inami, R. A. A. Bowler, P. Oesch, V. Gonzalez, M. Aravena, E. da Cunha, P. Dayal, A. Ferrara, L. Graziani, et al. The REBELS ALMA Survey: efficient Ly α transmission of UV-bright z ≈ 7 galaxies from large velocity offsets and broad line widths. MNRAS, volume 517(4):5642–5659, 2022. doi:10.1093/mnras/stac3064.

A. L. Faisst, D. Schaerer, B. C. Lemaux, P. A. Oesch, Y. Fudamoto, P. Cassata, M. Béthermin, P. L. Capak, O. Le Fèvre, J. D. Silverman, and et al. The alpine–alma [c ii] survey: Multiwavelength ancillary data and basic physical measurements. The Astrophysical Journal Supplement Series, volume 247(2):61, 2020. ISSN 1538-4365. doi:10.3847/1538-4365/ab7ccd.

A. L. Faisst, L. Yan, M. Béthermin, P. Cassata, M. Dessauges-Zavadsky, Y. Fudamoto, M. Ginolfi, C. Gruppioni, G. Jones, Y. Khusanova, O. LeFèvre, F. Pozzi, M. Romano, J. Silverman, and B. Vanderhoof. ALPINE: A Large Survey to Understand Teenage Galaxies. Universe, volume 8(6):314, 2022. doi:10.3390/universe8060314.

S. M. Fall and G. Efstathiou. Formation and rotation of disc galaxies with haloes. MNRAS, volume 193:189–206, 1980. doi:10.1093/mnras/193.2.189.

C.-A. Faucher-Giguère and S. P. Oh. Key Physical Processes in the Circumgalactic Medium. ARA&A, volume 61:131–195, 2023. doi:10.1146/annurev-astro-052920-125203.

G. J. Ferland, M. Chatzikos, F. Guzmán, M. L. Lykins, P. A. M. van Hoof, R. J. R. Williams, N. P. Abel, N. R. Badnell, F. P. Keenan, R. L. Porter, and P. C. Stancil. The 2017 Release Cloudy. , volume 53:385–438, 2017. doi:10.48550/arXiv.1705.10877.

A. Ferrara. Super-early JWST galaxies, outflows and Lyman alpha visibility in the EoR. arXiv e-prints, arXiv:2310.12197, 2023. doi:10.48550/arXiv.2310.12197.

A. Ferrara and A. Loeb. Escape fraction of the ionizing radiation from starburst galaxies at high redshifts. MNRAS, volume 431(3):2826–2833, 2013. doi:10.1093/mnras/stt381.

A. Ferrara, A. Pallottini, and P. Dayal. On the stunning abundance of super-early, luminous galaxies revealed by JWST. MNRAS, volume 522(3):3986–3991, 2023. doi:10.1093/mnras/stad1095.

A. Ferrara, L. Sommovigo, P. Dayal, A. Pallottini, R. J. Bouwens, V. Gonzalez, H. Inami, R. Smit, R. A. A. Bowler, R. Endsley, P. Oesch, S. Schouws, D. Stark, M. Stefanon, M. Aravena, et al. The ALMA REBELS Survey. Epoch of Reionization giants: Properties of dusty galaxies at z ≈ 7. MNRAS, volume 512(1):58–72, 2022. doi:10.1093/mnras/stac460.

A. Ferrara, L. Vallini, A. Pallottini, S. Gallerani, S. Carniani, M. Kohandel, D. Decataldo, and C. Behrens. A physical model for [C II] line emission from galaxies. MNRAS, volume 489(1):1–12, 2019. doi:10.1093/mnras/stz2031.

A. S. Ferrarotti and H. P. Gail. Composition and quantities of dust produced by AGB-stars and returned to the interstellar medium. A&A, volume 447(2):553–576, 2006. doi:10.1051/0004-6361:20041198.

P. Ferruit, P. Jakobsen, G. Giardino, T. Rawle, C. Alves de Oliveira, S. Arribas, T. L. Beck, S. Birkmann, T. Böker, A. J. Bunker, S. Charlot, G. de Marchi, M. Franx, A. Henry, D. Karakla, et al. The Near-Infrared Spectrograph (NIRSpec) on the James Webb Space Telescope. II. Multi-object spectroscopy (MOS). A&A, volume 661:A81, 2022. doi:10.1051/0004-6361/202142673.

S. L. Finkelstein, M. Bagley, M. Song, R. Larson, C. Papovich, M. Dickinson, K. Finkelstein, A. M. Koekemoer, N. Pirzkal, R. S. Somerville, L. Y. A. Yung, P. Behroozi, H. Ferguson, M. Giavalisco, N. Grogin, et al. A Census of the Bright z=8.5-11 Universe with the Hubble and Spitzer Space Telescopes in the CANDELS Fields. arXiv e-prints, arXiv:2106.13813, 2021. https://ui.adsabs.harvard.edu/abs/2021arXiv210613813F.

S. L. Finkelstein and M. B. Bagley. On the Coevolution of the AGN and Star-forming Galaxy Ultraviolet Luminosity Functions at $3 < z < 9$. ApJ, volume 938(1):25, 2022. doi:10.3847/1538-4357/ac89eb.

S. L. Finkelstein, M. B. Bagley, P. Arrabal Haro, M. Dickinson, H. C. Ferguson, J. S. Kartaltepe, C. Papovich, D. Burgarella, D. D. Kocevski, M. Huertas-Company, K. G. Iyer, R. L. Larson, P. G. Pérez-González, C. Rose, S. Tacchella, et al. A Long Time Ago in a Galaxy Far, Far Away: A Candidate z ∼14 Galaxy in Early JWST CEERS Imaging. arXiv e-prints, arXiv:2207.12474, 2022. https://ui.adsabs.harvard.edu/abs/2022arXiv220712474F.

S. L. Finkelstein, A. D'Aloisio, J.-P. Paardekooper, J. Ryan, Russell, P. Behroozi, K. Finlator, R. Livermore, P. R. Upton Sanderbeck, C. Dalla Vecchia, and S. Khochfar. Conditions for Reionizing the Universe with a Low Galaxy Ionizing Photon Escape Fraction. ApJ, volume 879(1):36, 2019. doi:10.3847/1538-4357/ab1ea8.

S. L. Finkelstein, G. C. K. Leung, M. B. Bagley, M. Dickinson, H. C. Ferguson, C. Papovich, H. B. Akins, P. Arrabal Haro, R. Dave, A. Dekel, J. S. Kartaltepe, D. D. Kocevski, A. M. Koekemoer, N. Pirzkal, R. S. Somerville, et al. The Complete CEERS Early Universe Galaxy Sample: A Surprisingly Slow Evolution of the Space Density of Bright Galaxies at z ∼8.5-14.5. arXiv e-prints, arXiv:2311.04279, 2023. doi:10.48550/arXiv.2311.04279.

S. L. Finkelstein, M. Song, P. Behroozi, R. S. Somerville, C. Papovich, M. Milosavljević, A. Dekel, D. Narayanan, M. L. N. Ashby, A. Cooray, G. G. Fazio, H. C. Ferguson, A. M. Koekemoer, B. Salmon, and S. P. Willner. An Increasing Stellar Baryon Fraction in Bright Galaxies at High Redshift. ApJ, volume 814(2):95, 2015. doi:10.1088/0004-637X/814/2/95.

F. Fiore, A. Ferrara, M. Bischetti, C. Feruglio, and A. Travascio. Dusty-wind-clear JWST Super-early Galaxies. ApJ, volume 943(2):L27, 2023. doi:10.3847/2041-8213/acb5f2.

J. Frieman, M. Turner, and D. Huterer. Dark energy and the accelerating universe. ARA&A, volume 46:385–432, 2008. doi:10.1146/annurev.astro.46.060407.145243.

Y. Fudamoto, P. A. Oesch, A. Faisst, M. Béthermin, M. Ginolfi, Y. Khusanova, F. Loiacono, O. Le Fèvre, P. Capak, D. Schaerer, J. D. Silverman, P. Cassata, L. Yan, R. Amorin, S. Bardelli, et al. The ALPINE-ALMA [CII] survey. Dust attenuation properties and obscured star formation at z ∼ 4.4-5.8. A&A, volume 643:A4, 2020. doi:10.1051/0004-6361/202038163.

Y. Fudamoto, P. A. Oesch, S. Schouws, M. Stefanon, R. Smit, R. J. Bouwens, R. A. A. Bowler, R. Endsley, V. Gonzalez, H. Inami, I. Labbe, D. Stark, M. Aravena, L. Barrufet, E. da Cunha, et al. Normal, dust-obscured galaxies in the epoch of reionization. Nature, volume 597(7877):489–492, 2021. doi:10.1038/s41586-021-03846-z.

Y. Fudamoto, P. A. Oesch, F. Walter, R. Decarli, C. L. Carilli, A. Ferrara, L. Barrufet, R. Bouwens, M. Dessauges-Zavadsky, E. J. Nelson, H. Dannerbauer, G. Illingworth, A. K. Inoue, R. Marques-Chaves, I. Pérez-Fournon, et al. NOEMA observations of GN-z11: Constraining Neutral Interstellar Medium and Dust Formation in the Heart of Cosmic Reionization at $z = 10.6$. arXiv e-prints, arXiv:2309.02493, 2023. doi:10.48550/arXiv.2309.02493.

Y. Fudamoto, R. Smit, R. A. A. Bowler, P. A. Oesch, R. Bouwens, M. Stefanon, H. Inami, R. Endsley, V. Gonzalez, S. Schouws, D. Stark, H. S. B. Algera, M. Aravena, L. Barrufet, E. da Cunha, et al. The ALMA REBELS Survey: Average [C II] 158 μm Sizes of Star-forming Galaxies from z 7 to z 4. ApJ, volume 934(2):144, 2022. doi:10.3847/1538-4357/ac7a47.

S. Fujimoto, M. Ouchi, A. Ferrara, A. Pallottini, R. J. Ivison, C. Behrens, S. Gallerani, S. Arata, H. Yajima, and K. Nagamine. First Identification of 10 kpc [C II] 158 μm Halos around Star-forming Galaxies at z = 5-7. ApJ, volume 887(2):107, 2019. doi:10.3847/1538-4357/ab480f.

S. Fujimoto, M. Ouchi, K. Nakajima, Y. Harikane, Y. Isobe, G. Brammer, M. Oguri, C. Giménez-Arteaga, K. E. Heintz, V. Kokorev, F. E. Bauer, A. Ferrara, T. Kojima, C. d. P. Lagos, S. Laura, et al. JWST and ALMA Multiple-Line Study in and around a Galaxy at $z = 8.496$: Optical to FIR Line Ratios and the Onset of an Outflow Promoting Ionizing Photon Escape. arXiv e-prints, arXiv:2212.06863, 2022. doi:10.48550/arXiv.2212.06863.

S. Fujimoto, J. D. Silverman, M. Bethermin, M. Ginolfi, G. C. Jones, O. Le Fèvre, M. Dessauges-Zavadsky, W. Rujopakarn, A. L. Faisst, Y. Fudamoto, P. Cassata, L. Morselli, R. Maiolino, D. Schaerer, P. Capak, et al. The ALPINE-ALMA [C II] Survey: Size of Individual Star-forming Galaxies at z = 4-6 and Their Extended Halo Structure. ApJ, volume 900(1):1, 2020. doi:10.3847/1538-4357/ab94b3.

M. Furlong, R. G. Bower, T. Theuns, J. Schaye, R. A. Crain, M. Schaller, C. Dalla Vecchia, C. S. Frenk, I. G. McCarthy, J. Helly, A. Jenkins, and Y. M. Rosas-Guevara. Evolution of galaxy stellar masses and star formation rates in the EAGLE simulations. MNRAS, volume 450(4):4486–4504, 2015. doi:10.1093/mnras/stv852.

S. Gallerani, A. Pallottini, C. Feruglio, A. Ferrara, R. Maiolino, L. Vallini, D. A. Riechers, and R. Pavesi. ALMA suggests outflows in z $\sim$ 5.5 galaxies. MNRAS, volume 473(2):1909–1917, 2018. doi:10.1093/mnras/stx2458.

F. Galliano, A. Nersesian, S. Bianchi, I. De Looze, S. Roychowdhury, M. Baes, V. Casasola, L. P. Cassará, W. Dobbels, J. Fritz, M. Galametz, A. P. Jones, S. C. Madden, A. Mosenkov, E. M. Xilouris, et al. A nearby galaxy perspective on dust evolution. Scaling relations and constraints on the dust build-up in galaxies with the DustPedia and DGS samples. A&A, volume 649:A18, 2021. doi:10.1051/0004-6361/202039701.

G. Gamow and E. Teller. On the Origin of Great Nebulae. Physical Review, volume 55(7):654–657, 1939. doi:10.1103/PhysRev.55.654.

J. P. Gardner, J. C. Mather, R. Abbott, J. S. Abell, M. Abernathy, F. E. Abney, J. G. Abraham, R. Abraham, Y. M. Abul-Huda, S. Acton, C. K. Adams, E. Adams, D. S. Adler, M. Adriaensen, J. A. Aguilar, et al. The James Webb Space Telescope Mission. PASP, volume 135(1048):068001, 2023. doi:10.1088/1538-3873/acd1b5.

P. M. Garnavich, R. P. Kirshner, P. Challis, J. Tonry, R. L. Gilliland, R. C. Smith, A. Clocchiatti, A. Diercks, A. V. Filippenko, M. Hamuy, C. J. Hogan, B. Leibundgut, M. M. Phillips, D. Reiss, A. G. Riess, et al. Constraints on Cosmological Models from Hubble Space Telescope Observations of High-z Supernovae. ApJ, volume 493(2):L53–L57, 1998. doi:10.1086/311140.

S. Genel, M. Vogelsberger, V. Springel, D. Sijacki, D. Nelson, G. Snyder, V. Rodriguez-Gomez, P. Torrey, and L. Hernquist. Introducing the Illustris project: the evolution of galaxy populations across cosmic time. MNRAS, volume 445(1):175–200, 2014. doi:10.1093/mnras/stu1654.

R. Giacconi, A. Zirm, J. Wang, P. Rosati, M. Nonino, P. Tozzi, R. Gilli, V. Mainieri, G. Hasinger, L. Kewley, J. Bergeron, S. Borgani, R. Gilmozzi, N. Grogin, A. Koeke-

moer, et al. Chandra Deep Field South: The 1 Ms Catalog. ApJS, volume 139(2):369–410, 2002. doi:10.1086/338927.

E. Giallongo, A. Grazian, F. Fiore, D. Kodra, T. Urrutia, M. Castellano, S. Cristiani, M. Dickinson, A. Fontana, N. Menci, L. Pentericci, K. Boutsia, J. A. Newman, and S. Puccetti. Space Densities and Emissivities of Active Galactic Nuclei at z > 4. ApJ, volume 884(1):19, 2019. doi:10.3847/1538-4357/ab39e1.

M. Giavalisco, H. C. Ferguson, A. M. Koekemoer, M. Dickinson, D. M. Alexander, F. E. Bauer, J. Bergeron, C. Biagetti, W. N. Brandt, S. Casertano, C. Cesarsky, E. Chatzichristou, C. Conselice, S. Cristiani, L. Da Costa, et al. The Great Observatories Origins Deep Survey: Initial Results from Optical and Near-Infrared Imaging. ApJ, volume 600(2):L93–L98, 2004. doi:10.1086/379232.

B. K. Gibson, Y. Fenner, A. Renda, D. Kawata, and H.-c. Lee. Galactic Chemical Evolution. PASA, volume 20(4):401–415, 2003. doi:10.1071/AS03052.

R. A. Gingold and J. J. Monaghan. Smoothed particle hydrodynamics: theory and application to non-spherical stars. MNRAS, volume 181:375–389, 1977. doi:10.1093/mnras/181.3.375.

M. Ginolfi, L. Graziani, R. Schneider, S. Marassi, R. Valiante, F. Dell'Agli, P. Ventura, and L. K. Hunt. Where does galactic dust come from? MNRAS, volume 473(4):4538–4543, 2018a. doi:10.1093/mnras/stx2572.

M. Ginolfi, L. Graziani, R. Schneider, S. Marassi, R. Valiante, F. Dell'Agli, P. Ventura, and L. K. Hunt. Where does galactic dust come from? MNRAS, volume 473(4):4538–4543, 2018b. doi:10.1093/mnras/stx2572.

M. Ginolfi, L. K. Hunt, C. Tortora, R. Schneider, and G. Cresci. Scaling relations and baryonic cycling in local star-forming galaxies. I. The sample. A&A, volume 638:A4, 2020a. doi:10.1051/0004-6361/201936304.

M. Ginolfi, G. C. Jones, M. Béthermin, A. Faisst, B. C. Lemaux, D. Schaerer, Y. Fudamoto, P. Oesch, M. Dessauges-Zavadsky, S. Fujimoto, S. Carniani, O. Le Fèvre, P. Cassata, J. D. Silverman, P. Capak, et al. The ALPINE-ALMA [CII] survey. Circumgalactic medium pollution and gas mixing by tidal stripping in a merging system at z ∼ 4.57. A&A, volume 643:A7, 2020b. doi:10.1051/0004-6361/202038284.

M. Ginolfi, G. C. Jones, M. Béthermin, A. Faisst, B. C. Lemaux, D. Schaerer, Y. Fudamoto, P. Oesch, M. Dessauges-Zavadsky, S. Fujimoto, S. Carniani, O. Le Fèvre, P. Cassata, J. D. Silverman, P. Capak, et al. The ALPINE-ALMA [CII] survey. Circumgalactic medium pollution and gas mixing by tidal stripping in a merging system at z ∼ 4.57. A&A, volume 643:A7, 2020c. doi:10.1051/0004-6361/202038284.

M. Ginolfi, G. C. Jones, M. Béthermin, Y. Fudamoto, F. Loiacono, S. Fujimoto, O. Le Févre, A. Faisst, D. Schaerer, P. Cassata, J. D. Silverman, L. Yan, P. Capak,

S. Bardelli, M. Boquien, et al. The ALPINE-ALMA [C II] survey: Star-formation-driven outflows and circumgalactic enrichment in the early Universe. A&A, volume 633:A90, 2020d. doi:10.1051/0004-6361/201936872.

M. Glatzle, B. Ciardi, and L. Graziani. Radiative transfer of ionizing radiation through gas and dust: the stellar source case. MNRAS, volume 482(1):321–336, 2019a. doi:10.1093/mnras/sty2514.

M. Glatzle, B. Ciardi, and L. Graziani. Radiative transfer of ionizing radiation through gas and dust: the stellar source case. MNRAS, volume 482(1):321–336, 2019b. doi:10.1093/mnras/sty2514.

M. Glatzle, L. Graziani, and B. Ciardi. Radiative transfer of ionizing radiation through gas and dust: grain charging in star-forming regions. MNRAS, volume 510(1):1068–1082, 2022a. doi:10.1093/mnras/stab3459.

M. Glatzle, L. Graziani, and B. Ciardi. Radiative transfer of ionizing radiation through gas and dust: grain charging in star-forming regions. MNRAS, volume 510(1):1068–1082, 2022b. doi:10.1093/mnras/stab3459.

N. Y. Gnedin, S. C. Glover, R. S. Klessen, and V. Springel. Star Formation in Galaxy Evolution: Connecting Numerical Models to Reality. 2016. doi:10.1007/978-3-662-47890-5.

Y. Gong, B. Yue, Y. Cao, and X. Chen. Fuzzy Dark Matter as a Solution to Reconcile the Stellar Mass Density of High-z Massive Galaxies and Reionization History. ApJ, volume 947(1):28, 2023. doi:10.3847/1538-4357/acc109.

I. Gott, J. R. and M. J. Rees. A theory of galaxy formation and clustering. A&A, volume 45:365–376, 1975. https://ui.adsabs.harvard.edu/abs/1975A&A....45..365G.

A. Grazian, A. Fontana, P. Santini, J. S. Dunlop, H. C. Ferguson, M. Castellano, R. Amorin, M. L. N. Ashby, G. Barro, P. Behroozi, K. Boutsia, K. I. Caputi, R. R. Chary, A. Dekel, M. E. Dickinson, et al. The galaxy stellar mass function at 3.5 $\leq$z $\leq$ 7.5 in the CANDELS/UDS, GOODS-South, and HUDF fields. A&A, volume 575:A96, 2015. doi:10.1051/0004-6361/201424750.

L. Graziani, B. Ciardi, and M. Glatzle. X-ray ionization of the intergalactic medium by quasars. MNRAS, volume 479(4):4320–4335, 2018. doi:10.1093/mnras/sty1367.

L. Graziani, M. de Bennassuti, R. Schneider, D. Kawata, and S. Salvadori. The history of the dark and luminous side of Milky Way-like progenitors. MNRAS, volume 469(1):1101–1116, 2017a. doi:10.1093/mnras/stx900.

L. Graziani, M. de Bennassuti, R. Schneider, D. Kawata, and S. Salvadori. The history of the dark and luminous side of Milky Way-like progenitors. MNRAS, volume 469(1):1101–1116, 2017b. doi:10.1093/mnras/stx900.

L. Graziani, A. Maselli, and B. Ciardi. CRASH3: cosmological radiative transfer through metals. MNRAS, volume 431(1):722–740, 2013. doi:10.1093/mnras/stt206.

L. Graziani, S. Salvadori, R. Schneider, D. Kawata, M. de Bennassuti, and A. Maselli. Galaxy formation with radiative and chemical feedback. MNRAS, volume 449(3):3137–3148, 2015. doi:10.1093/mnras/stv494.

L. Graziani, R. Schneider, M. Ginolfi, L. K. Hunt, U. Maio, M. Glatzle, and B. Ciardi. The assembly of dusty galaxies at z $\geq$ 4: statistical properties. MNRAS, volume 494(1):1071–1088, 2020. doi:10.1093/mnras/staa796.

N. Grevesse and E. Anders. Solar-system abundances of the elements: A new table. In C. J. Waddington, editor, Cosmic Abundances of Matter, volume 183 of American Institute of Physics Conference Series, pages 1–8. 1989. doi:10.1063/1.38013.

C. Gruppioni, M. Béthermin, F. Loiacono, O. Le Fèvre, P. Capak, P. Cassata, A. L. Faisst, D. Schaerer, J. Silverman, L. Yan, S. Bardelli, M. Boquien, R. Carraro, A. Cimatti, M. Dessauges-Zavadsky, et al. The ALPINE-ALMA [CII] survey. The nature, luminosity function, and star formation history of dusty galaxies up to z $\approx$ 6. A&A, volume 643:A8, 2020. doi:10.1051/0004-6361/202038487.

J. E. Gunn and I. Gott, J. Richard. On the Infall of Matter Into Clusters of Galaxies and Some Effects on Their Evolution. ApJ, volume 176:1, 1972. doi:10.1086/151605.

A. H. Guth. Inflationary universe: A possible solution to the horizon and flatness problems. Phys. Rev. D, volume 23(2):347–356, 1981. doi:10.1103/PhysRevD.23.347.

F. Haardt and P. Madau. Radiative Transfer in a Clumpy Universe. II. The Ultraviolet Extragalactic Background. ApJ, volume 461:20, 1996a. doi:10.1086/177035.

F. Haardt and P. Madau. Radiative Transfer in a Clumpy Universe. II. The Ultraviolet Extragalactic Background. ApJ, volume 461:20, 1996b. doi:10.1086/177035.

Y. Harikane, A. K. Inoue, K. Mawatari, T. Hashimoto, S. Yamanaka, Y. Fudamoto, H. Matsuo, Y. Tamura, P. Dayal, L. Y. A. Yung, A. Hutter, F. Pacucci, Y. Sugahara, and A. M. Koekemoer. A Search for H-Dropout Lyman Break Galaxies at z 12-16. ApJ, volume 929(1):1, 2022a. doi:10.3847/1538-4357/ac53a9.

Y. Harikane, K. Nakajima, M. Ouchi, H. Umeda, Y. Isobe, Y. Ono, Y. Xu, and Y. Zhang. Pure Spectroscopic Constraints on UV Luminosity Functions and Cosmic Star Formation History from 25 Galaxies at z $_{spec}$ = 8.61-13.20 Confirmed with JWST/NIRSpec. ApJ, volume 960(1):56, 2024. doi:10.3847/1538-4357/ad0b7e.

Y. Harikane, Y. Ono, M. Ouchi, C. Liu, M. Sawicki, T. Shibuya, P. S. Behroozi, W. He, K. Shimasaku, S. Arnouts, J. Coupon, S. Fujimoto, S. Gwyn, J. Huang, A. K. Inoue, et al. GOLDRUSH. IV. Luminosity Functions and clustering revealed with $\sim$ 4,000,000 Galaxies at z $\sim$ 2 – 7: galaxy-AGN transition, star formation efficiency, and implication for evolution at z $>$ 10. 2021. https://arxiv.org/abs/2108.01090.

Y. Harikane, M. Ouchi, M. Oguri, Y. Ono, K. Nakajima, Y. Isobe, H. Umeda, K. Mawatari, and Y. Zhang. A Comprehensive Study on Galaxies at z$\sim$9-17 Found in the Early JWST Data: UV Luminosity Functions and Cosmic Star-Formation

History at the Pre-Reionization Epoch. arXiv e-prints, arXiv:2208.01612, 2022b. https://ui.adsabs.harvard.edu/abs/2022arXiv220801612H.

Y. Harikane, M. Ouchi, Y. Ono, S. More, S. Saito, Y.-T. Lin, J. Coupon, K. Shimasaku, T. Shibuya, P. A. Price, L. Lin, B.-C. Hsieh, M. Ishigaki, Y. Komiyama, J. Silverman, et al. Evolution of Stellar-to-Halo Mass Ratio at z = 0 - 7 Identified by Clustering Analysis with the Hubble Legacy Imaging and Early Subaru/Hyper Suprime-Cam Survey Data. ApJ, volume 821(2):123, 2016. doi:10.3847/0004-637X/821/2/123.

T. Harvey, C. Conselice, N. J. Adams, D. Austin, I. Juodzbalis, J. Trussler, Q. Li, K. Ormerod, L. Ferreira, Q. Duan, L. Westcott, H. Harris, R. Bhatawdekar, D. Coe, S. H. Cohen, et al. EPOCHS IV: SED Modelling Assumptions and their impact on the Stellar Mass Function at $6.5 < z < 13.5$ using PEARLS and public JWST observations. arXiv e-prints, arXiv:2403.03908, 2024. doi:10.48550/arXiv.2403.03908.

T. Hashimoto, A. K. Inoue, K. Mawatari, Y. Tamura, H. Matsuo, H. Furusawa, Y. Harikane, T. Shibuya, K. K. Knudsen, K. Kohno, Y. Ono, E. Zackrisson, T. Okamoto, N. Kashikawa, P. A. Oesch, et al. "Big Three Dragons": a z = 7.15 Lyman BreakGalaxy Detected in [OIII] 88 μm, [CII] 158 μm, and Dust Continuum with ALMA. arXiv e-prints, 2018. http://adsabs.harvard.edu/abs/2018arXiv180600486H.

G. Hasinger, P. Capak, M. Salvato, A. J. Barger, L. L. Cowie, A. Faisst, S. Hemmati, Y. Kakazu, J. Kartaltepe, D. Masters, B. Mobasher, H. Nayyeri, D. Sanders, N. Z. Scoville, H. Suh, et al. The DEIMOS 10K Spectroscopic Survey Catalog of the COSMOS Field. ApJ, volume 858(2):77, 2018. doi:10.3847/1538-4357/aabacf.

M. Haslbauer, P. Kroupa, A. H. Zonoozi, and H. Haghi. Has JWST Already Falsified Dark-matter-driven Galaxy Formation? ApJ, volume 939(2):L31, 2022. doi:10.3847/2041-8213/ac9a50.

C. Hayden-Pawson, M. Curti, R. Maiolino, M. Cirasuolo, F. Belfiore, M. Cappellari, A. Concas, G. Cresci, F. Cullen, C. Kobayashi, F. Mannucci, A. Marconi, M. Meneghetti, A. Mercurio, Y. Peng, et al. The KLEVER survey: nitrogen abundances at z 2 and probing the existence of a fundamental nitrogen relation. MNRAS, volume 512(2):2867–2889, 2022. doi:10.1093/mnras/stac584.

A. Heger and S. E. Woosley. The nucleosynthetic signature of population III. The Astrophysical Journal, volume 567(1):532–543, 2002. doi:10.1086/338487.

L. Hernquist. An Analytical Model for Spherical Galaxies and Bulges. ApJ, volume 356:359, 1990. doi:10.1086/168845.

R. Herrera-Camus, A. D. Bolatto, M. G. Wolfire, J. D. Smith, K. V. Croxall, R. C. Kennicutt, D. Calzetti, G. Helou, F. Walter, A. K. Leroy, B. Draine, B. R. Brandl, L. Armus, K. M. Sandstrom, D. A. Dale, et al. [C II] 158 μm Emission as a Star Formation Tracer. ApJ, volume 800(1):1, 2015. doi:10.1088/0004-637X/800/1/1.

R. Herrera-Camus, N. Förster Schreiber, R. Genzel, L. Tacconi, A. Bolatto, R. L. Davies, D. Fisher, D. Lutz, T. Naab, T. Shimizu, K. Tadaki, and H. Übler. Kiloparsec view of a typical star-forming galaxy when the Universe was ∼1 Gyr old. I. Properties of outflow, halo, and interstellar medium. A&A, volume 649:A31, 2021. doi:10.1051/0004-6361/202039704.

R. Herrera-Camus, E. Sturm, J. Graciá-Carpio, D. Lutz, A. Contursi, S. Veilleux, J. Fischer, E. González-Alfonso, A. Poglitsch, L. Tacconi, R. Genzel, R. Maiolino, A. Sternberg, R. Davies, and A. Verma. SHINING, A Survey of Far-infrared Lines in Nearby Galaxies. II. Line-deficit Models, AGN Impact, [C II]-SFR Scaling Relations, and Mass-Metallicity Relation in (U)LIRGs. ApJ, volume 861(2):95, 2018. doi:10.3847/1538-4357/aac0f9.

S. Heß and V. Springel. Particle hydrodynamics with tessellation techniques. MNRAS, volume 406(4):2289–2311, 2010. doi:10.1111/j.1365-2966.2010.16892.x.

D. W. Hogg. Distance measures in cosmology. arXiv e-prints, astro-ph/9905116, 1999. doi:10.48550/arXiv.astro-ph/9905116.

D. J. Hollenbach and A. G. G. M. Tielens. Photodissociation regions in the interstellar medium of galaxies. Reviews of Modern Physics, volume 71(1):173–230, 1999. doi:10.1103/RevModPhys.71.173.

P. F. Hopkins. A new class of accurate, mesh-free hydrodynamic simulation methods. MNRAS, volume 450(1):53–110, 2015. doi:10.1093/mnras/stv195.

P. F. Hopkins, K. Bundy, D. Croton, L. Hernquist, D. Keres, S. Khochfar, K. Stewart, A. Wetzel, and J. D. Younger. Mergers and Bulge Formation in ΛCDM: Which Mergers Matter? ApJ, volume 715(1):202–229, 2010. doi:10.1088/0004-637X/715/1/202.

P. F. Hopkins, A. Wetzel, D. Kereš, C.-A. Faucher-Giguère, E. Quataert, M. Boylan-Kolchin, N. Murray, C. C. Hayward, S. Garrison-Kimmel, C. Hummels, R. Feldmann, P. Torrey, X. Ma, D. Anglés-Alcázar, K.-Y. Su, et al. FIRE-2 simulations: physics versus numerics in galaxy formation. MNRAS, volume 480(1):800–863, 2018. doi:10.1093/mnras/sty1690.

S. D. Horner and M. J. Rieke. The near-infrared camera (NIRCam) for the James Webb Space Telescope (JWST). In J. C. Mather, editor, Optical, Infrared, and Millimeter Space Telescopes, volume 5487 of Society of Photo-Optical Instrumentation Engineers (SPIE) Conference Series, pages 628–634. 2004. doi:10.1117/12.552281.

E. Hubble. A Relation between Distance and Radial Velocity among Extra-Galactic Nebulae. Proceedings of the National Academy of Science, volume 15(3):168–173, 1929. doi:10.1073/pnas.15.3.168.

D. H. Hughes, S. Serjeant, J. Dunlop, M. Rowan-Robinson, A. Blain, R. G. Mann, R. Ivison, J. Peacock, A. Efstathiou, W. Gear, S. Oliver, A. Lawrence, M. Longair, P. Goldschmidt, and T. Jenness. High-redshift star formation in the Hubble

Deep Field revealed by a submillimetre-wavelength survey. Nature, volume 394(6690):241–247, 1998. doi:10.1038/28328.

C. B. Hummels, B. D. Smith, P. F. Hopkins, B. W. O'Shea, D. W. Silvia, J. K. Werk, N. Lehner, J. H. Wise, D. C. Collins, and I. S. Butsky. The Impact of Enhanced Halo Resolution on the Simulated Circumgalactic Medium. ApJ, volume 882(2):156, 2019. doi:10.3847/1538-4357/ab378f.

L. K. Hunt, C. Tortora, M. Ginolfi, and R. Schneider. Scaling relations and baryonic cycling in local star-forming galaxies. II. Gas content and star-formation efficiency. A&A, volume 643:A180, 2020. doi:10.1051/0004-6361/202039021.

O. Ilbert, S. Arnouts, H. J. McCracken, M. Bolzonella, E. Bertin, O. Le Fèvre, Y. Mellier, G. Zamorani, R. Pellò, A. Iovino, L. Tresse, V. Le Brun, D. Bottini, B. Garilli, D. Maccagni, et al. Accurate photometric redshifts for the CFHT legacy survey calibrated using the VIMOS VLT deep survey. A&A, volume 457(3):841–856, 2006. doi:10.1051/0004-6361:20065138.

N. Imara, A. Loeb, B. D. Johnson, C. Conroy, and P. Behroozi. A Model Connecting Galaxy Masses, Star Formation Rates, and Dust Temperatures across Cosmic Time. ApJ, volume 854(1):36, 2018. doi:10.3847/1538-4357/aaa3f0.

H. Inami, H. S. B. Algera, S. Schouws, L. Sommovigo, R. Bouwens, R. Smit, M. Stefanon, R. A. A. Bowler, R. Endsley, A. Ferrara, P. Oesch, D. Stark, M. Aravena, L. Barrufet, E. da Cunha, et al. The ALMA REBELS Survey: dust continuum detections at z > 6.5. MNRAS, volume 515(3):3126–3143, 2022. doi:10.1093/mnras/stac1779.

P. Jakobsen, P. Ferruit, C. Alves de Oliveira, S. Arribas, G. Bagnasco, R. Barho, T. L. Beck, S. Birkmann, T. Böker, A. J. Bunker, S. Charlot, P. de Jong, G. de Marchi, R. Ehrenwinkler, M. Falcolini, et al. The Near-Infrared Spectrograph (NIRSpec) on the James Webb Space Telescope. I. Overview of the instrument and its capabilities. A&A, volume 661:A80, 2022. doi:10.1051/0004-6361/202142663.

J. Jeans. The Stability of a Spherical Nebula. Philosophical Transactions of the Royal Society of London Series A, volume 199:1–53, 1902. doi:10.1098/rsta.1902.0012.

L. Jiang, N. Kashikawa, S. Wang, G. Walth, L. C. Ho, Z. Cai, E. Egami, X. Fan, K. Ito, Y. Liang, D. Schaerer, and D. P. Stark. Evidence for GN-z11 as a luminous galaxy at redshift 10.957. Nature Astronomy, volume 5:256–261, 2021. doi:10.1038/s41550-020-01275-y.

B. D. Johnson, J. Leja, C. Conroy, and J. S. Speagle. Stellar Population Inference with Prospector. ApJS, volume 254(2):22, 2021. doi:10.3847/1538-4365/abef67.

J. L. Johnson, C. Dalla Vecchia, and S. Khochfar. The First Billion Years project: the impact of stellar radiation on the co-evolution of Populations II and III. Monthly Notices of the Royal Astronomical Society, volume 428(3):1857–1872, 2013. https://ui.adsabs.harvard.edu/abs/2013MNRAS.428.1857J.

G. C. Jones, M. Béthermin, Y. Fudamoto, M. Ginolfi, P. Capak, P. Cassata, A. Faisst, O. Le Fèvre, D. Schaerer, J. D. Silverman, L. Yan, S. Bardelli, M. Boquien, A. Cimatti, M. Dessauges-Zavadsky, et al. The ALPINE-ALMA [C II] survey: a triple merger at z $\sim$ 4.56. MNRAS, volume 491(1):L18–L23, 2020. doi:10.1093/mnrasl/slz154.

G. C. Jones, D. Vergani, M. Romano, M. Ginolfi, Y. Fudamoto, M. Béthermin, S. Fujimoto, B. C. Lemaux, L. Morselli, P. Capak, P. Cassata, A. Faisst, O. Le Fèvre, D. Schaerer, J. D. Silverman, et al. The ALPINE-ALMA [C II] Survey: kinematic diversity and rotation in massive star-forming galaxies at z 4.4-5.9. MNRAS, volume 507(3):3540–3563, 2021. doi:10.1093/mnras/stab2226.

M. Kaasinen, J. van Marrewijk, G. Popping, M. Ginolfi, L. Di Mascolo, T. Mroczkowski, A. Concas, C. Di Cesare, M. Killi, and I. Langan. To see or not to see a z $\sim$ 13 galaxy, that is the question. Targeting the [C II] 158 μm emission line of HD1 with ALMA. A&A, volume 671:A29, 2023. doi:10.1051/0004-6361/202245093.

R. Kannan, E. Garaldi, A. Smith, R. Pakmor, V. Springel, M. Vogelsberger, and L. Hernquist. Introducing the THESAN project: radiation-magnetohydrodynamic simulations of the epoch of reionization. MNRAS, volume 511(3):4005–4030, 2022. doi:10.1093/mnras/stab3710.

H. Katz, T. Kimm, D. Sijacki, and M. G. Haehnelt. Interpreting ALMA observations of the ISM during the epoch of reionization. MNRAS, volume 468(4):4831–4861, 2017. doi:10.1093/mnras/stx608.

N. Katz, D. H. Weinberg, and L. Hernquist. Cosmological Simulations with TreeSPH. ApJS, volume 105:19, 1996. doi:10.1086/192305.

S. Kaviraj, M. Huertas-Company, S. Cohen, S. Peirani, R. A. Windhorst, R. W. O'Connell, J. Silk, M. A. Dopita, N. P. Hathi, A. M. Koekemoer, S. Mei, M. Rutkowski, R. E. Ryan, and F. Shankar. The role of major mergers in the size growth of intermediate-mass spheroids. MNRAS, volume 443(2):1861–1866, 2014. doi:10.1093/mnras/stu1220.

J. Kennicutt, Robert C. The Global Schmidt Law in Star-forming Galaxies. ApJ, volume 498(2):541–552, 1998. doi:10.1086/305588.

D. Kereš, N. Katz, M. Fardal, R. Davé, and D. H. Weinberg. Galaxies in a simulated ΛCDM Universe - I. Cold mode and hot cores. MNRAS, volume 395(1):160–179, 2009. doi:10.1111/j.1365-2966.2009.14541.x.

Y. Khusanova, M. Bethermin, O. Le Fèvre, P. Capak, A. L. Faisst, D. Schaerer, J. D. Silverman, P. Cassata, L. Yan, M. Ginolfi, Y. Fudamoto, F. Loiacono, R. Amorin, S. Bardelli, M. Boquien, et al. The ALPINE-ALMA [CII] survey. Obscured star formation rate density and main sequence of star-forming galaxies at z $>$ 4. A&A, volume 649:A152, 2021. doi:10.1051/0004-6361/202038944.

S. Kikuchihara, M. Ouchi, Y. Ono, K. Mawatari, J. Chevallard, Y. Harikane, T. Kojima, M. Oguri, G. Bruzual, and S. Charlot. Early Low-mass Galaxies and Star-cluster Candidates at z $\sim$ 6-9 Identified by the Gravitational-lensing Technique and Deep Optical/Near-infrared Imaging. ApJ, volume 893(1):60, 2020. doi:10.3847/1538-4357/ab7dbe.

R. S. Klessen and S. C. O. Glover. The First Stars: Formation, Properties, and Impact. ARA&A, volume 61:65–130, 2023. doi:10.1146/annurev-astro-071221-053453.

A. Knebe, S. R. Knollmann, S. I. Muldrew, F. R. Pearce, M. A. Aragon-Calvo, Y. Ascasibar, P. S. Behroozi, D. Ceverino, S. Colombi, J. Diemand, K. Dolag, B. L. Falck, P. Fasel, J. Gardner, S. Gottlöber, et al. Haloes gone MAD: The Halo-Finder Comparison Project. MNRAS, volume 415(3):2293–2318, 2011. doi:10.1111/j.1365-2966.2011.18858.x.

S. R. Knollmann and A. Knebe. AHF: Amiga's Halo Finder. ApJS, volume 182:608–624, 2009. doi:10.1088/0067-0049/182/2/608.

C. Kobayashi and A. Ferrara. Rapid Chemical Enrichment by Intermittent Star Formation in GN-z11. ApJ, volume 962(1):L6, 2024. doi:10.3847/2041-8213/ad1de1.

D. D. Kocevski, M. Onoue, K. Inayoshi, J. R. Trump, P. Arrabal Haro, A. Grazian, M. Dickinson, S. L. Finkelstein, J. S. Kartaltepe, M. Hirschmann, J. Aird, B. W. Holwerda, S. Fujimoto, S. Juneau, R. O. Amorín, et al. Hidden Little Monsters: Spectroscopic Identification of Low-mass, Broad-line AGNs at z $>$ 5 with CEERS. ApJ, volume 954(1):L4, 2023. doi:10.3847/2041-8213/ace5a0.

V. Kokorev, K. I. Caputi, J. E. Greene, P. Dayal, M. Trebitsch, S. E. Cutler, S. Fujimoto, I. Labbé, T. B. Miller, E. Iani, R. Navarro-Carrera, and P. Rinaldi. A Census of Photometrically Selected Little Red Dots at 4 $<$ z $<$ 9 in JWST Blank Fields. arXiv e-prints, arXiv:2401.09981, 2024. doi:10.48550/arXiv.2401.09981.

E. W. Kolb and M. S. Turner. The early universe, volume 69. 1990. https://ui.adsabs.harvard.edu/abs/1990eaun.book.....K.

E. Komatsu, K. M. Smith, J. Dunkley, C. L. Bennett, B. Gold, G. Hinshaw, N. Jarosik, D. Larson, M. R. Nolta, L. Page, D. N. Spergel, M. Halpern, R. S. Hill, A. Kogut, M. Limon, et al. Seven-year Wilkinson Microwave Anisotropy Probe (WMAP) Observations: Cosmological Interpretation. ApJS, volume 192(2):18, 2011. doi:10.1088/0067-0049/192/2/18.

M. R. Krumholz, A. Dekel, and C. F. McKee. A Universal, Local Star Formation Law in Galactic Clouds, nearby Galaxies, High-redshift Disks, and Starbursts. ApJ, volume 745(1):69, 2012. doi:10.1088/0004-637X/745/1/69.

G. Kulkarni, G. Worseck, and J. F. Hennawi. Evolution of the AGN UV luminosity function from redshift 7.5. MNRAS, volume 488(1):1035–1065, 2019. doi:10.1093/mnras/stz1493.

N. Kumari, R. Maiolino, J. Trussler, F. Mannucci, G. Cresci, M. Curti, A. Marconi, and F. Belfiore. The extension of the fundamental metallicity relation beyond the BPT star-forming sequence: Evidence for both gas accretion and starvation. A&A, volume 656:A140, 2021. doi:10.1051/0004-6361/202140757.

I. Labbe, P. van Dokkum, E. Nelson, R. Bezanson, K. Suess, J. Leja, G. Brammer, K. Whitaker, E. Mathews, and M. Stefanon. A very early onset of massive galaxy formation. arXiv e-prints, arXiv:2207.12446, 2022. https://ui.adsabs.harvard.edu/abs/2022arXiv220712446L.

C. Lacey and S. Cole. Merger rates in hierarchical models of galaxy formation. MNRAS, volume 262(3):627–649, 1993. doi:10.1093/mnras/262.3.627.

C. Laigle, H. J. McCracken, O. Ilbert, B. C. Hsieh, I. Davidzon, P. Capak, G. Hasinger, J. D. Silverman, C. Pichon, J. Coupon, H. Aussel, D. Le Borgne, K. Caputi, P. Cassata, Y. Y. Chang, et al. The COSMOS2015 Catalog: Exploring the 1 $<$ z $<$ 6 Universe with Half a Million Galaxies. ApJS, volume 224(2):24, 2016. doi:10.3847/0067-0049/224/2/24.

N. Laporte, R. S. Ellis, F. Boone, F. E. Bauer, D. Quénard, G. W. Roberts-Borsani, R. Pelló, I. Pérez-Fournon, and A. Streblyanska. Dust in the Reionization Era: ALMA Observations of a z = 8.38 Gravitationally Lensed Galaxy. ApJ, volume 837(2):L21, 2017. doi:10.3847/2041-8213/aa62aa.

A. Lawrence, S. J. Warren, O. Almaini, A. C. Edge, N. C. Hambly, R. F. Jameson, P. Lucas, M. Casali, A. Adamson, S. Dye, J. P. Emerson, S. Foucaud, P. Hewett, P. Hirst, S. T. Hodgkin, et al. The UKIRT Infrared Deep Sky Survey (UKIDSS). MNRAS, volume 379(4):1599–1617, 2007. doi:10.1111/j.1365-2966.2007.12040.x.

O. Le Fèvre, M. Béthermin, A. Faisst, G. Jones, P. Capak, P. Cassata, J. Silverman, D. Schaerer, L. Yan, R. Amorin, S. Bardelli, M. Boquien, A. Cimatti, M. Dessauges-Zavadsky, M. Giavalisco, et al. The ALPINE-ALMA [CII] survey. Survey strategy, observations, and sample properties of 118 star-forming galaxies at 4 $<$ z $<$ 6. A&A, volume 643:A1, 2020. doi:10.1051/0004-6361/201936965.

O. Le Fèvre, L. A. M. Tasca, P. Cassata, B. Garilli, V. Le Brun, D. Maccagni, L. Pentericci, R. Thomas, E. Vanzella, G. Zamorani, E. Zucca, R. Amorin, S. Bardelli, P. Capak, L. Cassarà, et al. The VIMOS Ultra-Deep Survey: ∼10 000 galaxies with spectroscopic redshifts to study galaxy assembly at early epochs 2 $<$ z $\approx$ 6. A&A, volume 576:A79, 2015. doi:10.1051/0004-6361/201423829.

N. Leethochawalit, M. Trenti, P. Santini, L. Yang, E. Merlin, M. Castellano, A. Fontana, T. Treu, C. Mason, K. Glazebrook, T. Jones, B. Vulcani, T. Nanayakkara, D. Marchesini, S. Mascia, et al. Early results from GLASS-JWST. X: Rest-frame UV-optical properties of galaxies at 7 $<$ z $<$ 9. arXiv e-prints, arXiv:2207.11135, 2022. https://ui.adsabs.harvard.edu/abs/2022arXiv220711135L.

J. Leja, A. C. Carnall, B. D. Johnson, C. Conroy, and J. S. Speagle. How to Measure Galaxy Star Formation Histories. II. Nonparametric Models. ApJ, volume 876(1):3, 2019. doi:10.3847/1538-4357/ab133c.

J. Leja, J. S. Speagle, Y.-S. Ting, B. D. Johnson, C. Conroy, K. E. Whitaker, E. J. Nelson, P. van Dokkum, and M. Franx. A New Census of the 0.2< z <3.0 Universe, Part II: The Star-Forming Sequence. arXiv e-prints, arXiv:2110.04314, 2021. https://ui.adsabs.harvard.edu/abs/2021arXiv211004314L.

S. K. Leslie, E. Schinnerer, D. Liu, B. Magnelli, H. Algera, A. Karim, I. Davidzon, G. Gozaliasl, E. F. Jiménez-Andrade, P. Lang, M. T. Sargent, M. Novak, B. Groves, V. Smolčić, G. Zamorani, et al. The VLA-COSMOS 3 GHz Large Project: Evolution of Specific Star Formation Rates out to z $\sim$ 5. ApJ, volume 899(1):58, 2020. doi:10.3847/1538-4357/aba044.

A. Leśniewska and M. J. Michałowski. Dust production scenarios in galaxies at z ~6-8.3. A&A, volume 624:L13, 2019. doi:10.1051/0004-6361/201935149.

W. Li, K. Inayoshi, M. Onoue, and D. Toyouchi. The Assembly of Black Hole Mass and Luminosity Functions of High-redshift Quasars via Multiple Accretion Episodes. ApJ, volume 950(2):85, 2023a. doi:10.3847/1538-4357/accbbe.

Z. Li, A. Dekel, K. C. Sarkar, H. Aung, M. Giavalisco, N. Mandelker, and S. Tacchella. Feedback-Free Starbursts at Cosmic Dawn: Observable Predictions for JWST. arXiv e-prints, arXiv:2311.14662, 2023b. doi:10.48550/arXiv.2311.14662.

E. M. Lifshitz. On the gravitational stability of the expanding universe. Zhurnal Eksperimentalnoi i Teoreticheskoi Fiziki, volume 16:587–602, 1946. https://ui.adsabs.harvard.edu/abs/1946ZhETF..16..587L.

L. Lin, D. R. Patton, D. C. Koo, K. Casteels, C. J. Conselice, S. M. Faber, J. Lotz, C. N. A. Willmer, B. C. Hsieh, T. Chiueh, J. A. Newman, G. S. Novak, B. J. Weiner, and M. C. Cooper. The Redshift Evolution of Wet, Dry, and Mixed Galaxy Mergers from Close Galaxy Pairs in the DEEP2 Galaxy Redshift Survey. ApJ, volume 681(1):232–243, 2008. doi:10.1086/587928.

A. D. Linde. A new inflationary universe scenario: A possible solution of the horizon, flatness, homogeneity, isotropy and primordial monopole problems. Physics Letters B, volume 108(6):389–393, 1982. doi:10.1016/0370-2693(82)91219-9.

T. J. Looser, F. D'Eugenio, R. Maiolino, S. Tacchella, M. Curti, S. Arribas, W. M. Baker, S. Baum, N. Bonaventura, K. Boyett, A. J. Bunker, S. Carniani, S. Charlot, J. Chevallard, E. Curtis-Lake, et al. JADES: Differing assembly histories of galaxies – Observational evidence for bursty SFHs and (mini-)quenching in the first billion years of the Universe. arXiv e-prints, arXiv:2306.02470, 2023. doi:10.48550/arXiv.2306.02470.

C. López-Sanjuan, O. Le Fèvre, O. Ilbert, L. A. M. Tasca, C. Bridge, O. Cucciati, P. Kampczyk, L. Pozzetti, C. K. Xu, C. M. Carollo, T. Contini, J. P. Kneib, S. J. Lilly, V. Mainieri, A. Renzini, et al. The dominant role of mergers in the size evolution of massive early-type galaxies since z $\sim$1. A&A, volume 548:A7, 2012. doi:10.1051/0004-6361/201219085.

C. López-Sanjuan, O. Le Fèvre, L. A. M. Tasca, B. Epinat, P. Amram, T. Contini, B. Garilli, M. Kissler-Patig, J. Moultaka, L. Paioro, V. Perret, J. Queyrel, L. Tresse, D. Vergani, and C. Divoy. MASSIV: Mass Assembly Survey with SINFONI in VVDS. V. The major merger rate of star-forming galaxies at $0.9 < z < 1.8$ from IFS-based close pairs. A&A, volume 553:A78, 2013. doi:10.1051/0004-6361/201220286.

J. M. Lotz, A. Koekemoer, D. Coe, N. Grogin, P. Capak, J. Mack, J. Anderson, R. Avila, E. A. Barker, D. Borncamp, G. Brammer, M. Durbin, H. Gunning, B. Hilbert, H. Jenkner, et al. The Frontier Fields: Survey Design and Initial Results. ApJ, volume 837(1):97, 2017. doi:10.3847/1538-4357/837/1/97.

J. M. Lotz, J. Primack, and P. Madau. A New Nonparametric Approach to Galaxy Morphological Classification. AJ, volume 128(1):163–182, 2004. doi:10.1086/421849.

C. C. Lovell, I. Harrison, Y. Harikane, S. Tacchella, and S. M. Wilkins. Extreme value statistics of the halo and stellar mass distributions at high redshift: are JWST results in tension with ΛCDM? MNRAS, volume 518(2):2511–2520, 2023. doi:10.1093/mnras/stac3224.

C. C. Lovell, A. P. Vijayan, P. A. Thomas, S. M. Wilkins, D. J. Barnes, D. Irodotou, and W. Roper. First Light And Reionization Epoch Simulations (FLARES) - I. Environmental dependence of high-redshift galaxy evolution. MNRAS, volume 500(2):2127–2145, 2021. doi:10.1093/mnras/staa3360.

L. B. Lucy. A numerical approach to the testing of the fission hypothesis. AJ, volume 82:1013–1024, 1977. doi:10.1086/112164.

A. Lupi and S. Bovino. The [C II]-SFR correlation in dwarf galaxies across cosmic time. MNRAS, volume 492(2):2818–2827, 2020. doi:10.1093/mnras/staa048.

A. Lupi, A. Pallottini, A. Ferrara, S. Bovino, S. Carniani, and L. Vallini. Predicting FIR lines from simulated galaxies. MNRAS, volume 496(4):5160–5175, 2020. doi:10.1093/mnras/staa1842.

X. Ma, P. F. Hopkins, S. Garrison-Kimmel, C.-A. Faucher-Giguère, E. Quataert, M. Boylan-Kolchin, C. C. Hayward, R. Feldmann, and D. Kereš. Simulating galaxies in the reionization era with FIRE-2: galaxy scaling relations, stellar mass functions, and luminosity functions. MNRAS, volume 478(2):1694–1715, 2018. doi:10.1093/mnras/sty1024.

P. Madau and M. Dickinson. Cosmic Star-Formation History. Annual Review of Astron and Astrophys, volume 52:415–486, 2014a. doi:10.1146/annurev-astro-081811-125615.

P. Madau and M. Dickinson. Cosmic Star-Formation History. ARA&A, volume 52:415–486, 2014b. doi:10.1146/annurev-astro-081811-125615.

P. Madau and T. Fragos. Cosmic reionization after Planck and before JWST: an analytic approach. The Astrophysical Journal, volume 851(1):50, 2017. https://ui.adsabs.harvard.edu/abs/2017ApJ...851...50M/abstract.

P. Madau and F. Haardt. Cosmic Reionization after Planck: Could Quasars Do It All? ApJ, volume 813(1):L8, 2015. doi:10.1088/2041-8205/813/1/L8.

U. Maio, B. Ciardi, K. Dolag, L. Tornatore, and S. Khochfar. The transition from population III to population II-I star formation. MNRAS, volume 407:1003–1015, 2010. doi:10.1111/j.1365-2966.2010.17003.x.

U. Maio, B. Ciardi, N. Yoshida, K. Dolag, and L. Tornatore. The onset of star formation in primordial haloes. A&A, volume 503(1):25–34, 2009a. doi:10.1051/0004-6361/200912234.

U. Maio, B. Ciardi, N. Yoshida, K. Dolag, and L. Tornatore. The onset of star formation in primordial haloes. AAP, volume 503:25–34, 2009b. doi:10.1051/0004-6361/200912234.

R. Maiolino, J. Scholtz, J. Witstok, S. Carniani, F. D'Eugenio, A. de Graaff, H. Uebler, S. Tacchella, E. Curtis-Lake, S. Arribas, A. Bunker, S. Charlot, J. Chevallard, M. Curti, T. J. Looser, et al. A small and vigorous black hole in the early Universe. arXiv e-prints, arXiv:2305.12492, 2023a. doi:10.48550/arXiv.2305.12492.

R. Maiolino, H. Uebler, M. Perna, J. Scholtz, F. D'Eugenio, C. Witten, N. Laporte, J. Witstok, S. Carniani, S. Tacchella, W. Baker, S. Arribas, K. Nakajima, D. Eisenstein, A. Bunker, et al. JWST-JADES. Possible Population III signatures at z=10.6 in the halo of GN-z11. arXiv e-prints, arXiv:2306.00953, 2023b. doi:10.48550/arXiv.2306.00953.

M. Mancini, R. Schneider, L. Graziani, R. Valiante, P. Dayal, U. Maio, B. Ciardi, and L. K. Hunt. The dust mass in z > 6 normal star-forming galaxies. MNRAS, volume 451:L70–L74, 2015. doi:10.1093/mnrasl/slv070.

S. Marassi, G. Chiaki, R. Schneider, M. Limongi, K. Omukai, T. Nozawa, A. Chieffi, and N. Yoshida. The Origin of the Most Iron-poor Star. ApJ, volume 794(2):100, 2014. doi:10.1088/0004-637X/794/2/100.

S. Marassi, R. Schneider, M. Limongi, A. Chieffi, M. Bocchio, and S. Bianchi. The metal and dust yields of the first massive stars. MNRAS, volume 454(4):4250–4266, 2015. doi:10.1093/mnras/stv2267.

S. Marassi, R. Schneider, M. Limongi, A. Chieffi, L. Graziani, and S. Bianchi. Supernova dust yields: the role of metallicity, rotation, and fallback. MNRAS, volume 484(2):2587–2604, 2019. doi:10.1093/mnras/sty3323.

P. Marigo, A. Bressan, A. Nanni, L. Girardi, and M. L. Pumo. Evolution of thermally pulsing asymptotic giant branch stars - I. The COLIBRI code. MNRAS, volume 434(1):488–526, 2013. doi:10.1093/mnras/stt1034.

S. Mascia, L. Pentericci, A. Calabrò, P. Santini, L. Napolitano, P. Arrabal Haro, M. Castellano, M. Dickinson, P. Ocvirk, J. S. W. Lewis, R. Amorín, M. Bagley, R. N. J. Cleri, L. Costantin, A. Dekel, et al. New insight on the nature of cosmic reionizers from the CEERS survey. arXiv e-prints, arXiv:2309.02219, 2023a. doi:10.48550/arXiv.2309.02219.

S. Mascia, L. Pentericci, A. Calabrò, T. Treu, P. Santini, L. Yang, L. Napolitano, G. Roberts-Borsani, P. Bergamini, C. Grillo, P. Rosati, B. Vulcani, M. Castellano, K. Boyett, A. Fontana, et al. Closing in on the sources of cosmic reionization: First results from the GLASS-JWST program. A&A, volume 672:A155, 2023b. doi:10.1051/0004-6361/202345866.

A. Maselli, A. Ferrara, and B. Ciardi. CRASH: a radiative transfer scheme. MNRAS, volume 345(2):379–394, 2003. doi:10.1046/j.1365-8711.2003.06979.x.

C. A. Mason, M. Trenti, and T. Treu. The Galaxy UV Luminosity Function before the Epoch of Reionization. ApJ, volume 813(1):21, 2015. doi:10.1088/0004-637X/813/1/21.

C. A. Mason, M. Trenti, and T. Treu. The brightest galaxies at cosmic dawn. MNRAS, volume 521(1):497–503, 2023. doi:10.1093/mnras/stad035.

J. Matthee, R. P. Naidu, G. Brammer, J. Chisholm, A.-C. Eilers, A. Goulding, J. Greene, D. Kashino, I. Labbe, S. J. Lilly, R. Mackenzie, P. A. Oesch, A. Weibel, S. Wuyts, M. Xiao, et al. Little Red Dots: an abundant population of faint AGN at z∼5 revealed by the EIGER and FRESCO JWST surveys. arXiv e-prints, arXiv:2306.05448, 2023. doi:10.48550/arXiv.2306.05448.

J. Matthee, D. Sobral, L. A. Boogaard, H. Röttgering, L. Vallini, A. Ferrara, A. Paulino-Afonso, F. Boone, D. Schaerer, and B. Mobasher. Resolved UV and [C II] Structures of Luminous Galaxies within the Epoch of Reionization. ApJ, volume 881(2):124, 2019. doi:10.3847/1538-4357/ab2f81.

A. M. Matthews, J. J. Condon, W. D. Cotton, and T. Mauch. Cosmic Star Formation History measured at 1.4 GHz. The Astrophysical Journal, volume 914(2):126, 2021. https://ui.adsabs.harvard.edu/abs/2021ApJ...914..126M.

H. J. McCracken, B. Milvang-Jensen, J. Dunlop, M. Franx, J. P. U. Fynbo, O. Le Fèvre, J. Holt, K. I. Caputi, Y. Goranova, F. Buitrago, J. P. Emerson, W. Freudling, P. Hudelot, C. López-Sanjuan, F. Magnard, et al. UltraVISTA: a new ultra-deep near-infrared survey in COSMOS. A&A, volume 544:A156, 2012. doi:10.1051/0004-6361/201219507.

C. F. McKee and E. C. Ostriker. Theory of Star Formation. ARA&A, volume 45(1):565–687, 2007. doi:10.1146/annurev.astro.45.051806.110602.

R. McKinnon, P. Torrey, M. Vogelsberger, C. C. Hayward, and F. Marinacci. Simulating the dust content of galaxies: successes and failures. MNRAS, volume 468:1505–1521, 2017. doi:10.1093/mnras/stx467.

J. P. McMullin, B. Waters, D. Schiebel, W. Young, and K. Golap. CASA Architecture and Applications. In R. A. Shaw, F. Hill, and D. J. Bell, editors, Astronomical Data Analysis Software and Systems XVI, volume 376 of Astronomical Society of the Pacific Conference Series, page 127. 2007. https://ui.adsabs.harvard.edu/abs/2007ASPC..376..127M.

N. Menci, M. Castellano, P. Santini, E. Merlin, A. Fontana, and F. Shankar. High-redshift Galaxies from Early JWST Observations: Constraints on Dark Energy Models. ApJ, volume 938(1):L5, 2022. doi:10.3847/2041-8213/ac96e9.

E. Merlin, F. Fortuni, M. Torelli, P. Santini, M. Castellano, A. Fontana, A. Grazian, L. Pentericci, S. Pilo, and K. B. Schmidt. Red and dead CANDELS: massive passive galaxies at the dawn of the Universe. MNRAS, volume 490(3):3309–3328, 2019. doi:10.1093/mnras/stz2615.

P. Meszaros. The behaviour of point masses in an expanding cosmological substratum. A&A, volume 37(2):225–228, 1974. https://ui.adsabs.harvard.edu/abs/1974A&A....37..225M.

J. Mirocha and S. R. Furlanetto. Balancing the efficiency and stochasticity of star formation with dust extinction in z $\gtrsim$ 10 galaxies observed by JWST. MNRAS, volume 519(1):843–853, 2023. doi:10.1093/mnras/stac3578.

H. Mo, F. C. van den Bosch, and S. White. Galaxy Formation and Evolution. 2010. https://ui.adsabs.harvard.edu/abs/2010gfe..book.....M.

J. J. Monaghan. Smoothed particle hydrodynamics. ARA&A, volume 30:543–574, 1992. doi:10.1146/annurev.aa.30.090192.002551.

T. Morishita, M. Stiavelli, M. Trenti, T. Treu, G. W. Roberts-Borsani, C. A. Mason, T. Hashimoto, L. Bradley, D. Coe, and Y. Ishikawa. SuperBoRG: Exploration of Point Sources at z $\sim$ 8 in HST Parallel Fields. ApJ, volume 904(1):50, 2020. doi:10.3847/1538-4357/abba83.

B. P. Moster, T. Naab, and S. D. M. White. EMERGE - an empirical model for the formation of galaxies since z $\sim$ 10. MNRAS, volume 477(2):1822–1852, 2018. doi:10.1093/mnras/sty655.

T. Moutard, M. Sawicki, S. Arnouts, A. Golob, J. Coupon, O. Ilbert, X. Yang, and S. Gwyn. UV and U-band luminosity functions from CLAUDS and HSC-SSP - I. Using four million galaxies to simultaneously constrain the very faint and bright regimes to z $\sim$ 3. MNRAS, volume 494(2):1894–1918, 2020. doi:10.1093/mnras/staa706.

J. B. Muñoz, J. Mirocha, S. Furlanetto, and N. Sabti. Breaking degeneracies in the first galaxies with clustering. MNRAS, volume 526(1):L47–L55, 2023. doi:10.1093/mnrasl/slad115.

S. J. Mutch, P. M. Geil, G. B. Poole, P. W. Angel, A. R. Duffy, A. Mesinger, and J. S. B. Wyithe. Dark-ages reionization and galaxy formation simulation - III. Modelling galaxy formation and the epoch of reionization. MNRAS, volume 462(1):250–276, 2016. doi:10.1093/mnras/stw1506.

R. P. Naidu, P. A. Oesch, P. v. Dokkum, E. J. Nelson, K. A. Suess, G. Brammer, K. E. Whitaker, G. Illingworth, R. Bouwens, S. Tacchella, J. Matthee, N. Allen, R. Bezanson, C. Conroy, I. Labbe, et al. Two Remarkably Luminous Galaxy Candidates at z $\approx$ 10-12 Revealed by JWST. ApJ, volume 940(1):L14, 2022a. doi:10.3847/2041-8213/ac9b22.

R. P. Naidu, P. A. Oesch, D. J. Setton, J. Matthee, C. Conroy, B. D. Johnson, J. R. Weaver, R. J. Bouwens, G. B. Brammer, P. Dayal, G. D. Illingworth, L. Barrufet, S. Belli, R. Bezanson, S. Bose, et al. Schrodinger's Galaxy Candidate: Puzzlingly Luminous at $z \approx 17$, or Dusty/Quenched at $z \approx 5$? arXiv e-prints, arXiv:2208.02794, 2022b. doi:10.48550/arXiv.2208.02794.

R. P. Naidu, S. Tacchella, C. A. Mason, S. Bose, P. A. Oesch, and C. Conroy. Rapid Reionization by the Oligarchs: The Case for Massive, UV-bright, Star-forming Galaxies with High Escape Fractions. ApJ, volume 892(2):109, 2020. doi:10.3847/1538-4357/ab7cc9.

K. Nakajima, M. Ouchi, Y. Isobe, Y. Harikane, Y. Zhang, Y. Ono, H. Umeda, and M. Oguri. JWST Census for the Mass-Metallicity Star Formation Relations at z = 4-10 with Self-consistent Flux Calibration and Proper Metallicity Calibrators. ApJS, volume 269(2):33, 2023. doi:10.3847/1538-4365/acd556.

J. F. Navarro and S. D. M. White. Simulations of Dissipative Galaxy Formation in Hierarchically Clustering Universes - Part One - Tests of the Code. MNRAS, volume 265:271, 1993. doi:10.1093/mnras/265.2.271.

R. Navarro-Carrera, P. Rinaldi, K. I. Caputi, E. Iani, V. Kokorev, and S. E. van Mierlo. Constraints on the Faint End of the Galaxy Stellar Mass Function at z 4–8 from Deep JWST Data. ApJ, volume 961(2):207, 2024. doi:10.3847/1538-4357/ad0df6.

M. Niida, T. Nagao, H. Ikeda, M. Akiyama, Y. Matsuoka, W. He, K. Matsuoka, Y. Toba, M. Onoue, M. A. R. Kobayashi, Y. Taniguchi, H. Furusawa, Y. Harikane, M. Imanishi, N. Kashikawa, et al. The Faint End of the Quasar Luminosity Function at z $\sim$ 5 from the Subaru Hyper Suprime-Cam Survey. ApJ, volume 904(2):89, 2020. doi:10.3847/1538-4357/abbe11.

P. Ocvirk, C. Pichon, and R. Teyssier. Bimodal gas accretion in the Horizon-MareNostrum galaxy formation simulation. MNRAS, volume 390(4):1326–1338, 2008. doi:10.1111/j.1365-2966.2008.13763.x.

P. A. Oesch, R. J. Bouwens, G. D. Illingworth, I. Labbé, R. Smit, M. Franx, P. G. van Dokkum, I. Momcheva, M. L. N. Ashby, G. G. Fazio, J. S. Huang, S. P. Willner, V. Gonzalez, D. Magee, M. Trenti, et al. The Most Luminous z $\sim$9-10 Galaxy Candidates Yet Found: The Luminosity Function, Cosmic Star-formation Rate, and the First Mass Density Estimate at 500 Myr. ApJ, volume 786(2):108, 2014. doi:10.1088/0004-637X/786/2/108.

P. A. Oesch, G. Brammer, P. G. van Dokkum, G. D. Illingworth, R. J. Bouwens, I. Labbé, M. Franx, I. Momcheva, M. L. N. Ashby, G. G. Fazio, V. Gonzalez, B. Holden, D. Magee, R. E. Skelton, R. Smit, et al. A Remarkably Luminous Galaxy at z=11.1 Measured with Hubble Space Telescope Grism Spectroscopy. ApJ, volume 819(2):129, 2016. doi:10.3847/0004-637X/819/2/129.

L. Oser, T. Naab, J. P. Ostriker, and P. H. Johansson. The Cosmological Size and Velocity Dispersion Evolution of Massive Early-type Galaxies. ApJ, volume 744(1):63, 2012. doi:10.1088/0004-637X/744/1/63.

I. Oteo, D. Sobral, R. J. Ivison, I. Smail, P. N. Best, J. Cepa, and A. M. Pérez-García. On the nature of Hα emitters at z $\sim$ 2 from the HiZELS survey: physical properties, Lyα escape fraction and main sequence. MNRAS, volume 452(2):2018–2033, 2015. doi:10.1093/mnras/stv1284.

F. Pace, J. C. Waizmann, and M. Bartelmann. Spherical collapse model in dark-energy cosmologies. MNRAS, volume 406(3):1865–1874, 2010. doi:10.1111/j.1365-2966.2010.16841.x.

T. Padmanabhan. Theoretical Astrophysics - Volume 3, Galaxies and Cosmology, volume 3. 2002. doi:10.2277/0521562422.

P. Padovani and F. Matteucci. Stellar Mass Loss in Elliptical Galaxies and the Fueling of Active Galactic Nuclei. ApJ, volume 416:26, 1993. doi:10.1086/173212.

M. Palla, I. De Looze, M. Relaño, S. van der Giessen, P. Dayal, A. Ferrara, R. Schneider, L. Graziani, H. S. B. Algera, M. Aravena, R. A. A. Bowler, A. P. S. Hygate, H. Inami, I. van Leeuwen, R. Bouwens, et al. Metal and dust evolution in ALMA REBELS galaxies: insights for future JWST observations. arXiv e-prints, arXiv:2311.16071, 2023. doi:10.48550/arXiv.2311.16071.

A. Pallottini and A. Ferrara. Stochastic star formation in early galaxies: Implications for the James Webb Space Telescope. A&A, volume 677:L4, 2023. doi:10.1051/0004-6361/202347384.

A. Pallottini, A. Ferrara, D. Decataldo, S. Gallerani, L. Vallini, S. Carniani, C. Behrens, M. Kohandel, and S. Salvadori. Deep into the structure of the first galaxies: SERRA views. MNRAS, volume 487(2):1689–1708, 2019. doi:10.1093/mnras/stz1383.

A. Pallottini, A. Ferrara, S. Gallerani, C. Behrens, M. Kohandel, S. Carniani, L. Vallini, S. Salvadori, V. Gelli, L. Sommovigo, V. D'Odorico, F. Di Mascia, and E. Pizzati. A survey of high-z galaxies: SERRA simulations. MNRAS, volume 513(4):5621–5641, 2022a. doi:10.1093/mnras/stac1281.

A. Pallottini, A. Ferrara, S. Gallerani, C. Behrens, M. Kohandel, S. Carniani, L. Vallini, S. Salvadori, V. Gelli, L. Sommovigo, V. D'Odorico, F. Di Mascia, and E. Pizzati. A survey of high-z galaxies: SERRA simulations. MNRAS, volume 513(4):5621–5641, 2022b. doi:10.1093/mnras/stac1281.

A. Pallottini, A. Ferrara, S. Gallerani, L. Vallini, R. Maiolino, and S. Salvadori. Zooming on the internal structure of z 6 galaxies. MNRAS, volume 465(3):2540–2558, 2017. doi:10.1093/mnras/stw2847.

S. Parsa, J. S. Dunlop, and R. J. McLure. No evidence for a significant AGN contribution to cosmic hydrogen reionization. MNRAS, volume 474(3):2904–2923, 2018. doi:10.1093/mnras/stx2887.

C. Patrignani, Particle Data Group, K. Agashe, G. Aielli, C. Amsler, M. Antonelli, D. M. Asner, H. Baer, S. Banerjee, R. M. Barnett, T. Basaglia, C. W. Bauer, J. J. Beatty, V. I. Belousov, J. Beringer, et al. Review of Particle Physics. Chinese Physics C, volume 40(10):100001, 2016. doi:10.1088/1674-1137/40/10/100001.

D. R. Patton, R. G. Carlberg, R. O. Marzke, C. J. Pritchet, L. N. da Costa, and P. S. Pellegrini. New Techniques for Relating Dynamically Close Galaxy Pairs to Merger and Accretion Rates: Application to the Second Southern Sky Redshift Survey. ApJ, volume 536(1):153–172, 2000. doi:10.1086/308907.

J. A. Peacock. Cosmological Physics. 1999. https://ui.adsabs.harvard.edu/abs/1999coph.book.....P.

P. Peebles. Principles of Physical Cosmology. 1993. doi:10.1515/9780691206721.

M. Peeples, P. Behroozi, R. Bordoloi, A. Brooks, J. S. Bullock, J. N. Burchett, H.-W. Chen, J. Chisholm, C. Christensen, A. Coil, L. Corlies, A. Diamond-Stanic, M. Donahue, C.-A. Faucher-Giguère, H. Ferguson, et al. Understanding the circumgalactic medium is critical for understanding galaxy evolution. BAAS, volume 51(3):368, 2019. doi:10.48550/arXiv.1903.05644.

A. A. Penzias and R. W. Wilson. A Measurement of Excess Antenna Temperature at 4080 Mc/s. ApJ, volume 142:419–421, 1965. doi:10.1086/148307.

P. G. Pérez-González, G. Barro, G. H. Rieke, J. Lyu, M. Rieke, S. Alberts, C. Williams, K. Hainline, F. Sun, D. Puskas, M. Annunziatella, W. M. Baker, A. J. Bunker, E. Egami, Z. Ji, et al. What is the nature of Little Red Dots and what is not, MIRI SMILES edition. arXiv e-prints, arXiv:2401.08782, 2024. doi:10.48550/arXiv.2401.08782.

S. Perlmutter, G. Aldering, G. Goldhaber, R. A. Knop, P. Nugent, P. G. Castro, S. Deustua, S. Fabbro, A. Goobar, D. E. Groom, I. M. Hook, A. G. Kim, M. Y. Kim, J. C. Lee, N. J. Nunes, et al. Measurements of Ω and Λ from 42 High-Redshift Supernovae. ApJ, volume 517(2):565–586, 1999. doi:10.1086/307221.

C. Péroux and J. C. Howk. The Cosmic Baryon and Metal Cycles. ARA&A, volume 58:363–406, 2020. doi:10.1146/annurev-astro-021820-120014.

A. Pillepich, V. Springel, D. Nelson, S. Genel, J. Naiman, R. Pakmor, L. Hernquist, P. Torrey, M. Vogelsberger, R. Weinberger, and F. Marinacci. Simulating galaxy formation with the IllustrisTNG model. Monthly Notices of the Royal Astronomical Society, volume 473(3):4077–4106, 2017. http://dx.doi.org/10.1093/mnras/stx2656.

E. Pizzati, A. Ferrara, A. Pallottini, S. Gallerani, L. Vallini, D. Decataldo, and S. Fujimoto. Outflows and extended [C II] haloes in high-redshift galaxies. MNRAS, volume 495(1):160–172, 2020. doi:10.1093/mnras/staa1163.

E. Pizzati, A. Ferrara, A. Pallottini, L. Sommovigo, M. Kohandel, and S. Carniani. [C II] Haloes in ALPINE galaxies: smoking-gun of galactic outflows? MNRAS, volume 519(3):4608–4621, 2023. doi:10.1093/mnras/stac3816.

Planck Collaboration, P. A. R. Ade, N. Aghanim, M. Arnaud, M. Ashdown, J. Aumont, C. Baccigalupi, A. J. Banday, R. B. Barreiro, J. G. Bartlett, N. Bartolo, E. Battaner, R. Battye, K. Benabed, A. Benoît, et al. Planck 2015 results. XIII. Cosmological parameters. A&A, volume 594:A13, 2016. doi:10.1051/0004-6361/201525830.

Planck Collaboration, N. Aghanim, Y. Akrami, F. Arroja, M. Ashdown, J. Aumont, C. Baccigalupi, M. Ballardini, A. J. Banday, R. B. Barreiro, N. Bartolo, S. Basak, R. Battye, K. Benabed, J. P. Bernard, et al. Planck 2018 results. I. Overview and the cosmological legacy of Planck. A&A, volume 641:A1, 2020a. doi:10.1051/0004-6361/201833880.

Planck Collaboration, N. Aghanim, Y. Akrami, M. Ashdown, J. Aumont, C. Baccigalupi, M. Ballardini, A. J. Banday, R. B. Barreiro, N. Bartolo, S. Basak, R. Battye, K. Benabed, J. P. Bernard, M. Bersanelli, et al. Planck 2018 results. VI. Cosmological parameters. A&A, volume 641:A6, 2020b. doi:10.1051/0004-6361/201833910.

P. Popesso, A. Concas, G. Cresci, S. Belli, G. Rodighiero, H. Inami, M. Dickinson, O. Ilbert, M. Pannella, and D. Elbaz. The Main Sequence of star forming galaxies across cosmic times. MNRAS, 2022. doi:10.1093/mnras/stac3214.

G. Popping. An upper limit on [O III] 88 μm and 1.2 mm continuum emission from a JWST z $\approx$ 12-13 galaxy candidate with ALMA. A&A, volume 669:L8, 2023. doi:10.1051/0004-6361/202244831.

G. Popping, D. Narayanan, R. S. Somerville, A. L. Faisst, and M. R. Krumholz. The art of modelling CO, [C I], and [C II] in cosmological galaxy formation models. MNRAS, volume 482(4):4906–4932, 2019. doi:10.1093/mnras/sty2969.

G. Popping, R. S. Somerville, and M. Galametz. The dust content of galaxies from z = 0 to z = 9. MNRAS, volume 471(3):3152–3185, 2017. doi:10.1093/mnras/stx1545.

F. Pozzi, F. Calura, Y. Fudamoto, M. Dessauges-Zavadsky, C. Gruppioni, M. Talia, G. Zamorani, M. Bethermin, A. Cimatti, A. Enia, Y. Khusanova, R. Decarli, O. Le Fèvre, P. Capak, P. Cassata, et al. The ALPINE-ALMA [CII] survey. Dust mass budget in the early Universe. A&A, volume 653:A84, 2021. doi:10.1051/0004-6361/202040258.

N. Prantzos. An Introduction to Galactic Chemical Evolution. In C. Charbonnel and J. P. Zahn, editors, EAS Publications Series, volume 32 of EAS Publications Series, pages 311–356. 2008. doi:10.1051/eas:0832009.

W. H. Press and P. Schechter. Formation of Galaxies and Clusters of Galaxies by Self-Similar Gravitational Condensation. ApJ, volume 187:425–438, 1974. doi:10.1086/152650.

D. Price. Smoothed Particle Hydrodynamics. Ph.D. thesis, -, 2005. https://ui.adsabs.harvard.edu/abs/2005PhDT.....295P.

D. J. Price. Smoothed particle hydrodynamics and magnetohydrodynamics. Journal of Computational Physics, volume 231(3):759–794, 2012. doi:10.1016/j.jcp.2010.12.011.

D. J. Price, J. Wurster, T. S. Tricco, C. Nixon, S. Toupin, A. Pettitt, C. Chan, D. Mentiplay, G. Laibe, S. Glover, C. Dobbs, R. Nealon, D. Liptai, H. Worpel, C. Bonnerot, et al. Phantom: A Smoothed Particle Hydrodynamics and

Magnetohydrodynamics Code for Astrophysics. PASA, volume 35:e031, 2018. doi:10.1017/pasa.2018.25.

Y. Qu, J. C. Helly, R. G. Bower, T. Theuns, R. A. Crain, C. S. Frenk, M. Furlong, S. McAlpine, M. Schaller, J. Schaye, and S. D. M. White. A chronicle of galaxy mass assembly in the EAGLE simulation. MNRAS, volume 464(2):1659–1675, 2017. doi:10.1093/mnras/stw2437.

E. Rasmussen Cueto, A. Hutter, P. Dayal, S. Gottlöber, K. E. Heintz, C. Mason, M. Trebitsch, and G. Yepes. The impact of an evolving stellar initial mass function on early galaxies and reionisation. arXiv e-prints, arXiv:2312.12109, 2023. doi:10.48550/arXiv.2312.12109.

M. J. Rees and J. P. Ostriker. Cooling, dynamics and fragmentation of massive gas clouds: clues to the masses and radii of galaxies and clusters. MNRAS, volume 179:541–559, 1977. doi:10.1093/mnras/179.4.541.

A. M. M. Reeves and M. J. Hudson. How many stars form in galaxy mergers? arXiv e-prints, arXiv:2310.11503, 2023. doi:10.48550/arXiv.2310.11503.

S. Riaz, T. Hartwig, and M. A. Latif. Unveiling the Contribution of Population III Stars in Primeval Galaxies at Redshift $\geq$6. ApJ, volume 937(1):L6, 2022. doi:10.3847/2041-8213/ac8ea6.

A. Ricarte and P. Natarajan. The observational signatures of supermassive black hole seeds. MNRAS, volume 481(3):3278–3292, 2018. doi:10.1093/mnras/sty2448.

M. J. Rieke, S. A. Baum, C. A. Beichman, D. Crampton, R. Doyon, D. Eisenstein, T. P. Greene, K.-W. Hodapp, S. D. Horner, D. Johnstone, L. Lesyna, S. Lilly, M. Meyer, P. Martin, J. McCarthy, Donald W., et al. NGST NIRCam Scientific Program and Design Concept. In J. C. Mather, editor, IR Space Telescopes and Instruments, volume 4850 of Society of Photo-Optical Instrumentation Engineers (SPIE) Conference Series, pages 478–485. 2003. doi:10.1117/12.489103.

M. J. Rieke, D. M. Kelly, K. Misselt, J. Stansberry, M. Boyer, T. Beatty, E. Egami, M. Florian, T. P. Greene, K. Hainline, J. Leisenring, T. Roellig, E. Schlawin, F. Sun, L. Tinnin, et al. Performance of NIRCam on JWST in Flight. PASP, volume 135(1044):028001, 2023. doi:10.1088/1538-3873/acac53.

A. G. Riess, A. V. Filippenko, P. Challis, A. Clocchiatti, A. Diercks, P. M. Garnavich, R. L. Gilliland, C. J. Hogan, S. Jha, R. P. Kirshner, B. Leibundgut, M. M. Phillips, D. Reiss, B. P. Schmidt, R. A. Schommer, et al. Observational Evidence from Supernovae for an Accelerating Universe and a Cosmological Constant. AJ, volume 116(3):1009–1038, 1998. doi:10.1086/300499.

B. E. Robertson, R. S. Ellis, S. R. Furlanetto, and J. S. Dunlop. Cosmic Reionization and Early Star-forming Galaxies: A Joint Analysis of New Constraints from Planck and the Hubble Space Telescope. ApJ, volume 802(2):L19, 2015. doi:10.1088/2041-8205/802/2/L19.

B. E. Robertson, S. Tacchella, B. D. Johnson, R. Hausen, A. B. Alabi, K. Boyett, A. J. Bunker, S. Carniani, E. Egami, D. J. Eisenstein, K. N. Hainline, J. M. Helton, Z. Ji, N. Kumari, J. Lyu, et al. Morpheus Reveals Distant Disk Galaxy Morphologies with JWST: The First AI/ML Analysis of JWST Images. ApJ, volume 942(2):L42, 2023. doi:10.3847/2041-8213/aca086.

H. P. Robertson. Kinematics and World-Structure. ApJ, volume 82:284, 1935. doi:10.1086/143681.

G. Rodighiero, L. Bisigello, E. Iani, A. Marasco, A. Grazian, F. Sinigaglia, P. Cassata, and C. Gruppioni. JWST unveils heavily obscured (active and passive) sources up to z 13. MNRAS, volume 518(1):L19–L24, 2023. doi:10.1093/mnrasl/slac115.

G. Rodighiero, E. Daddi, I. Baronchelli, A. Cimatti, A. Renzini, H. Aussel, P. Popesso, D. Lutz, P. Andreani, S. Berta, A. Cava, D. Elbaz, A. Feltre, A. Fontana, N. M. Förster Schreiber, et al. The Lesser Role of Starbursts in Star Formation at z = 2. ApJ, volume 739(2):L40, 2011. doi:10.1088/2041-8205/739/2/L40.

M. Romano, P. Cassata, L. Morselli, G. C. Jones, M. Ginolfi, A. Zanella, M. Béthermin, P. Capak, A. Faisst, O. Le Fèvre, D. Schaerer, J. D. Silverman, L. Yan, S. Bardelli, M. Boquien, et al. The ALPINE-ALMA [CII] survey. The contribution of major mergers to the galaxy mass assembly at z ∼ 5. A&A, volume 653:A111, 2021. doi:10.1051/0004-6361/202141306.

M. Romano, L. Morselli, P. Cassata, M. Ginolfi, D. Schaerer, M. Béthermin, P. Capak, A. Faisst, O. Le Fèvre, J. D. Silverman, L. Yan, S. Bardelli, M. Boquien, M. Dessauges-Zavadsky, S. Fujimoto, et al. The ALPINE-ALMA [CII] survey: The population of [CII]-undetected galaxies and their role in the $L_{[CII]}$-SFR relation. A&A, volume 660:A14, 2022. doi:10.1051/0004-6361/202142265.

M. Romano, A. Nanni, D. Donevski, M. Ginolfi, G. C. Jones, I. Shivaei, Junais, D. Salak, and P. Sawant. Star-formation-driven outflows in local dwarf galaxies as revealed from [CII] observations by Herschel. A&A, volume 677:A44, 2023. doi:10.1051/0004-6361/202346143.

C. Rovelli. Quantum Gravity. 2004. https://ui.adsabs.harvard.edu/abs/2004qugr.book.....R.

E. E. Salpeter. The Luminosity Function and Stellar Evolution. ApJ, volume 121:161, 1955. doi:10.1086/145971.

R. L. Sanders, A. E. Shapley, M. W. Topping, N. A. Reddy, and G. B. Brammer. Excitation and Ionization Properties of Star-forming Galaxies at z = 2.0-9.3 with JWST/NIRSpec. ApJ, volume 955(1):54, 2023. doi:10.3847/1538-4357/acedad.

R. L. Sanders, A. E. Shapley, M. W. Topping, N. A. Reddy, and G. B. Brammer. Direct T_e-based Metallicities of z = 2–9 Galaxies with JWST/NIRSpec: Empirical Metallicity Calibrations Applicable from Reionization to Cosmic Noon. ApJ, volume 962(1):24, 2024. doi:10.3847/1538-4357/ad15fc.

L. Sandles, E. Curtis-Lake, S. Charlot, J. Chevallard, and R. Maiolino. Bayesian hierarchical modelling of the M_*-SFR relation from $1 \lesssim z \lesssim 6$ in ASTRODEEP. MNRAS, volume 515(2):2951–2969, 2022. doi:10.1093/mnras/stac1999.

P. Santini, M. Castellano, E. Merlin, A. Fontana, F. Fortuni, D. Kodra, B. Magnelli, N. Menci, A. Calabrò, C. C. Lovell, L. Pentericci, V. Testa, and S. M. Wilkins. The emergence of passive galaxies in the early Universe. A&A, volume 652:A30, 2021. doi:10.1051/0004-6361/202039738.

P. Santini, A. Fontana, M. Castellano, M. Di Criscienzo, E. Merlin, R. Amorin, F. Cullen, E. Daddi, M. Dickinson, J. S. Dunlop, A. Grazian, A. Lamastra, R. J. McLure, M. J. Michałowski, L. Pentericci, et al. The Star Formation Main Sequence in the Hubble Space Telescope Frontier Fields. ApJ, volume 847(1):76, 2017. doi:10.3847/1538-4357/aa8874.

P. Santini, A. Fontana, M. Castellano, N. Leethochawalit, M. Trenti, T. Treu, D. Belfiori, S. Birrer, A. Bonchi, E. Merlin, C. Mason, T. Morishita, M. Nonino, D. Paris, G. Polenta, et al. Early results from GLASS-JWST. XI: Stellar masses and mass-to-light ratio of z>7 galaxies. arXiv e-prints, arXiv:2207.11379, 2022. https://ui.adsabs.harvard.edu/abs/2022arXiv220711379S.

R. Sarmento, E. Scannapieco, and S. Cohen. Following the cosmic evolution of pristine gas. II. The search for Pop III–bright galaxies. The Astrophysical Journal, volume 854(1):75, 2018. https://arxiv.org/abs/1710.09878.

A. Saxena, A. J. Bunker, G. C. Jones, D. P. Stark, A. J. Cameron, J. Witstok, S. Arribas, W. M. Baker, S. Baum, R. Bhatawdekar, R. Bowler, K. Boyett, S. Carniani, S. Charlot, J. Chevallard, et al. JADES: The production and escape of ionizing photons from faint Lyman-alpha emitters in the epoch of reionization. arXiv e-prints, arXiv:2306.04536, 2023. doi:10.48550/arXiv.2306.04536.

D. Schaerer, M. Ginolfi, M. Béthermin, Y. Fudamoto, P. A. Oesch, O. Le Fèvre, A. Faisst, P. Capak, P. Cassata, J. D. Silverman, L. Yan, G. C. Jones, R. Amorin, S. Bardelli, M. Boquien, et al. The ALPINE-ALMA [C II] survey. Little to no evolution in the [C II]-SFR relation over the last 13 Gyr. A&A, volume 643:A3, 2020. doi:10.1051/0004-6361/202037617.

J. Schaye, R. A. Crain, R. G. Bower, M. Furlong, M. Schaller, T. Theuns, C. Dalla Vecchia, C. S. Frenk, I. G. McCarthy, J. C. Helly, A. Jenkins, Y. M. Rosas-Guevara, S. D. M. White, M. Baes, C. M. Booth, et al. The EAGLE project: simulating the evolution and assembly of galaxies and their environments. MNRAS, volume 446(1):521–554, 2015. doi:10.1093/mnras/stu2058.

A. Schimek, D. Decataldo, S. Shen, C. Cicone, B. Baumschlager, E. van Kampen, P. Klaassen, P. Madau, L. Di Mascolo, I. Montoya Arroyave, T. Mroczkowski, and J. H. K. Warraich. High resolution modeling of [CII], [CI], [OIII] and CO line emission from the ISM and CGM of a star forming galaxy at z ∼6.5. arXiv e-prints, arXiv:2306.00583, 2023. doi:10.48550/arXiv.2306.00583.

M. Schmidt. The Rate of Star Formation. ApJ, volume 129:243, 1959. doi:10.1086/146614.

R. Schneider, A. Ferrara, and R. Salvaterra. Dust formation in very massive primordial supernovae. MNRAS, volume 351(4):1379–1386, 2004. doi:10.1111/j.1365-2966.2004.07876.x.

R. Schneider and R. Maiolino. The formation and cosmic evolution of dust in the early Universe. I. Dust sources. arXiv e-prints, arXiv:2310.00053, 2023. doi:10.48550/arXiv.2310.00053.

R. Schneider, R. Valiante, A. Trinca, L. Graziani, M. Volonteri, and R. Maiolino. Are we surprised to find SMBHs with JWST at z $\geq$ 9? MNRAS, volume 526(3):3250–3261, 2023. doi:10.1093/mnras/stad2503.

S. Schouws, R. Bouwens, R. Smit, J. Hodge, M. Stefanon, J. Witstok, J. Hilhorst, I. Labbe, H. Algera, L. Boogaard, M. Maseda, P. Oesch, H. Röttgering, and P. van der Werf. ALMA as a Redshift Machine: Using [CII] to Efficiently Confirm Galaxies in the Epoch of Reionization. arXiv e-prints, arXiv:2202.04080, 2022a. https://ui.adsabs.harvard.edu/abs/2022arXiv220204080S.

S. Schouws, M. Stefanon, R. Bouwens, R. Smit, J. Hodge, I. Labbé, H. Algera, L. Boogaard, S. Carniani, Y. Fudamoto, B. W. Holwerda, G. D. Illingworth, R. Maiolino, M. Maseda, P. Oesch, et al. Significant Dust-obscured Star Formation in Luminous Lyman-break Galaxies at z 7-8. ApJ, volume 928(1):31, 2022b. doi:10.3847/1538-4357/ac4605.

C. Schreiber, M. Pannella, D. Elbaz, M. Béthermin, H. Inami, M. Dickinson, B. Magnelli, T. Wang, H. Aussel, E. Daddi, S. Juneau, X. Shu, M. T. Sargent, V. Buat, S. M. Faber, et al. The Herschel view of the dominant mode of galaxy growth from z = 4 to the present day. A&A, volume 575:A74, 2015. doi:10.1051/0004-6361/201425017.

N. Scoville, R. G. Abraham, H. Aussel, J. E. Barnes, A. Benson, A. W. Blain, D. Calzetti, A. Comastri, P. Capak, C. Carilli, J. E. Carlstrom, C. M. Carollo, J. Colbert, E. Daddi, R. S. Ellis, et al. COSMOS: Hubble Space Telescope Observations. ApJS, volume 172(1):38–45, 2007a. doi:10.1086/516580.

N. Scoville, H. Aussel, M. Brusa, P. Capak, C. M. Carollo, M. Elvis, M. Giavalisco, L. Guzzo, G. Hasinger, C. Impey, J. P. Kneib, O. LeFevre, S. J. Lilly, B. Mobasher, A. Renzini, et al. The Cosmic Evolution Survey (COSMOS): Overview. ApJS, volume 172(1):1–8, 2007b. doi:10.1086/516585.

X. Shen, P. F. Hopkins, C.-A. Faucher-Giguère, D. M. Alexander, G. T. Richards, N. P. Ross, and R. C. Hickox. The bolometric quasar luminosity function at z = 0-7. MNRAS, volume 495(3):3252–3275, 2020. doi:10.1093/mnras/staa1381.

X. Shen, M. Vogelsberger, M. Boylan-Kolchin, S. Tacchella, and R. Kannan. The impact of UV variability on the abundance of bright galaxies at z $\geq$ 9. MNRAS, volume 525(3):3254–3261, 2023. doi:10.1093/mnras/stad2508.

T. Shibuya, M. Ouchi, and Y. Harikane. Morphologies of ∼190,000 Galaxies at z = 0-10 Revealed with HST Legacy Data. I. Size Evolution. ApJS, volume 219(2):15, 2015. doi:10.1088/0067-0049/219/2/15.

S. Shin, M. Im, and Y. Kim. The Quasar Luminosity Function at z 5 via Deep Learning and Bayesian Information Criterion. ApJ, volume 937(1):32, 2022. doi:10.3847/1538-4357/ac854b.

M. Shuntov, H. J. McCracken, R. Gavazzi, C. Laigle, J. R. Weaver, I. Davidzon, O. Ilbert, O. B. Kauffmann, A. Faisst, Y. Dubois, A. M. Koekemoer, A. Moneti, B. Milvang-Jensen, B. Mobasher, D. B. Sanders, et al. COSMOS2020: Cosmic evolution of the stellar-to-halo mass relation for central and satellite galaxies up to z $\sim$ 5. A&A, volume 664:A61, 2022. doi:10.1051/0004-6361/202243136.

R. Smit, R. J. Bouwens, S. Carniani, P. A. Oesch, I. Labbé, G. D. Illingworth, P. van der Werf, L. D. Bradley, V. Gonzalez, J. A. Hodge, B. W. Holwerda, R. Maiolino, and W. Zheng. Rotation in [C II]-emitting gas in two galaxies at a redshift of 6.8. Nature, volume 553(7687):178–181, 2018. doi:10.1038/nature24631.

P. M. Solomon, D. Downes, and S. J. E. Radford. Warm Molecular Gas in the Primeval Galaxy IRAS 10214+4724. ApJ, volume 398:L29, 1992. doi:10.1086/186569.

R. S. Somerville, G. Popping, and S. C. Trager. Star formation in semi-analytic galaxy formation models with multiphase gas. Monthly Notices of the Royal Astronomical Society, volume 453(4):4338–4368, 2018. http://dx.doi.org/10.1093/mnras/stv1877.

L. Sommovigo, A. Ferrara, S. Carniani, A. Pallottini, P. Dayal, E. Pizzati, M. Ginolfi, V. Markov, and A. Faisst. A new look at the infrared properties of z 5 galaxies. MNRAS, 2022a. doi:10.1093/mnras/stac2997.

L. Sommovigo, A. Ferrara, S. Carniani, A. Zanella, A. Pallottini, S. Gallerani, and L. Vallini. Dust temperature in ALMA [C II]-detected high-z galaxies. MNRAS, volume 503(4):4878–4891, 2021. doi:10.1093/mnras/stab720.

L. Sommovigo, A. Ferrara, A. Pallottini, P. Dayal, R. J. Bouwens, R. Smit, E. da Cunha, I. De Looze, R. A. A. Bowler, J. Hodge, H. Inami, P. Oesch, R. Endsley, V. Gonzalez, S. Schouws, et al. The ALMA REBELS Survey: cosmic dust temperature evolution out to z 7. MNRAS, volume 513(3):3122–3135, 2022b. doi:10.1093/mnras/stac302.

L. Sommovigo, A. Ferrara, A. Pallottini, P. Dayal, R. J. Bouwens, R. Smit, E. da Cunha, I. De Looze, R. A. A. Bowler, J. Hodge, H. Inami, P. Oesch, R. Endsley, V. Gonzalez, S. Schouws, et al. The REBELS ALMA Survey: cosmic dust temperature evolution out to z 7. MNRAS, 2022c. doi:10.1093/mnras/stac302.

M. Song, S. L. Finkelstein, M. L. N. Ashby, A. Grazian, Y. Lu, C. Papovich, B. Salmon, R. S. Somerville, M. Dickinson, K. Duncan, S. M. Faber, G. G. Fazio, H. C. Ferguson, A. Fontana, Y. Guo, et al. The Evolution of the Galaxy Stellar Mass Function at z = 4-8: A Steepening Low-mass-end Slope with Increasing Redshift. ApJ, volume 825(1):5, 2016. doi:10.3847/0004-637X/825/1/5.

M. Sparre, C. C. Hayward, V. Springel, M. Vogelsberger, S. Genel, P. Torrey, D. Nelson, D. Sijacki, and L. Hernquist. The star formation main sequence and stellar mass assembly of galaxies in the Illustris simulation. MNRAS, volume 447(4):3548–3563, 2015. doi:10.1093/mnras/stu2713.

J. S. Speagle, C. L. Steinhardt, P. L. Capak, and J. D. Silverman. A Highly Consistent Framework for the Evolution of the Star-Forming "Main Sequence" from z ∼0-6. ApJS, volume 214(2):15, 2014. doi:10.1088/0067-0049/214/2/15.

V. Springel. The cosmological simulation code GADGET-2. MNRAS, volume 364(4):1105–1134, 2005. doi:10.1111/j.1365-2966.2005.09655.x.

V. Springel. E pur si muove: Galilean-invariant cosmological hydrodynamical simulations on a moving mesh. MNRAS, volume 401(2):791–851, 2010. doi:10.1111/j.1365-2966.2009.15715.x.

V. Springel and L. Hernquist. Cosmological smoothed particle hydrodynamics simulations: a hybrid multiphase model for star formation. MNRAS, volume 339:289–311, 2003. doi:10.1046/j.1365-8711.2003.06206.x.

V. Springel, R. Pakmor, O. Zier, and M. Reinecke. Simulating cosmic structure formation with the GADGET-4 code. MNRAS, volume 506(2):2871–2949, 2021. doi:10.1093/mnras/stab1855.

V. Springel, N. Yoshida, and S. D. M. White. GADGET: a code for collisionless and gasdynamical cosmological simulations. New Astron., volume 6(2):79–117, 2001. doi:10.1016/S1384-1076(01)00042-2.

M. Stefanon, R. Bouwens, R. A. A. Bowler, Y. Fudamoto, V. Gonzalez, L. Graziani, J. Hodge, H. Inami, P. Oesch, R. Schneider, S. Schouws, R. Smit, D. P. Stark, and P. van der Werf. A Spatially Resolved View of Star Formation in Two Luminous z>=8 Galaxies showing Prominent Dust-Continuum Emission. HST Proposal. Cycle 29, ID. #16879, 2021a. https://ui.adsabs.harvard.edu/abs/2021hst..prop16879S.

M. Stefanon, R. J. Bouwens, I. Labbé, G. D. Illingworth, V. Gonzalez, and P. A. Oesch. Galaxy Stellar Mass Functions from z 10 to z 6 using the Deepest Spitzer/Infrared Array Camera Data: No Significant Evolution in the Stellar-to-halo Mass Ratio of Galaxies in the First Gigayear of Cosmic Time. ApJ, volume 922(1):29, 2021b. doi:10.3847/1538-4357/ac1bb6.

M. Stefanon, I. Labbé, R. J. Bouwens, P. Oesch, M. L. N. Ashby, K. I. Caputi, M. Franx, J. P. U. Fynbo, G. D. Illingworth, O. Le Fèvre, D. Marchesini, H. J. McCracken, B. Milvang-Jensen, A. Muzzin, and P. van Dokkum. The Brightest z $\gtrsim$ 8 Galaxies over the COSMOS UltraVISTA Field. ApJ, volume 883(1):99, 2019. doi:10.3847/1538-4357/ab3792.

C. L. Steinhardt, V. Kokorev, V. Rusakov, E. Garcia, and A. Sneppen. Templates for Fitting Photometry of Ultra-High-Redshift Galaxies. arXiv e-prints, arXiv:2208.07879, 2022. https://ui.adsabs.harvard.edu/abs/2022arXiv220807879S.

C. L. Steinhardt, A. Sneppen, T. Clausen, H. Katz, M. P. Rey, and J. Stahlschmidt. The Highest-Redshift Balmer Breaks as a Test of ΛCDM. arXiv e-prints, arXiv:2305.15459, 2023. doi:10.48550/arXiv.2305.15459.

C. L. Steinhardt, J. S. Speagle, P. Capak, J. D. Silverman, M. Carollo, J. Dunlop, Y. Hashimoto, B.-C. Hsieh, O. Ilbert, O. Le Fevre, E. Le Floc'h, N. Lee, L. Lin, Y.-T. Lin, D. Masters, et al. Star Formation at $4 < z < 6$ from the Spitzer Large Area Survey with Hyper-Suprime-Cam (SPLASH). ApJ, volume 791(2):L25, 2014. doi:10.1088/2041-8205/791/2/L25.

K. R. Stewart, T. Kaufmann, J. S. Bullock, E. J. Barton, A. H. Maller, J. Diemand, and J. Wadsley. Orbiting Circumgalactic Gas as a Signature of Cosmological Accretion. ApJ, volume 738(1):39, 2011. doi:10.1088/0004-637X/738/1/39.

M. A. Strauss, D. H. Weinberg, R. H. Lupton, V. K. Narayanan, J. Annis, M. Bernardi, M. Blanton, S. Burles, A. J. Connolly, J. Dalcanton, M. Doi, D. Eisenstein, J. A. Frieman, M. Fukugita, J. E. Gunn, et al. Spectroscopic Target Selection in the Sloan Digital Sky Survey: The Main Galaxy Sample. AJ, volume 124(3):1810–1824, 2002. doi:10.1086/342343.

Y. Sugahara, M. Ouchi, Y. Harikane, N. Bouché, P. D. Mitchell, and J. Blaizot. Fast Outflows Identified in Early Star-forming Galaxies at $z = 5$-6. ApJ, volume 886(1):29, 2019. doi:10.3847/1538-4357/ab49fe.

F. Sun, E. Egami, N. Pirzkal, M. Rieke, M. Boyer, M. Correnti, M. Gennaro, J. Girard, T. P. Greene, D. Kelly, A. M. Koekemoer, J. Leisenring, K. Misselt, N. Nikolov, T. L. Roellig, et al. First Peek with JWST/NIRCam Wide-field Slitless Spectroscopy: Serendipitous Discovery of a Strong [O III]/Hα Emitter at $z = 6.11$. ApJ, volume 936(1):L8, 2022. doi:10.3847/2041-8213/ac8938.

G. Sun, C.-A. Faucher-Giguère, C. C. Hayward, and X. Shen. Seen and unseen: bursty star formation and its implications for observations of high-redshift galaxies with JWST. MNRAS, volume 526(2):2665–2672, 2023. doi:10.1093/mnras/stad2902.

G. Sun and S. R. Furlanetto. Constraints on the star formation efficiency of galaxies during the epoch of reionization. MNRAS, volume 460(1):417–433, 2016. doi:10.1093/mnras/stw980.

R. S. Sutherland and M. A. Dopita. Cooling Functions for Low-Density Astrophysical Plasmas. ApJS, volume 88:253, 1993. doi:10.1086/191823.

S. Tacchella, S. Bose, C. Conroy, D. J. Eisenstein, and B. D. Johnson. A Redshift-independent Efficiency Model: Star Formation and Stellar Masses in Dark Matter Halos at $z \gtrsim 4$. ApJ, volume 868(2):92, 2018. doi:10.3847/1538-4357/aae8e0.

S. Tacchella, D. J. Eisenstein, K. Hainline, B. D. Johnson, W. M. Baker, J. M. Helton, B. Robertson, K. A. Suess, Z. Chen, E. Nelson, D. Puskás, F. Sun, S. Alberts, E. Egami, R. Hausen, et al. JADES Imaging of GN-z11: Revealing the Morphology and Environment of a Luminous Galaxy 430 Myr after the Big Bang. ApJ, volume 952(1):74, 2023. doi:10.3847/1538-4357/acdbc6.

S. Tacchella, S. L. Finkelstein, M. Bagley, M. Dickinson, H. C. Ferguson, M. Giavalisco, L. Graziani, N. A. Grogin, N. Hathi, T. A. Hutchison, I. Jung, A. M. Koekemoer, R. L. Larson, C. Papovich, N. Pirzkal, et al. On the Stellar Populations of Galaxies at z = 9-11: The Growth of Metals and Stellar Mass at Early Times. ApJ, volume 927(2):170, 2022. doi:10.3847/1538-4357/ac4cad.

S. Tacchella, M. Trenti, and C. M. Carollo. A Physical Model for the 0 $<\sim$z $<\sim$8 Redshift Evolution of the Galaxy Ultraviolet Luminosity and Stellar Mass Functions. ApJ, volume 768(2):L37, 2013. doi:10.1088/2041-8205/768/2/L37.

Y. Tamura, K. Mawatari, T. Hashimoto, A. K. Inoue, E. Zackrisson, L. Christensen, C. Binggeli, Y. Matsuda, H. Matsuo, T. T. Takeuchi, R. S. Asano, K. Sunaga, I. Shimizu, T. Okamoto, N. Yoshida, et al. Detection of the Far-infrared [O III] and Dust Emission in a Galaxy at Redshift 8.312: Early Metal Enrichment in the Heart of the Reionization Era. ApJ, volume 874:27, 2019. doi:10.3847/1538-4357/ab0374.

L. A. M. Tasca, O. Le Fèvre, N. P. Hathi, D. Schaerer, O. Ilbert, G. Zamorani, B. C. Lemaux, P. Cassata, B. Garilli, V. Le Brun, D. Maccagni, L. Pentericci, R. Thomas, E. Vanzella, E. Zucca, et al. The evolving star formation rate: $M_\star$ relation and sSFR since z $\approx$ 5 from the VUDS spectroscopic survey. A&A, volume 581:A54, 2015. doi:10.1051/0004-6361/201425379.

L. A. M. Tasca, O. Le Fèvre, C. López-Sanjuan, P. W. Wang, P. Cassata, B. Garilli, O. Ilbert, V. Le Brun, B. C. Lemaux, D. Maccagni, L. Tresse, S. Bardelli, T. Contini, S. Charlot, O. Cucciati, et al. Evidence for major mergers of galaxies at 2 $\lesssim$ z $<$ 4 in the VVDS and VUDS surveys. A&A, volume 565:A10, 2014. doi:10.1051/0004-6361/201321507.

L. A. M. Tasca, O. Le Fèvre, B. Ribeiro, R. Thomas, C. Moreau, P. Cassata, B. Garilli, V. Le Brun, B. C. Lemaux, D. Maccagni, L. Pentericci, D. Schaerer, E. Vanzella, G. Zamorani, E. Zucca, et al. The VIMOS Ultra Deep Survey first data release: Spectra and spectroscopic redshifts of 698 objects up to z_{spec} 6 in CANDELS. A&A, volume 600:A110, 2017. doi:10.1051/0004-6361/201527963.

R. Teyssier. Cosmological hydrodynamics with adaptive mesh refinement. A new high resolution code called RAMSES. A&A, volume 385:337–364, 2002. doi:10.1051/0004-6361:20011817.

R. Teyssier. RAMSES: A new N-body and hydrodynamical code. Astrophysics Source Code Library, record ascl:1011.007, 2010. https://ui.adsabs.harvard.edu/abs/2010ascl.soft11007T.

A. R. Tomczak, R. F. Quadri, K.-V. H. Tran, I. Labbé, C. M. S. Straatman, C. Papovich, K. Glazebrook, R. Allen, G. B. Brammer, M. Cowley, M. Dickinson, D. Elbaz, H. Inami, G. G. Kacprzak, G. E. Morrison, et al. The SFR-M* Relation and Empirical Star-Formation Histories from ZFOURGE* at 0.5 $<$ z $<$ 4. ApJ, volume 817(2):118, 2016. doi:10.3847/0004-637X/817/2/118.

M. W. Topping, D. P. Stark, R. Endsley, R. J. Bouwens, S. Schouws, R. Smit, M. Stefanon, H. Inami, R. A. A. Bowler, P. Oesch, V. Gonzalez, P. Dayal, E. da

Cunha, H. Algera, P. van der Werf, et al. The ALMA REBELS Survey: specific star formation rates in the reionization era. MNRAS, volume 516(1):975–991, 2022. doi:10.1093/mnras/stac2291.

L. Tornatore, S. Borgani, K. Dolag, and F. Matteucci. Chemical enrichment of galaxy clusters from hydrodynamical simulations. MNRAS, volume 382(3):1050–1072, 2007a. doi:10.1111/j.1365-2966.2007.12070.x.

L. Tornatore, A. Ferrara, and R. Schneider. Population III stars: hidden or disappeared? MNRAS, volume 382(3):945–950, 2007b. doi:10.1111/j.1365-2966.2007.12215.x.

C. Tortora, L. K. Hunt, and M. Ginolfi. Scaling relations and baryonic cycling in local star-forming galaxies. III. Outflows, effective yields, and metal loading factors. A&A, volume 657:A19, 2022. doi:10.1051/0004-6361/202140414.

T. Treu, G. Roberts-Borsani, M. Bradac, G. Brammer, A. Fontana, A. Henry, C. Mason, T. Morishita, L. Pentericci, X. Wang, A. Acebron, M. Bagley, P. Bergamini, D. Belfiori, A. Bonchi, et al. The GLASS-JWST Early Release Science Program. I. Survey Design and Release Plans. ApJ, volume 935(2):110, 2022. doi:10.3847/1538-4357/ac8158.

A. Trinca, R. Schneider, R. Valiante, L. Graziani, A. Ferrotti, K. Omukai, and S. Chon. Exploring the nature of UV-bright $zrsim10$ galaxies detected by JWST: star formation, black hole accretion, or a non universal IMF? arXiv e-prints, arXiv:2305.04944, 2023. doi:10.48550/arXiv.2305.04944.

A. Trinca, R. Schneider, R. Valiante, L. Graziani, L. Zappacosta, and F. Shankar. The low-end of the black hole mass function at cosmic dawn. MNRAS, volume 511(1):616–640, 2022. doi:10.1093/mnras/stac062.

J. A. A. Trussler, N. J. Adams, C. J. Conselice, L. Ferreira, D. Austin, R. Bhatawdekar, J. Caruana, C. C. Lovell, W. J. Roper, A. Verma, A. P. Vijayan, and S. M. Wilkins. Seeing sharper and deeper: JWST's first glimpse of the photometric and spectroscopic properties of galaxies in the epoch of reionisation. arXiv e-prints, arXiv:2207.14265, 2022. https://ui.adsabs.harvard.edu/abs/2022arXiv220714265T.

J. Tumlinson, M. S. Peeples, and J. K. Werk. The Circumgalactic Medium. ARA&A, volume 55(1):389–432, 2017. doi:10.1146/annurev-astro-091916-055240.

G. Ucci, P. Dayal, A. Hutter, C. Kobayashi, S. Gottloeber, G. Yepes, L. Hunt, L. Legrand, and C. Tortora. Astraeus V: The emergence and evolution of metallicity scaling relations during the Epoch of Reionization. arXiv e-prints, arXiv:2112.02115, 2021. https://ui.adsabs.harvard.edu/abs/2021arXiv211202115U.

R. Valiante, R. Schneider, S. Salvadori, and S. Gallerani. High-redshift quasars host galaxies: is there a stellar mass crisis? MNRAS, volume 444:2442–2455, 2014. doi:10.1093/mnras/stu1613.

L. Vallini, A. Ferrara, A. Pallottini, S. Carniani, and S. Gallerani. Star formation law in the epoch of reionization from [C II] and C III] lines. MNRAS, volume 495(1):L22–L26, 2020. doi:10.1093/mnrasl/slaa047.

F. van de Voort, V. Springel, N. Mandelker, F. C. van den Bosch, and R. Pakmor. Cosmological simulations of the circumgalactic medium with 1 kpc resolution: enhanced H I column densities. MNRAS, volume 482(1):L85–L89, 2019. doi:10.1093/mnrasl/sly190.

M. H. P. M. van Putten. The Fast and Furious in JWST high-z galaxies. arXiv e-prints, arXiv:2312.16692, 2023. doi:10.48550/arXiv.2312.16692.

E. Vanzella, F. Loiacono, P. Bergamini, U. Meštrić, M. Castellano, P. Rosati, M. Meneghetti, C. Grillo, F. Calura, M. Mignoli, M. Bradač, A. Adamo, G. Rihtaršič, M. Dickinson, M. Gronke, et al. An extremely metal-poor star complex in the reionization era: Approaching Population III stars with JWST. A&A, volume 678:A173, 2023. doi:10.1051/0004-6361/202346981.

T. Velusamy and W. D. Langer. Origin and z-distribution of Galactic diffuse [C II] emission. A&A, volume 572:A45, 2014. doi:10.1051/0004-6361/201424350.

A. Venditti, V. Bromm, S. L. Finkelstein, L. Graziani, and R. Schneider. The first fireworks: A roadmap to Population III stars during the Epoch of Reionization through Pair-Instability Supernovae. MNRAS, 2023a. doi:10.1093/mnras/stad3513.

A. Venditti, L. Graziani, R. Schneider, L. Pentericci, C. Di Cesare, U. Maio, and K. Omukai. A needle in a haystack? Catching Population III stars in the epoch of reionization: I. Population III star-forming environments. MNRAS, volume 522(3):3809–3830, 2023b. doi:10.1093/mnras/stad1201.

E. Ventou, T. Contini, N. Bouché, B. Epinat, J. Brinchmann, R. Bacon, H. Inami, D. Lam, A. Drake, T. Garel, L. Michel-Dansac, R. Pello, M. Steinmetz, P. M. Weilbacher, L. Wisotzki, et al. The MUSE Hubble Ultra Deep Field Survey. IX. Evolution of galaxy merger fraction since z ≈ 6. A&A, volume 608:A9, 2017. doi:10.1051/0004-6361/201731586.

E. M. Ventura, Y. Qin, S. Balu, and J. S. B. Wyithe. Semi-analytic modelling of Pop. III star formation and metallicity evolution - I. Impact on the UV luminosity functions at z = 9 - 16. MNRAS, 2024. doi:10.1093/mnras/stae567.

P. Ventura, A. Zeppieri, I. Mazzitelli, and F. D'Antona. Full spectrum of turbulence convective mixing: I. theoretical main sequences and turn-off for 0.6 /\15 M_. A&A, volume 334:953–968, 1998. https://ui.adsabs.harvard.edu/abs/1998A&A...334..953V.

A. P. Vijayan, S. J. Clay, P. A. Thomas, R. M. Yates, S. M. Wilkins, and B. M. Henriques. Detailed dust modelling in the L-GALAXIES semi-analytic model of galaxy formation. MNRAS, volume 489(3):4072–4089, 2019. doi:10.1093/mnras/stz1948.

M. Volonteri. Formation of supermassive black holes. A&A Rev., volume 18(3):279–315, 2010. doi:10.1007/s00159-010-0029-x.

J. W. Wadsley, B. W. Keller, and T. R. Quinn. Gasoline2: a modern smoothed particle hydrodynamics code. MNRAS, volume 471(2):2357–2369, 2017. doi:10.1093/mnras/stx1643.

X. Wang, C. Cheng, J. Ge, X.-L. Meng, E. Daddi, H. Yan, T. Jones, M. A. Malkan, P. Arrabal Haro, G. Brammer, and M. Oguri. A strong He II λ1640 emitter with extremely blue UV spectral slope at $z = 8.16$: presence of Pop III stars? arXiv e-prints, arXiv:2212.04476, 2022. doi:10.48550/arXiv.2212.04476.

Y. Wang, E. O. Nadler, Y.-Y. Mao, S. Adhikari, R. H. Wechsler, and P. Behroozi. UniverseMachine: Predicting Galaxy Star Formation over Seven Decades of Halo Mass with Zoom-in Simulations. ApJ, volume 915(2):116, 2021. doi:10.3847/1538-4357/ac024a.

D. Watson, L. Christensen, K. K. Knudsen, J. Richard, A. Gallazzi, and M. J. Michałowski. A dusty, normal galaxy in the epoch of reionization. Nature, volume 519:327–330, 2015. doi:10.1038/nature14164.

K. E. Whitaker, M. Franx, J. Leja, P. G. van Dokkum, A. Henry, R. E. Skelton, M. Fumagalli, I. G. Momcheva, G. B. Brammer, I. Labbé, E. J. Nelson, and J. R. Rigby. Constraining the Low-mass Slope of the Star Formation Sequence at $0.5 < z < 2.5$. ApJ, volume 795(2):104, 2014. doi:10.1088/0004-637X/795/2/104.

S. D. M. White and M. J. Rees. Core condensation in heavy halos: a two-stage theory for galaxy formation and clustering. MNRAS, volume 183:341–358, 1978. doi:10.1093/mnras/183.3.341.

L. Whitler, D. P. Stark, R. Endsley, J. Leja, S. Charlot, and J. Chevallard. Star formation histories of UV-luminous galaxies at z $\sim$ 6.8: implications for stellar mass assembly at early cosmic times. MNRAS, volume 519(4):5859–5881, 2023. doi:10.1093/mnras/stad004.

S. M. Wilkins, A. P. Vijayan, C. C. Lovell, W. J. Roper, D. Irodotou, J. Caruana, L. T. C. Seeyave, J. K. Kuusisto, P. A. Thomas, and S. A. K. Parris. First light and reionisation epoch simulations (FLARES) V: The redshift frontier. MNRAS, 2022. doi:10.1093/mnras/stac3280.

C. C. Williams, E. Curtis-Lake, K. N. Hainline, J. Chevallard, B. E. Robertson, S. Charlot, R. Endsley, D. P. Stark, C. N. A. Willmer, S. Alberts, R. Amorin, S. Arribas, S. Baum, A. Bunker, S. Carniani, et al. The JWST Extragalactic Mock Catalog: Modeling Galaxy Populations from the UV through the Near-IR over 13 Billion Years of Cosmic History. ApJS, volume 236(2):33, 2018. doi:10.3847/1538-4365/aabcbb.

J. H. Wise and T. Abel. ENZO+MORAY: radiation hydrodynamics adaptive mesh refinement simulations with adaptive ray tracing. MNRAS, volume 414(4):3458–3491, 2011. doi:10.1111/j.1365-2966.2011.18646.x.

E. Wisnioski, N. M. Förster Schreiber, S. Wuyts, E. Wuyts, K. Bandara, D. Wilman, R. Genzel, R. Bender, R. Davies, M. Fossati, P. Lang, J. T. Mendel, A. Beifiori,

G. Brammer, J. Chan, et al. The KMOS^{3D} Survey: Design, First Results, and the Evolution of Galaxy Kinematics from 0.7 <= z <= 2.7. ApJ, volume 799(2):209, 2015. doi:10.1088/0004-637X/799/2/209.

J. Witstok, R. Smit, R. Maiolino, N. Kumari, M. Aravena, L. Boogaard, R. Bouwens, S. Carniani, J. A. Hodge, G. C. Jones, M. Stefanon, P. van der Werf, and S. Schouws. Dual constraints with ALMA: new [O III] 88-μm and dust-continuum observations reveal the ISM conditions of luminous LBGs at z 7. MNRAS, volume 515(2):1751–1773, 2022. doi:10.1093/mnras/stac1905.

E. Witten. Dynamical breaking of supersymmetry. Nuclear Physics B, volume 188(3):513–554, 1981. doi:10.1016/0550-3213(81)90006-7.

G. S. Wright, G. H. Rieke, A. Glasse, M. Ressler, M. García Marín, J. Aguilar, S. Alberts, J. Álvarez-Márquez, I. Argyriou, K. Banks, P. Baudoz, A. Boccaletti, P. Bouchet, J. Bouwman, B. R. Brandl, et al. The Mid-infrared Instrument for JWST and Its In-flight Performance. PASP, volume 135(1046):048003, 2023. doi:10.1088/1538-3873/acbe66.

G. S. Wright, D. Wright, G. B. Goodson, G. H. Rieke, G. Aitink-Kroes, J. Amiaux, A. Aricha-Yanguas, R. Azzollini, K. Banks, D. Barrado-Navascues, T. Belenguer-Davila, J. A. D. L. Blommaert, P. Bouchet, B. R. Brandl, L. Colina, et al. The Mid-Infrared Instrument for the James Webb Space Telescope, II: Design and Build. PASP, volume 127(953):595, 2015. doi:10.1086/682253.

C. K. Xu, Y. Zhao, N. Scoville, P. Capak, N. Drory, and Y. Gao. Major-merger Galaxy Pairs in the COSMOS Field—Mass-dependent Merger Rate Evolution since z = 1. ApJ, volume 747(2):85, 2012. doi:10.1088/0004-637X/747/2/85.

H. Yan, Z. Ma, C. Ling, C. Cheng, J.-s. Huang, and A. Zitrin. First Batch of Candidate Galaxies at Redshifts 11 to 20 Revealed by the James Webb Space Telescope Early Release Observations. arXiv e-prints, arXiv:2207.11558, 2022. https://ui.adsabs.harvard.edu/abs/2022arXiv220711558Y.

R. M. Yates, C. Péroux, and D. Nelson. Cosmic metal density evolution in neutral gas: insights from observations and cosmological simulations. MNRAS, volume 508(3):3535–3550, 2021. doi:10.1093/mnras/stab2837.

L. Y. A. Yung, R. S. Somerville, S. L. Finkelstein, G. Popping, R. Davé, A. Venkatesan, P. Behroozi, and H. C. Ferguson. Semi-analytic forecasts for JWST - IV. Implications for cosmic reionization and LyC escape fraction. MNRAS, volume 496(4):4574–4592, 2020a. doi:10.1093/mnras/staa1800.

L. Y. A. Yung, R. S. Somerville, S. L. Finkelstein, S. M. Wilkins, and J. P. Gardner. Are the ultra-high-redshift galaxies at z > 10 surprising in the context of standard galaxy formation models? MNRAS, volume 527(3):5929–5948, 2024. doi:10.1093/mnras/stad3484.

L. Y. A. Yung, R. S. Somerville, G. Popping, and S. L. Finkelstein. Semi-analytic forecasts for JWST - III. Intrinsic production efficiency of Lyman-continuum radiation. MNRAS, volume 494(1):1002–1017, 2020b. doi:10.1093/mnras/staa714.

L. Y. A. Yung, R. S. Somerville, G. Popping, S. L. Finkelstein, H. C. Ferguson, and R. Davé. Semi-analytic forecasts for JWST - II. Physical properties and scaling relations for galaxies at z = 4-10. MNRAS, volume 490(2):2855–2879, 2019. doi:10.1093/mnras/stz2755.

E. Zackrisson, A. Hultquist, A. Kordt, J. M. Diego, A. Nabizadeh, A. Vikaeus, A. K. Meena, A. Zitrin, G. Volpato, E. Lundqvist, B. Welch, G. Costa, and R. A. Windhorst. The detection and characterization of highly magnified stars with JWST: Prospects of finding Population III. arXiv e-prints, arXiv:2312.09289, 2023. doi:10.48550/arXiv.2312.09289.

H. J. Zahid, M. J. Geller, L. J. Kewley, H. S. Hwang, D. G. Fabricant, and M. J. Kurtz. The Chemical Evolution of Star-forming Galaxies over the Last 11 Billion Years. ApJ, volume 771(2):L19, 2013. doi:10.1088/2041-8205/771/2/L19.

J. A. Zavala, V. Buat, C. M. Casey, D. Burgarella, S. L. Finkelstein, M. B. Bagley, L. Ciesla, E. Daddi, M. Dickinson, H. C. Ferguson, M. Franco, E. F. Jim'enez-Andrade, J. S. Kartaltepe, A. M. Koekemoer, A. Le Bail, et al. A dusty starburst masquerading as an ultra-high redshift galaxy in JWST CEERS observations. arXiv e-prints, arXiv:2208.01816, 2022. https://ui.adsabs.harvard.edu/abs/2022arXiv220801816Z.

J. A. Zavala, C. M. Casey, S. M. Manning, M. Aravena, M. Bethermin, K. I. Caputi, D. L. Clements, E. d. Cunha, P. Drew, S. L. Finkelstein, S. Fujimoto, C. Hayward, J. Hodge, J. S. Kartaltepe, K. Knudsen, et al. The Evolution of the IR Luminosity Function and Dust-obscured Star Formation over the Past 13 Billion Years. ApJ, volume 909(2):165, 2021. doi:10.3847/1538-4357/abdb27.

Y. B. Zel'dovich. Gravitational instability: An approximate theory for large density perturbations. A&A, volume 5:84–89, 1970. https://ui.adsabs.harvard.edu/abs/1970A&A.....5...84Z.

W. Zheng, M. Postman, A. Zitrin, J. Moustakas, X. Shu, S. Jouvel, O. Høst, A. Molino, L. Bradley, D. Coe, L. A. Moustakas, M. Carrasco, H. Ford, N. Benítez, T. R. Lauer, et al. A magnified young galaxy from about 500 million years after the Big Bang. Nature, volume 489(7416):406–408, 2012. doi:10.1038/nature11446.

S. Zhukovska, H. P. Gail, and M. Trieloff. Evolution of interstellar dust and stardust in the solar neighbourhood. A&A, volume 479(2):453–480, 2008. doi:10.1051/0004-6361:20077789.

F. Ziparo, A. Ferrara, L. Sommovigo, and M. Kohandel. Blue monsters. Why are JWST super-early, massive galaxies so blue? MNRAS, volume 520(2):2445–2450, 2023. doi:10.1093/mnras/stad125.

Acknowledgements

I am deeply grateful to my thesis advisors, Prof. Raffaella Schneider, Dr. Luca Graziani and Dr. Michele Ginolfi, for their unwavering support and invaluable guidance throughout these years. Thanks for all the engaging discussions, meetings and the wealth of ideas and projects that have shaped both this thesis and my PhD activity.

I also want to thank all the people I have collaborated with since I visited the European Southern Observatory, where the ALMA data analysis took place. A special mention is owed to the GESO group.

I also wish to express my gratitude to the co-authors of the scientific publications included in this thesis, whose contributions and suggestions have significantly enhanced the quality of our work.

Lastly, I would like to thank the colleagues (friends) who I met during this journey. Your friendship and support have been a source of comfort during the daily challenges of doctoral life.

Claudia Di Cesare, Roma, May 2024